Searching for variable sources in the Rapid Temporal Survey

Thomas Barclay

Mullard Space Science Laboratory

Department of Space and Climate Physics

University College London

A thesis submitted to UCL

for the degree of Doctor of Philosophy

December 2010

I, THOMAS BARCLAY, confirm that the work presented in this thesis is my own. Where information has been derived from other sources, I confirm that this has been indicated in the thesis.

Abstract

The Rapid Temporal Survey explores the faint, variable sky. I have led the development of the data reduction and analysis pipeline for this survey and have played a leading role in the observation and analysis of follow-up data. The survey and follow-up work that is presented in this thesis. The strategy of the survey is to observe fields close to the Galactic plane at a cadence of ~1 min for around two hours down to a depth of $g' = 23$. The data presented in this thesis cover 31 square degrees of which 16 are within 10° of the Galactic plane. This is the first dedicated survey to explore this parameter space and such I have had to develop new techniques when dealing with the data. The photometry was performed using a difference imaging technique and resulted in over 3×10^6 light curves. This work primarily deals with periodic variability and with this aim I have developed a method which combines two algorithms (Lomb-Scargle and Analysis of Variance) to produce a sub-set of variable sources which contains a very low number of false positives –around 600 out of 1.2×10^5 detected variables. For sources brighter than $g' = 21$ this technique is able to detect – at a confidence above 90 per cent – variability on time-scales of less than 10 min to tens of minutes in source with semi-amplitudes of less than 0.04 mag.

Spectroscopic follow-up observations of a number of these targets has been performed and has resulted in the discovery of many different variables from several different classes of variable classes. I highlight three populations to study in more detail: short-period, variable A-stars; SX Phe and δ Scuti stars; and pulsating white dwarfs. Of particular interest are the SX Phe stars which I have found to be as far away as 30 kpc from us. I also provide a detailed examination of two variables sources: one is a dwarf nova which was discovered through quasi-periodic oscillations in quiescence, the other a pulsating white dwarf which appears to have a hot companion.

I conclude by looking to the future of the project which will continue with a similar strategy but surveying the *Kepler* field of view.

Acknowledgements

I have many people to thank for allowing me to be in the fortunate position I am now in. Firstly I would like to thank Gavin Ramsay – my supervisor, mentor and drinking buddy. He taught me many things but I think the most important were, firstly, how to be a think like a scientist, and secondly, that being a scientist and having a life are not mutually exclusive. His only failure is that I am still unable to appreciate the music of Wagner.

My thanks also go to those around me who have kept me sane in my years spent in Armagh. My office mates Eamon Scullion and Shenghua Yu, the other students who I have spent much time eating, drinking and partying with – David Perez-Suerez, Geert Barentsen, Colin Folsom, Srividya Subramanian, Caroline Pereira, Toby Hinse, N. Naslim and Kamalam Vanninathan. Equally I thank my housemates who have kept me fed and given me the most wonderful home to live in – John Butler, Prakash Atreya, Joachim Bestenlehner, Andy Pollack and John Driscoll.

My collaborators outside of Armagh also require a good deal of thanks for their assistance during my Ph.D. My particular thanks go to Pasi Hakala in Finland for help in algorithm developing and for the science meetings performed in Finnish breweries, something me and my liver will never forget! In addition I thank Ralf Napiwotzki for the assistance in fitting spectra, Gijs Nelemans for the help in space density calculations. I also wish to thank Mark Cropper at MSSL for the helpful advice and useful comments given throughout my Ph.D. and especially for reading through this thesis.

Finally I would like to thank Sarah Drew. She has given me help and advice whenever I have or haven't asked and for that I will be eternally grateful.

Contents

List of Figures

List of Tables

Chapter 1

Introduction

> We are all in the gutter, but some of us are looking at the stars.
>
> *O. Wilde, Lady Windermere's Fan, 1892*

1.1 The variable sky

1.1.1 A (very) brief history of variable star observations

Aristotle believed the heavens were eternal and perfect; he was wrong. All stars vary in brightness to some degree, be it on time-scales of milliseconds such as that seen in pulsars, or on time-scales of billions of years such as M-dwarf stars migrating across the Hertzsprung-Russell diagram. Even the amount of light we observe coming from our Sun changes over time. Eclipses by the Moon passing between the Earth and Sun have been observed since antiquity. Sun-spots have been observed since at least as early as 165 BC (Yau & Stephenson, 1988) and they have been known to appear and disappear since at least 807 AD when Benedictine monk Adelmus noted that a large spot on the solar surface remained visible for eight days (Wilson, 1917). However, many of these early observations of sun-spots which appeared and disappeared mistook the phenomena for planetary transits.

It was not till Galileo Galilei et al. (1613) observed dark patches on the solar surface with a telescope and noted they had average lifetimes of a few days, that it was confirmed that these events were intrinsic to the Sun. Since then it has been discovered that the Sun is variable on a number of different periods. Schwabe (1844) found there is an 11-year cycle in solar activity and later Carrington (1859) discovered a 25.38 day rotation period at the solar equator.

The first star, other than our Sun, to be observed to show regular changes in brightness was Mira (also known as Omicron Ceti)[1]. David Fabricius used Mira as a comparison star in 1596 when making observation of (what he thought was) Mercury (but it was probably Jupiter, Argelander, 1869). He observed Mira increase in brightness by a magnitude over the course 3 weeks. A few weeks later it disappeared from view and Fabricius assumed that it was a nova. However, when, in 1609 Mira reappeared, Fabricius realised this was not the case. Unfortunately Fabricius never gained fame for this discovery due his murder by a man he accused of stealing a goose (Poggendorff, 1863). Johann Fokkens Holwarda rediscovered the variability of Mira in 1638 and found the brightness variations occurred on an 11 month cycle. The importance of Mira to astronomy is exemplified by its name: Mira means "Wonderful" in Latin.

The development of telescopes allowed the detailed study of variable stars and has lead to the discovery of over 41,600 variable stars in our Galaxy which fit into one of over 100 different classes (Samus et al., 2009). However it has brought with it restrictions. Before the telescope, observers we able to see the whole of the visible sky but since astronomy became almost entirely telescope based the field of view has become much more restrictive. Wide-field observations were possible when using photographic plates but as the use of digital imaging became more important, our ability to observe the whole sky was lost. It was not until the development of large and mosaicked charge-coupled devices (CCDs) that was were able to regain the ability to survey the variable sky over wide scales.

There has been many wide-field variability surveys, some are still ongoing while more

[1]Much of the information on Mira comes from http://web.archive.org/web/20070405082807/http://www.aavso.org/vstar/vsots/mirahistory.shtml, a write-up of a talk by Dorrit Hoffleit in 1996

will begin operations soon. A number of these are shown in Table. 1.1. As the table shows they cover a large range in depth, cadence and coverage. Most wide-field surveys are designed for one of two purposes: detecting supernovae or finding exoplanets. In the former the cadence (time between observation) tends to be relatively long, an example of this is the Palomar Transient Factory (PTF, Law et al., 2009) whose aim is to discover transient phenomena. They use a camera which has a field of view of 7.78 deg^2 and in their primary mode of operation survey 2700 deg^2 every 5 days. The typical sources they find during this work are nova events (super, classical and dwarf) and gamma-ray burst afterglows. As these events tend to be quite faint they are able to observe objects as faint as $R = 21.0$. In comparison, exoplanet surveys tend to observe much brighter sources as they need high accuracy in their photometry. The SuperWASP survey (Pollacco et al., 2006) surveys the whole sky every night with a typical cadence of 40 min but only down to a depth of $V = 15$. PTF and SuperWASP both have modes of operation where they observe at a cadence as short as one minute but this is only done for a limited amont of sky – in the case of PTF, only for around 50,000 stars (Law et al., 2009). There are remarkably few projects that are able to observe the faint sky at short cadence. One survey that aimed to do this was the Faint Sky Variability Survey (FSVS, Groot et al., 2003). Their typical cadence was 12 min and they were able to find several thousand variables although the majority of the variable sources they found varied on time scales of hours to days (Morales-Rueda et al., 2006). There is a clear deficiency in our ability to characterise the faint sky on timescales of less than an hour. One project that aimed to address that is the Rapid Temporal Survey (RATS).

Survey	FoV [sq. deg.]	Cadence	Limiting mag [R]	Coverage sq. deg. night−1	Lifetime	Reference
Palomar Transient Factory	7.78	1 min–5 d[a]	21.0	1000	ongoing	Law et al. 2009
ROTSE-III	3.42	1 d	18.5[b]	450	ongoing	Quimby 2006
Palomar-Quest	9.4	30 min–days	21.0[c]	500	2003–08	Djorgovski et al. 2008
SDSS-II Supernova search	1.5	2d	22.6	150	2005–08	Frieman et al. 2008
Cataline Real-time Transient Survey	8	10 min–yr	19.5[d]	1200	ongoing	Drake et al. 2009
Supernova Legacy Surv1ey	5.7	3 d–5 yr	24.3	2	2003–08	Astier et al. 2006
SkyMapper	5.7	0.2 d – 1yr	19.0	1000	ongoing	Murphy et al. 2009
Pan-STARRS 3π	7	7 d	21.5	6000	ongoing	Young et al. 2008
Large Synoptic Survey Telescope	9.62	3 d	24.5	3300	starts 2014	Ivezic et al. 2008
Rapid Temporal Survey	0.28	1 min	23.0[e]	1	ongoing	**?**
Faint Sky Variability Survey	0.28	12 min	24[d]	1	1998-2001	Groot et al. 2003
SuperWASP	482	1–40 min[a]	15[b]	whole sky	ongoing	Pollacco et al. 2006

[a]Only a small amount of sky is observed at 1 min cadence
[b]Unfiltered
[c]RG610 filter
[d] V-band filter
[e] g'-band filter

Table 1.1: This is a summary of a number of un-targeted variability surveys which shows the name of the survey; the field of view in a single exposure; cadence (the time between exposures); depth (the faintest stars observed) in the R band unless stated and the dates when the survey has or will take place; the sky observed in a single night; and whether the project has finished, is ongoing or will stars soon. This table is a modified version of table 1 in Rau et al. (2009).

1.2 The RATS Project

Prior to the RATS project there had never been a systematic survey of stellar variability which could probe time-scales as short as a few minutes over an angular extent of tens of arcminutes. The strategy was to use wide-field cameras to take an image of a particular field close to the Galactic plane, but far enough away that crowding was not an issue, every minute for approximate two hours. No filter was used during the time-series observations but complementary colour information was obtained of each field in order to aid classification of variable sources (see Ramsay & Hakala, 2005, for an overview of the original project).

The primary aim of this survey was the discovery of new AM CVn systems in order that Galactic population models may be tested (see the next section for a more detailed description of AM CVn systems). AM CVn systems are binaries with orbital periods as short as 5 min and the period distribution goes up to ~65 min. Systems with periods less than ~40 min show optical modulations on periods related to their orbital period. This fact was the primary motivation for the short-cadence planned in these observations – sensitivity to modulations on a period ≤5 min.

The first epoch of observations took place on three nights in November 2003 using the Wide Field Camera on the 2.5-m Isaac Newton Telescope which is located on the Spanish island of La Palma. Twelve fields were observed which covered 3 deg^2 of the sky, most of which were roughly 20 degrees from the Galactic plane reached a depth of $V \sim 22.5$.

Photometry was performed using the AUTOPHOTOM routine (Eaton et al., 2003) and over 33,000 sources were detected. Variability detection was performed using the Lomb-Scargle algorithm (this algorithm is discussed in detail in Chapter 3). For each star the highest peak in the periodogram was divided by the mean power in the periodogram creating a 'weighted power'. Sources with a high 'weighted power' were then visually inspected and 'interesting sources' were flagged. As a test of the technique a field containing the AM CVn system, HM Cnc with a period of 321 s, was observed. HM Cnc was easily picked up by the routine as one of the most significantly variable sources.

Of the 33,000 sources, 45 were identified as having significant variability (Ramsay & Hakala, 2005). One source (RAT J0455+1305) displayed variability on a period of less than an 30 min (other than HM Cnc) – this source had a strong signal on a period of 374 s. Two sources have periods of around an hour, three sources showed an eclipse like feature while around half of the new sources showed variability on time-scales longer than an hour.

Follow-up photometric and spectroscopic observations of four of these variables were performed using the Nordic Optical Telescope, the William Herschel Telescope and the Kryoneri Telescope (Ramsay et al., 2006). Photometry of the shortest period source RAT J0455+1305 confirmed the short period and spectroscopic data revealed it to be a pulsating sub dwarf B star. The other three sources were found to be SX Phe stars.

Since this initial run a further five epochs of observations were performed. Four using the Isaac Newton Telescope and one on the ESO/MPG 2.2-m telescope at La Silla Observatory in Chile (**?**). An analysis of these data and a reanalysis of the first epoch of data are presented in this thesis.

1.3 The AM CVn stars

As mentioned in the previous section, the primary goal of the RATS project is to test the Galactic population models of AM CVn stars. AM CVn stars (or ultra-compact binaries) are binary systems consisting of two degenerate stars (or one degenerate and one semi-degenerate star) and have orbital periods less than ~65 min (Solheim, 2010). The more massive primary accretes helium-rich material from a less massive donor star and there is (almost always) no trace of hydrogen in their spectra. They are formed after one or two common envelope phases and then gradually evolve closer together, losing angular momentum due to gravitation wave radiation (in a manner proposed by Kraft et al., 1962). At the point when the stars are close enough that the secondary fills its Roche lobe, mass transfer begins (the large yellow star in Fig. 1.1 can be seen transferring mass which impacts a disc). It is at this point that the star becomes known as an AM CVn star. As the mass

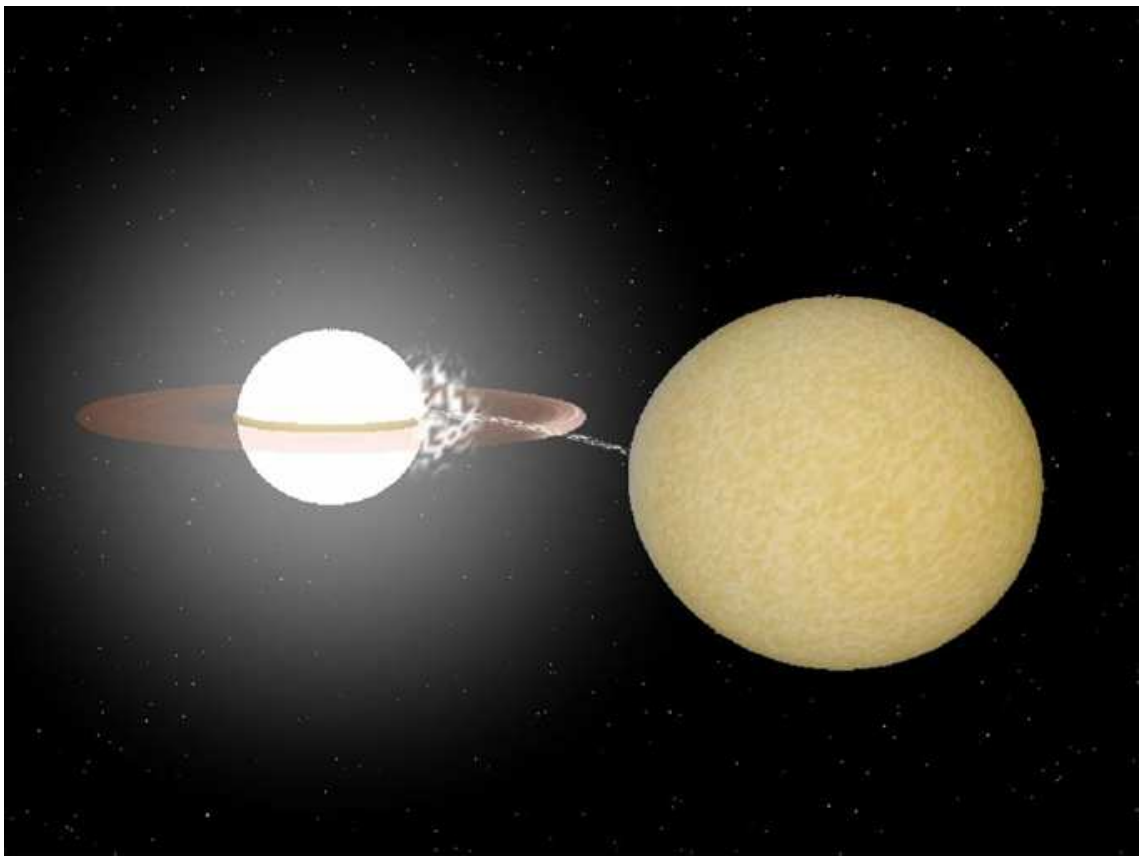

Figure 1.1: An artist's impression of an AM CVn system with an accretion stream of helium flowing from the less massive to the more massive star. Image made by Rob Hynes and Paul Groot.

transfer continues it quickly comes to dominate the evolution of the system and reverses the trend of decreasing period. The star will continue to evolve to longer periods with a decreasing rate of mass transfer. The mass transfer typically forms an accretion disc around the primary which dominates the optical emission from the system, indeed most of the light is coming from a hot-spot where the accretion stream impacts the disc. As the system evolves to longer periods the disc will shrink because of the low rate of mass transfer and light from the primary white dwarf begins to be seen. Eventually the mass transfer rate will become so low as to be undetectable and finally it will stop leaving a helium-rich white dwarf with a planetary mass object orbiting it (Solheim, 2010).

1.3.1 Known AM CVn stars

Up until the year 2000 there were only eight AM CVn systems known and all these systems were found serendipitously. However, this number has dramatically increased since the Sloan Digital Sky Survey (SDSS York et al., 2000) providing a large sample of photometric colours and spectra with which to search. There are now 26 known AM CVn systems, 13 of which were found during dedicated searches of the SDSS archive (Roelofs et al., 2006; Anderson et al., 2005, 2008; Roelofs et al., 2009; Rau et al., 2010). Below I describe the methods used to discover AM CVn systems. I do not include details of the discovery of all system and the list is not strictly chronological. Rather, iIt merely highlights the processes which have led to their discovery.

1.3.1.1 The prototype of the class – AM CVn

The first system to be discovered was the prototype for the class – AM CVn. It was noted to be a particularly blue star by Malmquist (1936). In 1947 Humason & Zwicky noted a "decidedly blue" star which they designated HZ29 in their catalogue of faint blue sources. Greenstein & Matthews (1957) found the spectrum of HZ29 was that of a "peculiar DB star" (where DB refers to a helium-rich white dwarf) with an absence of hydrogen. They note that the helium absorption lines were "shallow and so diffuse as to appear almost double" and that the star was quite hot as it has a colour of $(B - V) = -0.23$ mag. Variability was detected at the level of 0.04 mag in the B band by Smak (1967) on a period of 18 min with a "slightly distorted double sinusoidal" shape to the light curve which Paczyński (1967) interpreted as the signature of an orbital period whose evolution was dominated by gravitational wave radiation. The question of whether the period detected was truly the orbital period was not answered conclusively till 2001 when Nelemans et al. obtained time resolved spectra of AM CVn and saw clear 'S-waves' in neutral helium lines at 4471, 4387 and 4143 Å on a period of 1028.73 s (an 'S-wave' is the name for the pattern seen in spectral lines as they move oscillate from redder to bluer and back because of the Doppler shift caused by orbital motion, an example is shown in Fig. 1.2). There was no 'S-wave' modula-

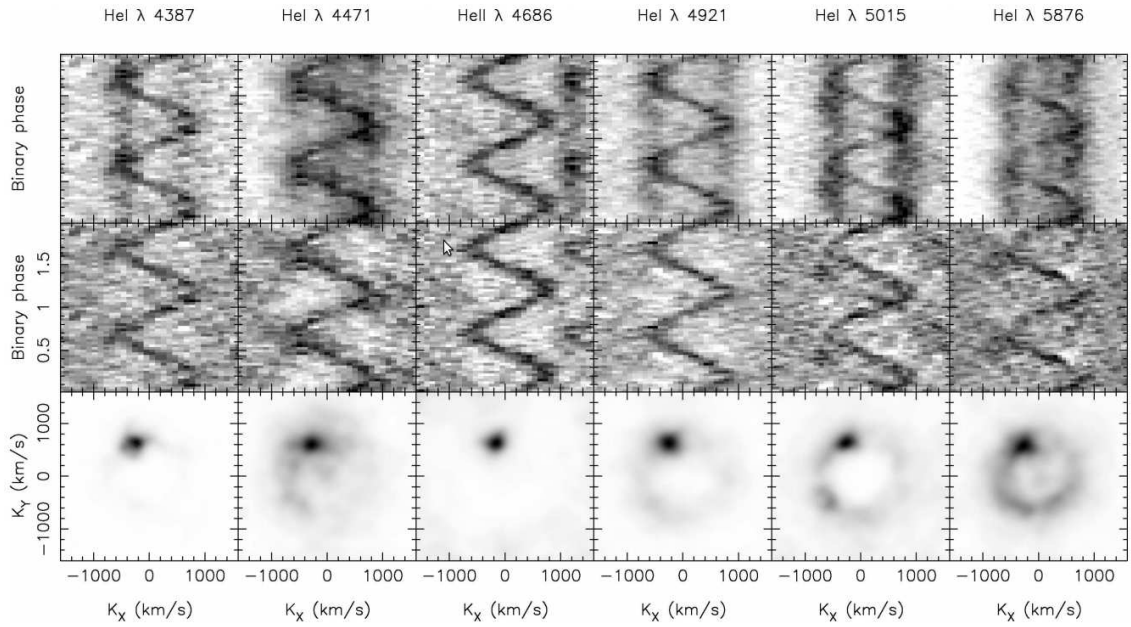

Figure 1.2: The upper row shows spectra of V406 Hya which were observed with the Very Large Telescope in Chile. They show the trailed spectra of six different Helium lines. An 'S-wave' pattern can clearly be seen oscillating about 0 km s^{-1} on a period of 2028 s which is thought to be a signitude of the orbital period of the system. The middle row shows these same spectra with an average spectrum subtracted. The lower row shows Doppler tomograms of these data. This figure is taken from Roelofs et al. (2006).

tion on the periods of 1011.4 s which Solheim et al. (1984), amongst others, had suggested was the orbital period of the system.

1.3.1.2 The next five systems – variable, blue helium stars

The next five AM CVn systems to be discovered (GP Com, CR Boo, V803 Cen, CP Eri and HP Lib) were found in a similar manner – blue stars with unexplained periodic variability and spectra devoid of hydrogen. GP Com had a number of periods on which variability was reported. Warner (1972) found variability on 20 s periods and deduced an orbital period of 6.3 h based on an erroneous suggestion of a detected eclipse on the system. Richer et al. (1973) also found short period variability, this time at 105 s but it was not till Nather et al. (1981) obtained time resolved spectra that an orbital period of 46.5 min was established. This result hints at an interesting feature of AM CVn systems: no optical variability related to the orbital period has ever been seen in the light curve of GP Com. In fact no systems with periods longer than ~40 min show photometric variability on periods related to their orbital period (any optical variability has been caused by flickering which is related to the

accretion process). These longer period systems can be discovered from their spectra and colour alone.

Nather et al. (1984) looked at photographic plates of CR Boo spanning 6 years and found the star underwent dramatic changes in brightness varying from 13.0 to 17.5 mag, spending 59 per cent of the time brighter than 14th mag. He noted changes of 0.01–0.04 mag on various periods from 745–1490 s. Wood et al. (1985, 1987) identified the source as an AM CVn type variable with an orbital period of 1487.3 s which was later refined to 1471 s (Roelofs et al., 2007a). Another source which showed similar outbursts, but spent more time in the fainter state, was V803 Cen (Westin, 1980), and was proposed as the fourth AM CVn star by O'Donoghue et al. (1987) with a period of 1613 s. V803 Cen and CR Boo highlighted the highly variable nature of AM CVn systems, both show a change in brightness of several magnitudes in a similar manner to dwarf novae. This property lead to the discovery of two more systems.

1.3.1.3 When is a supernova not a supernova?

KL Dra and V406 Hya were originally designated SN1998di and SN2003aw. As is suggested by these initial designations, they were thought to be supernovae. Schwartz (1998) detected a 16.8 mag source which had not been present in an image taken 11 days previously with a limiting magnitude of 19. However a spectrum revealed the source, which was 4 arcsec from a galaxy, was in fact a star with 3000 km s^{-1} wide neutral helium absorption lines and was likely similar in nature to CR Boo. A modulation in its light curve on a period of 25.03 min (Wood et al., 2002) revealed it to be another member of the AM CVn class of variables. Similarly, Wood-Vasey et al. (2003) found SN 2003aw in NEAT survey data but a spectrum of the source consisted of blue continuum with broad and weak HeI emission lines at nearly zero redshift (Chornock & Filippenko, 2003). Fast-photometry by Woudt & Warner (2003) showed a 2041 s period revealing its true nature. A third AM CVn system was identified because of its outbursting behaviour in SDSS survey data (SDSS J204739.40+000840.3 Prieto et al., 2006), this time the supernova designation was not prematurely applied and a spectrum revealed remarkably similar features to KL Dra.

1.3.1.4 Ultra-short period systems

V407 Vul and HM Cnc discovered as variable X-ray sources using *ROSAT* (Voges, 1992). Motch et al. (1996) discovered a 568 s modulation in the X-ray light curve of V407 Vul and Israel et al. (1999) found a 321 s modulation in HM Cnc. Both sources were initially believed to be intermediate polars and the modulation was due to the spin period of an accreting white dwarf. However no other periods were detected in either V407 Vul (Cropper et al., 1998) or HM Cnc (Burwitz & Reinsch, 2001) which led to speculation that the modulation was orbital in nature. The optical counterparts of V407 Vul (Ramsay et al., 2000) and HM Cnc (Ramsay et al., 2002a) were found to vary on the same period as the X-ray observations though the modulations were not in phase. These was still significant debate as to whether the measured period really was related to the orbital period of these systems. However, for HM Cnc at least, this debate was was settled when Roelofs et al. (2010) found the spectral lines of HM Cnc were Doppler shifted in a sinusoidal manner on the period detected in the light curve, thus confirming that the 321 s modulation was the orbital period.

It was the discovery of these ultra-short period systems that provided the impetus for the RATS project. They show optical modulation on their orbital period which changes the brightness of them by up to 30 per cent (Ramsay et al., 2002a). It is for this reason a survey was planned that would be able to detect short-period optical modulations in faint sources.

1.3.1.5 Sources found in SDSS data

The number of AM CVn systems took a huge leap forward with the release of SDSS survey data. The primary aim of SDSS was to measure redshifts of distant galaxies and quasars and in the course of this obtained photometry of around 3.5×10^8 sources and spectra of more than a 1.6 million sources, 4.6×10^5 of which are stars (Abazajian et al., 2009). These enormous quantities of data were systematically searched for AM CVn system, the spectroscopic side being primarily led by Anderson et al. (2005, 2008) and the photometric search led by Roelofs et al. (2009).

The first AM CVn systems to be discovered in the SDSS archive was found in the early release data by Roelofs et al. (2004, 2005). A search for helium emission lines was performed and from the broad lines indicating the presence of a disc SDSS J124058.03-015919.2 was tentatively classified as an AM CVn system. No photometric variation was detected (Woudt et al., 2004) suggesting that if the system were to be an AM CVn then it would likely be a longer period system similar to GP Com. Time-resolved spectra revealed the characteristic S-wave pattern which is a sure sign of orbital motion.

A search of the early release data had proved the method worked, and sure enough with more SDSS data came more AM CVn systems. Anderson et al. (2005) and the SDSS Serendipity Working Group search through 286,000 spectra visually and amongst the many unusual spectra, four had broad helium emission lines with evidence for double peakedness indicating the presence of a rotating disc. These were identified as AM CVn systems though follow-up photometric observations revealed a periodic modulation in only one of the sources – SDSS J092638.71+362402.4 (hereafter SDSS J0926). SDSS J0926 had a strong 28.3 min period, but most strikingly had sharp decreases in brightness of over 1 mag during every periodic cycle. The 28.3 min period is orbital in nature and the dips are eclipses of the hop-spot by the donor star. SDSS J0926 is an important discovery marking the first eclipsing AM CVn system to be discovered. As well as being able to derive the masses of the two components of the binary and the radius of the secondary ($M_1 = 0.85 \pm 0.04 M_\odot$, $M_2 = 0.035 \pm 0.003 M_\odot$, $R_2 = 0.047 \pm 0.001 R_\odot$, Copperwheat et al., 2011) precise timing of the eclipse will allow for a measure of the change in period over time. During the course of several years it will be possible to measure the effect gravitational wave radiation has on the period of the system from which it will be possible to test the prediction of general relativity in a similar manner as is done using observations of pulsars (e.g. Kramer et al., 2006).

Anderson et al. (2008) noted that all the AM CVn systems found in SDSS data (six up to that point) appeared in a remarkably tight range on a colour-colour diagram. Shown in Fig. 1.3 is a portion of figure 2 from Anderson et al. (2008) which shows the position of AM CVn systems as black triangles in $(u' - g')$, $(g' - r')$ colour space (a similar plot is

given in Anderson et al. (2008) for $(g'-r')$, $(r'-i')$ colour space with a similarly restrictive colour regime). This property has been used to extend the search from SDSS spectra to the photometric database. Roelofs et al. (2009) used the small colour space where AM CVn stars exist to query the SDSS database. Their search parameters were:

1. Object is a point source
2. Object is not saturated in any filter
3. $g' < 20.5$
4. $(u' - g') < \min[0.14, 1.35(g' - r') + 0.32] - \sigma_{(u'-g')}$
5. $-0.42 + \sigma_{[g'-r')} < (g' - r') < 0.02 - \sigma_{(g'-r')}$
6. $-0.33 + \sigma_{[r'-i')} < (r' - i') < 0.03 - \sigma_{(r'-i')}$
7. Not previously identified (not in Simbad[2])

where σ is the error on the colour measure. The brightness limit is set because they expected a low 'hit rate' on finding AM CVn systems (or order 1 in 40) and it was therefore not practical to include faint targets which require more time or 8-m class telescope. The search parameters yielded 1523 candidates after sources with photometric errors were removed through visual inspection. They observed 15 per cent of these spectroscopically and found one source with features matching an AM CVn system – J080449.49+161624.8. Further time-resolved spectroscopy revealed the characteristic S-wave on a period of 44.5 min. Their remarkably low 'hit rate' hinted that the space density of AM CVn systems may be lower than the models predict (i.e. Nelemans et al., 2001a, 2004, models predict one AM CVn for every 40 spectra observed but they found only one in ~230). Rau et al. (2010) continued this work finding another four systems after obtaining spectra of half the 1532 candidates, still significantly below the ~19 that would be expected from population models (Roelofs et al., 2007c).

[2] http://simbad.u-strasbg.fr/

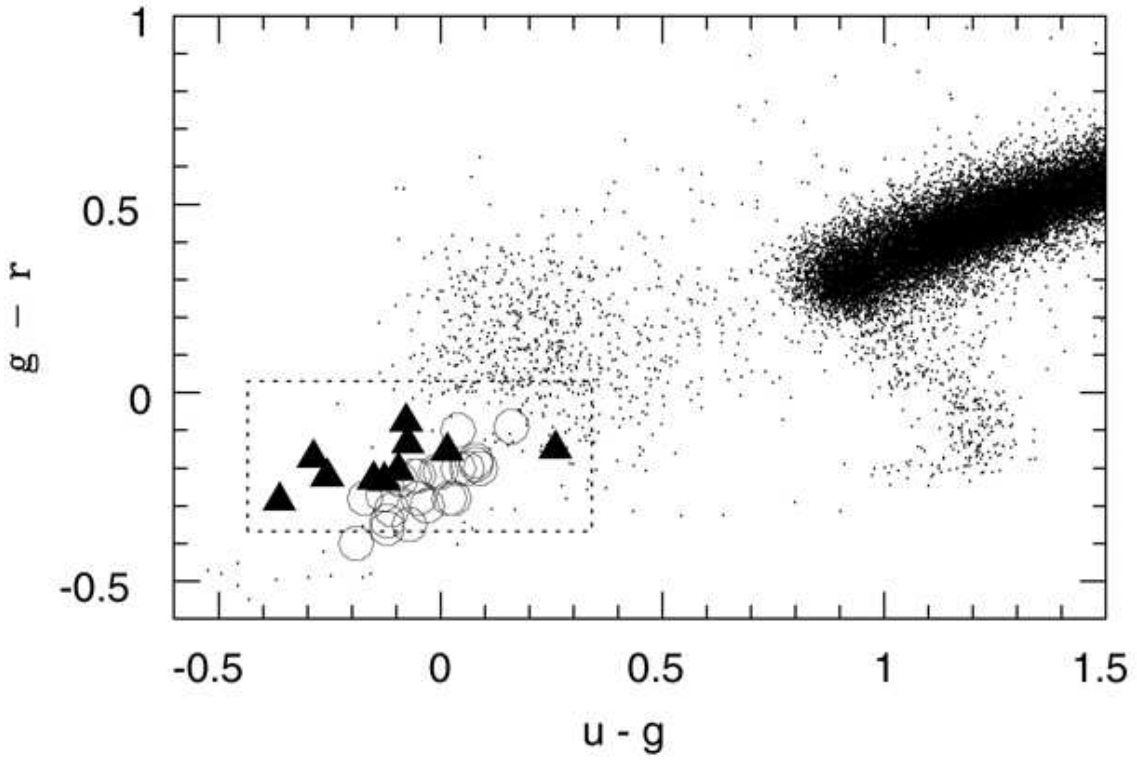

Figure 1.3: Stars from the SDSS survey that have good photometric measure are plotted as black dots. Ten AM CVn systems that have well defined photometric colours are plotted as black triangles. The AM CVn systems occupy a small area in colour-colour space as indicated by the dashed box. For comparison DB white dwarfs are plotted as open circles. The plot is taken from figure 2 of Anderson et al. (2008).

1.3.1.6 The newest member – its not a helium pulsator

SDSS J190817.07+394036.4 (hereafter SDSS J1908) was observed during the SEGUE phase of the SDSS project (Yanny et al., 2009) and found to be very blue in colour ($g' - r' = -0.22$). It was added to the list of targets to be observed by the *Kepler* satellite in short cadence mode (one data-point every 58.85 s) and was observed for 26 days. Low amplitude variability was found with several periods ranging from 222–953 s; it was suspected that the sources was either a DAV (ZZ Cet) or a DBV (V777 Her) pulsator. Spectroscopy revealed broad neutral helium lines which added weight to the DBV classification (Østensen et al., 2011). However, when it became clear that it was not possible to fit the source with a DB white dwarf model atmosphere other classification were considered. It was noticed that the spectrum of this source was remarkably similar to that of V803 Cen in its high state. The variability in its light curve was found to be caused by a 938.5 s orbital period. The discovery of SDSS J1908 showed a remarkable similarity to the processes which led to the discovery of the first six AM CVn systems – a blue star is found to have variability and broad helium lines in its spectrum.

1.3.2 Evolutionary sequence

From the observations of AM CVn systems it has become clear that there is a well defined evolutionary sequence for these systems. There are thought to be two main formation mechanisms for these systems. The starting point for both mechanisms is a main sequence binary system. Both stars must be of a low enough mass that they will never produce a core collapse supernova, the upper limit on the mass of either star is therefore $8 \pm 1 M_{\odot}$ (Smartt, 2009). The minimum mass of the two components is in the region of one solar mass lower mass stars will not have had the time to evolve off the main sequence. These two stars are not interacting and so initially evolve as single stars. The more massive star will evolve off the main sequence first. The unevolved star must be on a close enough orbit with the evolved star that when the evolved star enters a red giant phase the unevolved star exists within the radius of the red giant atmosphere. The unevolved star remains fully

Name	Period (s)	Amp. (g')	Outbursts	Mag (g')	Ref.
HM Cnc	321			21.1	Ramsay et al. 2002a[1,2]
V407 Vul	569			19.9	Ramsay et al. 2002b[1,2]
ES Cet	621	0.15		17.1	Warner & Woudt 2002[1,2]
SDSS J1908	939	0.02		16.1	Fontaine et al. 2011[1,2]
AM CVn	1028	0.04		14.0	Smak 1967[1]
					Roelofs et al. 2007a[2]
HP Lib	1103	0.02		13.6	O'Donoghue et al. 1994[1]
					Roelofs et al. 2007b[2]
CR Boo	1471	0.05	Yes	14.5	Nather et al. 1984[1]
					Roelofs et al. 2007a[2]
KL Dra	1500	0.04	Yes	20.0	Wood et al. 2002[1,2]
V803 Cen	1596	0.01	Yes	14.0	Elvius 1975[1]
					Roelofs et al. 2007b[2]
SDSS J0926	1699		Yes	20.2	Anderson et al. 2005[1,2]
CP Eri	1701	0.2	Yes	19.7	Howell et al. 1991[1]
					Roelofs et al. 2006[2]
V406 Hya	2028	0.1	Yes	20.5	Woudt & Warner 2003
					Roelofs et al. 2006[2]
2QZ J1427-01	2194		Yes	20.3	Woudt et al. 2005[1,2]
SDSS J1240	2224			19.7	Woudt et al. 2004[1]
					Roelofs et al. 2005[2]
SDSS J0804	2670			18.2	Roelofs et al. 2009[1,2]
SDSS J1411	2760			19.4	Anderson et al. 2005[1,2]
GP Com	2794			15.9	Nather et al. 1981[1]
SDSS J0902	2899			20.2	Rau et al. 2010[1,2]
SDSS J1552	3376			20.2	Anderson et al. 2005[1,2]
					Roelofs et al. 2007b[2]
V396 Hya	3906			17.6	Woudt & Warner 2001[1,2]
SDSS J0129	unknown		Yes	19.8	Anderson et al. 2005[1,2]
SDSS J1208	unknown			18.8	Anderson et al. 2008[1]
SDSS J2047	unknown		Yes	20.8	Prieto et al. 2006[1]
SDSS J1525	unknown			19.8	Rau et al. 2010[1]
SDSS J1642	unknown			20.3	Rau et al. 2010[1]
SDSS J1721	unknown			20.1	Rau et al. 2010[1]

Table 1.2: The known AM CVn systems. [1]Discovered by. [2]Period taken from. The information on whether the system has high and low states (i.e. whether it undergoes outbursts) is taken from Barclay et al. (in prep.). Most of these system have been given alternate names when they were discovered, where possible I use the correct variable star designation, for a list of the original names see Solheim (2010). For the SDSS sources an abbreviated name is given, for their full names see Solheim (2010) or the coordinate given in http://www.astro.ru.nl/~nelemans/dokuwiki/doku.php?id=verification_binaries:am_cvn_stars.

intact as a red giant atmosphere is tenuous and of low density. This is known as a common envelope (CE) phase and may result in the spiralling in of the unevolved star as it loses angular momentum owing to the drag it experiences (Tutukov & Yungelson, 1996), although Nelemans et al. (2001a) find this effect is minimal as the envelope quickly co-rotates with the binary orbital period. The envelope is eventually ejected leaving a white dwarf-main sequence star binary.

In the next stage of their evolution the initially unevolved star must go through a red giant phase which leads to a second common envelope. During this phase the white dwarf does not co-rotate with the envelope and loses considerable angular momentum because of frictional forces inside the common envelope which decrease the orbital period of the system (Roelofs, 2007). What comes out of the second common envelope phase is dependant on what went in. If the unevolved star had a mass lower than $2.3 M_{\odot}$ the resultant source will evolve into a helium white dwarf (Solheim, 2010), this is the double white dwarf branch. On the other hand, if it has a mass between $2.3-5 M_{\odot}$ it is massive enough to ignite helium and the star will leave the common envelope phase with a non-degenerate helium core which is burning helium (Savonije et al., 1986; Iben & Tutukov, 1987).

In both the double white dwarf channel and helium star channel the two components in the system are brought closer because of the emission of gravitational wave radiation which removes angular momentum from the system (Roelofs, 2007). In the white dwarf channel, when the sources get close enough for the lower mass star to fill its Roche lobe (an approximate 3D teardrop shape of gravitational equipotential), mass transfer will begin. Since mass is being transfered from the less massive star to the more compact object, material is getting closer to the centre of mass. An equilibrium is reached between the emission of gravitational wave radiation and the mass loss rate but as white dwarfs get larger when they lose mass, this equilibrium can only be reached by increasing the separation of the two stars (Roelofs et al., 2007b). The system will evolve to longer and longer periods at a decreasing rate of mass transfer as is shown in Fig. 1.4.

In the helium star channel the opposite situation occurs initially relative to the white dwarf channel. The non-degenerate helium star will get smaller as it loses mass and hence

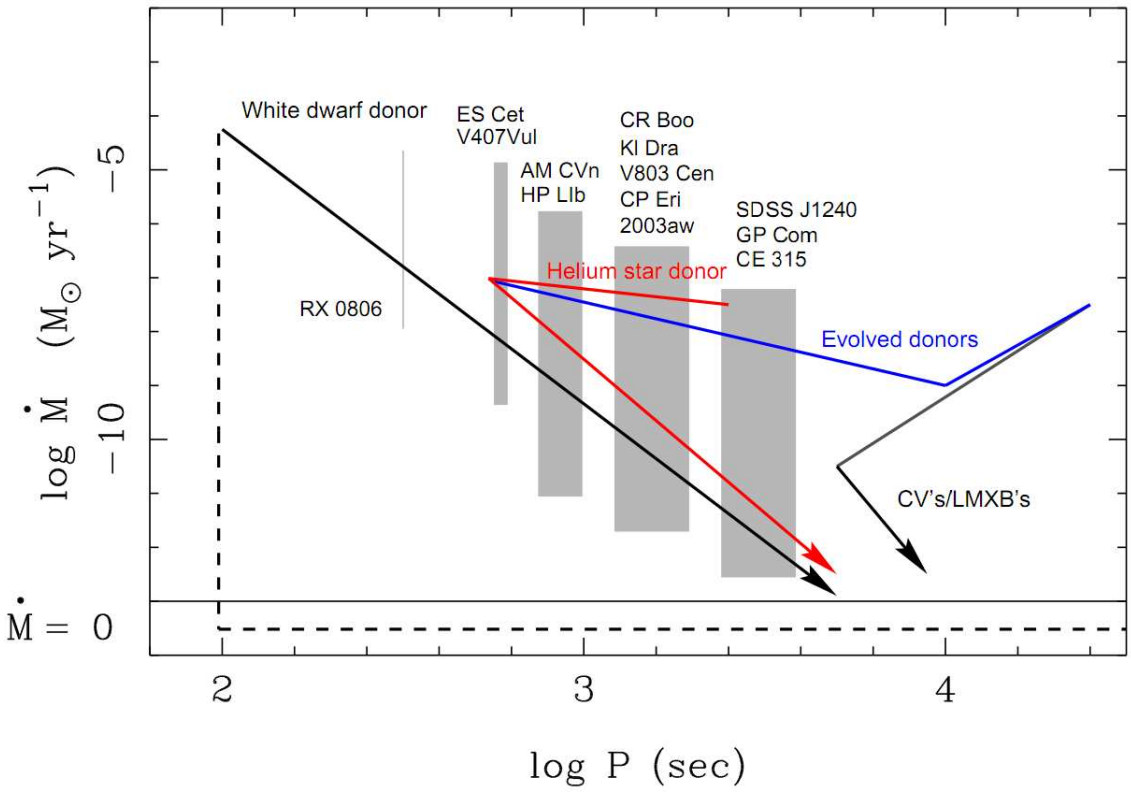

Figure 1.4: The evolution of AM CVn periods and the dependence on the formation mechanism of the system. Labelled as 'CVs' is the evolution of hydrogen-rich cataclysmic variables which cannot evolve to have orbital periods below ~60 min. In the evolved CV channel is may be possible to evolve to periods shorter than this a join the helium star channel. The helium star channel contains a 'bounce period' when the degeneracy pressure begins to dominate over radiation pressure. This figure is taken from Nelemans (2005).

the binary orbit will initially shrink. Eventually the helium star will have lost enough mass that it no longer produces enough radiation to overcome the degeneracy pressure and become semi-degenerate (Roelofs, 2007). This occurs when the helium star has a mass of around $0.2 M_{\odot}$. Now when it loses mass the period will increase. The 'bounce point', the reversal in the sign of the mass loss rate, occurs when the system has a period of roughly 11 min (Iben & Tutukov, 1987), as can be seen in Fig. 1.4.

A third proposed formation channel initially consists of a cataclysmic variable with a hydrogen-rich, slightly evolved donor (Podsiadlowski et al., 2003) which is shown as evolving from CVs in Fig. 1.4. However, these sources are thought to be vary rare – Nelemans et al. (2004) predict the number of sources resulting from this mechanism is 2400 while other channels will lead to 140,000 visible sources.

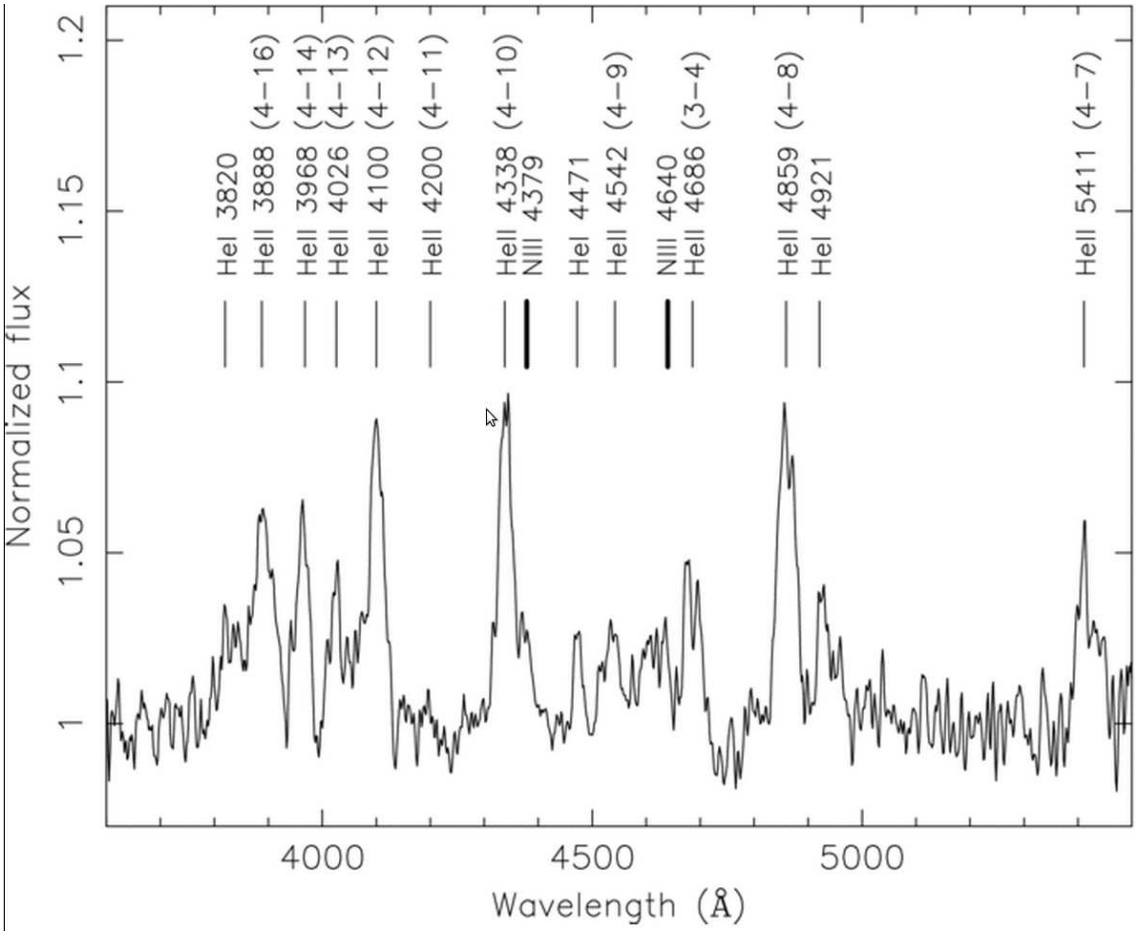

Figure 1.5: The optical spectrum of HM Cnc, the shortest period binary system. This is an average of 400 exposure lasting 60 s each obtained using the 10-m Keck telescope in Hawaii. While the lines are prominent here, consider that the spectrum was obtained using the world's (second) biggest optical telescope with total exposure time of nearly 7 h and the lines heights are only a few times greater than the scatter in the continuum. Figure taken from Roelofs et al. (2010).

Once mass transfer begins, the two stars will evolve apart. They will pass through 3 or 4 phases in evolution during which their observational properties change.

1. **Ultra-short period phase**. When AM CVn systems evolve on the double white dwarf formation channel, they will being their life as an AM CVn system with an ultra-short period. These systems are rather different to the other three AM CVn evolutionary stages and much rarer (only 2 are known). Their optical spectra are almost featureless – there are weak helium emission lines in one source (HM Cnc, Ramsay et al., 2002a; Roelofs et al., 2010) as can be seen in Fig. 1.5.

   Their orbital motion can be seen in the optical as periodic modulations in their light curves at high amplitudes – up to 30 per cent variation (Ramsay et al., 2002a). They

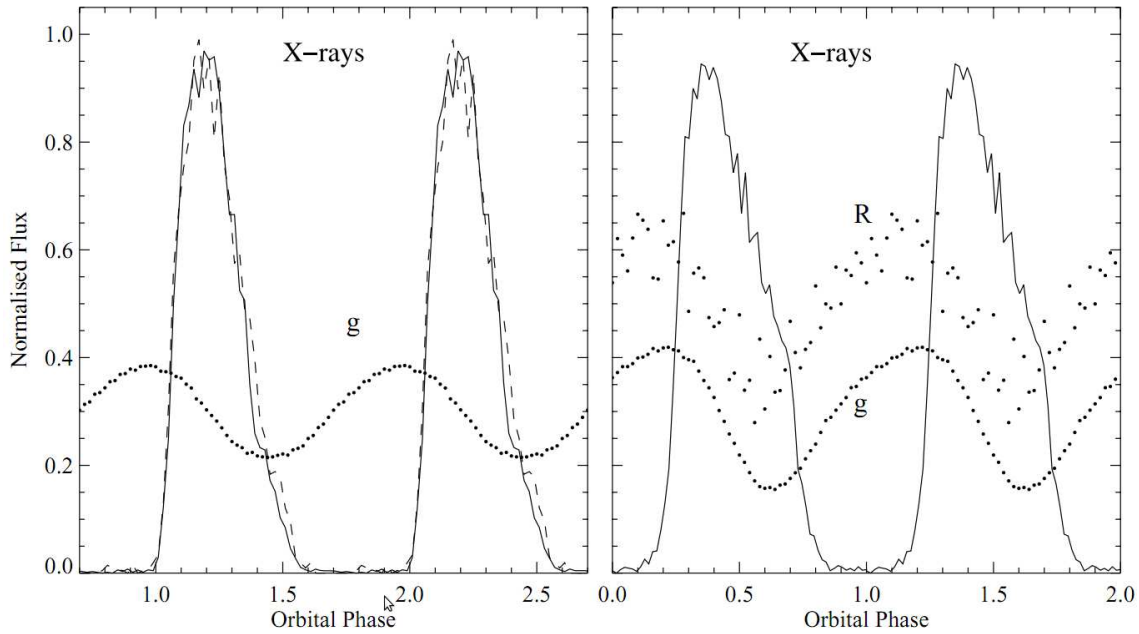

Figure 1.6: The optical and X-ray light curves of V407 Vul (left) and HM Cnc (right) folded on their respective orbital periods [5.5 min is the orbital period of HM Cnc (Roelofs et al., 2010) and 9.5 min for V407 Vul which is thought to be the orbital period]. The X-ray and optical light curves are shifted in phase by 0.2 which suggestes that the accretion regions may be vary at different wavelengths. The X-rays drop to zero which suggests that the X-rays are formed in a single region which is not visible for around half of the orbit. The plot is taken from Barros et al. (2007).

also exhibit soft X-ray emission which varies on the orbital period. Shown in Fig. 1.6 are the optical and X-ray modulations of HM Cnc and V407 Vul folded on the orbital period of the systems (5.5 min for HM Cnc and 9.5 min for V407 Vul which is thought to be the orbital period). The most popular model for these system is that the material from the donor star does not form a disk but directly impact the surface of the primary white dwarf and it is the eclipsing of this impact point that causes x-ray modulations. The optical variability may also come from the accretion spot though it has also been suggested that it is caused by the heated side of an irradiated donor passing in and out of sight as the donor orbits the centre of mass (Ramsay et al., 2002a; Barros et al., 2007).

2. **High state** Systems formed from the low mass helium star channel start their life in the high state while double white dwarf systems evolve into this state when the orbital period increases enough for a disc to be formed. In the high state the mass transfer rate is high enough to maintain a disc that outshines the primary white dwarf. They have short orbital periods (10–20 min) and are identified through their optical

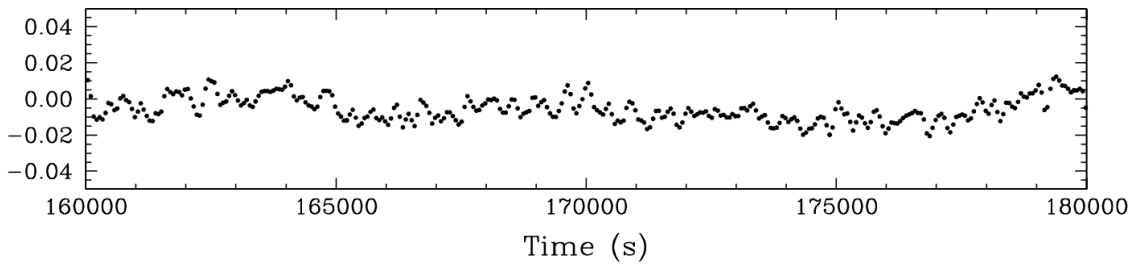

Figure 1.7: A section of the optical light curve of SDSS J1908 which was made using observations from the *Kepler* satellite. The period of this system is 958 s and the mean full-amplitude is close to 1 per cent. However the amplitude changes as does the shape of the light curve. this is likely caused by flickering in the disc. This figure is taken from Fontaine et al. (2011).

variability and their helium-rich spectra. The optical variability manifests itself as a modulation in a sources light curve on a period related to the orbital motion of the system (and example light curve is shown in Fig. 1.7. Their spectra have broad, sometime double peaked, helium lines in absorption (shown in Fig. 1.8). Material from the donor star forms an optically thick disc round the accretor and the light from the system is dominated by the disc with a contribution from the impact of the accretion stream onto this disc – called the hot-spot. The optical modulation comes from the hot-spot moving in and out of sight as the system rotates about the centre of mass. Their spectra look very similar to DB (helium-rich) white dwarfs' and the most effective way to distinguish these from pulsating DB stars is through fitting models to their spectra (e.g. Fontaine et al., 2011).

3. **Outbursting systems** As the orbital period increases further the states enter an 'in-between' phases. They have orbital periods between the high state and and a lower luminosity state. These system spend some of their time in the high state and some in this low state. The orbital periods range from 20–45 min and the time they spend in each state is loosely related to their orbital period. For example, CR Boo has an orbital period of 24.5 min and spends over 70 per cent of its time in the high state (Wood et al., 1987) while V406 Hya has a period of 33.8 min and spends only a few weeks a year in the high state (Barclay et al., 2009, Barclay et al., in preparation). Their spectra change dependant on whether they are in the high or low state, with emission lines in the low state and absorption lines in the high state (e.g. figure 2 of Ramsay et al., 2010)

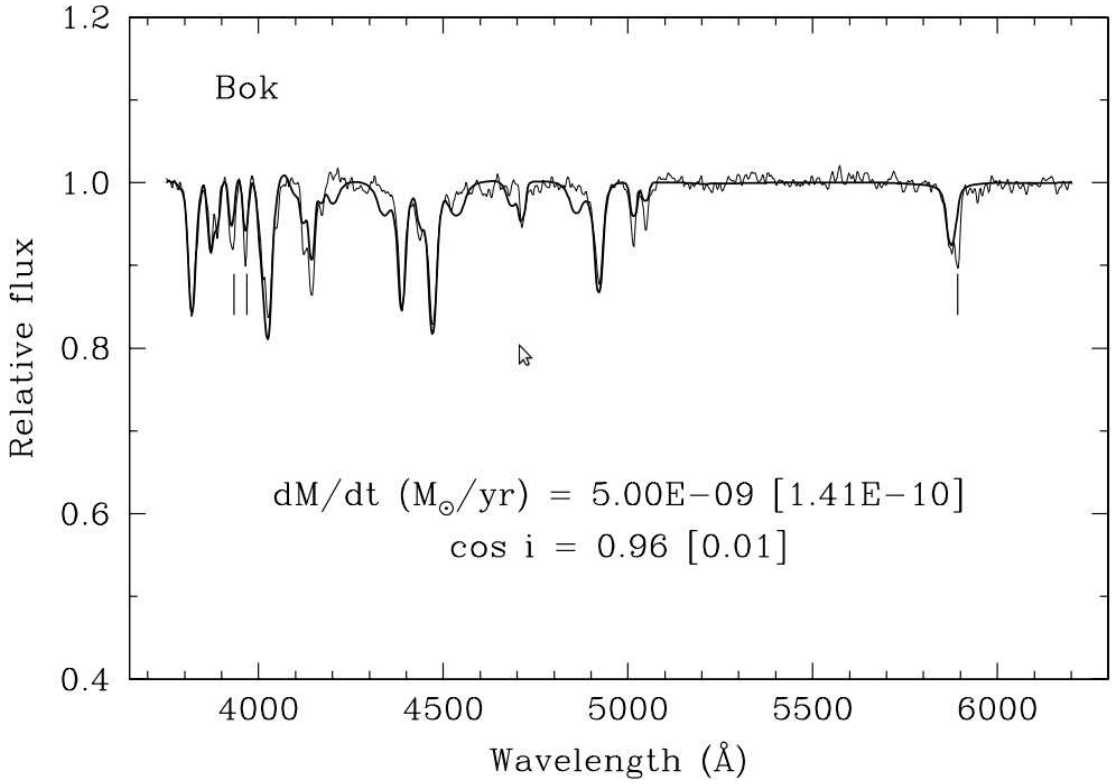

Figure 1.8: An optical spectrum of SDSS J1908, a high state AM CVn system with an orbital period of 939 s. The spectrum was obtained using the Bok Telescope and the spectrum contained no hydrogen lines and the helium lines are all broad and in absorption. The heavy line is a model fit to the observed data (fainter line). This figure is taken from Fontaine et al. (2011).

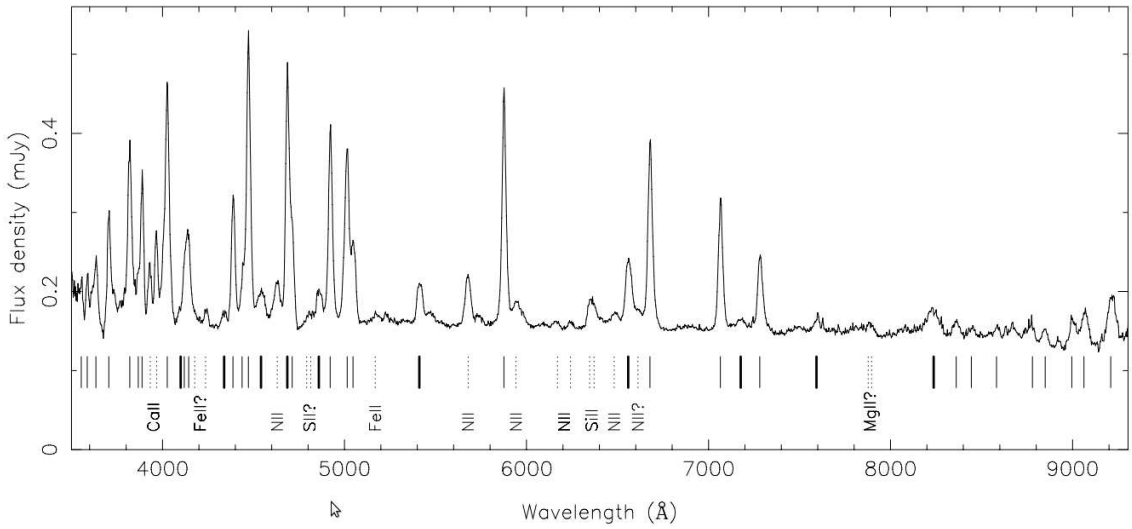

Figure 1.9: This figure shows the optical spectrum of an AM CVn system in the low state. The source, SDSS J0804, has an orbital period of 48 min. The solid lines beneather the spectrum mark neutral helium emission while the fainter lines mark ionised helium. This figure is taken from Roelofs et al. (2009).

4. **Low state systems** When the orbital period of a system is greater than ~40 min the source has little or no photometric variability related to the orbital motion of the system. The source still has a disc but the mass transfer rate is low and the light detected from the source is dominated by the primary white dwarf (or white dwarf + disc) with helium emission lines from an optically thin disc which may be double peaked owing to Doppler shifting from the orbital motion (an example spectrum is shown in Fig. 1.9).

1.3.3 Space Density

One of the key reasons to study AM CVn systems is that their Galactic population has important implications for binary population synthesis models. There are three paths which close white dwarf binary systems may follow: they will merge; they form a type Ia supernova; or they form an AM CVn system. Whether they merge or form a supernova depends on whether the total system mass exceeds the Chandrasekhar mass ($\sim 1.4 M_{\odot}$). Either way, they leave no remnant from which we can easily identify the progenitor. With AM CVn system however, there is a clear remnant – the AM CVn star itself – from which is is possible to deduce the progenitor objects. By carefully counting (and accounting for any bias

in the sample) the number of AM CVn system it is possible to tune the binary population synthesis models which in turn allows for better prediction on the number of mergers and thermonuclear supernovae.

Nelemans et al. (2001a, 2004) make predictions of the local space density of AM CVn system which can be tested by observations. They make two models; one optimistic, the other pessimistic. In the optimistic model the angular momentum is fed back into the system because of tidal coupling in the system and has a low probability of an edge-lit detonation of the primary CO white dwarf destroying the system. In the pessimistic model the opposite conditions exist. The local space density these model predict are shown in Table 1.3. The predicted space density varies greatly dependent on the Galactic latitude: at latitudes of $|b| < 20°$ the number of AM CVn systems is significantly greater than at higher Galactic latitudes.

The number of AM CVn systems found in the SDSS leads to a direct test of these population models. Anderson et al. (2008) find a sky surface density of approximately 3×10^{-3} per square degree which is somewhat lower than the optimistic model predicts but higher than seen in the pessimistic model.

A more complete analysis of the galactic population was performed by Roelofs et al. (2007c) who found the observed space density was a factor of 20 lower that that predicted by the optimistic model and a factor of 2 lower than predicted by the pessimistic model. The differences between the AM CVn population estimated by Roelofs et al. (2007c) and that of Anderson et al. (2008) was due to a more rigorous analysis of the completeness of observations by Roelofs et al. (2007c).

It should be noted that Anderson et al. (2008) and Roelofs et al. (2007c) only searched for emission line AM CVns and hence was limited to looking at the longer period, low state systems. It is unclear whether the deficiency in systems extends to lower periods. This thesis describes the work being undertaken to address this question.

Model	Number	Observable	Space density [pc^{-3}]
Pessemistic	1.82×10^7	33	0.4^{-4}
Optimistic	8.0×10^7	116	1.7^{-4}

Table 1.3: This table, modified from a table 1 in Nelemans et al. (2001a), gives details of the numbers of AM CVn systems. The first column is the model: optimistic or pessimistic. The number column is the total number of systems in the Galaxy while the observable column details the number of systems observable brighter than $V = 15$. The final column are the different local space densities.

1.4 Astrophysical sources with short time-scale variability

While the Rapid Temporal Survey is designed to discover new AM CVn systems, there are other classes of variable sources that vary in the time-frame where RATS is sensitive. These include pulsating, erupting and eclipsing stars, to name a few. A number of these classes are discussed below.

1.4.1 Stellar pulsators

Stellar pulsations are caused by instabilities beneath the surface of a star which cause the radius to change. In some cases the radius changes are constant in every direction (i.e. the star retains spherical symmetry), these are known as radial pulsators. In others the change in the radius of a star is not the same in all directions, these are non-radial pulsators. Pulsators typically have a one or more periods of pulsation.

In pulsating stars the pulsations are powered by envelope ionisation mechanisms which involve the ionisation of an abundant element at a critical depth below the surface of the star (Cox, 1980). Specifically, it is the ionisation of singly ionised helium to doubly ionised helium (HeI⇌ HeII) at a depth where the temperature of the envelope is $\sim 4 \times 10^4$K that causes the excitation of pulsations in most pulsating stars because of the large increase in opacity at this layer (Chevalier, 1971; Cox, 1980). This depth varies depending on the stellar temperature, mass and radius. When looking at a Hertzsprung-Russell diagram there is a band from the top-right to the bottom left where stars will be unstable which is known as the instability strip. At the red end of the strip exists Cepheid variables and it passes

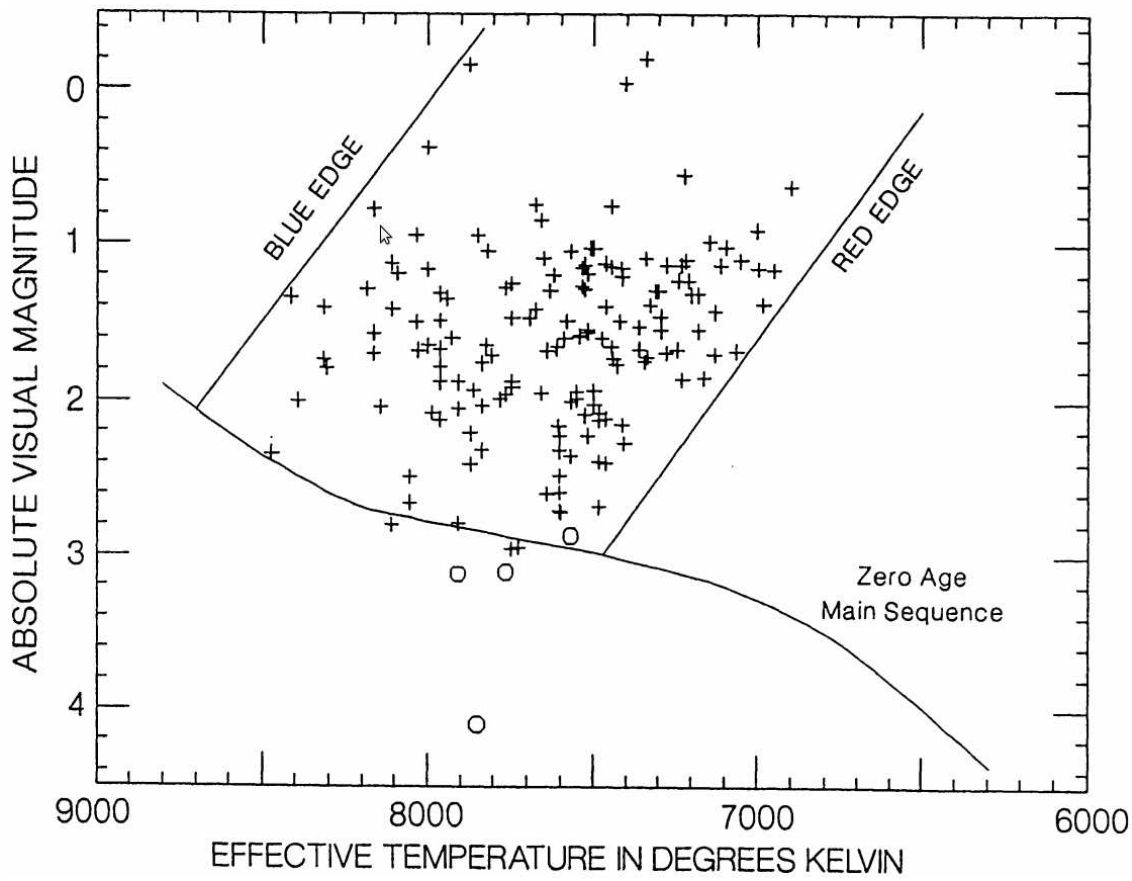

Figure 1.10: A Hertzsprung-Russell diagram showing the red and blue edges of the instability strip. Inside this region are δ Scuti stars marked as crosses and SX Phe stars as open circles. Figure taken from Breger (1995).

through the main sequence at spectral type A and F as shown in Fig. 1.10. Those stars close to the main sequence were known as short or ultra-short period Cepheids (USPC Eggen, 1970) and can be radial or non-radial pulsators (Poretti, 1989). It was found that most of these USPCs were Population I objects with high metal abundances. These became known as the δ Scuti stars (Nemec & Mateo, 1990) of which at least 636 are known (Rodríguez et al., 2000). The remaining USPCs have Population II characteristics – low metallicity, found in the old disc and halo and have kinematics not associated with the spiral arm structure – but do not share the age of other Population II stars: they are typically 2–5 billion years old (Nemec & Mateo, 1990). There are at least 83 SX Phe stars known (Poretti et al., 2008) but the vast majority of these are found in globular clusters. It should be noted that not all stars within this instability region pulsate. To pulsate stars likely need a high helium abundance (Cox et al., 1973), a high metallicity or are fast rotators (Breger, 1972).

Observationally SX Phe and δ Scuti stars look very similar. Both classes include only

stars of A and F spectral type and therefore have similar colours $[(B - V) = 0.1 - 0.35]$. SX Phe stars have periods ranging from 56–172 min (Rodriguez et al., 1990; Poretti et al., 2008) and amplitudes of 0.05–0.80, though in SX Phe stars there is a tendency for higher amplitudes in longer period variables which is not seen the δ Scutis (Nemec & Mateo, 1990). δ Scutis have a greater period range than SX Phe stars – the shortest period δ Scuti has a period of 18 min (Amado et al., 2004) while the longest period star has a period of 7.0 h (McNamara & Redcorn, 1977) – though only two δ Scutis have periods shorter than 40 min. The range of periods seen in δ Scutis extends to lower periods than the SX Phe distribution but this may be due to the smaller sample size, while at longer periods the boundary between δ Scuti and RR Lyr stars becomes blurred. The pulsation amplitudes seen in δ Scuti stars ranges from 0.002–1.30 mag (Rodríguez et al., 2000) which is broadly similar to SX Phe stars (Rodriguez et al., 1990). Even in low resolution spectra they look very similar (e.g Ramsay et al., 2006) and generally require metal lines to be visible in order to separate these two classifications.

A third class of main sequence pulsators are the rapidly oscillating Ap (roAp) stars. These are magnetic, chemically peculiar A-type stars which have have pulsations on periods of around 10 min. They always pulsate non-radially and unlike the δ Scuti and the SX Phe stars, these pulsations are driven a hydrogen ionisation zone (Balmforth et al., 2001). Periods are seen ranging from 4–21 min (Dupret et al., 2008) in the 37 known roAp stars (Kochukhov et al., 2009). Other than their pulsation periods, they are notable because of their unusual spectra which contain rare earth elements (e.g. Ryabchikova et al., 2002) a fact which can be used to distinguish between these stars and the δ Scutis.

White dwarfs are the degenerate cores of stars that have exhausted all their fuel. They cool over time from very high temperatures (up to 200,000 K Kurtz et al., 2008) and will eventually end their lives as dense object at the ambient temperature of the inter-stellar medium. As they cool, they eventually pass through one of the white dwarf instability strips. The temperature at which this happens depends on the composition of the star. In DA (hydrogen-rich) white dwarfs the pulsations are due to the recombination of hydrogen and this happens at temperature of around 13,000 K, the stars stop pulsating when they

cool to around 10,000 K (Fontaine & Brassard, 2008). The instability region is shown in Fig 1.11. Helium-rich DB white dwarfs – which make up around 20 per cent of all white dwarfs – have a higher terperature at which recomination occurs and therefore pulsate at temperatures of around 25,000 K (Fontaine & Brassard, 2008). Hydrogen-rich pulsators are known as DAV or ZZ Cet stars while the helium-rich sources are known as DBV or V777 Her stars. There are at least 148 DAV white dwarfs known (Castanheira et al., 2010); these have periods ranging from 100–1400 s with amplitudes at the dominant frequency of a few per cent (Fontaine & Brassard, 2008). The DBVs number around 18 (Nitta et al., 2009) and have a very similar range of periods and amplitudes to the DAVs (Fontaine & Brassard, 2008; Nitta et al., 2009). Unlike the non-degenerate pulsators, all stars within the DAV and DBV instability strips pulsate (Castanheira et al., 2010; Fontaine & Brassard, 2008). This important as it implies that the mechanism that triggers the pulsations is only a function of the effective temperaure of the white dwarf (Fontaine et al., 1982).

1.4.2 Eclipsing and contact binaries

It is thought that the majority of stars are in binary system, for example Duquennoy & Mayor (1991) estimate that 57 per cent of G-type stars are components in a binary or multiple star system. A proportion of these (of the order a few percent) are eclipsing binaries, systems where the stars pass in front of each other along our lines of sight. This produces two eclipses every orbit as each star passes in front of the other one. An eclipse is noticeable from Earth as a sharp decrease in brightness followed by an increase at the star moves out of eclipse. An example of an eclipsing binary light curve is shown in Fig. 1.12 – two eclipses can be seen, the deeper is caused by the larger star passing in front of the smaller. The duration of the eclipse is related to the distance between the two stars and the centre of mass and the stellar radii while the depth is related to their relative radii and their luminosities. The duration of eclipses can vary from a few 10's of minutes if the stars are very close together, to many hours or days if the systems are in a wide binary (Budding et al., 2004). In order to identify an eclipsing system it is necessary to observe an eclipse (and at least two eclipses to determine an orbital period) and as a result, short period systems are much

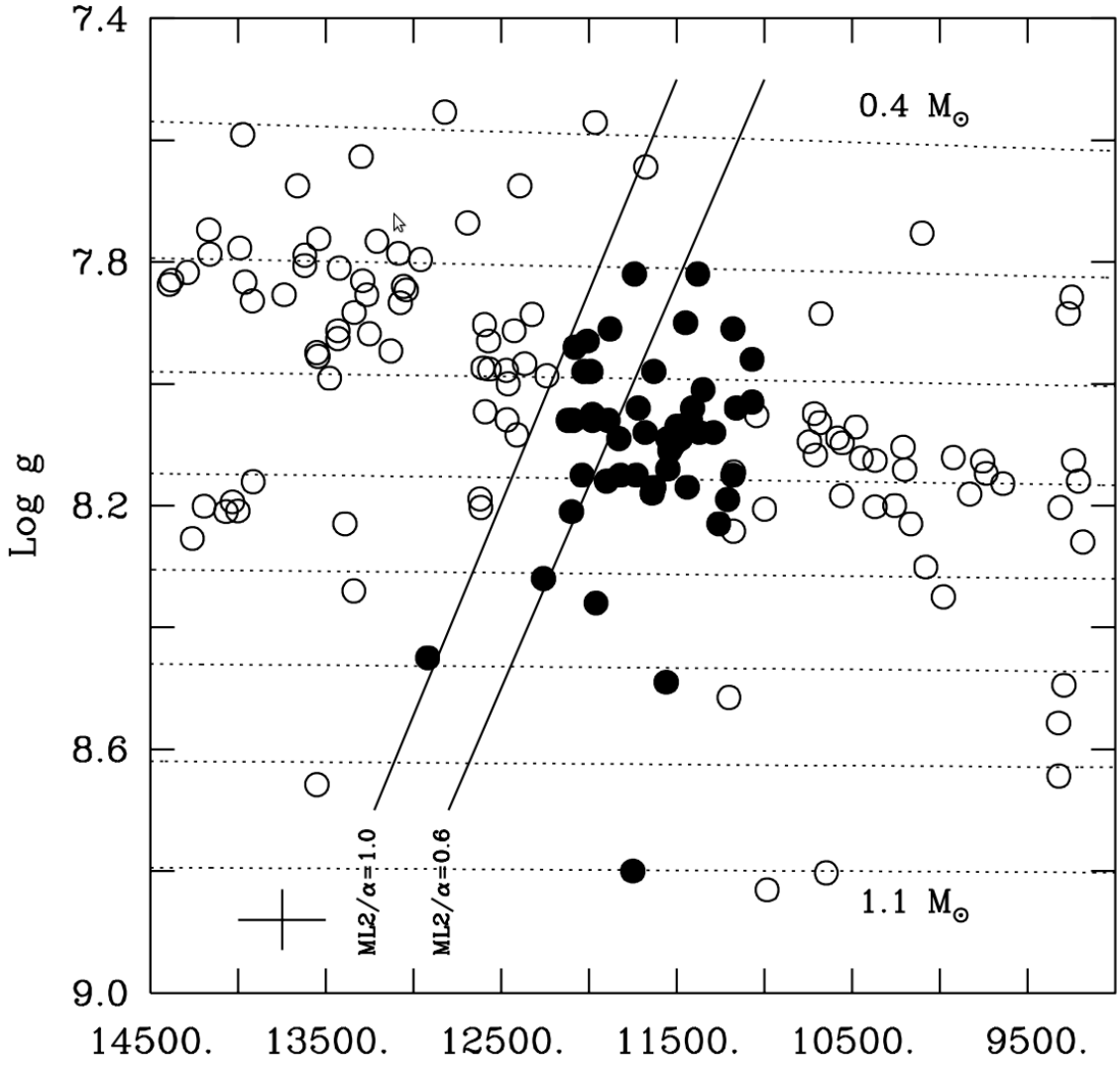

Figure 1.11: The DAV instability region in effective temperature, surface gravity space. Variable stars are shown as filled circles while non-variables are shown as open circles. The dotted lines show the evolutionary tracks taken by different masses of white dwarfs from $0.4M_{\odot}$ at the top to $1.1M_{\odot}$ at the bottom. The solid lines are the theoretical blue edge of the DAV instability strip using two different models. Figure taken from Fontaine & Brassard (2008).

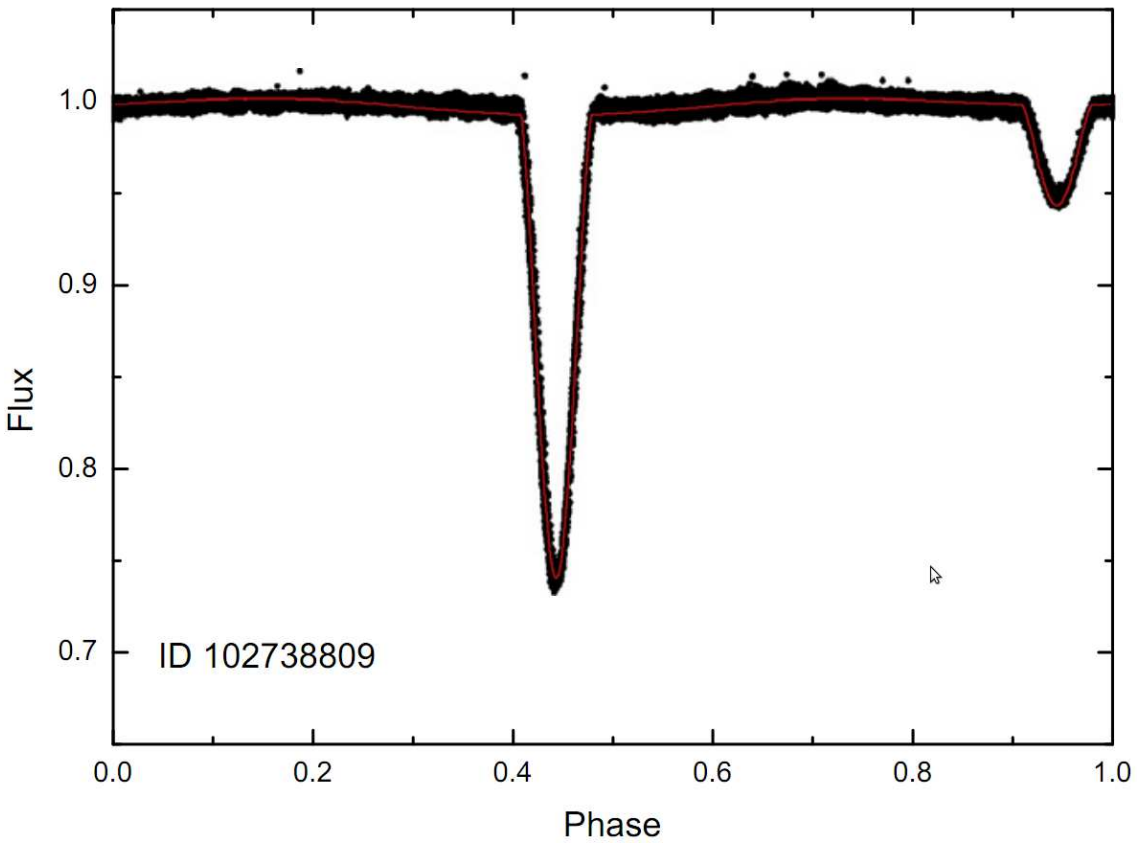

Figure 1.12: This light curve of an eclipsing binary was obtained using the *CoRoT* satellite. This light curve has been folded on the orbital period and two eclipses can be seen. The deeper, primary eclipse happens when the larger star passes in front of the smaller, while in the shallower, secondary eclipse the smaller passes in front of the larger. This figure is taken from Maciel et al. (2011).

more commonly identified that longer period ones. For example in the eclipsing binary catalogue of Budding et al. (2004), the median period of eclipsing sources is 1.9 days. The reason that these systems are astrophysically important is that that it is one of the few ways to directly measure the radii of stars and so to determine masses, which helps to contrain stellar models.

Contact binaries or W Ursae Majoris systems share many similarities with classical eclipsing binaries. They consist of a binary star system where the two stars are so close to each other that they are in contact. The stars are not spherical; the gravity of each star warps the shape of the other. At the point of contact they are able to transfer material and are therefore usually close to being in thermal equilibrium. Such systems are more common that one would expect with some estimates indicating that their frequency may be as high as 1 per cent of main sequence star systems (Rucinski, 1998, though they exclude stars with

spectral type K5 and later). They have typical periods ranging from 0.23–0.7 d though are occasionally seen with longer periods (Pribulla et al., 2003) and can have periods as short as 0.21 d (Rucinski & Pribulla, 2008). Their light curves are highly variable and do not have the same restrictions as eclipsing systems where one must observe an eclipse to discover their nature. The heating of one side of each star more than the other (i.e. the side that faces the other star) causes the stars vary in brightness continually as they orbit a common centre of mass.

1.4.3 Flare stars

Stellar flares are large increases in brightness of a star in optical, UV and X-ray light caused by the releasing of stored energy from surface magnetic loops (Kowalski et al., 2009). These eruptions on the surface of the star last for as short a time as only a few minutes and which can increase the optical brightness of the star by a factor of over 100 (e.g. Kowalski et al., 2010). The cause of these events is thought to be similar to the cause of solar flares: magnetic reconnection events on the stellar surface. They normally occur on M-type stars though they have been seen in stars of earlier spectral type (e.g. Andrews, 1967).

There is currently significant interest in M-type stars amongst the exoplanet community as host stars for habitabable planets (a detailed discussion of M-star habitability is given in Scalo et al., 2007). The reason for this is twofold; transits by Earth-mass planets are easier to detect if the stellar radius is low, and the habitable zone (the semi-major axis range where the temperature of a planet would be conducive to life, usually defined as the region where liquid water could exist) is closer to the star than in higher mass stars, which makes the detection of transits easier as there are more of them in a given time-frame. One possible problem for M-stars making good hosts for habitable planets is the prevalence of flaring in M stars. Little work has been undertaken on the effect flaring has on any life that may be present on the planetary surface but there are suggestions that habitability may be highly sensitive to the rate of flaring from a host star (Segura et al., 2010). An ozone layer which protects a planet's surface from ultra-violet radiation may be able to survive after a

single flare but if there are more than one in a give time frame this could strip the ozone layer away (Segura et al., 2010). An unbiased study of the flaring rate of M-stars would be able to provide interesting constraints on the potential habitability of these sources. Such a study would need to have a high time resolution in order not to miss any short flares. A survey such as RATS will be able to provide this

1.4.4 Cataclysmic variables

Cataclysmic variables are a class of binary system where a low mass main sequence (or evolved) donor fills its Roche lobe and transfers mass onto a white dwarf (Warner, 1995). They evolve in a similar way to AM CVn systems but do not go through the second common envelope phase and instead evolve together via a combination of magnetic breaking – coupling of the magnetic field of the white dwarf to the stellar wind of a tidally locked donor – and gravitational wave radiation (Ritter, 2008). The presence of a hydrogen dominated donor star causes the orbital period of these source to never gets below ~60 min (Augusteijn et al., 1996).

Spectroscopically they are blue and have hydrogen lines which are often in emission, while their light curves modulate on a period related to the orbital period of the system. They also exhibit other phenomena such as dwarf novae outbursts which are dramatic increases in brightness [4 mag is typical (Warner, 1995)] and typically last for several weeks. During outbursts short time period variability known as dwarf nova oscillations and quasi-periodic oscillation (QPOs) are often observed. These are modulations on a period of seconds to several tens of minutes which remain coherent for several hours because of the orbit of 'blobs' between the inner disc and star (Warner & Woudt, 2008, and §6.1 where this phenomenon is discussed in more detail). However, they have also been observed when the system is quiescent (e.g. Ramsay et al., 2009, and §6.1).

1.5 Summary of Thesis

This thesis describes my work on the RATS project. I have been leading the writing of data reduction and the analysis pipeline. This pipeline processes the images, performs the photometry and identifies variable sources. In Chapters 2 and 3 I describe the development of this pipeline and the choices made when deciding how to detect variability. In Chapter 4 I discuss the primary objective of the project: testing the AM CVn Galactic population models of Nelemans et al. (2001a, 2004). I describe how I developed a list of candidate AM CVn systems and the follow-up observations made of the prime candidates. I go on to discuss some of the variable sources that have been detected and elaborate on in Chapter 5 when I look at some of the populations of pulsating stars in the RATS data. In the Chapter 6 I go into some detail describing the follow-up observations I have performed and the physics that can be deduced in a study of two different variable stars. I conclude by assessing the success of the project and look to the future of both this survey and variability surveys in general.

Chapter 2

Wide-field observations and data reduction

> We had the sky up there, all speckled with stars, and we used to lay on our backs and look up at them, and discuss about whether they was made or only just happened.
>
> *M. Twain, Adventures of Huckleberry Finn, 1884.*

The Rapid Temporal Survey (RATS) will, when completed, cover 40 deg^2 of sky within $\pm 10^\circ$ of the Galactic plane. For this area we will have variability information for every star down to a brightness of $g' \sim 23$ as well as complementary colour information. This Chapter describes the data reduction and analysis of the first 5 years of this project.

2.1 Observations

2.1.1 Strategy

We take a series of 30 s exposures of a particular field for 2–2.5 h in white light and before this we observe the field using 3 standard filters (cf.§2.1.2.3). We use white light (i.e. no fil-

ter) for the time series in order to maximize the number of photons we are detecting which in turn allows us to use shorter exposures and therefore to have higher time resolution for a given limiting brightness. We perform the photometry using the difference image analysis technique (Alard & Lupton, 1998, see §2.2.1 for details of this technique) and identify sources that merit follow-up observations (cf. Chapter 3). These follow-up observations are used to determine the nature of these variables (cf. Chapters 4, 5 and 6).

RATS fields are biased towards the Galactic plane as the models of Nelemans et al. (2001a, 2004) predict that AM CVn systems are much more numerous at low Galactic latitudes (as shown in Fig. 2.1). Using these models, the estimated number of AM CVn systems (close to the Galactic plane) with periods less than 25 min (a conservative limit on those sources which show optical variability) is 0.15 per square degree brighter than $g' = 20$ and 0.4 brighter than $g' = 22$. The reason 40 deg^2 is selected as the target sky coverage for the RATS project is that is will allow us to to the Galactic population models with statistical significance – there are predicted to be ~18 in 40 deg^2.

2.1.2 Instruments

The wide-field survey strand of this work makes use of two instruments: the Wide Field Camera (WFC) on the 2.5m Isaac Newton Telescope (INT) at the Observatorio del Roque de los Muchachos, La Palma; and the Wide Field Imager (WFI) on the MPG/ESO 2.2m telescope at La Silla Observatory, Chile.

2.1.2.1 WFC on the INT

The WFC is placed at the prime focus of the INT (shown in Fig.2.2) and consists of four thinned 4096 × 2048 pixel EEV CCDs. The pixel size is 13.5 micron which corresponds to a 0.33 arcsec per pixel. The total field of view of 0.28 deg^2. The CCDs have a quantum efficiency over 50 per cent from 3500–8000 Å when run at the operating temperature of 153 K and their efficiency peaks at 4600 Å(see Fig. 2.3). The camera has fast and slow readout

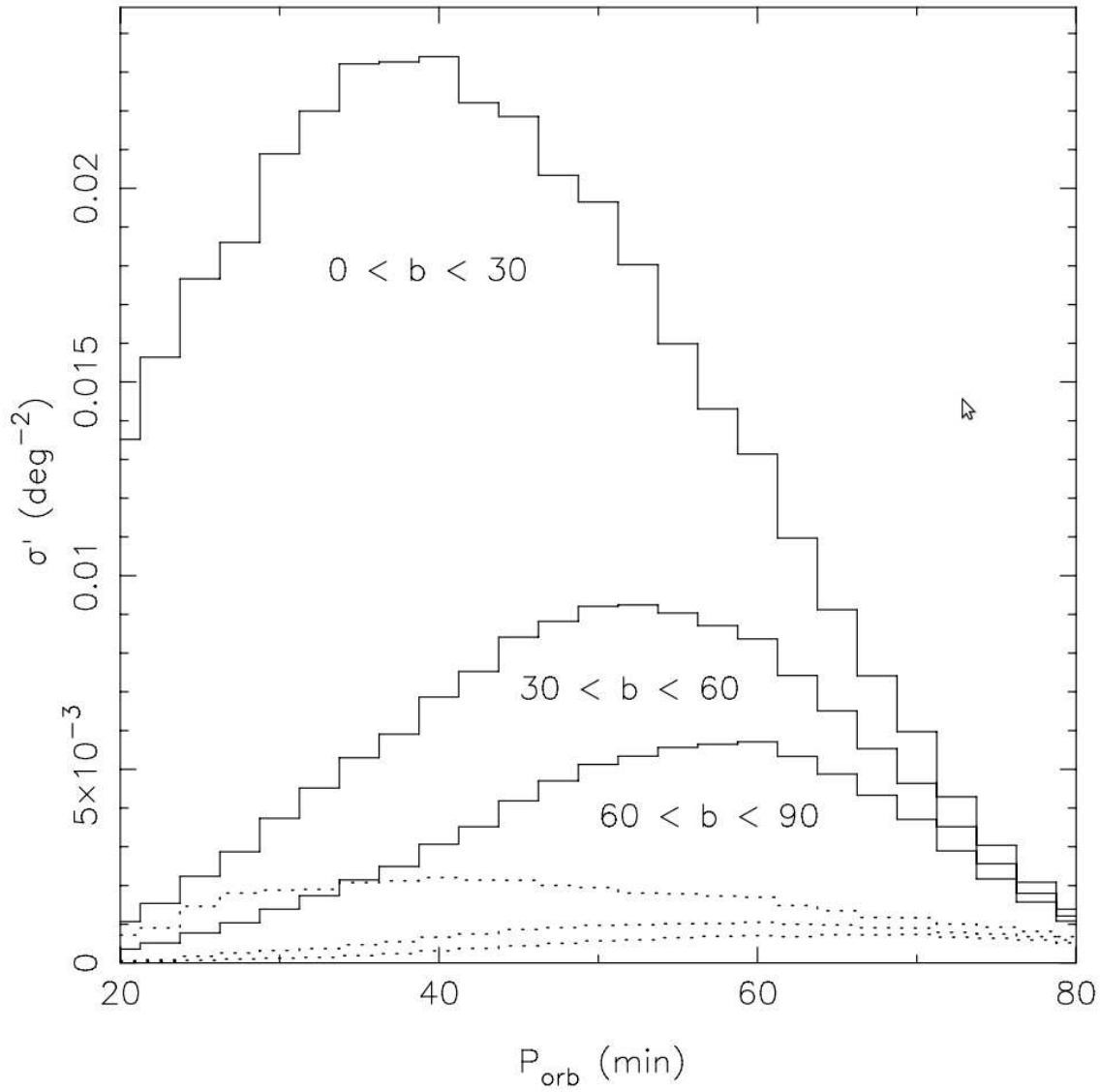

Figure 2.1: The surface density of AM CVn systems at different Galactic latitudes. The solid line is for 'optimistic' model and the dotted line for the 'pessimistic' model. The y-axis is the number of systems per square degree for systems brighter than $g' = 21$. Systems with $b < 30°$ are much more numerous than systems further from the Galactic plane. This plot of shows the positive Galactic latitudes, the distribution is expected to be symmetrical. This plot is taken from Roelofs et al. (2007c).

Figure 2.2: The WFC mounted at the prime focus of the INT. The telescope is in the park position where it may be filled with liquid nitrogen which is used to cool the instrument. The dewar for filling the camera with the coolant is below the instrument in this image. The image was taken from the website of the ING group of telescope[a].

[a] http://www.ing.iac.es/astronomy/instruments/wfc/

modes; we use the fast mode which has a readout time of 29 s with an average readout noise over the four CCDs of 8.8 electrons per pixel.

2.1.2.2 WFI on the MPG/ESO 2.2m

The WFI is mounted at the Cassegrain focus of the MPG/ESO 2.2m and has eight 4098 × 4046 CCDs and a total field of view of 0.29 deg^2. The pixel scale is 0.238 arcsec per pixel and a readout noise of 4.5 electrons per pixel. The CCDs which make up the WFI have a quantum efficiency which peaks in the blue and spans wavelengths from 3500 Å to the near infra-red and the readout time is ~110 s (much higher than the WFC which is due to there being double the number of CCDs).

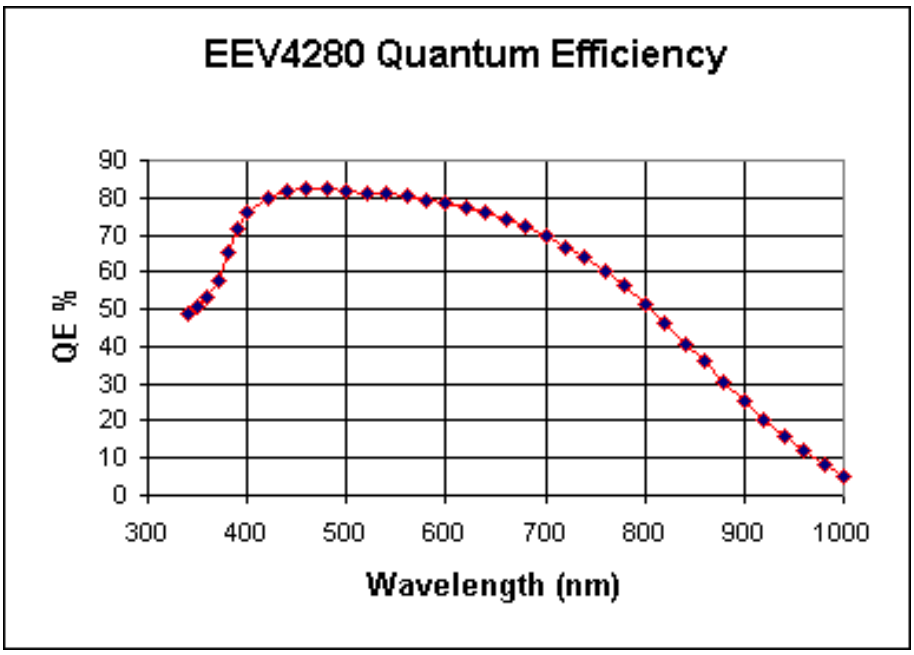

Figure 2.3: A plot showing the quantum efficiency of the WFC CCDs as a function of wavelength. The CCDs are most efficient at the blue end of the spectrum with the peak efficiency at 4600 Å. This plot is taken from the WFC information website[a].

[a] http://www.ing.iac.es/Engineering/detectors/ultra_wfc.htm

2.1.2.3 Filters

At each epoch we used 3 filters which are shown in Tab. 2.1. For the first two epochs of INT observations we used the Harris B and V filters and the Sloan i' filter. In the later epochs we used Sloan g' and r' filters and the RGO U filter. In the final epoch we also used a HeII 4686 Å filter. The change of filters was made for two reason. Firstly, the Sloan filters are of higher throughput than the Harris filters, the maximum throughput of B and V is 66 and 88 per cent, respectively whereas the g' and r' filters both have a maximum throughput of 90 per cent. Secondly, it allows for direct comparison with observations from the Sloan Digital Sky Survey (York et al., 2000). On top of this, there is some scratches in the centre of the Harris B filter, whereas the Sloan filters are in better condition[1]. In Figures 2.4 and 2.5 are shown the transmission for the filters used in the earlier and later epochs, respectively.

When observing using the WFI on the MPG/ESO 2.2m we used Bessel B, V and I filters. The transmission curves for these filters are shown in Fig. 2.6. These filters were

[1] http://catserver.ing.iac.es/filter/list.php?instrument=WFC

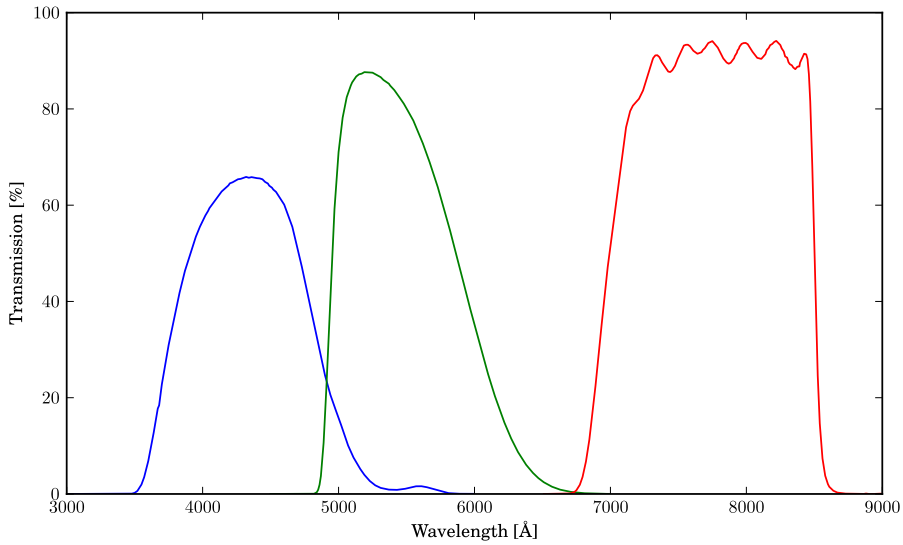

Figure 2.4: The transmission of the filters using during the INT1 and 2 epochs. The blue, green and red curves are the Harris B and V and the Sloan i' filters, respectively.

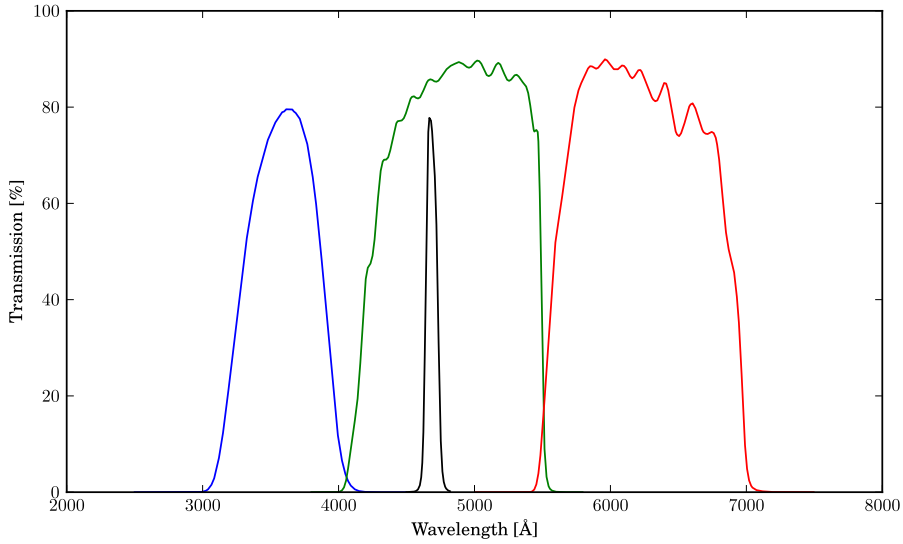

Figure 2.5: The transmission of the filters using during the INT3, 4 and 5 epochs. The blue, green and red curves are the RGO U and the Sloan g' and r' filters, respectively. In the INT5 epoch we also used a HeII 4686Å filter, the transmission of this filter is plotted in black.

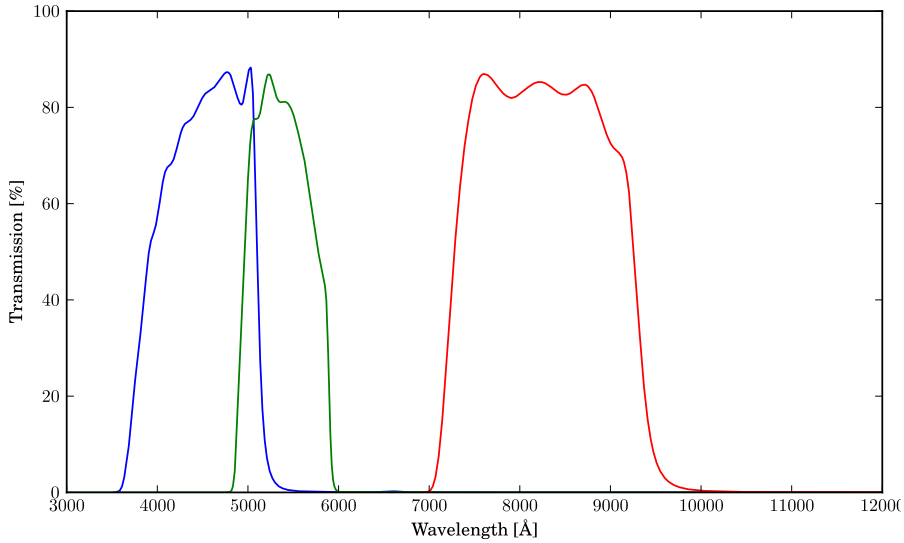

Figure 2.6: The transmission of the filters using during the ESO1 epoch. The blue, green and red curves are the Bessel *B*, *V* and *I* filters, respectively.

Filter System	Filter Name	Epoch	Central Wavelength Å	FWHM Å	Peak transmission %
Harris	*B*	INT1,2	4298	1065	66
Harris	*V*	INT1,2	5425	975	88
Sloan	*i′*	INT1,2	7743	1519	94
RGO	*U*	INT3,4,5	3581	638	80
Sloan	*g′*	INT3,4,5	4846	1285	90
Sloan	*r′*	INT3,4,5	6240	1347	90
	HeII	INT5	4686	100	78
Bessel	*B*	ESO1	4491	1235	88
Bessel	*V*	ESO1	5396	894	87
Bessel	*I*	ESO1	8268	2031	87

Table 2.1: Summary of the filters used.

chosen as they give relatively good coverage over optical wave-bands, though poorer than the later INT observations because the Bessel *B* and *V* filters overlap and there is no transmission from 6000–7000 Å. More infra-red flux is obtained with the Bessel *I* filter relative to the SDSS *i′* filter.

2.1.3 Fields observed

All fields are selected in such a way that no stars brighter than *g* ~12 are present. In addition, fields are typically chosen to be close to the zenith to reduce differential atmospheric

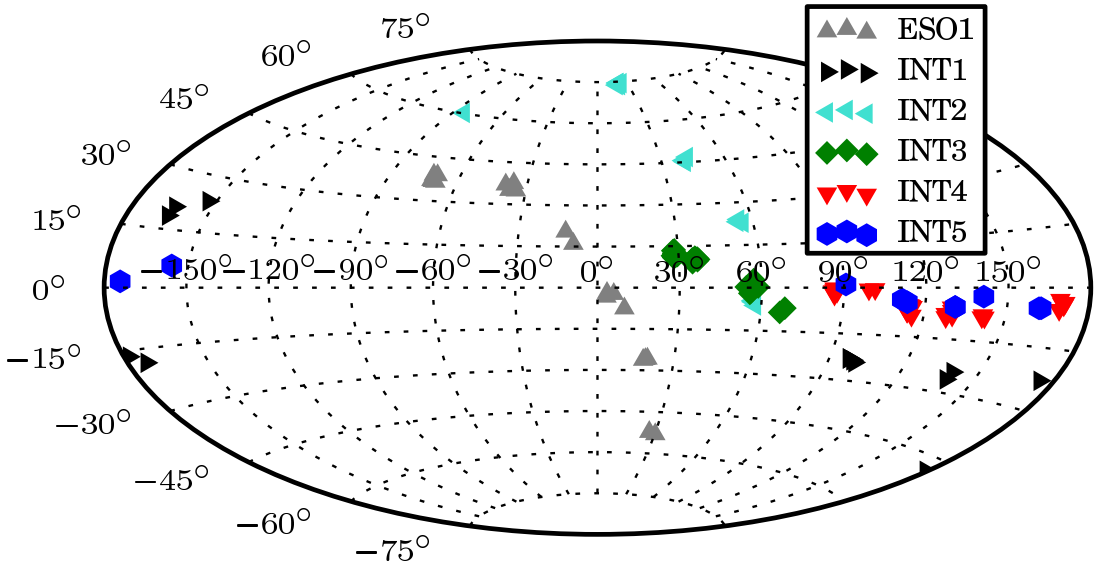

Figure 2.7: The position of the field centres of all the fields observed during the first five years of the RATS project. The fields are plotted in Galactic coordinates using an Aitoff projection. Many of the fields are spatially close and so appear only as a single point in this figure.

diffraction.

In the first three epoch of observations (INT1 and 2 and ESO1), the fields were located at Galactic latitudes with $20° < |b| < 30°$. Since then our fields have been biased towards $|b| < 15°$. The distribution of RATS fields are shown in Figs. 2.7 and 2.8.

A number of fields in the INT3 epoch were observed at high airmass (1.4–2.0) in order to observe close to the Galactic plane. On these occasions we did not observe in white light but instead used a g' filter in order to limit the effects of wavelength dependent atmospheric extinction.

Our data were taken at 6 separate epochs: 5 using the Wide Field Camera (WFC) on the INT and 1 using the Wide Field Imager (WFI) on the MPG/ESO 2.2m telescope (cf. Tab. 2.2). We have observed a total of 110 fields which cover 31.3 deg^2 of which 16.2 deg^2 are at low galactic latitudes ($|b| < 10°$). Full details of these observations are given in Table 2.3. The fields observed in the earlier epochs – INT1 and 2 and ESO1 – were mostly observed

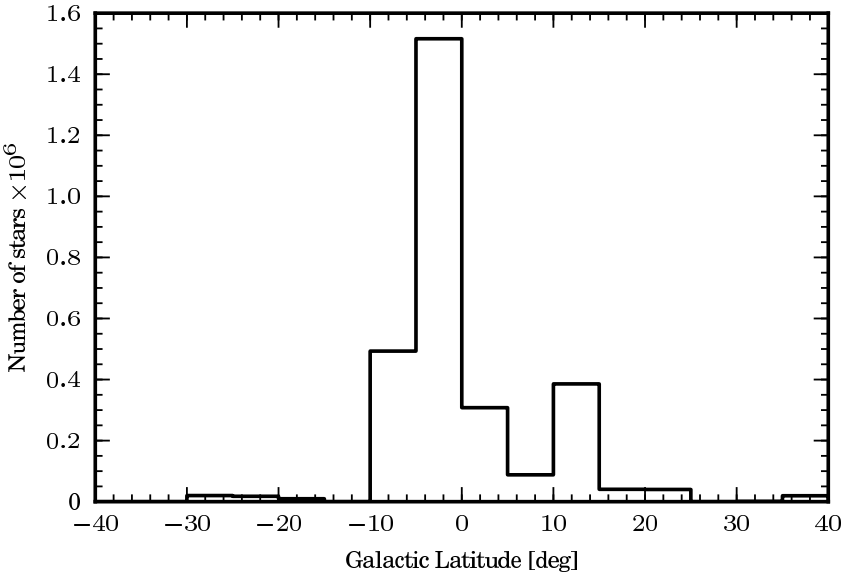

Figure 2.8: The galactic latitudes of all the stars observed during the first 5 years of the RATS project that have more than 60 photometric data-points. Our field are biased towards the Galactic equator: 78 percent of the stars in our sample lie within $|b| < 10°$.

Epoch ID	Dates	# of fields	Galactic latitudes	Total stars	Filters
INT1	20031128-30	12	$> \|16°\|$	45572	BVi'
INT2	20050528-31	14	a	234029	BVi'
ESO1	20050603-07	20	b	750109	BVi'
INT3	20070612-20	26	$< \|15°\|$	1223803	$Ug'r'$
INT4	20071013-20	29	$< \|10°\|$	678025	$Ug'r'$
INT5	20081103-09	9	$< \|10°\|$	112788	$Ug'r'$

[a] 3 fields $< |10°|$ and 11 fields $> |22°|$
[b] 4 fields $< |10°|$ and 16 fields $> |16°|$

Table 2.2: Summary of the 6 epochs in which our observations were taken. The total stars column refers to sources with at least 60 photometric data-points.

at Galactic greater than $|b| > 15°$. The reason for this was to enable us to develop our data reduction software in fields with relatively low stellar density. However, this does have the added benefit of allowing us to determine Galactic scale-heights of stellar populations. On top of this, we are also able to calibrate our photometry against the Sloan Digital Sky Survey in a few fields where our observations overlap.

Field ID	Date	RA DEC (J2000)	l, b (J2000)	Duration	Seeing ($''$)	# light curves
INT1-2	2003-11-28	22:57:08.9 +34:13:02	97.5 −22.9	2h 33m	0.8–1.3	4061
INT1-6	2003-11-28	02:08:10.7 +36:16:13	139.8 −24.1	2h 23m	1.0–1.5	2786
INT1-11	2003-11-28	04:11:31.1 +19:24:55	174.6 −22.8	2h 04m	1.0–1.5	2762
INT1-21	2003-11-28	07:29:20.0 +23:25:36	195.4 +18.4	2h 31m	1.0–1.5	4097
INT1-1	2003-11-29	23:10:43.9 +34:19:48	100.3 −24.1	2h 47m	1.2–2.0	3464
INT1-8	2003-11-29	02:02:15.6 +34:21:40	139.2 −26.3	2h 22m	1.3–2.6	3321
INT1-16	2003-11-29	04:55:55.5 +13:04:42	186.9 −18.4	2h 02m	0.9–1.3	4783
INT1-806	2003-11-29	08:06:23.0 +15:27:31	206.9 +23.4	2h 06m	0.8–1.1	4518
INT1-3	2003-11-30	23:04:48.0 +34:26:19	99.1 −23.4	2h 18m	0.7–1.1	4576
INT1-307	2003-11-30	03:06:07.2 −00:31:14	179.1 −48.1	1h 59m	1.0–1.4	1722
INT1-17	2003-11-30	04:50:42.5 +18:11:59	181.8 −16.4	2h 30m	0.9–1.3	4838
INT1-22	2003-11-30	07:39 51.9 +23:50:03	196.0 +20.8	2h 41m	0.9–1.3	4644

Table 2.3: Summary of the fields observed in the first 6 epochs of our survey. Field ID is in the format epoch-field#, see table 2.2 for a summary of each epoch. Field centre refers to the centre of CCD4 in the INT WFC observations and close to the centre in the case of ESO WFC observations. The duration is the time-span for the series of 30 sec exposures. The seeing was determined from the FWHM of the images; the number of light curves is those stars for which more than 60 data-points were obtained.

Field ID	Date	RA DEC (J2000)	l, b (J2000)	Duration	Seeing (″)	Number of light curves
INT2-1	2005-05-28	13:57:08.6 +22:48:16	20.3 +74.5	1h 53m	1.5–3.0	988
INT2-2	2005-05-28	16:05:45.8 +25:51:45	42.8 +46.8	1h 53m	0.8–1.2	2209
INT2-3	2005-05-28	20:01:53.9 +18:47:41	57.8 −6.2	1h 57m	1.5–1.9	32428
INT2-4	2005-05-29	12:00:00.0 −00:00:00	276.3 +60.2	0h 56m	0.7–1.2	1517
INT2-5	2005-05-29	13:59:31.7 +22:10:56	18.9 +73.8	1h 51m	0.8–1.3	1590
INT2-6	2005-05-29	16:09:10.0 +24:00:13	40.4 +45.6	1h 51m	0.7–1.0	2634
INT2-7	2005-05-29	18:03:29.9 +29:56:25	56.1 +22.8	2h 09m	0.8–1.0	4333
INT2-8	2005-05-30	14:00:37.2 +22:45:59	21.2 +73.7	1h 57m	0.7–0.9	2511
INT2-10	2005-05-30	17:59:12.6 +28:25:20	54.2 +23.2	1h 51m	0.6–0.8	8465
INT2-11	2005-05-30	19:53:46.1 +18:46:42	56.7 −4.6	1h 40m	1.4–1.5	90451
INT2-12	2005-05-31	13:58:40.1 +23:34:19	23.5 +74.4	2h 26m	0.6–0.8	1983
INT2-13	2005-05-31	17:56:28.9 +29:09:39	54.7 +24.0	2h 02m	1.3–1.5	8172
INT2-14	2005-05-31	19:55:30.5 +18:42:04	56.9 −5.0	1h 57m	1.3–1.5	76748

Field ID	Date	RA DEC (J2000)	l, b (J2000)	Duration	Seeing ($''$)	Number of light curves
ESO-1	2005-06-03	12:04:20 −24:50:31	289.6 +36.8	1h 46m	1.0–1.3	1573
ESO-2	2005-06-03	14:03:32 −22:17:05	324.1 +37.6	1h 56m	0.8–1.1	2872
ESO-5	2005-06-03	20:04:50 −24:04:46	17.9 −26.2	2h 32m	0.8–1.2	8000
ESO-4	2005-06-03	16:23:36 −26:31:39	351.0 +16.0	3h 28m	0.7–1.0	36424
ESO-7	2005-06-04	12:08:15 −22:56:35	290.1 +38.9	2h 37m	1.4–2.6	1356
ESO-8	2005-06-04	13:53:46 −23:41:48	320.9 +37.0	2h 25m	1.2–2.4	2567
ESO-10	2005-06-04	18:01:03 −26:54:22	3.5 −1.9	2h 16m	0.7–1.2	142523
ESO-13	2005-06-05	12:02:40 −22:32:40	288.4 +38.9	2h 28m	0.6–1.4	1696
ESO-14	2005-06-05	14:03:47 −24:55:05	323.1 +35.1	2h 27m	0.7–1.1	4402
ESO-16	2005-06-05	18:07:54 −24:56:23	5.9 −2.3	2h 32m	0.7–1.4	173696
ESO-17	2005-06-05	20:05:13 −22:32:36	19.6 −25.8	2h 35m	0.8–1.4	8711
ESO-19	2005-06-06	12:01:38 −24:25:27	288.7 +37.1	2h 28m	0.8–1.4	2556
ESO-21	2005-06-06	16:00:16 −25:33:01	347.9 +20.4	2h 27m	0.6–0.9	9877
ESO-22	2005-06-06	18:36:26 −23:55:04	9.9 −7.6	2h 32m	0.7–1.0	162417
ESO-6540	2005-06-07	18:06:01 −27:44:40	3.3 −3.3	2h 25m	0.6–0.8	185173
ESO-25	2005-06-07	12:08:07 −25:14:10	290.7 +36.6	1h 52m	0.6–2.0	3512
ESO-30	2005-06-07	22:03:11 −24:43:56	26.8 −52.3	2h 00m	0.6–0.9	2754

Field ID	Date	RA DEC (J2000)	l, b (J2000)	Duration	Seeing ($''$)	Number of light curves
INT3-2	2007-06-12	17:59:00 +01:38:00	28.4 +12.4	1h 45m	1.1–1.4	34275
INT3-3	2007-06-12	19:42:00 +19:06:00	55.6 −2.0	1h 19m	1.0–1.3	117341
INT3-4	2007-06-13	18:04:00 +02:20:00	29.6 +11.6	2h 08m	1.1-1.7	13194
INT3-5	2007-06-13	18:00:30 +01:35:00	28.5 +12.0	2h 00m	0.9–1.2	43524
INT3-6	2007-06-13	19:41:00 +19:48:00	56.1 −1.4	1h 53m	0.8–1.1	135686
INT3-7	2007-06-14	18:04:00 +01:31:00	28.8 +11.2	2h 05m	0.9–1.5	17583
INT3-8	2007-06-14	17:55:00 +01:46:00	28.0 +13.4	2h 00m	0.8–1.2	34249
INT3-9	2007-06-14	19:37:00 +19:47:00	55.6 −0.6	2h 00m	0.8–1.0	117956
INT3-10	2007-06-15	18:00:00 +02:13:00	29.0 +12.4	2h 16m	1.3–2.6	10358
INT3-11	2007-06-15	18:04:00 +00:46:00	28.2 +10.9	2h 20m	1.0–1.4	43084
INT3-12	2007-06-15	19:40:00 +22:50:00	58.6 +0.3	2h 00m	0.8–1.1	41726
INT3-13	2007-06-16	17:55:00 +02:22:00	28.5 +13.6	2h 06m	1.3–1.8	10323
INT3-14	2007-06-16	18:01:00 +00:42:00	27.7 +11.5	2h 00m	1.2–1.5	38365
INT3-15	2007-06-16	19:31:00 +19:03:00	54.3 +0.2	2h 04m	1.1–1.5	84418
INT3-16	2007-06-17	18:23:04 +05:53:25	35.0 +9.0	2h 17m	1.3–2.0	9553
INT3-17	2007-06-17	18:22:51 +08:25:34	37.3 +10.3	2h 10m	0.9–1.2	51788
INT3-18	2007-06-17	19:27:00 +22:40:00	57.0 +2.8	2h 09m	0.9–1.0	93095
INT3-20	2007-06-18	18:19:42 +05:52:01	34.6 +9.7	2h 04m	1.9–3.0	4622
INT3-21	2007-06-18	18:18:00 +07:35:41	36.0 +10.9	2h 00m	1.4–2.6	30470
INT3-22	2007-06-18	19:39:00 +20:24:00	56.4 −0.7	2h 00m	1.1–1.4	78067
INT3-24	2007-06-19	18:18:18 +06:31:15	35.0 +10.3	2h 00m	1.1–1.5	48472
INT3-25	2007-06-19	20:32:00 +25:11:00	67.0 −8.5	2h 00m	1.2–1.7	52974
INT3-26	2007-06-20	18:20:21 +08:11:47	36.8 +10.6	2h 00m	1.0–1.6	13554
INT3-27	2007-06-20	18:23:47 +07:51:23	36.8 +9.7	2h 00m	0.9–1.2	59027
INT3-28	2007-06-20	20:31:00 +27:26:00	68.7 −7.0	2h 00m	0.8–1.1	40099

Field ID	Date	RA DEC (J2000)	l, b (J2000)	Duration	Seeing ($''$)	Number of light curves
INT4-1	2007-10-13	21:04:25.9 +45:40:34	87.2 −0.8	2h 16m	1.2–1.6	52237
INT4-2	2007-10-13	21:57:14.8 +54:01:00	99.1 −0.6	1h 56m	1.3–1.7	33917
INT4-3	2007-10-13	01:27:01.0 +53:50:51	128.2 −8.7	2h 09m	1.2–1.8	9355
INT4-4	2007-10-13	02:52:26.6 +50:42:29	141.7 −7.7	2h 55m	1.1–2.0	5707
INT4-5	2007-10-14	21:01:15.0 +44:30:47	85.9 −1.2	2h 20m	0.8–1.1	51566
INT4-6	2007-10-14	23:48:10.0 +56:26:08	114.2 −5.4	2h 29m	0.9–1.1	22154
INT4-7	2007-10-14	01:42:15.0 +55:21:46	130.2 −6.8	2h 10m	0.9–1.3	16942
INT4-8	2007-10-14	04:55:19.0 +34:42:02	169.2 −5.5	2h 19m	0.9–1.2	9030
INT4-9	2007-10-15	20:59:15.0 +45:34:42	86.5 −0.2	2h 21m	1.0–1.3	57117
INT4-10	2007-10-15	23:48:04.0 +54:19:49	113.7 −7.4	2h 19m	1.1–1.3	17730
INT4-11	2007-10-15	01:41:42.0 +54:33:14	130.2 −7.6	2h 10m	1.0–1.2	15605
INT4-12	2007-10-15	05:03:31.0 +34:56:22	170.0 −4.0	2h 16m	0.9–1.2	12597
INT4-13	2007-10-16	21:08:06.0 +44:14:06	86.5 −2.3	2h 10m	1.2–1.4	37264
INT4-14	2007-10-16	23:48:04.0 +54:19:49	113.7 −7.4	2h 00m	1.1–1.4	11212
INT4-16	2007-10-17	21:05:39.0 +46:20:27	87.8 −0.6	2h 10m	1.3–1.7	56719
INT4-17	2007-10-17	01:26:19.0 +54:49:00	128.0 −7.7	1h 54m	0.9–1.1	12945
INT4-19	2007-10-17	05:04:51.0 +36:14:33	169.1 −3.0	2h 35m	0.8–1.2	14854
INT4-20	2007-10-18	21:01:49.0 +45:10:21	86.5 −0.8	2h 10m	0.9–1.2	33033
INT4-21	2007-10-18	23:57:34.0 +56:11:06	115.4 −5.9	2h 10m	0.9–1.2	23038
INT4-22	2007-10-18	01:42:22.0 +53:58:47	130.5 −8.1	2h 25m	1.0–1.4	13504
INT4-24	2007-10-19	21:07:34.0 +45:31:43	87.4 −1.3	2h 10m	1.1–1.4	52761
INT4-25	2007-10-19	23:52:37.0 +56:20:59	114.8 −5.6	2h 10m	1.2–1.4	16588
INT4-26	2007-10-19	02:54:43.0 +49:49:49	142.4 −8.3	2h 00m	0.9–1.4	10470
INT4-27	2007-10-19	05:07:38.0 +34:18:48	171.0 −3.7	2h 00m	1.0–1.4	10242
INT4-28	2007-10-20	22:09:27.0 +55:27:30	101.3 −0.5	2h 11m	1.0–1.4	43867
INT4-29	2007-10-20	00:02:06.0 +53:34:37	115.6 −8.6	2h 00m	1.0–1.4	14069
INT4-30	2007-10-20	02:49:23.0 +50:17:50	141.5 −8.3	2h 00m	0.9–1.3	12571
INT4-31	2007-10-20	05:03:57.0 +34:16:49	170.6 −4.3	2h 00m	0.8–1.3	12571

Field ID	Date	RA DEC (J2000)	l, b (J2000)	Duration	Seeing ($''$)	Number of light curves
INT5-2	2008-11-03	01:49:58.6 +56:19:39	131.0 −5.6	2h 46m	0.7–1.1	9497
INT5-3	2008-11-03	04:34:33.4 +39:55:22	162.5 −5.2	2h 31m	0.7	7541
INT5-4	2008-11-06	21:10:10.0 +49:31:56	90.7 +1.0	2h 10m	0.8–0.9	21967
INT5-5	2008-11-06	23:40:09.0 +57:01:33	113.3 −4.5	2h 49m	0.8–1.0	14379
INT5-6	2008-11-06	04:31:45.0 +40:27:12	161.7 −5.3	2h 11m	0.7	10837
INT5-7	2008-11-06	06:55:57.5 +10:37:54	203.9 +5.8	2h 01m	0.7–0.9	11288
INT5-8	2008-11-07	23:24:50.2 +57:13:57	111.4 −3.7	2h 10m	0.7–0.8	15334
INT5-9	2008-11-07	03:05:05.7 +55:35:15	141.1 −2.5	2h 00m	0.7	10605
INT5-10	2008-11-07	06:04:33.8 +24:42:45	185.8 +1.5	2h 20m	0.7	11340

2.1.4 Image preparation

Each night, before science observations, we took bias frames and twilight flat-field images in each filter. Each night's bias frames were combined to make a median image using the MEDSKY program which is included as part of the FIGARO package which, in turn, is part of the STARLINK suite of software. I then subtracted a nightly master bias from flat-field and science images. The de-biased flat-fields images for the whole epoch were combined using MEDSKY but this time each image was scaled to the first image in the list of flat-fields, this was to reduce the effects caused by having a different number of average counts in each flat-field image. I was careful to exclude any flat-field images that were saturated. The science images were then divided by a master flat image which limits the effects of differences in the sensitivity of different pixels on the CCD.

Fringing is a pattern which occurs on a CCD consisting alternating brighter and darker bands. They are caused by interference between reflected light and incoming light within the CCD or long wavelength light passing through the CCD and being reflected back into the CCD, essentially forming a pattern of Newton's rings which is detected at red and near infra-red wavelengths. The formation of them is usually caused by OH emission lines in the upper atmosphere (Pecker, 1970). They are forbidden transitions and appear as a very narrow feature if observed spectroscopically. They can be variable over the course of several nights (Howell, 2000). Fringing is highly undesirable as when stars move in x, y space across the CCD over the course of the time series observations they pass over an alternating bright/dark pattern and they appear to be variable, depending on the pattern even periodically variable. In the case of our white light and i' band images, fringing was present in most images. However, when there was thin cloud the fringing disappeared. I removed the effects of fringing in all but a handful of fields where thin clouds were present. I did this by making a super-flat – also known as a fringe-map. In most epochs I made this by taking a number of images throughout the night (typically one from each field observed) and removing the stars from the image using DAOPHOT and ALLSTAR. The super-flat was then created from the median of these. In INT5 observations we observed blank fields, which contain minimal numbers of stars, and created a median of these using MEDSKY.

Each blank field was observed for approximately 5 times with an offset of ±20 arcsec in both the right ascension and declination directions from the first blank image. This has the effect of removing any stars that are in the image when the median is created. All the science images were then divided by a super-flat. I found that fringing patterns did not show significant variations over the course of the night but changed subtly over several nights. The fringing left in the data is below the level of 1 per cent which is below the level of other photometric errors and therefore not considered any further.

2.2 Photometry

2.2.1 Extracting light curves

In our first set of observations (Ramsay & Hakala, 2005) the STARLINK aperture photometry package, AUTOPHOTOM was used. This technique provides accurate photometry at a reasonable computational speed for fields with low stellar density but proved to be unsuitable for fields containing more than a few 1000 stars owing to the computational processing time involved and – for very crowded fields – its inability to separate blended stars. The computational time was so great that it would have taken longer than the length of my Ph.D to reduce our whole data-set.

I opted to switch to a different method of photometry, difference image analysis (DIA Alard & Lupton, 1998), which is more suitable for crowded fields and takes into account changes in seeing conditions over the course of the observation. The principle of DIA is to take reference image of a field and then subtract each individual science image from that reference image. The intensity of any residuals can then be measured, which gives the brightness of the source relative to the reference. The reference is generally made from a median of several images – usually those with the best seeing – and before images are subtracted the reference must be degraded to the seeing of the science image.

I use a use a modified version of the DANDIA (Bond et al., 2001; Bramich, 2008; Todd

et al., 2005) implementation of DIA. A summary of the parameters used in this technique are given in Table 2.4. The reference image is made from the four images with the best seeing which are aligned and averaged to increase the signal-to-noise in the reference image. Sources are detected on each science image if their flux is more than 3σ above the background and are then used to align the images. Each CCD is split into eight 1024×1024 pixel sub-frames. The point-spread function (PSF) for each sub-frame is calculated using the stars that are a minimum of 14σ above the background and have no bad pixels nearby. I split each CCD into sub-frames to reduce the effects of changes in the PSF across the CCD. A maximum of 22 stars were used in calculating the PSF. Each frame is aligned to the reference image and subtracted using the equation

$$D(x, y) = I(x, y) - M(i, j) \tag{2.1}$$

where $D(x, y)$ is the resultant difference image, $I(x, y)$ is the science image, and $M(i, j)$ is the model which is created to represent the PSF degraded reference frame, which is defined as,

$$M(i, j) = [R(x, y) \otimes K(u, v) + B(x, y)] \tag{2.2}$$

where $R(x, y)$ is the reference image, $K(u, v)$ is the kernel that matches the image and the reference PSF and $B(x, y)$ is the spatially varying differential background. x and y refer to the column and row of pixels the image; u and v refer to the row and column for the kernel. Reducing this to a least-squares problem, I try to minimize

$$\chi^2 = \sum_{x,y} \left(\frac{I(x, y) - [R(x, y) \otimes K(u, v) + B(x, y)]}{\sigma(x, y)} \right)^2 \tag{2.3}$$

where $\sigma(x, y)$ are the uncertainties on each pixel. The kernel used is circular and degrades the PSF of all sources in the reference image, $R(x, y)$, to that of the science image, $I(x, y)$.

The task is now to create an acceptable model (i.e. degraded reference frame). As shown in Bramich (2008), I can rewrite Equation 2.2 to represent the kernel as a pixel array $K_{u,v}$ with N_K pixels which u and v represent the pixel columns and rows numbers for the kernel. The differential background is rewritten as a constant B_0 and, hence, Equation 2.2 can be

rewritten as:

$$M_{x,y} = \sum_{u,v} K_{u,v} R_{(x+u)(y+v)} + B_0 \tag{2.4}$$

which has $N_K + 1$ unknowns and the kernel contains pixel $K_{0,0}$. The χ^2 in Equation 2.3 has a minimum when the gradient of χ^2 with respect to $K_{u,v}$ and B_0 is zero (Bramich, 2008). We use this to solve Equation 2.4. by performing $N_K + 1$ differentiations. Rewriting the set of linear equation in matrix form give the matrix equation **Ua** = **b** where:

$$U_{p,q} = \begin{cases} \sum_{x,y} \frac{R_{(x+u),(y+v)} R_{(x+u'),(y+v')}}{\sigma^2_{x,y}} & \text{for } 1 \le p \le N_K \text{ and } 1 \le q \le N_K \\ \sum_{x,y} \frac{R_{(x+u'),(y+v')}}{\sigma^2_{x,y}} & \text{for } p = N_K + 1 \text{ and } 1 \le q \le N_K \\ \sum_{x,y} \frac{R_{(x+u),(y+v)}}{\sigma^2_{x,y}} & \text{for } 1 \le p \le N_K \text{ and } q = N_K + 1 \\ \sum_{x,y} \frac{1}{\sigma^2_{x,y}} & \text{for } p = q = N_K + 1 \end{cases}$$

$$a_p = \begin{cases} K_{u,v} & \text{for } 1 \le p \le N_K \\ B_0 & \text{for } p = N_K + 1 \end{cases}$$

$$b_p = \begin{cases} \sum_{x,y} \frac{I_{x,y} R_{(x+u),(y+v)}}{\sigma^2_{x,y}} & \text{for } 1 \le p \le N_K \\ \sum_{x,y} \frac{I_{x,y}}{\sigma^2_{x,y}} & \text{for } p = N_K + 1 \end{cases} \tag{2.5}$$

p and q are the indices of the vector **a** associated with the kernel indices (u, v) and the differentiated (u', v'), respectively. To find the values of **a**, that is, $K_{u,v}$ and B_0, requires the calculating of **a** = $\mathbf{U}^{-1}$**b**.

Dead and saturated pixels are ignored in both the science image and the reference image when calculating **U** and **b** which limits the maximum kernel size that can be used if there are many bad and saturated pixels in the images. What is left after the subtraction of the model from the science image is a 'difference image' which consists of photon and other random noise except where the stars have changed in brightness from the reference or where the background has changed. Aperture photometry is then performed on the residuals to create a light curve made up of positive and negative residuals.

For the uncertainties in each pixel we use the equation

$$\sigma_{x,y}^2 = \sigma_0^2 + \frac{M_{x,y}}{G} \tag{2.6}$$

where σ_0^2 is the CCD readout noise and G is the gain. As $\sigma_{x,y}^2$ is dependent on $M_{x,y}$ the calculation of $M_{x,y}$ is an iterative process (Bramich, 2008), I set 120 as the maximum number of iterations. It is assumed that the reference image pixels have no uncertainties as these pixels are from a high signal-to-noise image. The initial value for background is set by manually defining a region devoid of stars and bad pixels in the reference image and calculating the median value. This region typically has a size of 50 × 50 pixels, though this varies depending on how many stars are in the image (if the image has very high stellar density the background region is forced to be smaller). The initial kernel value is set by defining a region of the reference image which contains a large number of bright – but not saturated – stars and calculating the mean PSF. The size of with region varies depending on the stellar density, with larger regions having to be used if the stellar density is small. The initial values for the background and kernel are constant over all sub-frames.

The mean photometric scale factor between the reference image and each science image is given by the sum of the pixel values in the kernel, $P = \sum_{u,v} K_{u,v}$. In order to convert from flux to magnitudes I first calculate the total flux of a star at time t using equation 3 from Todd et al. (2005):

$$f_{\mathrm{tot}}(t) = f_{\mathrm{ref}} + \frac{f_{\mathrm{diff}}(t)}{P(t)} \tag{2.7}$$

and then covert to magnitudes using

$$m(t) = 25.0 - 2.5\log(f_{\mathrm{tot}}(t)) \tag{2.8}$$

The total flux at time time, $f_{\mathrm{tot}}(t)$, is the combined flux from the reference and the differential flux. The photometric scale factor $P(t)$ accounts for extinction which effects the whole sub-frame relative to the reference image.

Only stars that appear in the reference image have a light curve created. This prevents us from finding transient events unless they appear in any of the reference images. In future

Group	Parameter	Value
CCD parameters	Good pixel values	0–50000 ADU
	Bad pixel value	-1
	Number of subframes	8
	Subframe size	1024 × 1024 pixels
	CCD region in use, (x,y)	(0–2048,0–4096)
Alignment	Star detection threshold	3σ
	Kernel radius for reference image generation	12 pixels
	Number of stars used for alignment	1500
	Match range	10 pixles
	Match step	1 pixel
	Match radius	1 pixel
Kernel model	Number of Gaussian functions	3
	Polynomial order used to model background	3
DI generation	Sigma clipping of outliers	3σ
	Max. number of outliers before stopping	70
	Max. iterations	120
DI measurement	Kernel radius	22
	Aperture radius	18

Table 2.4: Parameters used when performing difference image analysis (DIA) photometry. The parameters are grouped by which part of the DIA code they are used in. When performing the alignment, the alignment program will search within 'match range' in steps of 'match step' for a star within 'match radius' in each star. The offset with the most matched stars is set as the real offset. DI is an abbreviation for difference image

work it will be possible to look for these events in the data but this in not within the scope of this work.

2.2.2 Removing systematic effects

All variability surveys of this type suffer from sources of systematic error and RATS is no different (for a detailed discussion of systematic errors present in survey data see Collier Cameron et al., 2006). There are many sources of systematic errors which are field and source dependent. Changes in airmass causes changes in the atmospheric absorption of flux from a stars and effects stars differently depending on their colour. Despite our best efforts in reducing the effects of pixel-to-pixel variations by dividing the science images by a flat-field and a super-flat, some variation still remains. Part of this is due to the sensitivity of pixels changing over the course of the night. One reason for this is temperature variations of the CCD over the course of a night. Changes in the transparency also causes systematic

errors as this can vary on scales less than the size of the CCD (Howell, 2000). Thin cloud can also decreases the effect of fringing, as I am dividing the image by a super-flat, if the fringing pattern changes, I am adding a systematic error to the images.

In order to minimise the effects of these trends I apply the SYSREM algorithm (Tamuz et al., 2005). The SYSREM algorithm assumes that systematic trends are correlated in a way analogous to colour-dependent atmospheric extinction, which is a function of airmass and the colour of each source. The colour term is unique to each source (i.e. does not vary between images of the same source) and the airmass term to each individual image. The airmass and colour terms do not necessarily refer to the true airmass at which we observed and the true colour (i.e. a measure of differential extinction) of the star but instead applies to any linear combination of systematic trends. The algorithm minimises the global expression

$$S^2 = \sum_{ij} \frac{(r_{ij} - c_i a_j)^2}{\sigma_{ij}^2} \tag{2.9}$$

Where r_{ij} is the residual of each photometric data-point in an individual light curve when the mean value of the whole light curve is subtracted, c_i is the colour term for light curve i and a_j is the airmass term for image j, σ_{ij} is the error on the photometric data-point and i and j are star number and image number, respectively. Put simply, the algorithm subtracts the product $c_i a_j$ from each data-point of each light curve. The global minimum of S^2 is found by using a criss-cross iteration process (Gabriel & Zamir, 1979) which first calculates c_i, where

$$c_i = \frac{\sum_j (r_{ij} a_j / \sigma_{ij}^2}{\sum_j (a_j^2 / \sigma_{ij}^2)}, \tag{2.10}$$

and then uses the value new value of c_i to calculate a_j, where

$$a_j = \frac{\sum_i (r_{ij} c_i / \sigma_{ij}^2}{\sum_i (c_i^2 / \sigma_{ij}^2)}. \tag{2.11}$$

I set the initial values for both a_j and c_i at unity. Tamuz et al. (2005) find using any sensible initial values does not effect the final values: my testing agrees with these results. I find that using the true airmass as opposed to unity does not affect the result of the de-trending.

The algorithm runs through 20 iterations and once the process is complete the dom-

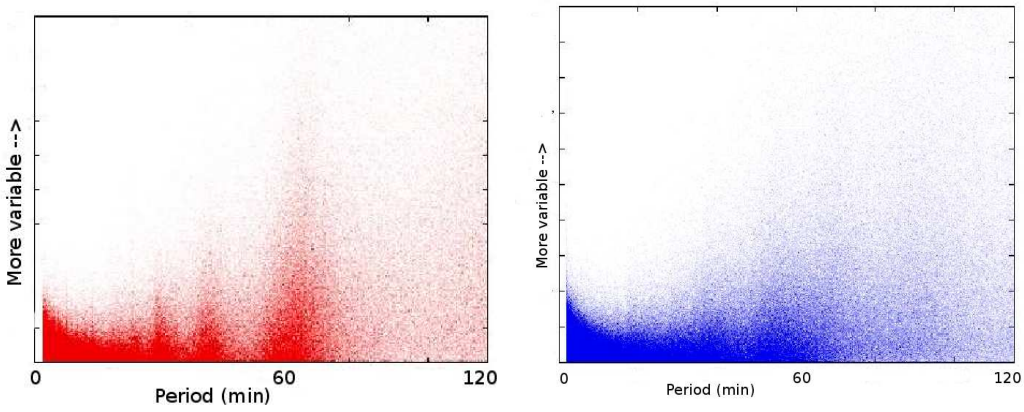

Figure 2.9: These two plots have the significance of the variability seen in a star increasing on the y-axis and the period detected by a variability algorithm on the x-axis. Non-variable sources should be at the bottom of the plot. The left plot has had no detrending performed and it there is a large number of significantly variable sources at ~60 periods as well as other peaks at lower periods – these are trends in the data. In the right plot the majority of this trending has been removed.

inant source of systematic trends is removed. I then run the cycle again using the newly de-trended residuals to remove the next most important source of trends. I continue this till the value of S^2 decreases by less than 5 per cent over the previous cycle. This is done individually for each CCD, though I limit the algorithm to a maximum of six cycles as I find that more than this starts to noticeably degrade signals in high-amplitude variables such as sources those featuring deep eclipses. This then leaves me with light curves which no longer contain strong systematic trends. In Fig. 2.9 I should two plots, in each plot the y-axis is a measure of variability significance, the x-axis is the period detected that each source varies on and each dot represent one star. In the top plot it is possible to see that at some periods (i.e. 60 min) there are peaks in the number of sources detected at high significance. In the right-hand plot Sysrem detrending has been performed and the peaks at certain periods are mostly removed.

To determine the quality of the resulting light curves I calculated the root mean square (rms) from the mean for each light curve. When calculating the rms I sigma-clip each light curve at the 5σ level in order to remove the effects of, say, single spurious data-points. In Fig. 2.10 the measured rms is shown as a function of the g' mag for all stars in the RATS data. The mean rms of all the data is 0.046 mag, with sources brighter and fainter than $g' = 21.0$ having a mean rms of 0.024 and 0.051 mag, respectively. If I look at the mean rms

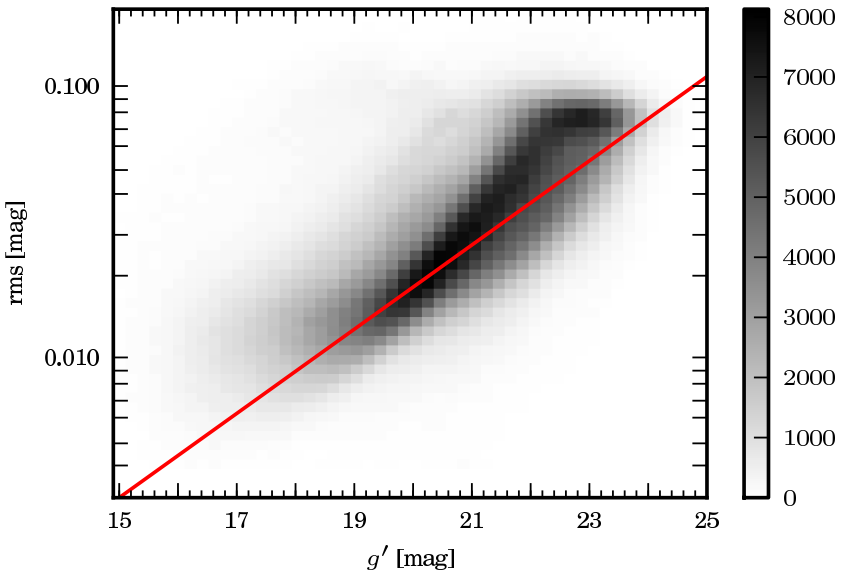

Figure 2.10: The rms noise of each light curve plotted against g' magnitude. The grey-scale refers to the number of sources in each bin. The red line is the best-fit exponential function to the expected rms – that is, the mean error of each light curve

of each field individually, I find two fields in our whole data-set with mean rms outside of 3 standard deviations which I attribute to very large variations in atmospheric transparency during these observations. I show the best-fitting exponential function to the expected rms (equivalent to the average error on each light curve) in Fig. 2.10 and find it to be consistent with the measured rms except of the very faintest stars ($g' > 22$). This implies that for all but the faintest stars, the RATS data, after de-trending, does not suffer from any significant systematic errors.

2.3 Colours

2.3.1 Determining colours[2]

When conditions appeared photometric we obtained images in different filters of a number of Landolt standard fields (Landolt, 1992). We made use of data kindly supplied by www.astro-wise.org who give the magnitude of Landolt stars in a range of different filters.

[2]Taken from **?**

We assumed the mean atmospheric extinction coefficients for the appropriate observing site. The resulting zero-points were very similar to that expected[3].

For our target fields we initially used SExtractor (Bertin & Arnouts, 1996) to obtain the magnitude of each star in each filter. However, in comparison to Daophot (Stetson, 1987), SExtractor gave systematically fainter magnitudes for faint sources. Since the photometric zero-point for Daophot is derived from the PSF (and therefore different from field-to-field) we calculated an offset between the magnitudes of brighter stars determined using SExtractor and Daophot. We then applied this offset to the magnitudes derived using Daophot. To convert our BVi' data (Table 2.2) to $g'r'$ magnitudes we used the transformation equations of Jester et al. (2005).

Although our light curves were obtained in white light, the depths are given the appropriate value as implied in the g' filter. For stars with $(g-r)$ ~1.0, the typical depth for fields observed in photometric conditions and with reasonable seeing (better than 1.2 arcsec) is $g \sim 22.8 - 23.0$, while for redder stars ($g - r$ ~2.0) the depth is $g \sim 23.6 - 24.0$.

To test the accuracy of our resulting photometry, we obtained a small number of images of SDSS fields (York et al., 2000). For stars $g' < 20$ we found that for $g_{\rm RATS} - g_{\rm SDSS}$, σ=0.12 mag and for $(g_{\rm RATS} - r_{\rm RATS}) - (g_{\rm SDSS} - r_{\rm SDSS})$, σ=0.22. For stars $20 < g < 22$ we find for $g_{\rm RATS} - g_{\rm SDSS}$, σ=0.29 mag and $(g_{RaTS} - r_{RATS}) - (g_{\rm SDSS} - r_{\rm SDSS})$, σ=0.27. Given our project is not optimised to achieve especially accurate photometry these tests show that our photometric accuracy is sufficient for our purposes, namely determining an objects brightness and approximate colour.

2.3.2 Colours of sources in our data

A colour-magnitude diagram of all the stars in our data in the $g' - r'$, g' plane is shown in top panel of Fig. 2.11. Two broad populations are present: one which is bright ($g' \sim 19 - 21$) and blue ($g' - r' \sim 0.6 - 0.7$); the other is fainter ($g' \sim 22 - -23$) and redder ($g' - r' \sim 1.5 - 2.0$).

[3] e.g www.ast.cam.ac.uk/ wfcsur/technical/photom/zeros/

The bluer population is thought to originate in the Galactic halo or thick disc, while the redder population is thought to originate in the thin disc (e.g. Robin et al., 2003). Data similar to these has been used to model the structure of the Milky Way as a function of Galactic latitude and longitude (cf. Chen et al., 2001), but this is beyond the scope of this present work.

In the low panel of Fig. 2.11 I show a colour-colour plot of the RATS data in the $(U - g', g' - r')$ plane. If I compare this to the colour-colour diagram in fig.5 of Morales-Rueda et al. (2006) which shows data from the Faint Sky Variability Survey (FSVS), the RATS data have a much broader width over the strip where the main sequence lies. This is likely to be because the RATS observations are biased to low Galactic latitudes whereas the FSVS field were predominantly at mid to high Galactic latitudes. Our fields will be affected to a far greater effect by interstellar reddening/extinction than the FSVS which causes the greater spread of colours. Similarly to the colour-magnitude plot, there appears to be two populations in colour-colour space, one bluer in the $(U - g')$ filters than the other. The bluer population is attributable to the thick disc population and the redder population to the thin disc (Schultheis et al., 2006).

2.4 Astrometry[4]

As part of our pipeline we embedded sky co-ordinates into our images using software made available by Astrometry.net (Lang et al., 2010). This uses a cleaned version of the USNO-B catalogue (Barron et al., 2008) as a template for matching sources in the given field. The only input we provide is the scale for the detectors and the approximate position of the field, which is taken from the header information in the images. The Astrometry.net software works well in either sparsely or relatively dense fields. By comparing the resulting sky co-ordinates of stars with matching sources in the 2MASS (Jarrett et al., 2000) the typical error was 0.3–0.5 arcsec.

[4]Taken from **?**

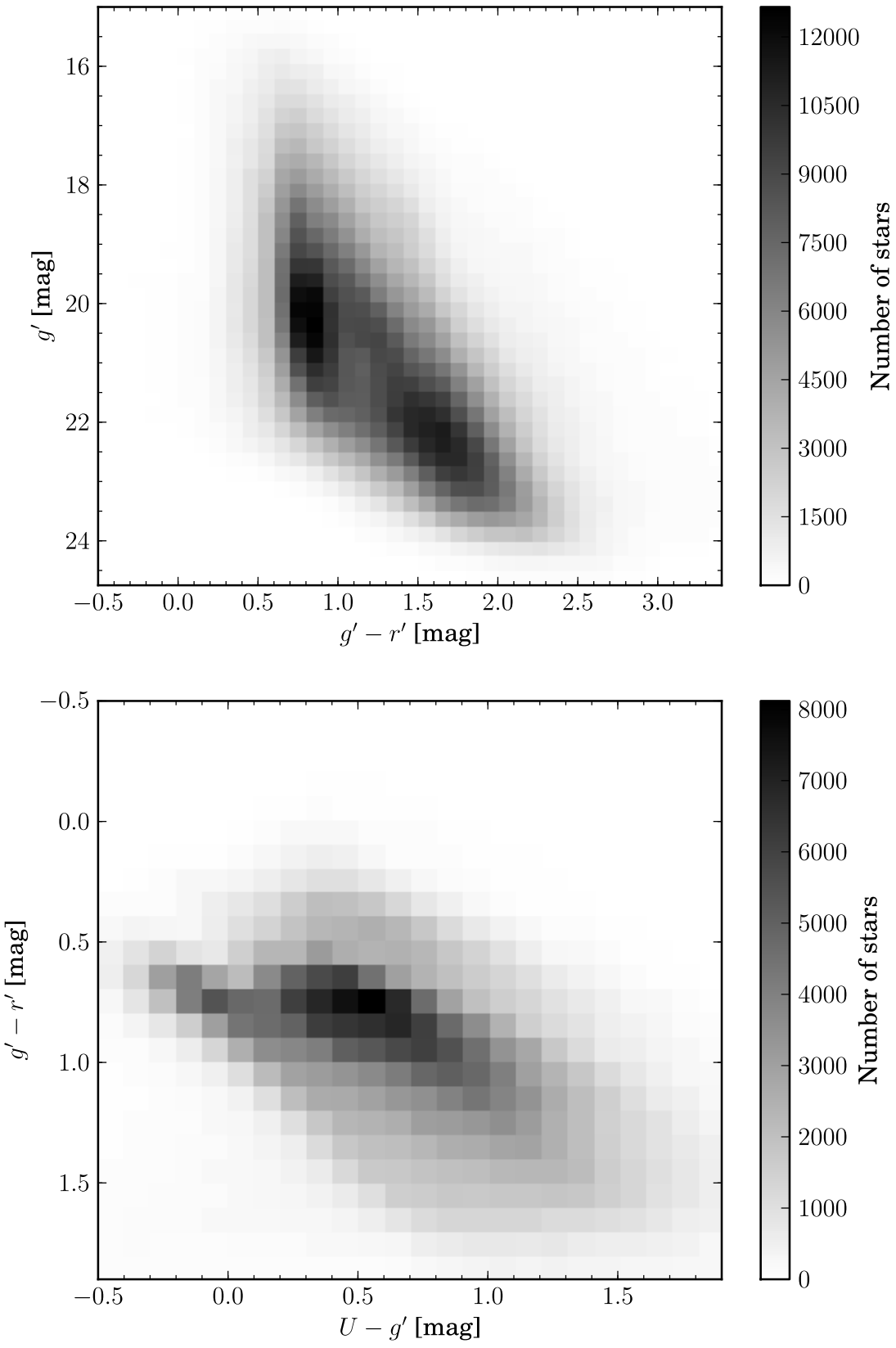

Figure 2.11: The top plot shows a colour-magnitude diagram [in $(g' - r', g')$ space] of the source in the RATS data. The redder and bluer populations are due to the thin disc and the thick disc,respectively. The low plot is a colour-colour diagram [in $(U - g', g' - r')$ space] of the same data as the top plot. Again, there are two populations. The redder and blue populations are due to the thin and think disc, respectively.

2.5 Summary

In this Chapter I have described the wide-field observation which comprise the majority of the RATS data-set. I have described our strategy of observing fields every minute for around two hours and the difference imaging technique used to determine the brightness of these sources. I finish the Chapter by describing some of the information contained in the data such as colour and spatial position. The primary aim of this survey, however, is the detection of variability. The next Chapter will address this aspect of the survey. I describe how to detect variability in the light curves which have been produced. These variability data form a database which can be searched for sources matching the description of various different populations of variable sources.

Chapter 3

Searching for variability

> A safe but sometimes chilly way of recalling the past is to force open a crammed drawer. If you are searching for anything in particular you don't find it, but something falls out at the back that is often more interesting.
>
> *J. M Barrie, Peter Pan; or, The Boy Who Wouldn't Grow Up, 1902.*

The RATS data-set contains over 3 million fully reduced light curves, many of which I expect to be scientifically interesting. The aim of this Chapter is to explain how I identify the most interesting light curves for further study. Put simply, how do we separate the wheat from the chaff?

The first question to ask is, what am I looking for? I expect to find many classes of systems in the RATS data such, e.g. flare stars, eclipsing and contact binaries and pulsating stars. Below I discuss a number of algorithms which can be used to detect periodic variability, their strengths and weaknesses and how they are used to detect variable sources.

3.1 Variability algorithms

Writing bespoke software for the purpose of detecting variability would be time consuming and relatively pointless as there is a wealth of tools available for this task. I settled on using

the VARTOOLS package written by Hartman et al. (2008) for the majority of the variability tests I run. This software contains a good selection of variability detection algorithms, is computationally fast to run, and can easily be incorporated into a software pipeline.

Of the algorithms which are available in VARTOOLS for the purposes of variability detection and classification I selected; alarm, Stetson J, kurtosis, χ^2, analysis of variance, Lomb-Scargle periodogram and Fourier series fitting. I excluded some exoplanet specific algorithms such as the Mandel & Agol (2002) transit model and others such as box least-squares fitting (BLS Kovács et al., 2002) as they provide little in the way of useful information when compared with the extra computational expense, which for BLS is significant.

Before the light curves are processed by the variability detection and classification algorithms the light curves are first 'cleaned'. First, any data-point in light curve which are more than 5 standard deviations from the mean are clipped – I do not remove these data from the light curves, they are just ignored by the variability algorithms. I pick 5σ as the clipping cut-off as this provides a good balance between removing bad data-points while not clipping any short period variability such as short eclipses or flares. This clipping is done to improve the results given by statistics such as alarm, χ^2, and analysis of variance which are heavily influenced spurious data-points. I also remove light curves from the data which contain less than 60 data-points. This, again, is done as a number of algorithms can give spurious detections of variability is a significant portion of the data is missing. Of the initial 3.7 million stars I am left with 3.1 million which have 60 or more data-points. It should be noted that this does limit my potential to find optical transient sources although these are unlikely to be detected anyway as they would have to appear in the image with the best seeing (cf. Chapter 2).

Below is a description of the algorithms that are used. They are split into non-periodic and periodic variability detection based on whether they determine a period for a given source.

3.1.1 Non-periodic variability

Chi-squared test The chi-squared test is a measure of the variance of a population from a model. The model I use is the mean brightness of the light curve, giving the chi-squared equation as

$$\chi^2 = \sum_{i=1}^{n} \frac{(O_i - \overline{O})^2}{\sigma_i^2} \tag{3.1}$$

where $O(i)$ is the observed brightness, $\overline{O}$ is the mean brightness of the light curve weighted to take account of the errors and σ_i is the error on the brightness. Sources where the variability is significantly greater than the size of the errors will have a high chi-squared value whereas non-variable sources will have a chi-squared that tends to unity. There are, however, a number of weaknesses in using this algorithm alone to detect variability. Firstly, it gives no information on what type of variability is present, be it periodic or non-periodic. A high amplitude, short lived flare could have the same value as a low amplitude pulsator. As we are dealing with millions of stars, it is not particularly useful to know that, say, 100,000 of them are variable as one does not particular relish the prospect of visually classifying 10^5 or more stars. A second issue is that sources that pass over hot and dead pixels and other non-uniformities in the CCD, which have not been removed during the flat-fielding process, are detected as highly significant variables (though a visual inspection of the processed images suggests that this is not a significant issue). These weaknesses mean I do not use the chi-squared test for detecting variable sources in this work. Chi-squared does have some redeeming features, however. It is useful when trying to describe the variability of the RATS data-set as a whole. The chi-squared distribution shown in Fig.3.1 closely approximates a normal distribution with a long tail which represents the variable sources. The mean chi-squared of our data is 2.8, while the standard deviation on the chi-squared values (σ) is 440, although because of the very long tail in the distribution these statistics are rather meaningless. More robust statistics are the median and the median absolute deviation from the median (MAD, Hampel, 1974) which I use as a measure of the distribution. MAD is defined for parameters $\{x_1, \ldots, x_n\}$ as

$$\mathrm{MAD}_n = b\ \mathrm{med}_i |x_i - \mathrm{med}_j x_j| \tag{3.2}$$

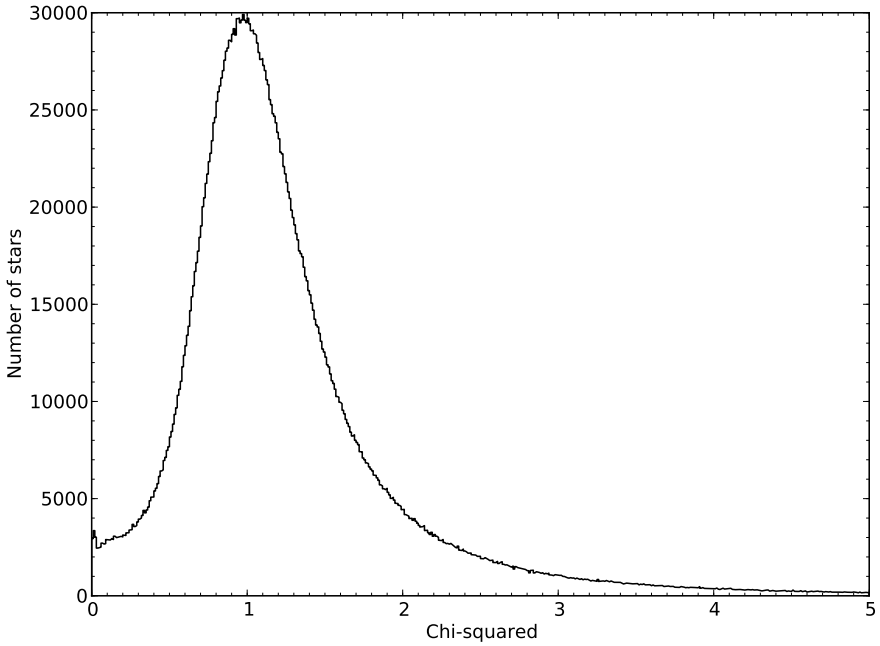

Figure 3.1: The distribution of Chi-squared values for the light curves in the RATS data. The data have been binned with a bin width of 0.01 in chi-squared. The distribution peaks very close to unity.

where b is a constant which makes the MAD consistent with the standard deviation. For a Gaussian distribution $b = 1.4826$ (Rousseeuw & Croux, 1993) which I use for simplicity. The median of the chi-squares is 1.01 and the MAD is 0.31. Given that our data consist of 3.1 million sources, one would expect 4110 sources to have a chi-squared value three times the MAD or more above the median, and 96 have chi-squares of five times the MAD or more above the median if the distribution of chi-squares were normal and the data contained no variables sources. In fact, I find that 1.94×10^5 have a chi-squared values of three or more MADs above the median and 1.16×10^5 are five MADs above the median. This suggests that our data contains a more than 10^5 variables (or at least sources which mimic variability such as sources which pass over non-uniformities in the CCD which have not been removed by flat-fielding).

Alarm The alarm variability statistic (Tamuz et al., 2006) is designed to detect eclipsing binaries. It measures correlated residuals to a fit of a mean to the light curve. A run of negative residuals which is followed by a later run of positive residuals in the light curve then indicates that the light curve contains an eclipse. A run is defined as the number of

consecutive residuals with the same sign and if k_i is the number of residuals in the ith run the alarm statistic $\mathcal{A}$ is defined (from eq. 3 in Tamuz et al., 2006) as

$$\mathcal{A} = \frac{1}{\chi^2} \sum_{i=1}^{M} \left(\frac{r_{i,1}}{\sigma_{i,1}} + \frac{r_{i,2}}{\sigma_{i,2}} + \ldots + \frac{r_{i,k_i}}{\sigma_{i,k_i}} \right)^2 - \left(1 + \frac{4}{\pi} \right), \tag{3.3}$$

where $r_{i,j}$ is the jth measurement of the ith run and $\sigma_{i,j}$ is the uncertainty. The sum is over all measurements in the run and then over M runs and χ^2 is the chi-squared which is defined in Equ. 3.1. If the residuals are uncorrelated, $\mathcal{A}$ is low; the more runs of correlated residuals, the higher the statistic.

The algorithm is equally adept at detection of eclipsing binaries, flare stars and even solar system bodies such as asteroids which pass through the point-spread function of stars.

Stetson J The Stetson (1996) J statistic (SJS) is, like the alarm statistic, a measure of correlated residuals and is designed to detect high amplitude variables with low photometric errors. The algorithm measures whether pairs of residuals [a brightness with the weighted mean (see Equ. 3.7) subtracted] have the same sign. The SJS is given by:

$$J = \frac{\sum_{k=1}^{n} w_k + \Lambda}{\sum_{k=1}^{n} w_k} \tag{3.4}$$

where there are k pairs of observations each with weight w_k and,

$$\Lambda = \begin{cases} +\sqrt{(P_k)}, \text{if } P_k \geq 0 \\ -\sqrt{(P_k)}, \text{if } P_k < 0 \end{cases} \tag{3.5}$$

The value of w_k is 1.0 for observations that are close together in time (with 3 min for INT epochs and 5 min for ESO) and 0.1 for all other observations. P_k is the product of normalised residuals of the observation pairs i and j, where:

$$P_k = \begin{cases} \delta_{i(k)} \delta_{j(k)}, \text{if } i(k) \neq j(k) \\ \delta_{i(k)}^2 - 1, \text{if } i(k) = j(k) \end{cases} \tag{3.6}$$

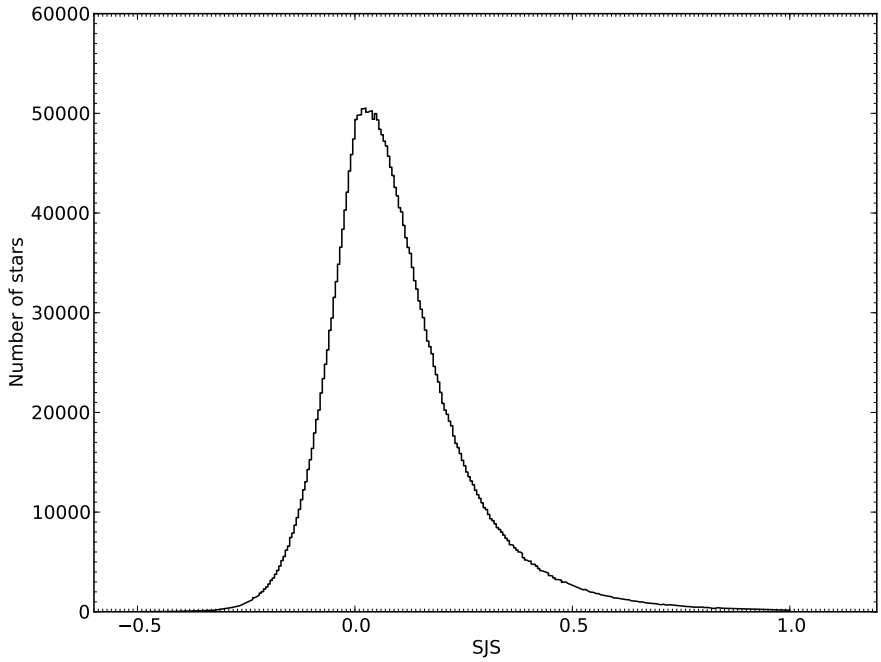

Figure 3.2: The distribution of Stetson J statistics for the light curves in the RATS data. The data have been binned with a bin width of 0.005 in SJS. The distribution peaks close to zero but is not symmetric.

δ, the magnitude residual is defined as:

$$\delta = \sqrt{\frac{n}{n-1}} \frac{x - \overline{x}}{\sum x} \tag{3.7}$$

where x is the brightness and n is the number of data-points in the light curve. The SJS should be close to zero for a non-variable star and be positive for a variable source.

In the RATS data the mean of the SJS distribution (which is plotted in Fig. 3.2) is 0.44 and the median is 0.072 while the MAD is 0.13. The distribution does indeed peak around zero which is what would be expected if the majority of stars are non-variable. The distribution is not symmetric about zero but has a longer tail on the positive side than the negative side.

The SJS was designed to identify Cepheid variables. These are high amplitude long period variables and as such this algorithm is good at finding long period and non-periodic variables with high amplitudes, these include sources such as contact binaries, flares, and pulsators with periods longer than the observation length. The weakness in using the SJS alone is that it gives no information on the type of variability per cent, so while 6.2×10^4

sources have a SJS 5 MADs above the median of the distribution, nothing is known about this variability.

Kurtosis The kurtosis of a light curve is a measure of the peakedness of a distribution relative to a normal distribution (Press et al., 1992). In my case I define the light curves and its brightness as the two axes of the distribution. Distributions can be either platykurtic, which has negative kurtosis and a shape similar to that of Navan Fort, shown in 3.3(a), or leptokurtic which is more similar to the Matterhorn, shown in 3.3(b) which has positive kurtosis.

(a) The Navan fort, just outside Armagh, has a platykurtic shape which has nagative kurtosis.

(b) The outline of the Matterhorn has the shape of a leptokurtic distribution which has positive kurtosis. The image is a retouched version by Zacharie Grossen of an origianal photo by Marcel Wiesweg. Image licensed under the Creative Commons Attribution-Share Alike 3.0 Unported license.

Figure 3.3: Navan Fort, outside Armagh, N. Ireland and the Matterhorn on the border of Italy and Switzerland. The outline of these two landmarks have the shape of negative and positive kurtosis, respectively.

Kurtosis is calculated using the equation:

$$K = \frac{\frac{1}{n}\sum_{i=1}^{n}(x_i - \overline{x})^4}{\frac{1}{n}\sum_{i=1}^{n}\left((x_i - \overline{x})^2\right)^2} - 3 \tag{3.8}$$

where n is the number of data-points in the light curve, x_i is the ith data-point and $\overline{x}$ is the mean of the light curve.

This parameter is not used on its own but combined with other algorithms to identify classes of variables. For example when identifying flare stars we combine alarm with

kurtosis.

Uncertainties on the second and third coefficients of polynomials This technique involves fitting a third order polynomial to the light curve. To do this we use the IDL routine POLY_FIT which performs least-squares fitting. We then look at the 1σ uncertainties on the coefficients to the x^2 and x^3 terms. Contact binaries have light curves that are typically well fit by either a second of third order polynomial. This work is being done in collaboration with Pasi Hakala at the Finnish Centre for Science with ESO and is still ongoing but intial results suggest that there are several thousand contact binaries in RATS data.

3.1.2 Periodic variability

I use two algorithms in order to identify periodic variable sources: analysis of variance (AoV), and the Lomb-Scargle periodogram (LS). From these algorithms we determine the analysis of variance formal false-alarm probability, AoV-FAP; and the Lomb-Scargle formal false-alarm probability, LS-FAP. As before, I use the VARTOOLS suite of software to calculate these parameters (Hartman et al., 2008).

3.1.2.1 Lomb-Scargle periodogram and Analysis of Variance

The Lomb-Scargle periodogram (Lomb, 1976; Scargle, 1982; Press & Rybicki, 1989; Press et al., 1992) is an algorithm designed to pick out periodic variables in unevenly sampled data by performing least-squares fitting of sinusoids. The advantage to using this method over Fourier techniques (such as the Fast Fourier Transform) is that the fit is only evaluated at t_i, where t_i is a measurement (in our case, a flux measurement), whereas Fourier techniques need to interpolate missing data (Press et al., 1992).

To use the LS technique one must pick a start frequency and end frequency and the

steps in which to evaluate the equation:

$$P_N(\omega) = \frac{1}{2\sigma^2}\left[\frac{\left(\sum_j (h_j - \overline{h})\cos\omega(t_j - \tau)\right)^2}{\sum_j \cos^2\omega(t_j - \tau)} + \frac{\left(\sum_j (h_j - \overline{h})\sin\omega(t_j - \tau)\right)^2}{\sum_j \sin^2\omega(t_j - \tau)}\right] \tag{3.9}$$

where $P_N(\omega)$ is the spectral power as a function of frequency, $\omega \equiv 2\pi f$ where f is the frequency, hj flux measurement taken at time t_j and $\overline{h}$ is the mean flux of the light curve. σ^2 is the variance of the data where:

$$\sigma^2 \equiv \frac{1}{N-1}\sum_1^N \left(h_i - \overline{h}\right)^2 \tag{3.10}$$

τ is defined by:

$$\tan(2\omega\tau) = \frac{\sum_j \sin(2\omega t_j)}{\sum_j \cos(2\omega t_j)} \tag{3.11}$$

Here τ is an offset that makes $P_N(\omega)$ independent of shifting the t_j's by any constant (Press et al., 1992) as well as making solving Equation 3.9 equivalent to fitting

$$h(t) = A\cos\omega t + B\sin\omega t \tag{3.12}$$

using linear least-squares fitting at a frequency ω.

In a periodic variable the spectrum of $P_N(\omega)$ is a sum of Gaussian noise and the periodic signal. It is important to know how significant a peak in the spectrum of $P_N(\omega)$ is (and therefore, whether a source is variable). I use a technique described by Press et al. (1992). The probability that $P_N(\omega)$ lies between some positive value z and $z + dz$ is $e^{-z}dz$. Therefore, if I scan M independent frequencies, the probability that none are greater than z is $(1 - e^z)^M$. The Lomb-Scargle False Alarm Probability (LS-FAP) is them defined as

$$\text{LS} - \text{FAP} = 1 - (1 - e^{-z})^M \tag{3.13}$$

which is the probability that any peak we see in the spectrum is due to random noise. A small value indicates that the source has significant periodic modulation. I search for periods ranging from the Nyquist frequency (~2 min for INT observation) to the total observation length in steps of 0.5 min.

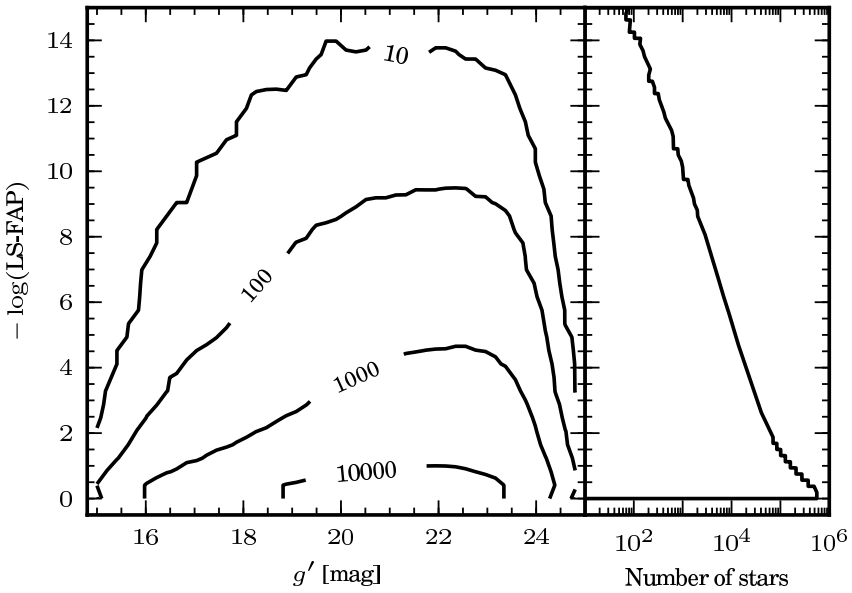

Figure 3.4: The distribution of the LS-FAP statistic in magnitude and number. The contours refer to the number of stars. This plot contains data from the INT1, 3, 4 and 5 epochs as these have similar distributions (cf. §3.2).

The distribution of LS-FAP as a function of magnitude is shown in Fig. 3.4: the vast majority of source have LS-FAP close to unity, in other words, the probability that they do not show periodic modulation is close to one. As this parameter is a measure of the probability that the highest peak in the periodogram is due to random noise, if the noise present in our data were frequency independent the LS-FAP would refer to the probability of the detected period being caused by random (Gaussian) noise. However, my data is subject to sources of systematic error which I attribute to red noise: these include the number of data-points in the light curve and the range in airmass at which a star is observed. Hence, I use it as a relative measure of variability.

I use a modified implementation of the analysis of variance periodogram (Schwarzenberg-Czerny, 1989; Devor, 2005). The AoV algorithm folds the light curve and selects the period which minimises the variances of a second-order polynomial in 8 phase-bins. A periodic variable will have a small scatter around its intrinsic period and high scatter on all other periods. The statistic Θ_{AoV} is a measure of the goodness of the fit to the best fitting period, with larger values indicating a better fit. In order to be consistent with the LS-FAP I calculate the formal false-alarm probability of the detected period being due to random noise (AoV-FAP) – with the same caveats as with the LS-FAP – using the

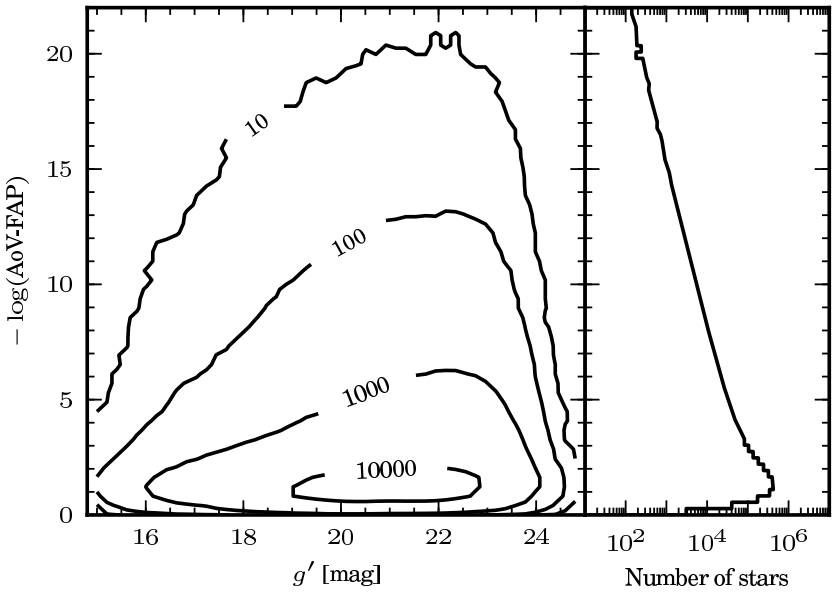

Figure 3.5: A similar plot to Fig. 3.4 but this time showing the distributions for AoV-FAP. This plot contains data from the INT1, 3, 4 and 5 epochs as these have similar distributions (cf. §3.2).

method described by Horne & Baliunas (1986). I show the distribution of the AoV-FAP statistic in number and as a function of magnitude in Fig. 3.5. I note that unlike LS-FAP in which the distribution peaks close to zero, AoV-FAP peaks close to 0.1.

The AoV algorithm, while similar to the LS method, should allow better variable detection as it fits a constant term to the data as opposed to subtracting from the mean as is done in the LS routine (Hartman et al., 2008). However, I find that AoV is subject to a number of problems. It suffers from severe aliasing at periods of 2–3 min and for this reason I only search for periods longer than 4 minutes. In addition there is a tendency to detect a multiples of the true period when the true period is less than ~40 min. In tests with simulated light curves I found approximately 10 per cent of sources with a period of 20 minutes were detected by AoV as having 40 min periods. The main weakness of the LS algorithm is that if a source has a periodic modulation in brightness for only a short duration then – according to the LS-FAP – it is detected as significantly variable. This leads to a large number of false-positive detection which are caused by random noise. To combat this I have developed a technique to combine the AoV and LS algorithms.

3.2 LS-FAP + AoV method

I have developed a method for detecting sources that show periodic or quasi-periodic modulations on time-scales less than two hours. My technique, which combines the LS-FAP and AoV-FAP statistics is a multi-stage process. The first step is determine if the source is detected as significantly variable by both the LS and AoV algorithms, I then test whether the period each algorithm detects is the same. Shown in Figure 3.7 are the AoV-FAP and LS-FAP statistics plotted against the period that is measured by the respective methods. Here it can be seen that the distributions of AoV-FAP and LS-FAP are not constant with period, but tend to higher significance at longer periods. In order to account for the bias of the distribution I use an approach whereby I bin the data in period with each bin 2 minutes wide. A source passes the first two stages of the algorithm if it is above a specific significance in both AoV-FAP and LS-FAP with respect to the other sources in the period bin. In order to determine this significance I use the median absolute deviation from the median (MAD, see §3.1.1). I use the median, as using the mean is not appropriate when the first moment of the distribution tail is large (Press et al., 1992); the large tails in the distributions of AoV-FAP and LS-FAP are shown in the right-hand plots in Figs. 3.4 and 3.5. The median and MAD are more robust statistics.

I vary the number of MADs a source must be above the median to be classed as variable depending on epoch as the distributions of LS-FAP and AoV-FAP parameters are different at different epochs. In order to identify this cut-off I visually inspected several hundred sources from each epoch with MADs ranging from 100 to 1500 above the median in their respective period bin. I looked at both the full light curve and a light curve which was phase folded and binned on the period which this source was detected as having. I then set the cutoff independantly for each epoch by finding the value below which light curves ceased to be obviously variable. For INT2 and ESO1 I use 200 MADs, for INT1, INT4 and INT5 I use 800 MADs. These number of MADs above the median are used as they provide an appropriate balance between low amplitude detections and false positives – which I discuss in §3.2.1 and §3.2 – I attribute the need for different numbers of MAD above the median to the use of an autoguider on INT2 and ESO1 and not on the other epochs. As different

epochs have different distributions of variability parameters I have calculated the median independently for each epoch. I acknowledge that this method is fairly subjective but the fact that I get similar values for epochs where the instrumental set-ups were similar at least show that I am consistent in where I set the cut-off.

Both the AoV and LS algorithms produce a periodogram; from the highest peak in the periodogram I calculate the most likely period of a given light curve. I take all the candidate variables and test whether the period detected by AoV matches that detected by LS. I class a period as a match if

$$P_{AoV} \pm \Delta P_{AoV} = P_{LS} \mp \Delta P_{LS} \tag{3.14}$$

where P_{AoV} and P_{LS} are periods detected by the two algorithms AoV and LS, respectively. ΔP is the error in measured period. I determine ΔP using an approximation of equation (25) in Schwarzenberg-Czerny (1991) whereby I assume that

$$\Delta P/P^2 \sim k. \tag{3.15}$$

This assumption holds for all but the lowest signal-to-noise detection of variability. In order to determine an appropriate value for the constant, k, I inject sinusoidal signals of various periods into non-variable light curves and measure the standard deviation on $|P_{AoV} - P_{LS}|$. I set the constant, k, in Eq. 3.15 so as to give a ΔP at a given period equal to twice the standard deviation of $|P_{AoV} - P_{LS}|$. I find $k = 0.002$ to be a appropriate. The AoV algorithm has an annoying habit of detecting a multiple of the true period, so for this reason I modify Eq. 3.14 to

$$\frac{P_{AoV}}{n} \pm \Delta P_{AoV} = P_{LS} \mp \Delta P_{LS} \tag{3.16}$$

where $n = \{1, 2, 3, 4\}$.

Sources that have matching periods and have been classified as candidate variable sources by both AoV-FAP and LS-FAP are then regarded as 'significantly' variable sources. I detect 124,334 stars which show variability on a timescale of 4–115 minutes: the distribution of the measured periods are shown in Fig. 3.6. I caution that this technique can detect variables that are not truly periodic – many flare stars are detected periods near the ob-

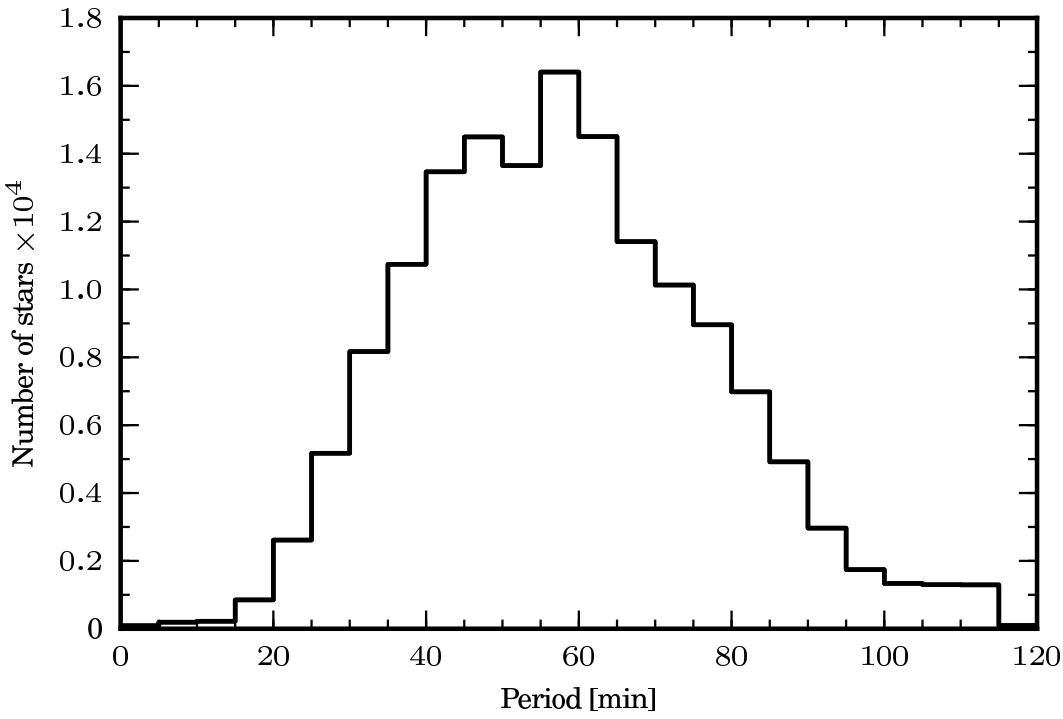

Figure 3.6: The distribution of the period detected as variable by the technique for combining LS-FAP and AoV-FAP.

servation length – or may have periods longer than that detected by our method – contact binaries typically have a true twice the period that which I measure. If a period of less than half the observation length is measured then this is likely to be a true period. However, longer periods detected by the LS and AoV algorithms indicate only that the source varies significantly on time-scales less than ~2 hours.

3.2.1 False positives

In order to determine the false positive detection rate, that is, the chance of a source with variability caused by noise being identified as a real variable, I pick a light curve at random from the whole data-set and construct a new light curve using a bootstrap approach. The light curve consists of three columns of data: time, flux and error on the flux. I keep the time column as it is, and for a light curve with N individual photometric observations, randomly select N fluxes and errors from the N points in the original light curve. I do not limit the number of times a flux-error combination is selected. An example of an original

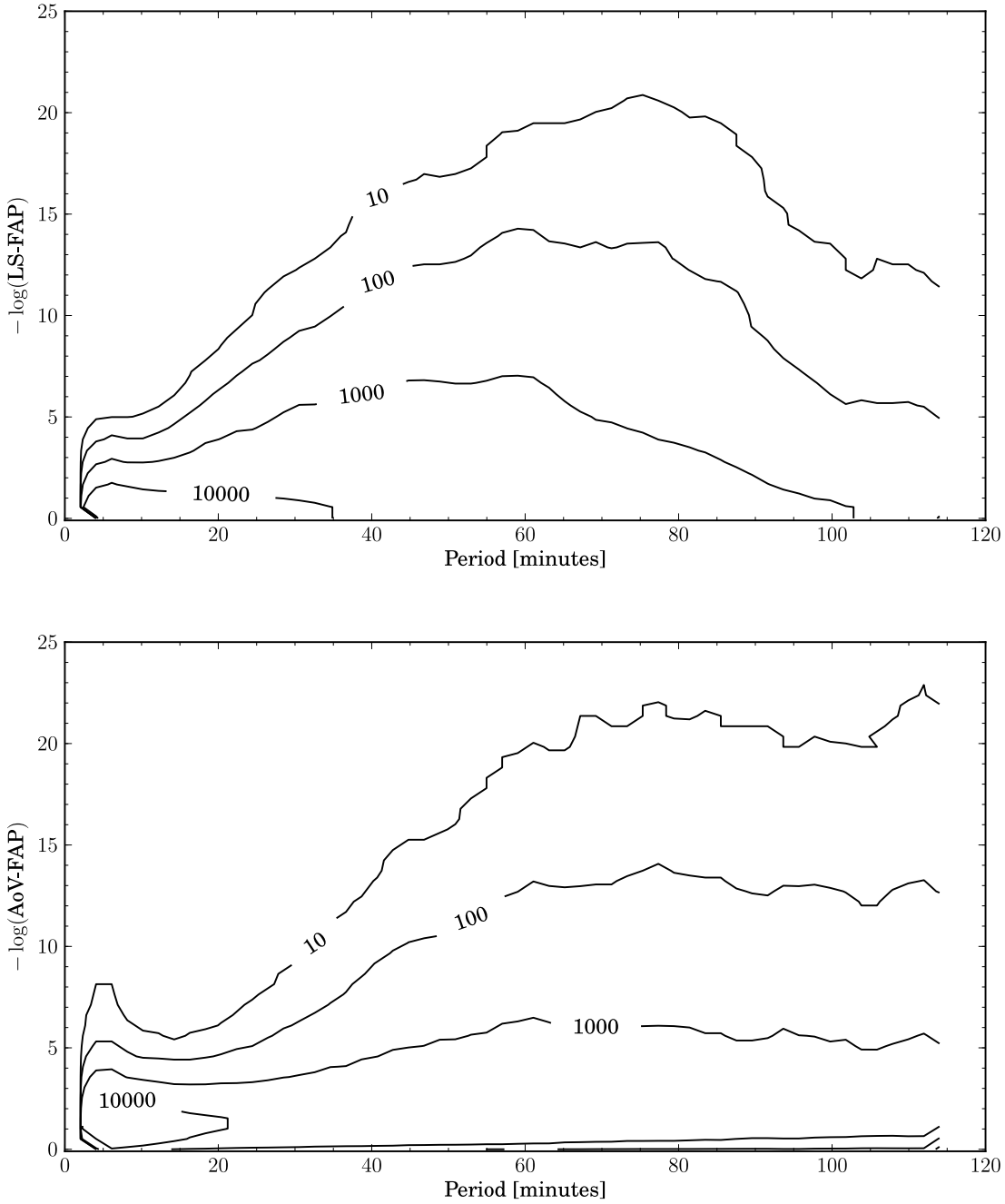

Figure 3.7: LS-FAP and AoV-FAP statistics in the top and bottom plot, respectively, plotted against the period measured by those statistics. There is spurious variability obvious at very short periods in AoV-FAP, while LS-FAP is less sensitive to longer period variability.

Original			Reconstructed		
Time	Flux	Error	Time	Flux	Error
1	10.0	2.0	1	11.4	2.3
2	11.5	2.1	2	11.5	2.1
3	12.2	2.2	3	10.0	2.0
4	11.4	2.3	4	11.5	2.1
5	10.2	2.4	5	10.0	2.0

Table 3.1: An example of the light curve data (left) and a reconstruction made up from randomly selected flux-error combinations (right). The technique removes any periodic signal present and therefore any detection of variability is due to random noise.

and reconstructed light curve is shown in Table 3.1. Note the use of flux-error combinations more than once. The reason for reconstructing a light curve in this fashion is that any periodic variability which is present in the original light curve is removed, allowing me to measure the chance that any variability present is due to noise.

I reconstruct 10^5 bright and 10^5 faint randomly selected light curves and attempt to detect variability using the method for combining the AoV and LS algorithms. Bright and faint refers to sources brighter than and fainter than $g' = 21.0$, respectively where 21.0 is approximately the median g' magnitude. For the bright sample I class 10 stars as variable and for the faint sample this increases to 17. This equates to a false positive rate of 0.01 and 0.02 per cent for bright and faint sources, respectively.

3.2.2 Sensitivity and completeness of survey

To determine the space densities for different classes of sources which vary on time-scales of less than ~2 h it is essential that I determine the sensitivity of the RATS data to different brightness, periods and amplitudes. To do this I inject sinusoids of known period and amplitude into non-variable light curves and then attempt to detect it using our LS-FAP + AoV-FAP test. Similarly to the false positive test, I split the data into two groups based on whether they are brighter or fainter than $g' = 21.0$ and I refer to as the bright and the faint group, respectively. For each brightness range I inject a periodic signal into a non variable light curve. The non variable light curve is drawn randomly from a pool of light curves that have AoV-FAP and LS-FAP statistics within 0.5 median absolute deviations of

the median AoV-FAP and LS-FAP of all light curves with g' greater than and less than 21.0 for the bright and faint groups, respectively. The periodic signal injected is drawn from a grid of period-amplitude combinations where the periods range from 4 – 120 minutes and amplitudes from 0.02 – 0.2 mag. I define amplitude as peak-to-peak. The advantage of using real (non-variable) light curves over simulated data is that it preserves the noise values which may be non-Gaussian.

I run the entire grid 100 times for each brightness range which allows me to build up confidence of a variable with a given period and amplitude being detected. The results of this are plotted in Fig. 3.8 and show that in the brighter sample, sources with a period less than 90 min have a ~70 per cent chance of being detected if they have amplitudes greater than 0.05 mag, rising to above a 90 per cent chance for amplitudes greater than ~ 0.10 mag. Stars fainter than $g' = 21.0$ with injected period less than 90 min have ~ 50 per cent detection chance if they have an amplitude greater than 0.08 mag and only sources with a period less than 40 min and an amplitude greater than ~0.15 mag have a 90 per cent chance of detection.

From these results I find that our LS-FAP + AoV-FAP method is relatively good at identifying variables with periods less than 90 min in bright sources but is weaker at identifying periodic variability in the fainter sources. The advantage of this method is the small number of false-positives expected to be detected.

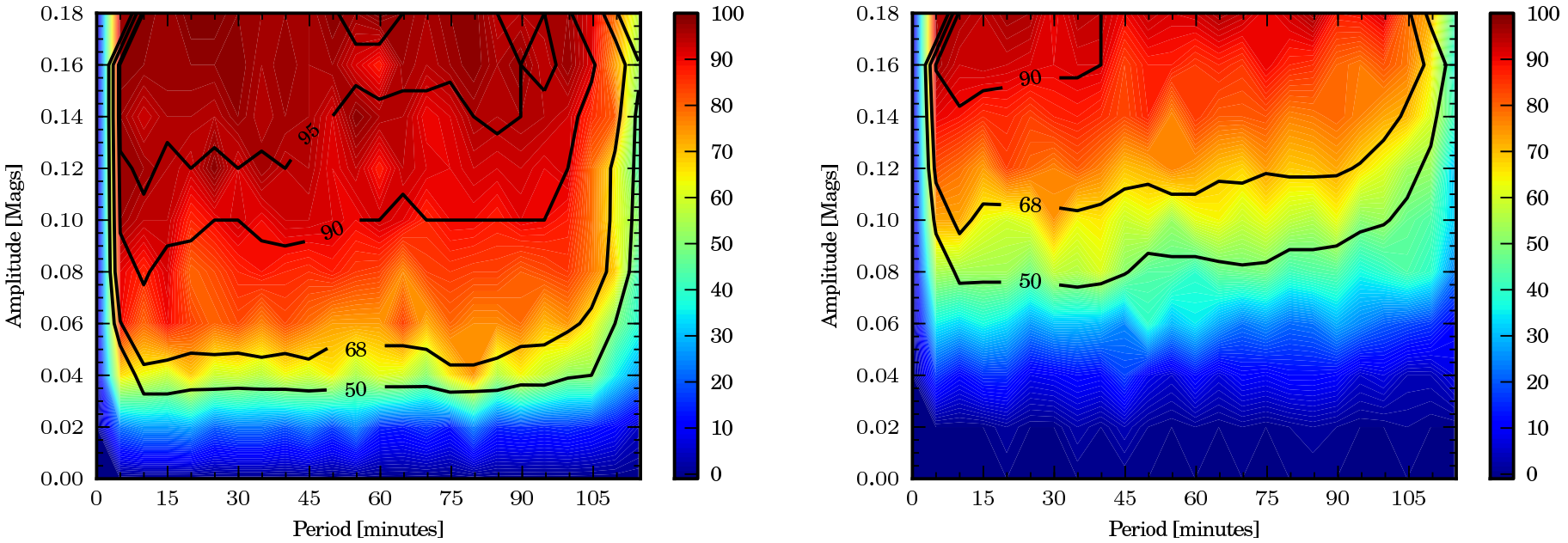

Figure 3.8: Our sensitivity to periodic sources of different period and peak-to-peak amplitudes. In the left plot, the contours refer to the percentage of sources detected as variable when the original non-variable light curve was brighter than $g' = 21.0$. The right plot show the same but for sources fainter than $g' = 21.0$.

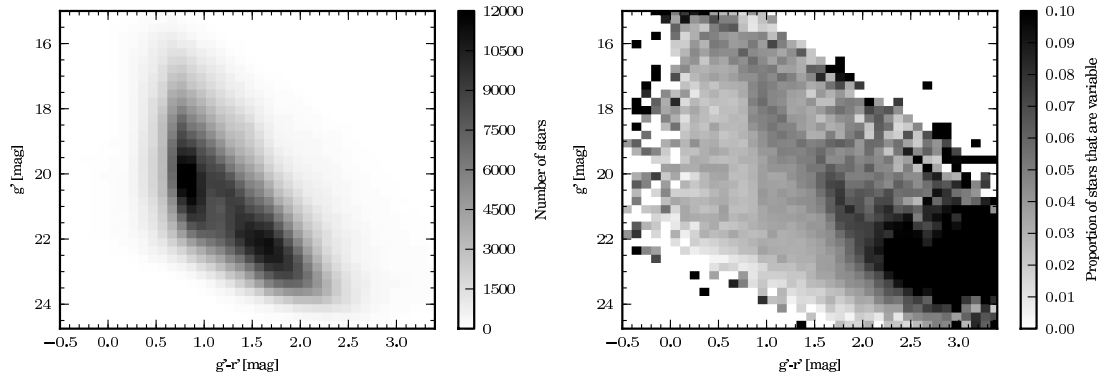

Figure 3.9: Colour-magnitude diagram showing $g' - r'$ against g' magnitude. The left plot contains all the stars in our data, the right plot show the proportion of stars in each bin that are classified as variable using the method in Chapter 3.

3.3 Colour of sources which vary on time-scales of less than two hours

In this section I will discuss only the colours of sources that have been classified as variable (for a discussion of the colours of all the RATS sources, see §2.3.2). Shown in the right-hand panel of Figure 3.9 are the stars which have been classified as variable (cf. Chapter 3) in the $(g' - r', g')$ plane. In the left-hand panel of Fig. 3.9 is shown the colour of all the stars in our data for reference. The variable sources are concentrated at the faint, red end of the of the colour-magnitude diagram. In contrast, the Faint Sky variability Survey (FSVS) found that the variable sources they detected were biased towards bluer colours (Morales-Rueda et al., 2006). I attribute this difference to the fact that the FSVS was typically more sensitive to longer time-scale variations than our survey, coupled with the fact that they observed fields at mid to high Galactic latitudes (Groot et al., 2003).

3.4 Discussion

In this Chapter I have described the algorithms that are used to identify sources as variable and how they are able to give an idea as to what the type of variability is present (i.e periodic, non-periodic). All these algorithms have their own particular strengths and weaknesses

and therefore we nearly always use more than one when classifying a variable source. As the primary aim of the RATS project is to identify short-period variables most of the work in algorithm development is geared towards this aim. The technique for combining AoV and LS algorithms goes a long way to removing the issues when only using a single variability algorithm. A potential issue with this technique is that, as sources must be detected by both AoV and LS, we are missing out on variables which are only picked up by one or other of the algorithms. These concerns are eased because the results from the sensitivity testing shows that this technique detects sources with low-amplitudes in the brighter targets. However, this testing is done using sinusoids. Many of the variable sources we find are not strictly sinusoidal and the AoV+LS technique may not be optimal for the detection of these. The increase in the number of wide-field surveys (particularly in the field of exoplanet searches) has in turn led to a number of newly developed period searching algorithms. Future work in the RATS project focusing in this area will need to look at recently developed algorithms such as Plavchan (Plavchan et al., 2008) and The Fast Chi-squared Period Search (Palmer, 2009).

An important question to ask is whether the RATS project is able find AM CVn systems which are present in the data. From the sensitivity plots in Fig. 3.8, it is clear that high amplitude AM CVn systems such as CP Eri and HM Cnc will be detected even at magnitudes fainter than $g' = 21$. Systems with smaller amplitudes prove more challenging. The project will likely detect any source brighter than $g' = 21$ if the semi-amplitude is above 0.05 mag and in sources brighter than $g' \sim 19$ the project will detect even a 0.02 mag semi-amplitude. Only one of the known AM CVn systems which show optical variability would likely be missed by our observations if it were in the data and that is V803 Cen which has only a 0.01 semi-amplitude.

The success of this project relies on the detection of interesting new variables. The enormous number of new (quasi-)periodic variable (over 10^5) moves the problem on from the discovery of variables to how to decide what is interesting and worthy of follow-up work and what is not. This is a highly subjective assessment but in the next Chapter I will discuss which sources we selected for follow-up (particularly focusing on the new short-

period variables) and the results of this work.

Chapter 4

Short-period blue variables

> I do not know what I may appear to the world, but to myself I seem to have been only like a boy playing on the sea-shore, and diverting myself in now and then finding a smoother pebble or a prettier shell than ordinary, whilst the great ocean of truth lay all undiscovered before me.
>
> *I. Newton, spoken a short time before his death, Memoirs of the Life, Writings, and Discoveries of Sir Isaac Newton, D. Brewster, 1855*

In this Chapter I will describe the process of developing a list of candidate AM CVn system from an initial set of over 10^5 sources which show variability on time-scales less than 2 hours. I go on to discuss follow-up observations of these systems which reveal their nature. The final part of this Chapter deals with the implications our results have on the space density of AM CVn systems.

4.1 Short period blue variables

AM CVn systems which an show optical modulation on a period close to their orbital period are intrinsically blue in colour – the reddest have $g' - r'$ colours of -0.1 – and modulate on periods of < 40 min with amplitudes between 0.01 (V803 Cen, Kepler, 1987) and 0.20 mag (CP Eri, Howell et al., 1991). HM Cnc has an amplitude of 0.30 mag (Ramsay et al.,

2002a) though because of the unusual properties of this system – see §1.3.2 – this amplitude is probably not typical of AM CVn systems. In this section I restrict my search to stars with parameters fulfilling these criteria.

The known AM CVn systems found in SDSS data have de-reddened $g' - r' < -0.1$ (Roelofs et al., 2009). The majority of RATS stars are close to the Galactic plane where the interstellar reddening is high. The total average neutral hydrogen column density (N_H) of the RATS fields which are close to the Galactic place ($|b| < 15°$) is 3.7×10^{21} cm^{-2} (Kalberla et al., 2005). I calculate the optical extinction in the V band, A_V, using the relation found by Güver & Özel (2009):

$$N_H = (2.21 \pm 0.09) \times 10^{21} A_V. \tag{4.1}$$

and

$$A_V = 3.10 \times E(B - V) \tag{4.2}$$

from Fitzpatrick (1999) which gives $A_V = 1.66$ and $E(B-V) = 0.54$. This result is consistent with Joshi (2005) who observe open clusters close to the Galactic plane ($|b| < 5°$) and find $E(B-V) = 0.6$. If I convert this extinction to Sloan g' and r' filters I find $E(g'-r') = 0.60$. Adding this to the red cut-off for AM CVn systems ($g' - r' < -0.1$) I get a cutoff for AM CVn systems in my data of $g' - r' < 0.5$

After these cuts the number of sources left as candidate AM CVn systems is 250. I visually inspected these as a final level of quality control, and class 66 of these short-period blue variables as 'good' candidates – that is, having a strong period and no obvious systematic effects present. The 66 sources presented should be regarded as the top candidates. The rest of the sources were excluded for a number of reasons. Some showed signs of systematic errors that were not removed during detrending. These include cases where several stars from the same field had similar periodic variations, i.e. they had similar periods and phases. Others were excluded where there were large sections of the data missing or when the source was faint and the amplitude was very low – below what I would reasonably expect to detect (cf. §3.2.2). Though my false positive testing suggests that the variability seen in these sources should be trusted to be astrophysical, the weakness of the false pos-

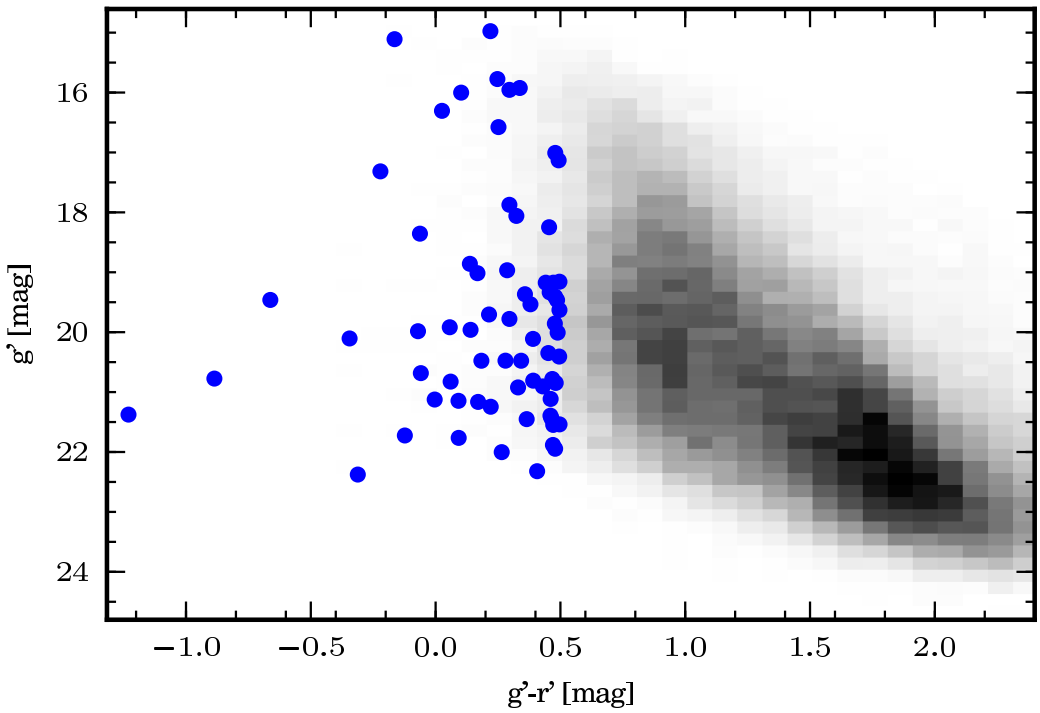

Figure 4.1: Colour-magnitude diagram of all the detected variable stars plotted as grey-scale. Those stars identified as short period ($P < 40$ min) blue variables – shown in Tab. 4.1 and 4.2 – are indicated by blue dots.

itive testing is that I only injected sinusoidal variations. Other shapes of waveforms will have a different false positive rate. As short-period blue sources are considered a priority for follow-up observations, when considering faint, low amplitude sources I am inclined to take a more conservative view because of the significant amount of telescope time required to obtain spectra.

In Tabs. 4.1 and 4.2 I show the short period blue variables for those sources with periods less than 25 minutes and for those with periods 25–40 minutes, respectively. I split these into two tables for ease of comparison with the Nelemans et al. (2001a, 2004) model of the Galactic population of AM CVn systems which is only relevant for sources with periods less than 25 minutes (see Section 4.3). The sources contained in these two tables are plotted as blue dots in Fig. 4.1. The light curves of these sources are shown in Figures. 4.2–4.7. The light curves are over-plotted with the best-fitting sine curve which was obtained by fitting a sine function to the light curve at the peak period found in the Lomb-Scargle periodogram.

Table 4.1: Sources identified as periodic variable stars with periods less than 25 minutes and a $g' - r'$ colour of less than 0.5. They have also passed a visual quality check. The period is determined from the Lomb-Scargle periodogram and the amplitude is peak-to-peak of the best fitting sine curve. If classification of the source has been possible then this is stated in the notes column. For the previously know sources the classification come from the literature, for the newly discovered variables we classify the sources based on spectral type and the spectral fitting described in Section 5.1.

Cat. name	R.A. (J2000)	Dec. (J2000)	Period [min]	g' [mag]	$g' - r'$ [mag]	Amplitude [mag]	Notes	Ref.
4-7-3-9108	01:41:31.42	+55:34:11.3	5.3	20.48	0.18	0.03		3
4-11-1-2519	01:42:26.37	+54:16:33.1	13.2	21.12	−0.00	0.13	1	3
5-6-3-4828	04:32:10.40	+40:33:33.9	8.4	20.10	−0.34	0.25	1	3
1-16-4-1316	04:55:15.22	+13:05:29.8	6.2	17.32	−0.22	0.12	Pulsating sdB star	4
4-27-3-662	05:07:51.28	+34:31:55.5	22.2	16.31	0.03	0.03	2	3
1-22-4-1415	07:39:19.05	+23:52:39.9	14.7	20.83	0.06	0.07	Pulsating white dwarf	3
1-806-4-713	08:06:22.95	+15:27:31.2	5.4	20.77	−0.89	0.28	AM CVn star	5
3-2-3-14617	17:58:46.34	+01:45:59.8	9.6	22.00	0.26	0.10		3
3-5-1-25551	17:59:52.90	+01:22:19.4	22.1	20.01	0.49	0.03		3
3-5-3-4143	18:00:57.72	+01:42:03.0	20.4	20.48	0.34	0.04		3
2-7-2-1301	18:01:52.91	+29:42:30.4	8.6	19.92	0.06	0.06		3

[1]Low signal-to-noise spectrum – no obvious emission lines,[2]A-type star spectrum

[3]**?** and this thesis, [4]Ramsay et al. (2006), [5]Ramsay et al. (2002a), [6]Ramsay et al. (2009)

Table 4.1 – Continued

Cat. name	R.A. (J2000)	Dec. (J2000)	Period [min]	g' [mag]	$g' - r'$ [mag]	Amplitude [mag]	Notes	Ref.
3-26-1-604	18:20:56.80	+07:58:33.5	14.2	19.96	0.14	0.13		3
3-27-2-6182	18:22:20.95	+07:48:02.1	14.2	21.24	0.22	0.10	1	3
2-11-4-34562	19:53:24.03	+18:50:59.6	12.4	20.68	−0.06	0.11		3
2-11-3-25021	19:53:27.17	+18:59:14.4	20.0	19.98	−0.07	0.24	Dwarf nova	6
4-9-2-9694	20:58:00.24	+45:32:32.8	7.2	19.16	0.50	0.04		3
4-9-4-14918	20:59:02.93	+45:37:35.9	15.3	18.36	−0.06	0.08	Pulsating white dwarf	3
4-16-4-21281	21:05:14.75	+46:15:41.9	22.4	15.77	0.25	0.01	2	3
1-3-2-46	23:03:11.95	+34:31:04.1	9.2	20.78	0.47	0.04		3
4-6-4-2813	23:49:06.89	+56:24:40.4	22.7	18.06	0.32	0.04	2	3
4-6-3-470	23:49:29.00	+56:34:26.2	5.8	16.58	0.25	0.02		3
4-25-3-9719	23:52:42.07	+56:31:53.2	12.9	19.46	−0.66	0.10		3

[1]Low signal-to-noise spectrum – no obvious emission lines,[2]A-type star spectrum

[3]**?** and this thesis, [4]Ramsay et al. (2006), [5]Ramsay et al. (2002a), [6]Ramsay et al. (2009)

Table 4.2: The same as Tab. 4.1 for sources with periods between 25 and 40 min.

Cat. name	R.A. (J2000)	Dec. (J2000)	Period [min]	g' [mag]	$g' - r'$ [mag]	Amplitude [mag]	Notes	Ref.
5-7-2-1129	06:54:32.71	+10:31:52.8	35.9	16.00	0.10	0.03		3
5-7-4-9019	06:55:15.30	+10:38:59.0	33.9	15.92	0.34	0.02	2	3
5-7-4-7787	06:55:26.31	+10:36:48.4	39.2	15.96	0.30	0.01		3
5-7-4-7234	06:55:31.08	+10:35:31.8	30.7	17.13	0.49	0.02		3
5-7-4-3601	06:56:04.22	+10:34:35.3	28.6	17.01	0.48	0.02		3
5-7-3-1149	06:56:33.59	+10:45:41.4	33.9	19.02	0.17	0.04	1	3
3-8-1-21492	17:54:29.79	+01:37:52.2	29.8	21.38	–1.23	0.06		3
3-5-3-16324	17:59:58.53	+01:50:28.5	38.6	19.46	0.49	0.02		3
3-14-2-12275	18:00:02.54	+00:34:08.4	34.8	19.53	0.38	0.03		3
3-14-3-6993	18:01:06.36	+00:54:18.1	36.9	21.16	0.17	0.10		3
3-5-3-1384	18:01:11.05	+01:46:36.4	38.4	21.39	0.46	0.09		3
3-11-2-3507	18:02:50.62	+00:43:52.8	34.1	18.97	0.29	0.05		3

[1]Low signal-to-noise spectrum – no obvious emission lines,[2]A-type star spectrum

[3]**?** and this thesis

Table 4.2 – Continued

Cat. name	R.A. (J2000)	Dec. (J2000)	Period [min]	g' [mag]	$g' - r'$ [mag]	Amplitude [mag]	Notes	Ref.
3-11-3-14721	18:03:18.71	+00:57:30.1	28.6	21.88	0.47	0.09		3
3-11-3-14333	18:03:20.82	+00:52:40.9	33.1	20.91	0.43	0.05		3
3-11-3-14041	18:03:22.48	+00:52:07.8	33.7	21.11	0.46	0.05		3
3-11-3-176	18:04:45.09	+00:53:26.4	37.5	21.72	−0.12	0.15		3
3-24-3-21598	18:16:48.03	+06:16:11.4	39.5	21.54	0.50	0.12		3
3-24-3-27252	18:17:41.11	+06:39:30.2	33.9	21.95	0.48	0.14		3
3-24-3-27068	18:17:41.80	+06:39:55.2	33.9	19.17	0.47	0.02		3
3-24-3-26839	18:17:42.61	+06:39:47.5	37.5	20.11	0.39	0.03		3
3-24-3-25379	18:17:47.71	+06:42:21.7	37.6	19.63	0.50	0.02		3
3-24-3-24553	18:17:50.35	+06:40:36.7	38.2	19.37	0.36	0.03		3
3-24-4-10602	18:17:52.98	+06:31:33.2	37.0	21.55	0.47	0.08		3
3-24-3-23361	18:17:54.38	+06:41:38.7	38.2	20.92	0.33	0.07		3
3-24-3-22275	18:17:58.05	+06:42:55.7	39.0	19.86	0.48	0.03		3

[1]Low signal-to-noise spectrum – no obvious emission lines,[2]A-type star spectrum

[3]**?** and this thesis

Table 4.2 – Continued

Cat. name	R.A. (J2000)	Dec. (J2000)	Period [min]	g' [mag]	$g' - r'$ [mag]	Amplitude [mag]	Notes	Ref.
3-24-3-20681	18:18:03.13	+06:39:50.2	25.2	19.78	0.30	0.02		3
3-24-4-7636	18:18:12.79	+06:26:23.7	29.7	22.38	−0.31	0.11		3
3-24-3-13813	18:18:26.67	+06:44:01.8	37.6	21.45	0.36	0.07		3
3-24-3-13658	18:18:27.31	+06:47:06.2	36.7	19.33	0.46	0.02		3
3-24-1-8755	18:18:32.46	+06:23:19.9	35.9	19.41	0.48	0.02		3
3-24-3-11788	18:18:33.04	+06:37:17.9	39.5	18.25	0.45	0.02		3
3-24-3-11343	18:18:34.46	+06:37:09.7	35.0	20.85	0.48	0.05		3
3-24-3-11006	18:18:35.62	+06:38:43.4	35.0	21.44	0.46	0.07		3
3-17-2-5279	18:21:41.24	+08:22:28.3	27.9	19.70	0.21	0.04		3
3-27-1-24759	18:23:14.11	+07:36:50.9	34.1	20.48	0.28	0.05		3
3-27-3-9867	18:23:36.70	+07:58:00.5	29.7	19.17	0.44	0.02		3
3-27-3-9744	18:23:37.56	+07:59:07.1	28.9	22.32	0.41	0.13		3
3-25-3-11740	18:42:54.64	+00:21:48.7	36.1	21.76	0.09	0.17		3

[1]Low signal-to-noise spectrum – no obvious emission lines,[2]A-type star spectrum

[3]**?** and this thesis

Table 4.2 – Continued

Cat. name	R.A. (J2000)	Dec. (J2000)	Period [min]	g' [mag]	$g' - r'$ [mag]	Amplitude [mag]	Notes	Ref.
2-11-4-41975	19:53:06.30	+18:48:39.4	32.2	17.87	0.30	0.02	2	3
2-11-1-24882	19:53:35.94	+18:38:08.7	25.5	18.86	0.14	0.03	1	3
2-3-4-4027	20:02:18.77	+18:49:37.9	34.4	20.41	0.50	0.11		3
4-16-3-16761	21:05:03.14	+46:27:45.5	33.0	15.11	−0.16	0.03	2	3
4-16-4-21946	21:05:12.19	+46:20:38.3	31.8	14.98	0.22	0.02	2	3
4-6-4-11525	23:47:46.82	+56:28:52.0	31.3	21.15	0.09	0.09		3

[1]Low signal-to-noise spectrum – no obvious emission lines,[2]A-type star spectrum

[3]**?** and this thesis

The Simbad database[1] was searched for previously known sources. Three matches were found within 5 arcsec of our target. One is HM Cnc, an AM CVn system (Ramsay et al., 2002a, this source is discussed is Chapter 1) and two are previously published RATS sources: RAT J0455+1305, a high amplitude pulsating sub-dwarf B star (Ramsay et al., 2006), which is a rare object as it exhibits both gravity and pressure mode pulsations (Baran et al., 2010); and RAT J1953+1859 (Ramsay et al., 2009), a dwarf nova, which is discussed in detail in §6.1.

Of the other sources; 22 have periods less than 25 min, of which 9 have periods of less than 10 min. The amplitudes of the short-period blue sources ranges from 0.012–0.284 mag with a mean of 0.066 mag and the g' band brightness range from 14.9–22.4 mag with a mean of 19.6 mag.

4.2 Follow-up observations

The RATS project includes a programme to obtain optical spectroscopic observations of variable sources found in our survey (cf. Chapter 3). These data are low resolution spectra with which to determine the nature of sources. AM CVn systems have no hydrogen evident in their spectra and have neutral and ionised helium lines typically double peaked indicating the presence of a disc. Hydrogen-rich (DA) white dwarfs have very broad Balmer absorption lines and are well fit by DA models and helium-rich (DB) white dwarfs have broad and deep helium absorption lines. It is possible to tell AM CVns and DBs apart as AM CVn systems are not well fit by DB model atmospheres though at first sight they can look remarkably similar. To identify main sequence stars I use the library of stellar spectra produced by Jacoby et al. (1984) to compare my spectra with the standards which they observed.

Five instruments have been used for this work. These instruments are described below.

[1]The SIMBAD database is operated at CDS, Strasbourg, France

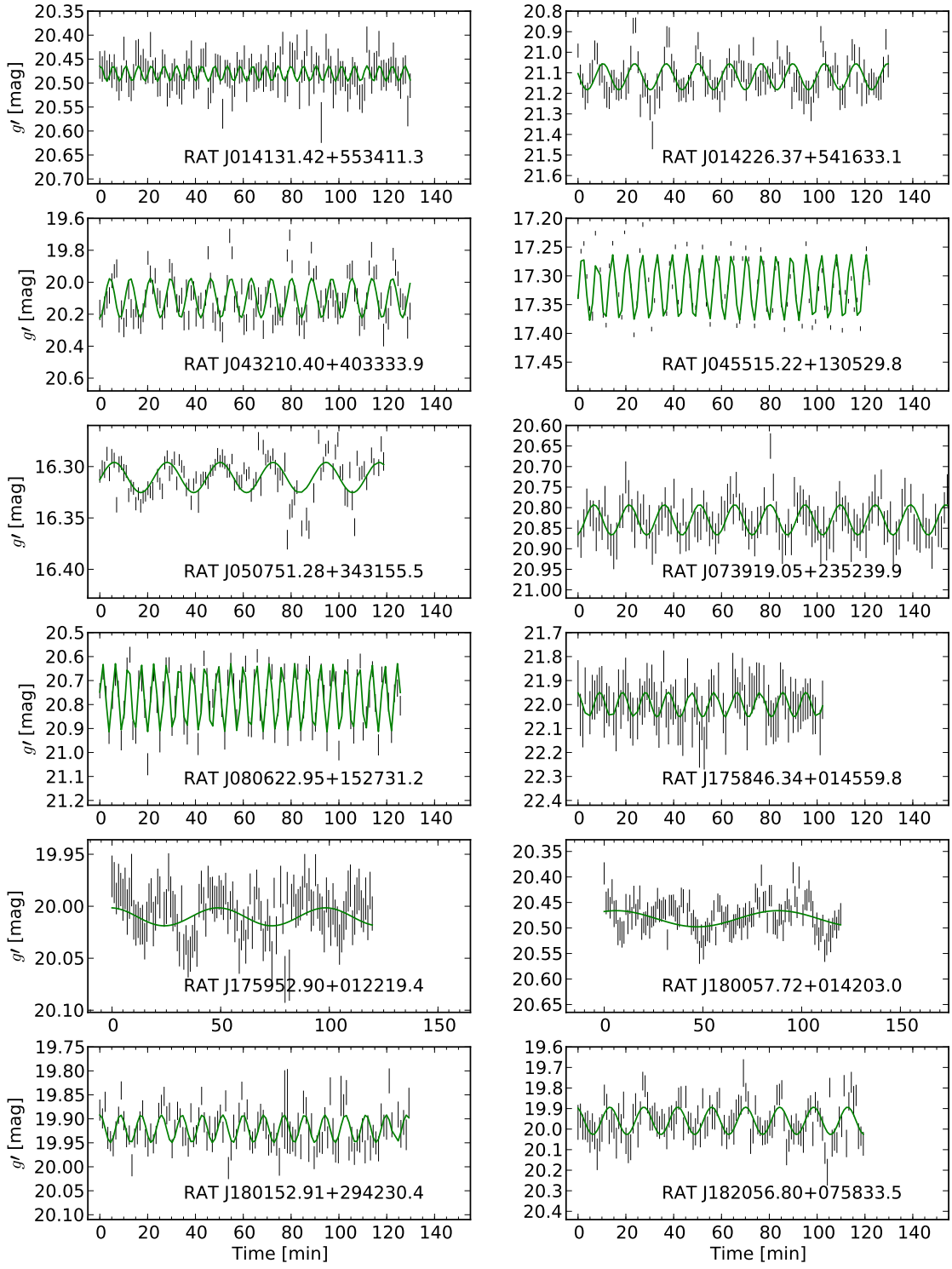

Figure 4.2: The blue short-period variable stars shown in Tables 4.1 and 4.2. The green curve shows of the best-fitting amplitude, period and phase of the light curve. The period was found using the Lomb-Scargle periodogram algorithm, the amplitude and phase from fitting a sine function to the light curve on that period.

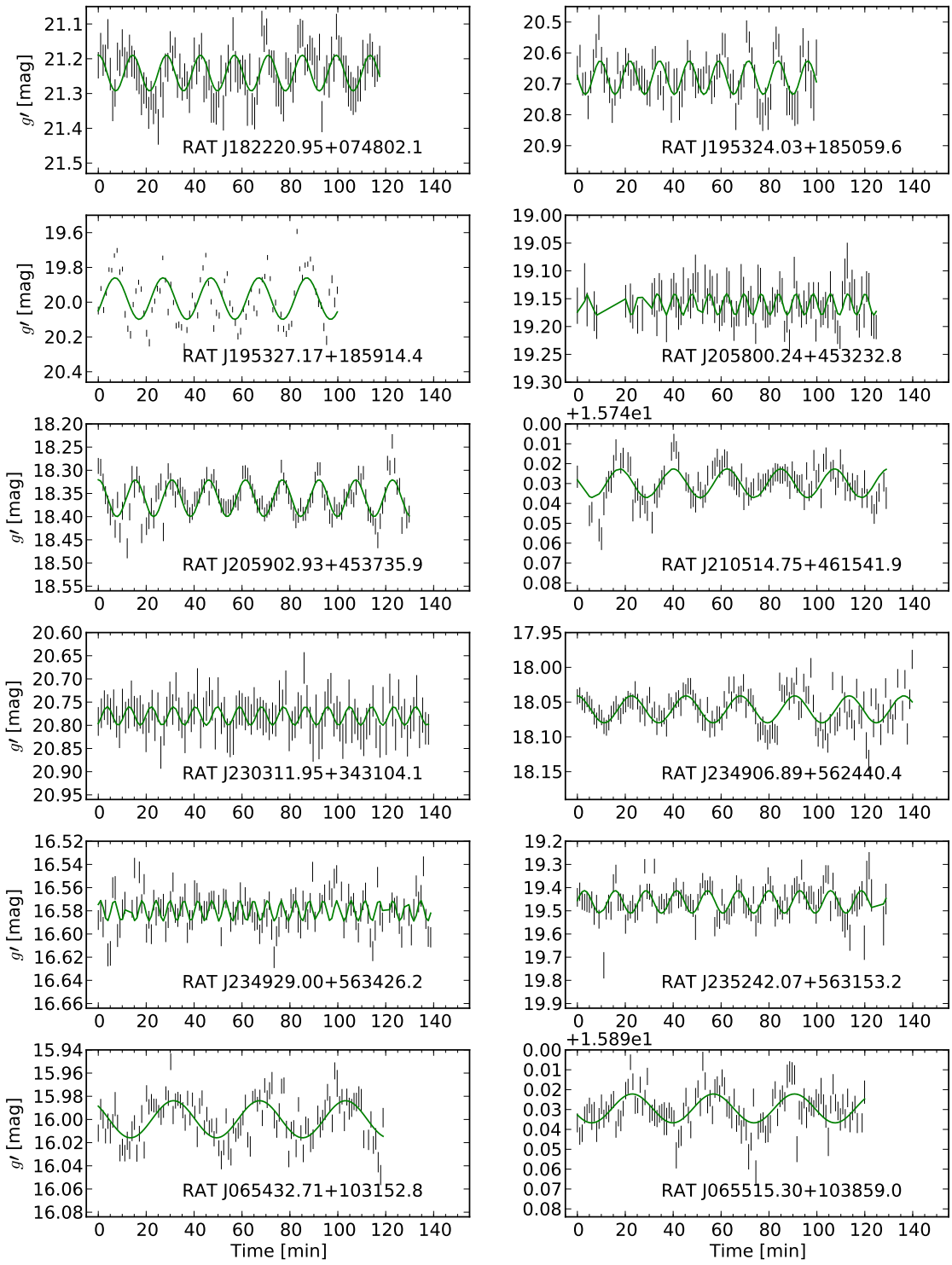

Figure 4.3: Light curves of the blue short-period variable stars shown in Tables 4.1 and 4.2.

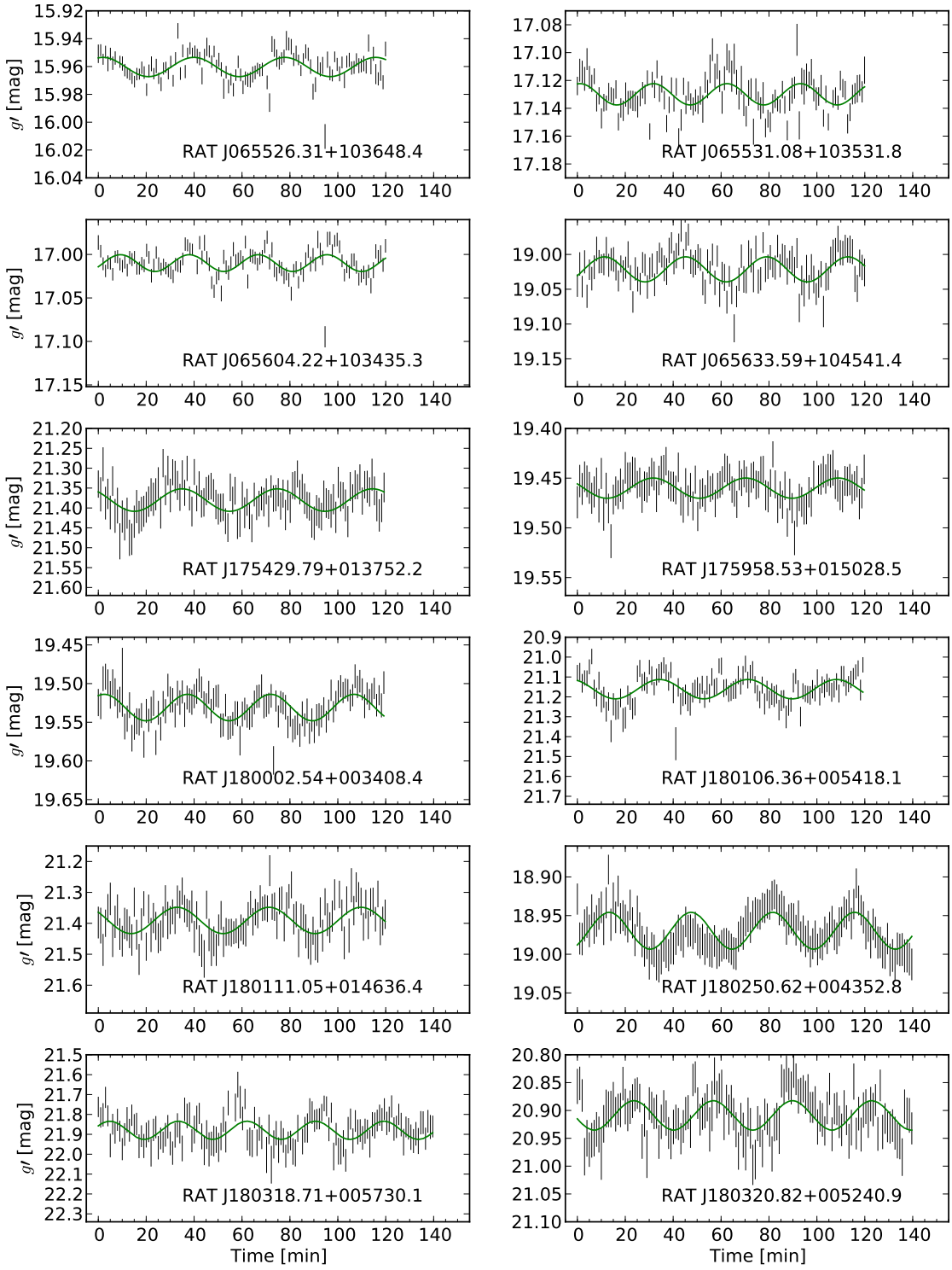

Figure 4.4: Light curves of the blue short-period variable stars shown in Tables 4.1 and 4.2.

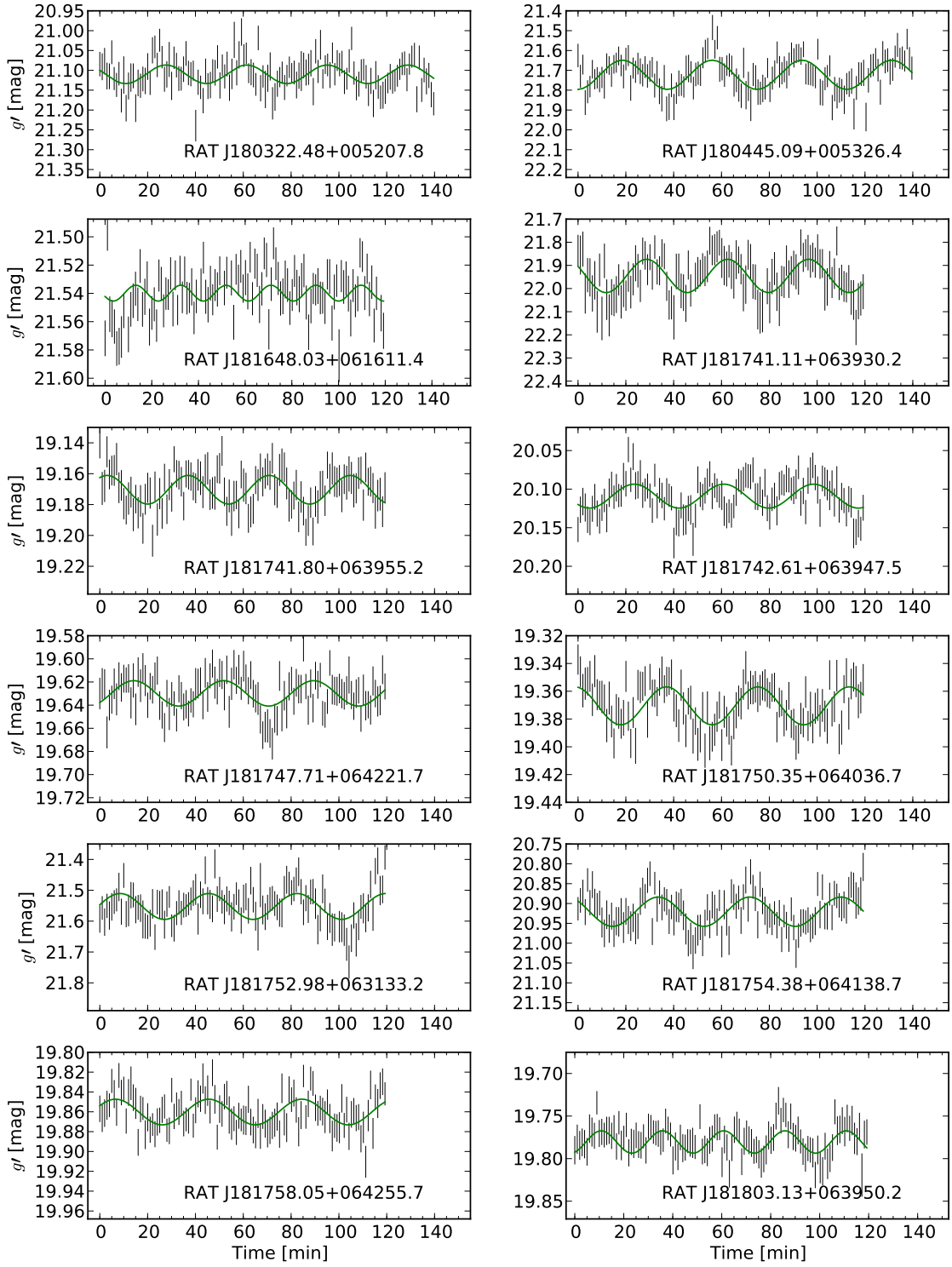

Figure 4.5: Light curves of the blue short-period variable stars shown in Tables 4.1 and 4.2.

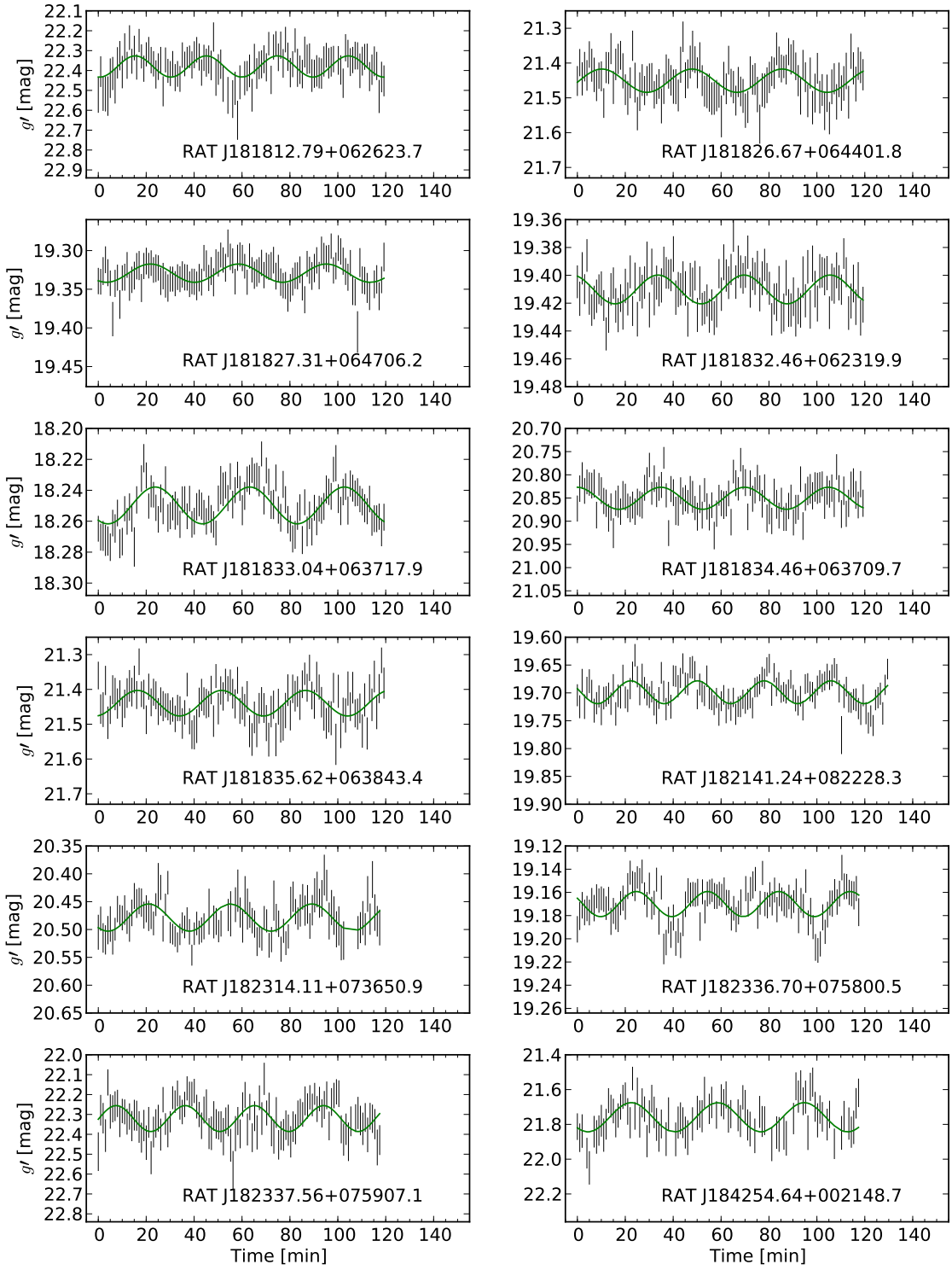

Figure 4.6: Light curves of the blue short-period variable stars shown in Tables 4.1 and 4.2.

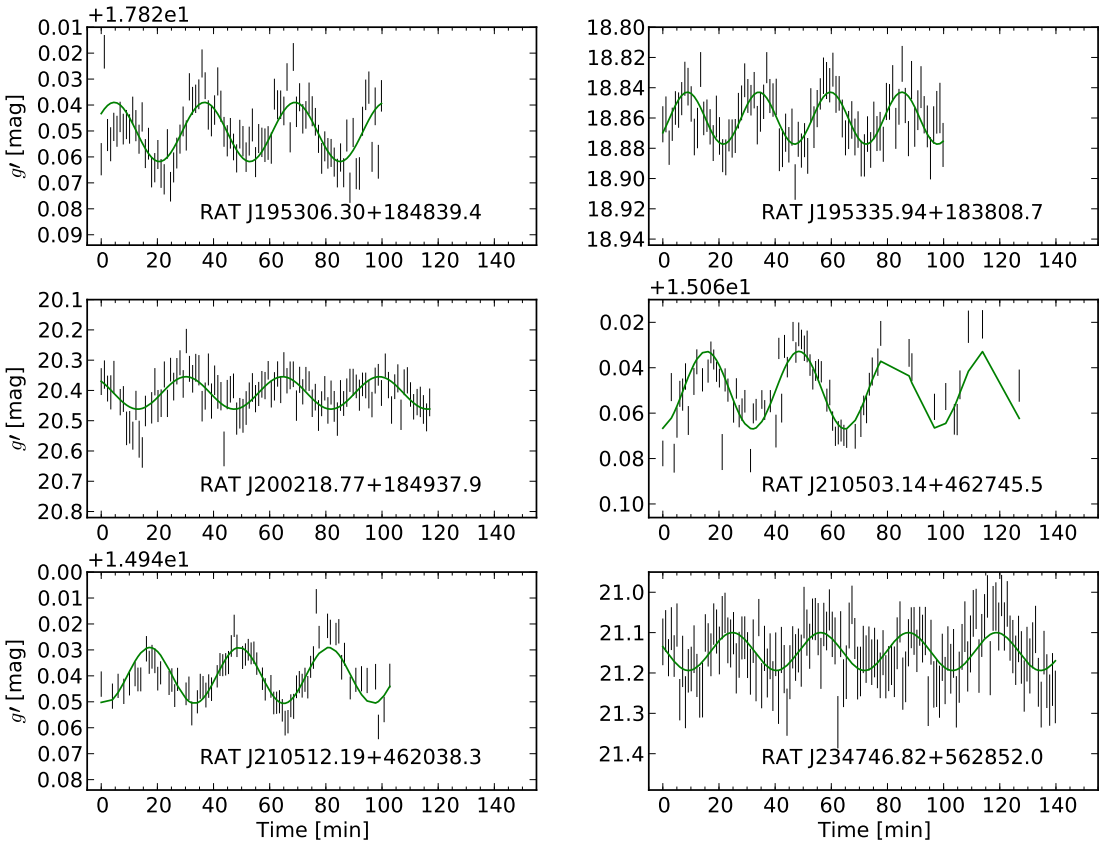

Figure 4.7: Light curves of the blue short-period variable stars shown in Tables 4.1 and 4.2.

4.2.1 The ISIS instrument on the WHT

Most spectra were obtained with the 4.2-m William Herschel Telescope on La Palma using the dual-beam Intermediate dispersion Spectrograph and Imaging System (ISIS) instrument which is mounted at the Cassegrain focus of the WHT. ISIS splits the light into a red component and a blue component via a dichroic at approximately 5500 Å, each beam passes though a blazed grating and is exposed onto a separate CCDs allowing simultaneous exposures in each arm. The blue CCD is a 4096 × 2048 pixel EEV12 array, while the CCD used by the red arm is a RED+ array of 4096 × 2048 pixels. RATS observations have typically used the R300B and R158R gratings in the red and blue arms, respectively, and a slit width of 0.8 arcsec giving wavelength coverage from 3500–10000 Å. The R300B grating has a blaze (maximum efficiency) at 4000 Å and a dispersion of 0.86 Å per pixel. The R158R has a blaze wavelength of 6500Å and a dispersion of 0.93 Å per pixel. The unvignetted wavelength ranges are 3024 and 2302 Å for the blue and red arms, respectively. The throughput of the instrument over this wavelength range is illustrated in Fig. 4.8. The sensitively peaks is the blue which means the instrument is ideally suited for our needs.

4.2.2 The ALFOSC instrument on the NOT

The Andalucia Faint Object Spectrograph and Camera (ALFOSC) instrument is mounted at the Cassegrain focus of the Nordic Optical Telescope on the island of La Palma. This very versatile instrument is capable of both imaging, spectroscopy and (spectro-)polarimetry. In the course of RATS follow-up observations I have used ALFOSC in imaging mode (as described in §6.1.2) but in this section I will discuss the use of ALFOSC in spectroscopic observations.

Our observations have used the #7 grism which has a blaze wavelength of 5300 Å. The wavelength covered when using this grism is 3850–6850 Å. Grism #7 was chosen as it gives good coverage in the optical and covers the Balmer lines as well as helium lines with a resolution of 4.1 Å which is good enough for identification of the nature of the sources as well as simple fitting of model atmospheres.

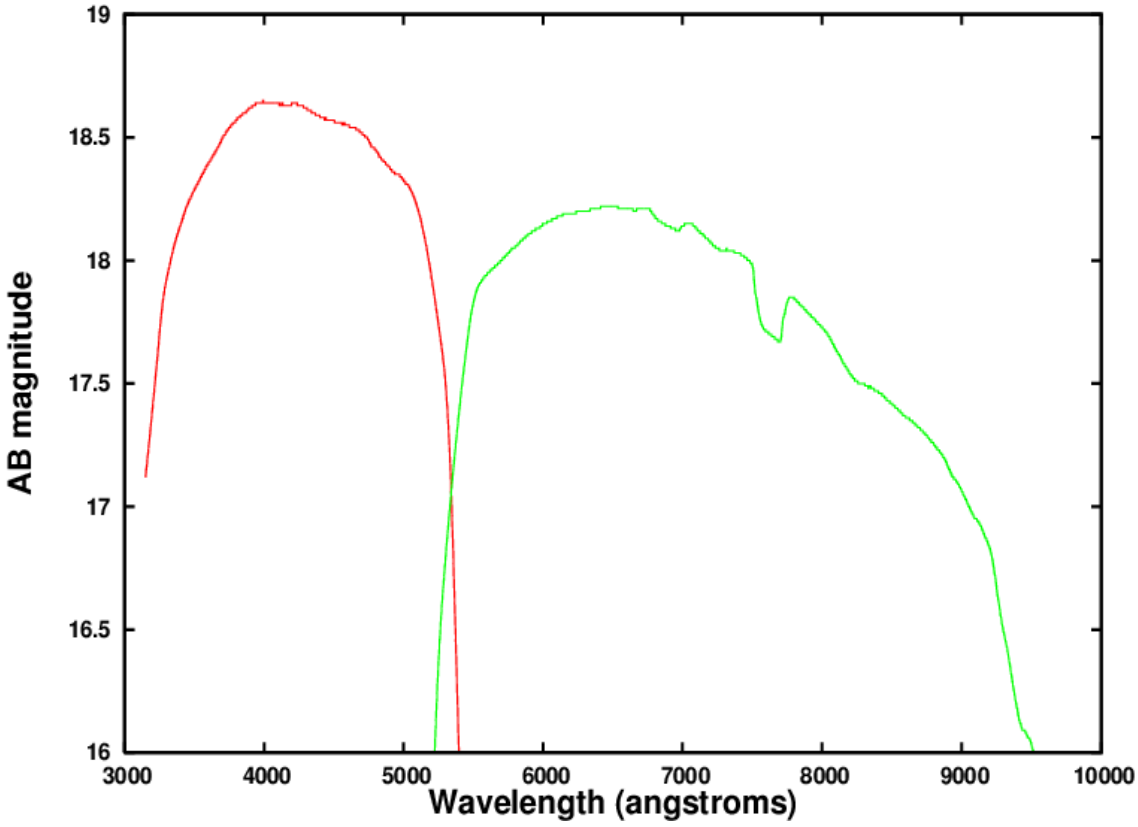

Figure 4.8: The throughput of the ISIS instrument when mounted on the WHT. The grisms used in this plot are the R300B and the R158R. Plotted on the x-axis is wavelength and on the y-axis is the apparent AB magnitude of star observed at zenith which gives one detected photon per second per Angstrom obtained when the condition were photometric. The image is taken from the ISIS instrument guide on the ING website.

4.2.3 The Grating Spectrograph on the SAAO 1.9-m telescope

From South Africa we observed bright targets ($g' < 17$) in the southern sky. We used the Grating Spectrograph mounted at the Cassegrain focus on the 1.9-m Radcliffe telescope at the South African Astronomical Observatory at Sutherland. We used grism #7 which has a blaze wavelength of 4600 Å and a wavelength coverage of 1600 Å.

4.2.4 The EFOSC2 instrument on the ESO 3.6-m telescope

Our southern target follow-up of sources too faint for the SAAO 1.9-m telescope has been performed using the ESO Faint Object Spectrograph and Camera version 2 (EFOSC2) on the ESO 3.6-m telescope at La Silla Observatory in Chile. We used grism Gr#04 which covers the wavelength range 4085–7520 Å. The blaze wavelength is 4700 Å and the dispersion is 1.68 Å per pixel. The resolution of this instrument (FWHM) when using the Gr#04 grism is 10.5 Å.

4.2.5 GMOS on the Gemini South telescope

For the faintest targets ($g' < 19$) we need to use 8 m class telescopes when obtaining spectra in order to get a sufficient signal-to-noise ratio. For these targets we have used the Gemini Multi-Object Spectrograph on the Gemini-South telescope at the Cerro Pachón observatory in Chile.

The camera consists of 3 CCDs which each have a length of 2048 pixels. We have used the B600 grism which has a blaze wavelength of 4610 Å and covers a wavelength of 2760 Å. This results in a spectral resolution of 0.45 Å per pixel and a $\Delta\lambda/\lambda$ of 1688. We chose a central wavelength of 4800 Å in order to cover the main hydrogen and helium lines visible in the optical. The efficiency of GMOS when using the B600 grism is plotted in Fig. 4.9. The efficiency is greatest at the blue end of the spectrum which is the area exposed on the CCDs.

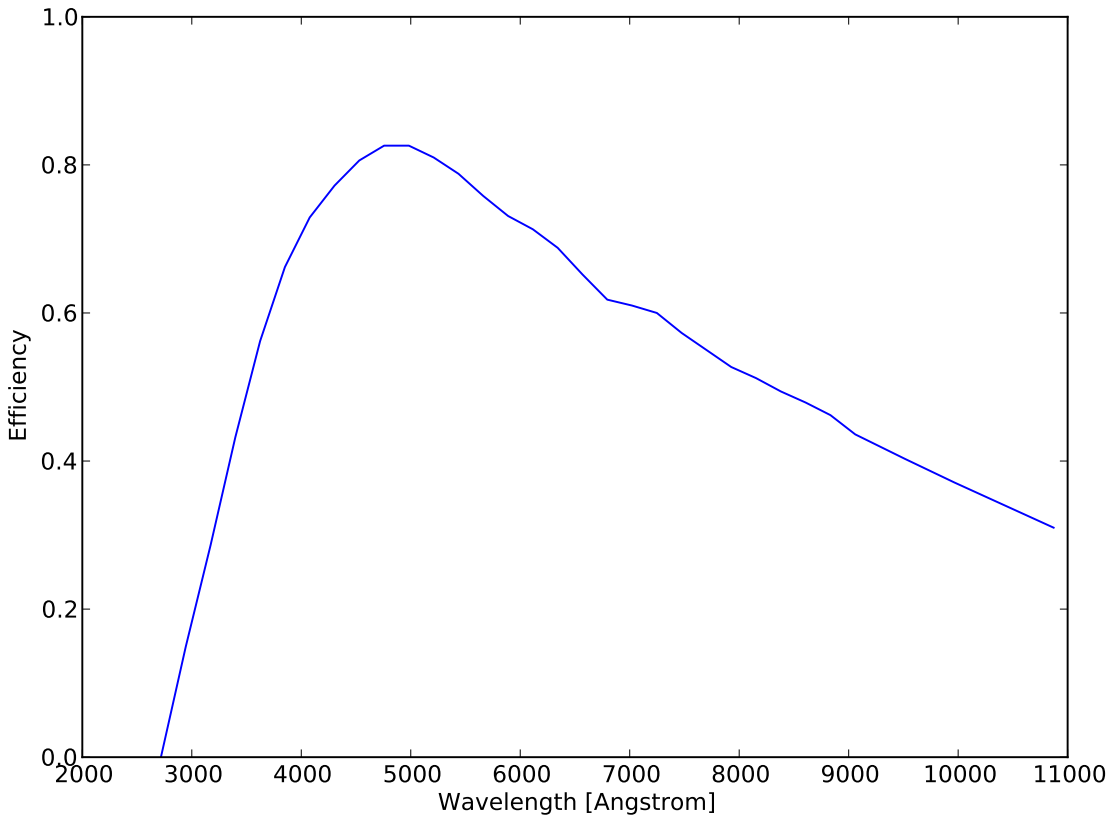

Figure 4.9: The efficiency of the GMOS instrument which is mounted the Cassegrain focus of the Gemini-South telescope. The efficiency plotted here is for the B600 grism which was used for our observations.

4.2.6 Spectral data reduction

I reduced these spectroscopic observations using the STARLINK[2] packages FIGARO and KAPPA and MOLLY and PAMELA which were written by Tom Marsh[3]. For this process I based my reduction procedure on a guide written by John Southworth[4]

I de-biased the images and created master lamp flats. The flat images then need to have the response of the flat-field lamp removed to leave only the slit response and the CCD pixel-to-pixel variations. This is done by summing up each pixel of the CCD along the spectral dispersion axis using the YSTRACT routine in FIGARO and then taking the log of the counts in this spectrum using LOG10. This is the spectral response of the master flat-field image. I fit a third order polynomial to this (in the case of the redder CCD on the WHT I use a fifth order polynomial) and, after taking the anti-log of the response using EXP10, I divide the master flat image by the response using ISYDIV. The final steps to create the flat-field are to divide the image by its mean and then to take the inverse of the image (i.e. for replace every pixel $p_{x,y}$ by $1/p_{x,y}$) as this image is used directly by the tools used for extracting the spectrum.

The extraction of the spectrum is done using the PAMELA 2D spectrum analysis program. The first step is to use TRACK to which tracks the position of the spectrum on the CCD along the spacial axis by fitting a third order polynomial. The next step is to use REGPIC to pick the regions of the CCD from which to extract the spectrum and where to extract a sky spectrum which will later be subtracted from the source spectrum. The source spectrum region is picked so that it is as small as possible without losing any flux while the sky regions are are typically 50–100 pixels wide on each side of the source spectrum. It is at this point that the inverse flat field image created earlier is multiplied by the science image. The third step is to fit a polynomial to the sky regions using SKYFIT. I typically use a third order polynomial but for red spectra a fifth order is needed for a good fit. Pixels with flux

[2]The Starlink Software Group homepage can be found at http://starlink.jach.hawaii.edu/starlink

[3]MOLLY and PAMELA were written by T. Marsh and can be found at http://www.warwick.ac.uk/go/trmarsh

[4]John Southwoth's guide can be found at http://www.astro.keele.ac.uk/~jkt/GrSpInstructions/GrSpInstructions.html

3σ away from the fits are excluded iteratively.

I use optimal extraction of the spectrum using the PROFIT and OPTEXT procedures, this method is based on a technique developed by Marsh (1989) which is analogous to profile fitting photometry. PROFIT performs the fitting of third order polynomials along the spectrum with polynomials fit every 0.5 pixels along the spectrum. OPTEXT then extracts the spectrum.

The next step is to wavelength calibrate the spectrum. At the WHT I took Cu-Ne and Cu-Ar arc lamp images several times through the night, with similar arcs taken at other telescopes. I use the 1D spectrum analysis program called MOLLY for the calibration. The process involves identifying lines in the arc spectrum from an arc map. A third order polynomial is then fit to the wavelengths identified. A wavelength calibration is then applied to the spectra of our sources, interpolating between the different arc calibrations which were taken over the course of the night.

On the WHT the typical FWHM of the lines in the arc spectra were 5 and 3 Å for the red and blue arms, respectively. This is the spectral resolution of our spectra. The SAAO 1.9-m spectra have a typical resolution of 5 Å, our Gemini spectra have a higher resolution of ~1 Å while the EFOSC2 spectra have a resolution of 10.5 Å.

4.2.7 The nature of short period blue sources

The RATS follow-up observations have included spectra of 10 sources with periods less than 25 min which appear in Table 4.1, and 7 sources from Table 4.2 which contains sources with periods from 25 to 40 min. The details of these observations is given in Table 4.3. The classification which I have given individual sources are shown in Tab. 4.1 and 4.2. Six of these spectra are very low signal-to-noise and I can put no constraints on the nature of these sources other than to say there are no obvious emission lines. As mentioned above, one source is a pulsating sdB star and one is a dwarf nova (see §6.1), the spectra of these two sources are shown in Fig. 4.12. Two sources are pulsating white dwarfs (their spectra

Date	Telescope	Target (RAT J ...)	Exposure (s)
2004 12 07	NOT	045515.22+130529.8	600
2008 08 03	WHT	205902.9+453735.9	240
		195327.17+185914.4	420
2009 10 09	WHT	065515.30+103859.0	420
		180250.62+004352.8	600
		195306.30+184839.4	600
		210503.14+462745.5	400
		210512.19+462038.3	600
		210514.75+461541.9	400
		234906.89+562440.4	400
2009 10 10	WHT	050751.28+343155.5	600
	Gemini-South	073919.05+235239.9	600

Table 4.3: Details of the spectroscopic observations of AM CVn candidates. Only the targets with a high enough signal to noise with which to determine the nature of the source are included in this table.

are shown in Fig. 4.11), these are discussed in §5.4 and §6.2. Eight sources have spectra of A and early F-type stars, the spectra of these are shown in Fig. 4.10. These spectra were all obtained with the WHT and are discussed further in §5.2.

None of the spectra are indicative of an AM CVn star. The implication of this are discussed in the next section.

4.3 The space density of AM CVn stars

The space density of a population is the distribution of the number of stars per unit volume and is usually express as pc^{-3}. This quantity is usually calculated theoretically from population models and is then compared to the observed *local* space density. From the predicted space density it is possible to estimate the number of sources which should be detected if the models are correct provided a realistic estimate of the completeness of the observed sample can be made (i.e. what proportion are missed by the observations). Roelofs et al. (2007a) performed a calculation based on the spectroscopic observations made by the SDSS survey and calculated the predicted number of AM CVn systems which should have been found spectroscopically and compared this to the actual observed number. In order to calculate

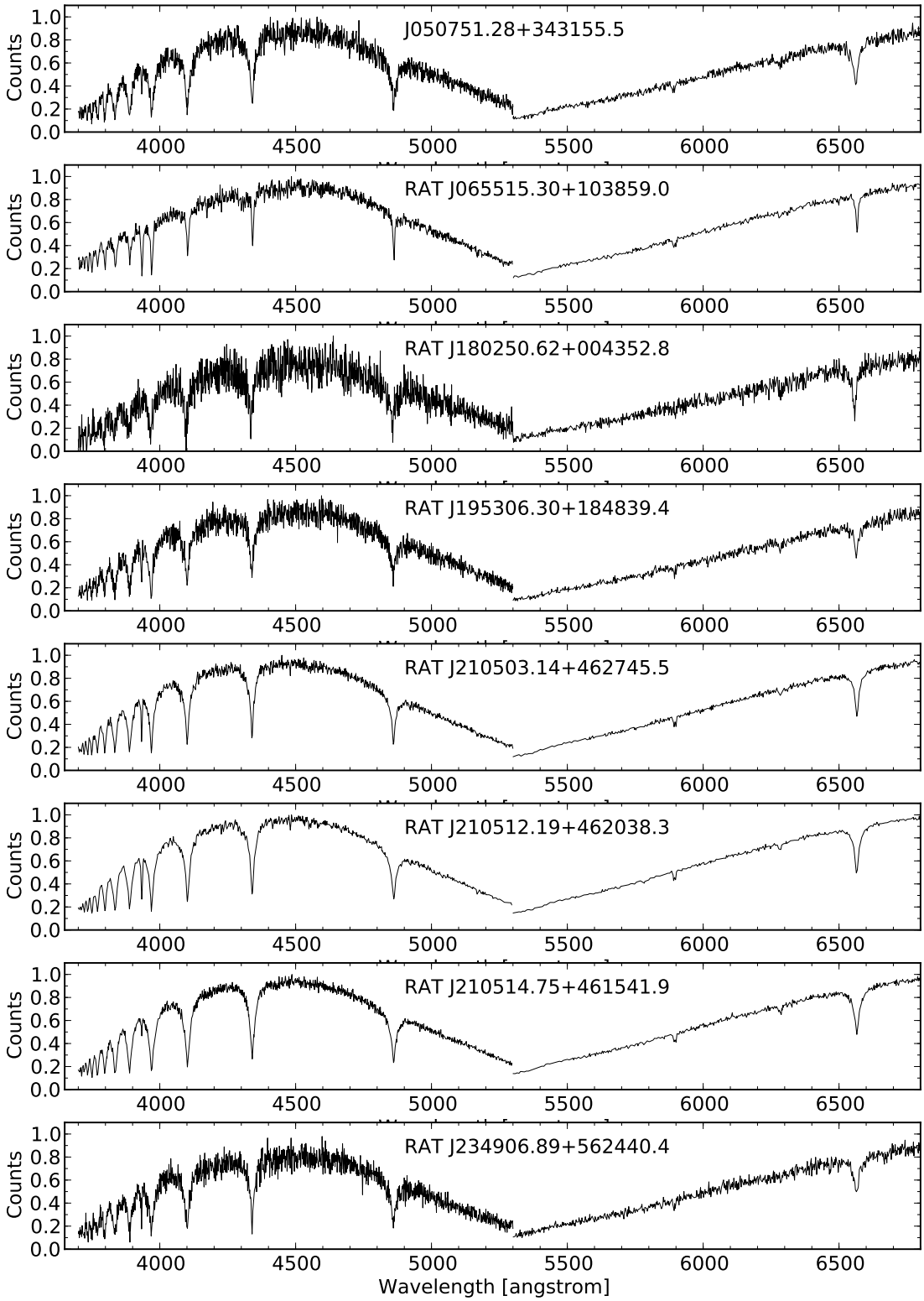

Figure 4.10: Spectra of 7 A-type and one F-type stars (the F star is second from the top). All are variable on periods between 20 and 35 min. The blue and red arms of the spectra have been normalised separately, such that the bin with the highest number of counts now has value unity and the other bin have been normalised relative to this. This preserves the shape of a spectrum whilst allowing for comparison with other spectra.

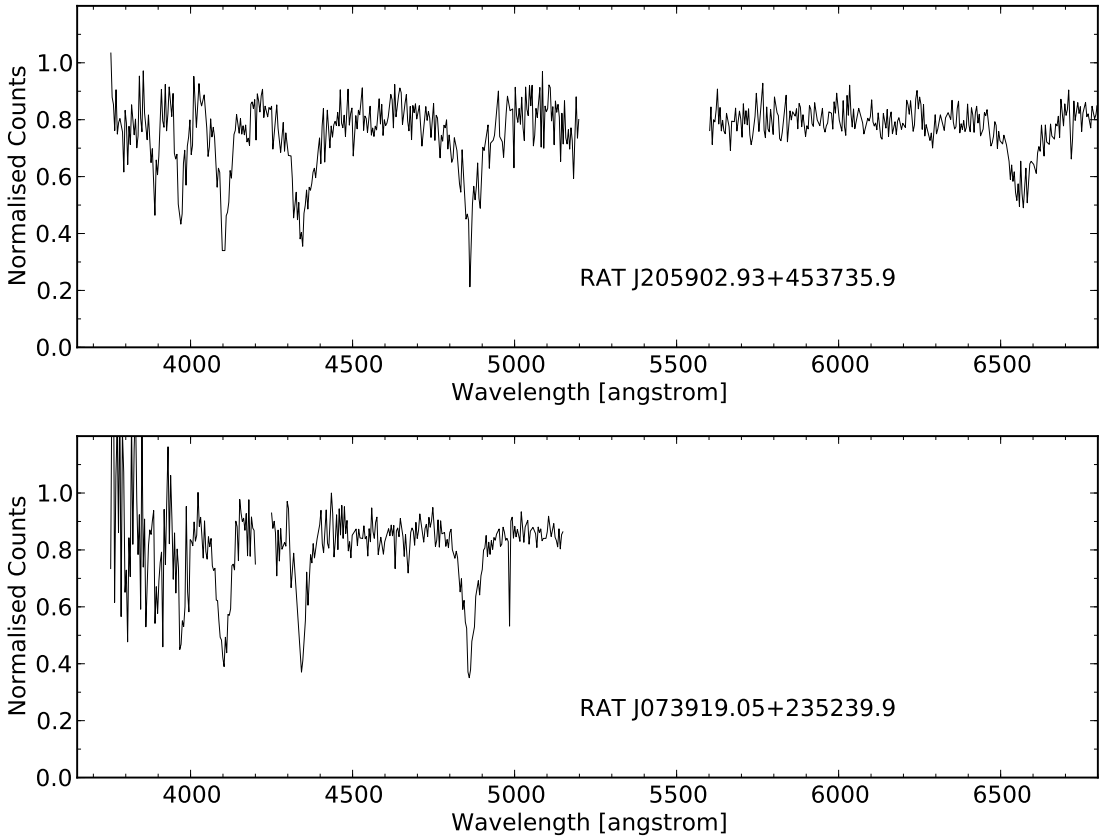

Figure 4.11: The spectra shown here are of two DA white dwarfs. The top source was found in INT4 data and the spectrum was obtained using the ISIS instrument on the WHT. The lower spectrum is of a source found in INT1 data. The spectrum was obtained using the Gemini-South telescope and the GMOS camera. The spectral ranges of these instrument differ – ISIS has a larger spectral ranges than GMOS. Both spectra have a gap which is where the gap between CCDs is. In the case of ISIS this is because the light passes through a dichroic. The spectra have been normalised to the continuum.

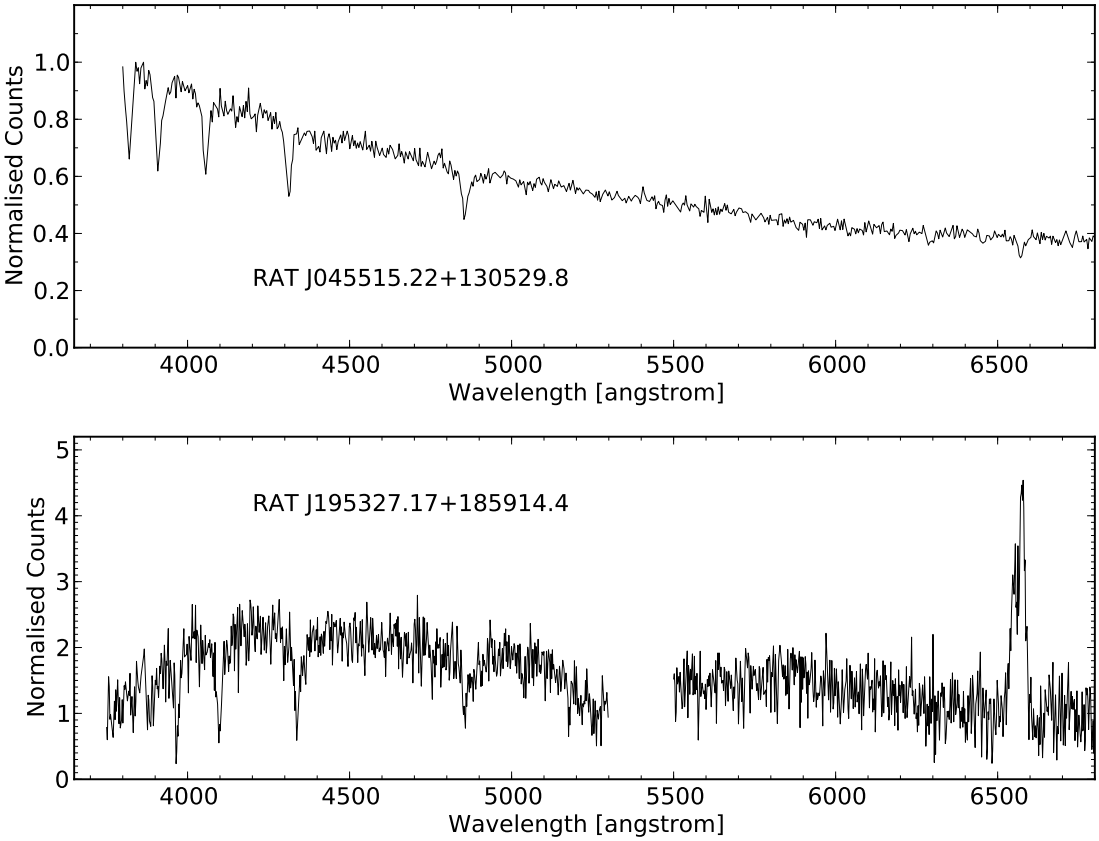

Figure 4.12: The two spectra shown here are of a sub-dwarf B star (top) and an accreting source (bottom) which was later discovered to be a dwarf nova. The emission lines in the accreting source are double peaking indicating the presence of a disc. The top spectra has been flux calibrated using a flux standard star. The top spectrum was obtained using the ALFOSC instrument on the NOT while the lower spectrum was obtained using the WHT and the ISIS instrument.

the theoretical space density they used the equation

$$N'_{\rm spec} = \sum_{\rm tiles} \int_{P_{\rm min}}^{\infty} {\rm d}P \int_{0}^{d_{\rm max}(P)} \Omega_{\rm tile} d^2 \, C(P, b_{\rm tile}, d) \, \rho'(P, b_{\rm tile}, d) \, {\rm d}d \tag{4.3}$$

This is an integration over the distance to the source, d, and the orbital period, P. $N'_{\rm spec}$ is the predicted number of spectra which could be detected in the SDSS archive. $C(P, b_{\rm tile}, d)$ is the completeness of the spectroscopic observations as a function of orbital period, the Galactic latitude, $b_{\rm tile}$, and the distance. The lower limit on the period integral, $P_{\rm min}$, is becauseRoelofs et al. (2007a) search only for sources with emission line spectra, as mentioned in §1.3.2, only AM CVn systems in the low state have emission lines spectra (aside from one ultra-short period system). This, therefore, sets the lower period range which they are able to detect. The upper limit, $d_{\rm max}(P)$, on the distance integration is the distance at which a source with period P would have apparent magnitude $g_{\rm max}$, where $g_{\rm max}$ is the limiting brightness of the survey. The sum of solid angle covered by each spectroscopic pointing, $\Omega_{\rm tile}$, gives the total area of the survey and each spectroscopic pointing encompasses a volume $\int \Omega_{\rm tile} \, d^2 \, {\rm d}d$. The modelled space density, $\rho'(P, b_{\rm tile}, d)$, is calculated from population synthesis models and is a function of orbital period, Galactic latitude and distance. The observed local space density can be calculated using the equation

$$\rho_0 = \frac{N_{\rm spec}}{N'_{\rm spec}} \rho'_0 \tag{4.4}$$

where ρ'_0 is the modelled local space density and $N_{\rm spec}$ is the observed number of AM CVn sources with an SDSS spectrum.

Roelofs et al. (2007a) use the population synthesis models of Nelemans et al. (2001a, 2004) to calculate the predicted space density and local space density. They take $P_{\rm min}$ as 30 min, the number of tiles over which they sum, $N_{\rm tile}$ = 1700, and $\Omega_{\rm tiles} = \Omega_{\rm spec}/N_{\rm tile}$ where $\Omega_{\rm spec}$ = 5700. To calculate their completeness and the model population they use a three-dimensional grid in P, b and d and assume g_{max} = 21. They calculate the modelled local space density for two different assumptions, one 'optimistic' and one 'pessimistic' (see §1.3.3 for a description of the differences between these assumptions). The values they find are $\rho'_0 = 2.6 \times 10^{-5}$ and 1.5×10^{-6} for the optimistic and pessimistic models, respectively. The

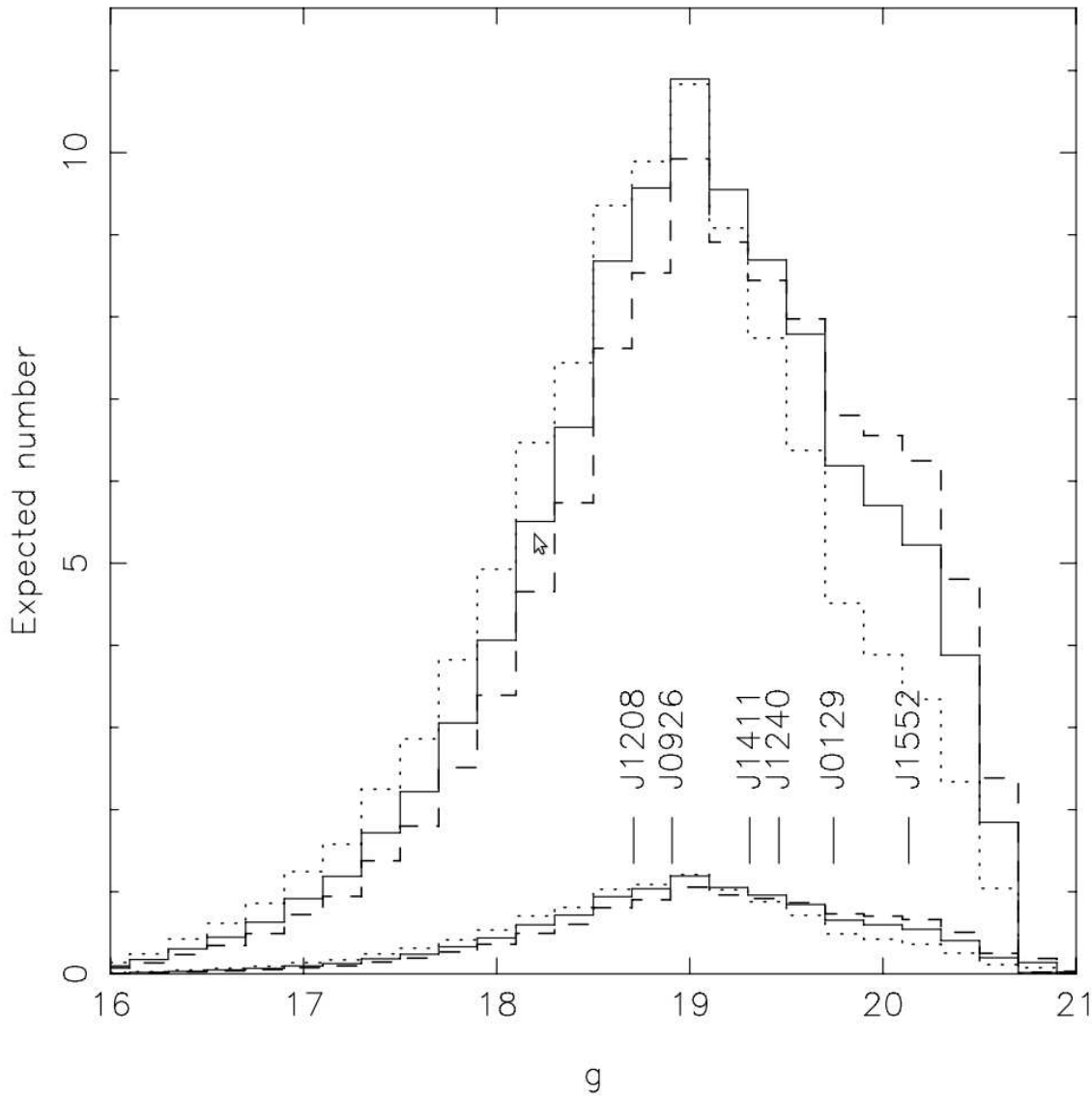

Figure 4.13: The predicted number of AM CVn systems which should have been found in SDSS data using the optimistic (upper lines) and pessimistic (lower lines) models, as a function of g' magnitude. The tress different lines associated with each model are for different assumption on the scale high of the AM CVn population (200, 300 and 400 pc for the dotted, solid and dashed lines, respectively. The 6 known systems (at the time the paper was written) are marked. This plot is taken from Roelofs et al. (2007a).

expected number of systems to have been detected in the SDSS survey using the each model is shown in Fig. 4.13. Given that when the paper was written, $N_{\rm spec} = 6$, the observed $\rho_0 = 1.5 \times 10^{-6}$ and 3.2×10^{-6} for the optimistic and pessimistic models, respectively. Note that the observed space density in the pessimistic model is higher, this is due to the pessimistic model forming more fainter systems and thus the 6 observed systems exist in a smaller volume.

The combined sky coverage of the first 5 years of RATS data is 31.3 deg^2. To apply

Roelofs et al. (2007a) formulation to the RATS data means modifying Equ. 4.3 to give

$$N'_{\rm phot} = \sum_{\rm fields} \int_0^{P_{\rm max}} {\rm d}P \int_0^{d_{\rm max}(P)} \Omega_{\rm fields} d^2 \, C(P, b_{\rm field}, d, a) \, \rho'(P, b_{\rm field}, d) \, {\rm d}d \qquad (4.5)$$

The changes made to Equ. 4.3 are to calculate the sum the fields we observe and to integrate the periods from 0 to $P_{\rm max}$ which is the maximum period at which AM CVn systems how photometric variability – we assume $P_{\rm max}$ = 25 min. Our completeness, $C(P, b_{\rm field}, d, a)$, will be a function of an extra term, a which is the amplitudes to which we are sensitive. An assessment of the completeness is still ongoing but here I assume that we detect every AM CVn brighter than g' = 20 and half the AM CVn systems with brightnesses between g' = 20 and 22. With these assumptions, the optimistic model predicts we should discover are 6.8 in the RATS data [2.7 for $g' < 20$, (0.5×8.2) for $g' = 20 - 22$][5].

I have identified 11 candidate AM CVn systems brighter than g' = 20 with a period shorter than 25 min (21 brighter than g' = 22, excluding HM Cnc). We have obtained optical spectra of 11 of these candidates; none of which are consistent with an AM CVn system (cf. Table 4.1). Removing these sources leaves five candidate AM CVn systems brighter than g' = 20 for which we are yet to obtain spectra (10 brighter than g' = 22). One could speculate that the observed sample, once follow-up is completed, will indicate the need to revise the simulations, but for the time being we are left with an upper limit of ten, which is consistent with the model predicted number.

Our result is in contrast to the finding of Roelofs et al. (2007a) which suggests the model of Nelemans et al. over-predicts the number of long period systems ($P_{\rm orb}$ < 30 min) by a factor > 10 for the optimistic model and 2 for the pessimistic model. If this were to be replicated at shorter periods we would expect to find < 1 AM CVn systems in our observations so far. It remains to be seen whether there is also a deficit of systems compared to the models at shorter periods, or whether there are relatively many more younger, short period systems compared with older systems. This is particularly important for future low-frequency gravitational wave detectors such as *LISA* as AM CVn systems are predicted to form the dominant sources of background noise which limits the detection of

[5]These calculations were performed by Gijs Nelemans

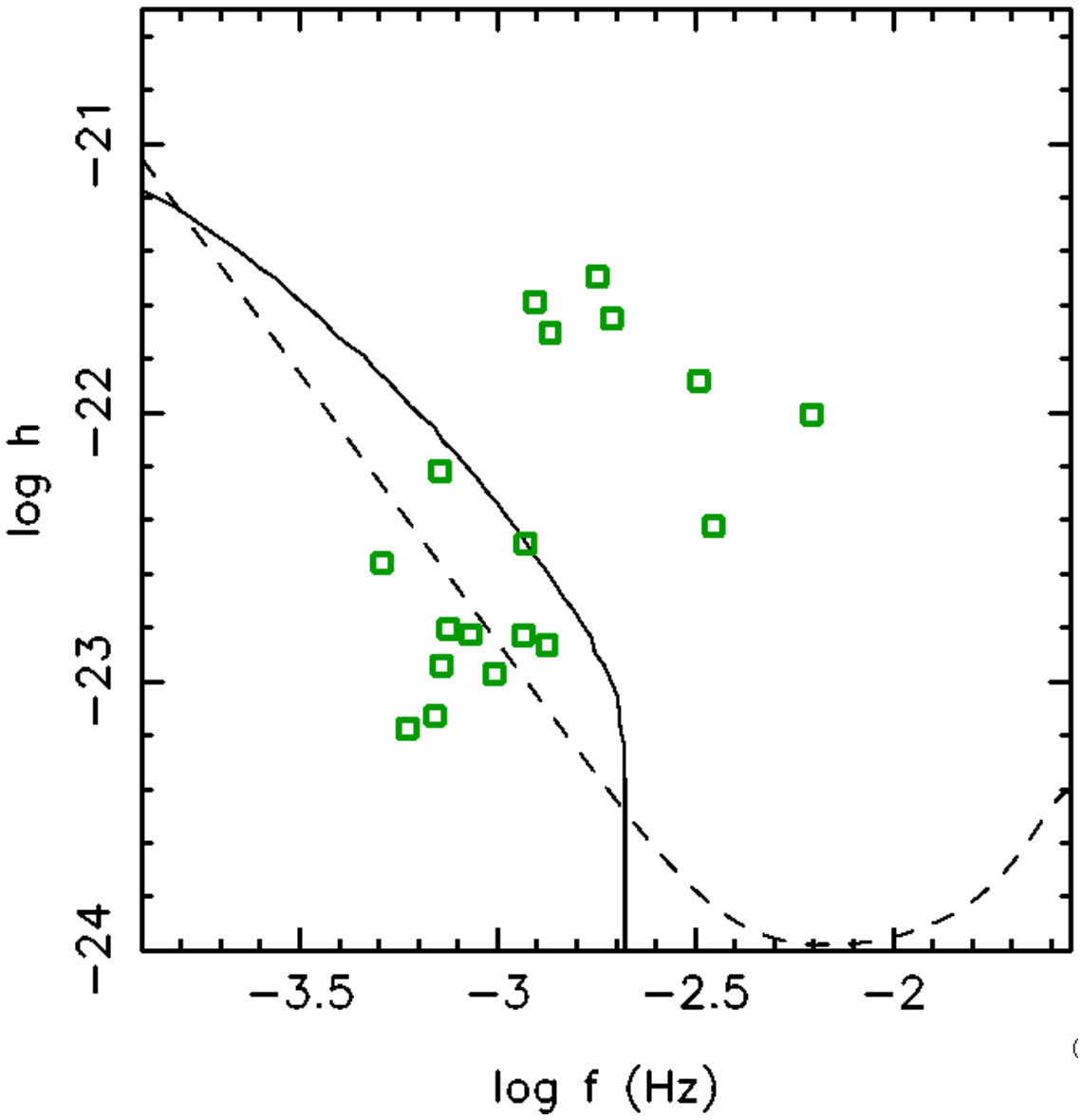

Figure 4.14: This is a plot showning the gravitational wave signal from AM CVn systems as green boxes. The y-axis is the strain of the GW signal and the x-axis is frequency [equal to $1/(2P_{\rm orb})$]. The dashed line is the *LISA* 1σ detection after a year of observations and the solid line is the gravitational wave background from double white dwarfs using the model from Nelemans et al. (2004). The plot was created using an web applet created by G. Nelemans.

extra-galactic gravitational waves sources (Nelemans et al., 2001a). In Fig. 4.14 the 1σ *LISA* sensitivity is shown as a dashed line and the double white dwarf background as the solid lines. If the AM CVn systems are much less numerous than predicted then the solid line can be pushed downwards, hence *LISA* is more sensitive to extra-galactic signals.

4.4 Summary

This Chapter deals with primary aim of the RATS survey – testing the space density models of AM CVn systems. It describes the path taken to move from having a number of light curves which show variability on periods of less than 40 min, through the follow-up work to determine their nature and ends by stating the number of AM CVn systems found and how this impacts the space density models. We are yet to find any AM CVn systems and currently are not able to strongly constrain the space density. However, the survey is not finished and more photometric data is in the process of being analysed. More follow-up observation are also planned including observations of three sources from Table 4.1 with the Gemini-South telescope in the second half of 2011. When all these data are collected and analysed we will be able to constrain the space density of AM CVn systems. Importantly, we will be able to distinguish whether the models of Nelemans et al. correctly estimate the number of AM CVn systems or whether the space density is consistent with that seen in longer period systems by Roelofs et al. (2007a).

In the next Chapter I will go onto discuss some of the populations of variable sources that we have found in the data. The unique cadence and depth of the RATS projects allows to probe populations which have either not been observed before or not in a systematic way such as is done by RATS.

Chapter 5

Stellar pulsators

> Pleasure is very seldom found where it is sought. Our brightest blazes of gladness are commonly kindled by unexpected sparks.
>
> *S. Johnson, The Idler, 26th May 1759*

In the previous Chapter I discussed how I identified and obtained follow-up observations of AM CVn candidates systems. The Rapid Temporal Survey is much more than a one-trick pony, however. In this Chapter I will describe some work undertaken to determine the nature of a number of types stellar pulsations. In the first Section I discuss the process used to fit stellar models to spectra which have been obtained as part of the RATS follow-up programme. The technique for fitting stellar spectra with models is then exploited in the remaining sections to help understand the nature of variable sources in the RATS data. The first class I consider are the variable A-type stars discussed in the previous chapter, then move on to consider a class of longer period blue pulsator and finish the Chapter examining a sample of degenerate pulsators.

5.1 Fits to model spectra using FITSB2

The spectra we obtain are primarily for identification purposes (e.g. is the source a main sequence star or a hydrogen-rich white dwarf?). However, when the signal-to-noise is high enough I am able to determine a number of physical properties of the star through spectral fitting.

The effective temperature, surface gravity and metallicity of stellar sources can be determined by fitting their spectra with model atmospheres. To do this I use the FITS2B fitting programme (Napiwotzki et al., 2004). FITS2B was developed primarily for fitting model atmosphere to spectroscopic binaries though it is equally adept at fitting a single star model to a spectrum. The program uses a grid of model atmospheres which vary in effective temperature, surface gravity and abundance. In the case of a two component fit it is also able to calculate radial velocities or orbital parameters.

The fitting routine is performed by minimising the chi-squared using the AMOEBA downhill simple algorithm (Press et al., 1992). The method was developed by Nelder & Mead (1965) and uses simplicies – a geometrical figure consisting of N dimensions and $N+1$ vertices, $N = 2$ is a triangle, $N = 3$ is a tetrahedron, etc. – a to find a solution. The algorithm takes a number of steps to move the simplex downhill, closer to a minimum. Each step is either an expansion, contraction or reflection of the simplex. An issue with all fitting techniques is the chance of missing the global minimum and getting trapped in a local minimum. FITS2B attempts to get round this by restarting the algorithm with initial values set at the values of the minimum but using the initial, large simplex. If the chi-squared of this is better than the previous one then the algorithm continues. However, this technique is far from fool-proof and it is therefore important that the initial parameters are set to plausible values values.

When calculating errors on the fit found using FITS2B a bootstrapping approach is used, replacing the N points in the spectrum with N points picked at random from the data. Each point may be picked more than once and the error is computed from the variance of the fitted spectra. Bootstrapping is good at measuring errors when they are non-Gaussian

Setting	Typical Value	Meaning
FIT-MODE	ATMOS	Fit spectrum to model atmospheres
SB-MODE	SB1	Single component fitting – use SB2 for two component fitting
CLIP-MODE	CLIP	Clip points 3σ from fit when calculating χ^2
SIGMA-MODE	ATMOS	Calculate error using model fit
ERROR-MODE	BOOTSTRAP AUTO	Use a bootstrapping technique to calculate errors and automatically determine number of iterations
HELIUM-MODE	VARIABLE	Calculate metal abundances, use NONE to use solar metallicity

Table 5.1: Typical settings used in the PARAM.IN file.

though can be slower than other methods such as Monte Carlo techniques.

Three files are used to define how the fitting is performed: PARAMS.IN which defines the parameters used in the fit; SPEC.LIST which contains information on the spectrum to be fit and wavelength ranges to use in the fit; and MODELGRID.DAT which defines the model grids to be read. The parameters which I use when fitting are described below.

5.1.1 PARAMS.IN

The parameters which are used in PARAMS.IN are summarised in Table 5.1. SB-MODE is set to either SB1 or SB2 depending on whether single or double line fitting should be performed. Single line fitting is used when there is no evidence for a second component (this is true for all sources except one, this is described in §6.2). Setting BOOTSTRAP AUTO as the ERROR-MODE uses bootstrapping to calculate errors on the fit and to automatically determine the number of bootstrap iterations to perform (bootstrapping is slow so when modifying the initial temperatures/log g's, I run the fitting routine without calculating errors - NOERROR). HELIUM-MODE refers to whether or not to include the metal abundance in the fit. This is set to VARIABLE if abundance fitting is to be performed.

The next step is to set the initial parameters and to define the positions of lines in the spectrum. The temperature and gravity need to be set to plausible values to prevent the algorithm getting stuck in a local minimum. Estimating these is straight forward for hydrogen white dwarfs as because the RATS sources are all variable and variable hydrogen-rich white dwarfs occupy relatively restrictive parameter range (see §1.4.1). The initial temperature and gravity are set at $T_{\rm eff}$ = 11500 K and $\log g$ = 8 which are typical for pulsating white dwarfs. For main sequence spectra the temperature is set to an approximate temperature consistent with the spectral type of the spectrum, e.g. 8000 K for an A-type star, and a $\log g$ of 4. I use an initial fitting step size in temperature and gravity of 100 K and in 0.1, respectively. The lines which I define are the Balmer lines from Hα to H10.

5.1.2 SPEC.LIST

The SPEC.LIST file required details of which spectra should be read and which regions are included in the fit. I specify the Balmer lines to be fit in this file which takes the form: line-number (i.e. 2 for Hβ), W1, W2; where W1 and W2 refer blue and red limits of the region to be included in the fit. In the case of the WHT and Gemini-South spectra two spectra are included in this file as the spectra obtained on these instruments are split across several CCDs. Our spectra are relatively low resolution so for white dwarfs we include only the regions around the Balmer lines. For main sequence stars I include extra regions between lines if I am fitting an abundance to the spectra.

5.1.3 MODELGRID.DAT

The model grids used in the fits are defined in the MODELGRID.DAT file. The first line tells the software how many effective temperatures to include, how many surface gravities and the number of abundances. The values are set by the models which will be fit to the data. The number of abundances is typically one, save for when fitting metallicity (as is done for the SX Phe stars later in this section). For stars with DA white dwarf spectra the Balmer

lines are fit using a grid of hot white dwarf models[1] with temperatures ranging from 6000 to 100000 K and log g from 5.5 to 9.5. For all other spectra I use ATLAS9 model atmospheres (Castelli & Kurucz, 2004) which range from 5000–50000 K and from gravities from 2.8 to 6.0. When using the ATLAS9 models it is possible to vary the metallicity, the models which I used vary from solar metallicity (Z = 0.0) to -3.0 dex below solar in steps of 0.5 dex.

In the following sections I will discuss some of the pulsating stars discovered by the RATS project. Many of these sources have spectroscopic data. I describe how the spectral fitting allows for the determination of the nature of the sources.

5.2 Short-period pulsating A and F-type stars

As mentioned in Chapter 4, I have discovered 8 sources with spectra of A, and F-type stars and show modulations on periods of between 20 and 40 min. I fit the spectra with ATLAS9 models (Castelli & Kurucz, 2004), with the results shown in Table 5.2. The metallicities varies from solar to -3.0 dex below solar metallicity. The regions where the metal abundance is fit are either side of the $H\beta$, $H\gamma$ and $H\delta$. An example fit is shown in Fig. 5.1 which shows the continuum regions where metal lines are included in the fit.

The cause of this modulation is very likely to be because of pulsations given that the modulation is relatively sinusodial and period is too short to originate from orbital motion as geometrically main sequence stars are too large to have such orbital periods. In this case the pulsation is likely caused by the sources existing on the δ Scuti instability strip – all the sources have temperatures in the regime of this instability strip. Variable sources on this strip pulsate because of either ionisation of singly ionised helium to doubly ionised helium or from hydrogen ionisation (Cox, 1980).

One possibility is that the A-type stars are long period examples of rapidly oscillating, chemically peculiar A (roAp) stars which have typical pulsation periods of 10 minutes (e.g. Kochukhov et al., 2009) although longer periods – up to 21 minutes – have been seen

[1] A grid of hot white dwarf models was kindly supplied by Detlev Koester

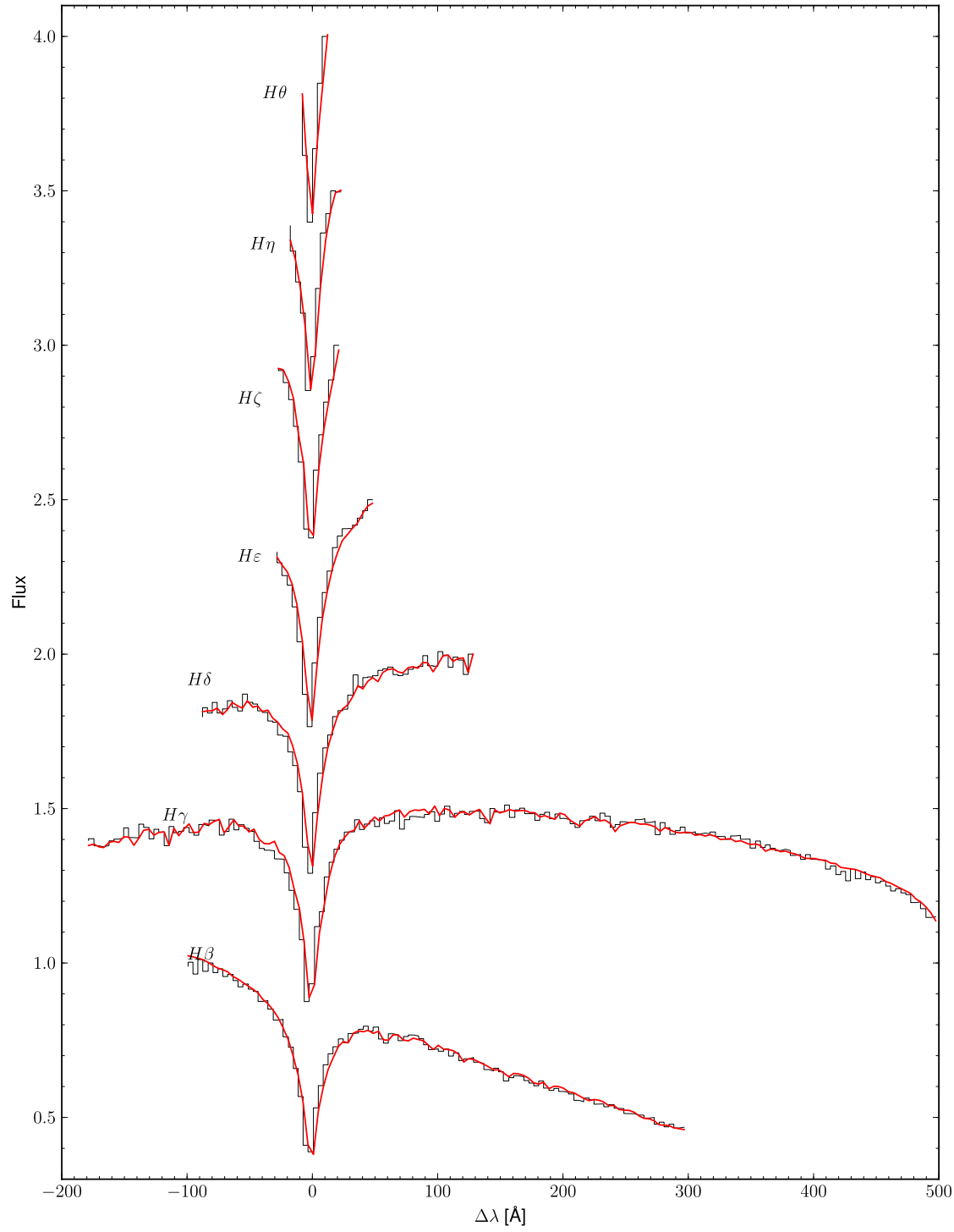

Figure 5.1: The best fitting model is shown in red and the spectrum of variable A-type star RAT J210503.14+462745.5 is shown in black. The best fitting parameters are $T_{\rm eff} = 8138 \pm 36$ K, $\log g = 5.03 \pm 0.17$ and $Z = -0.60 \pm 0.07$. In the continuum regions between the Balmers lines it is possible to see the fit to unresolved metal lines. After $H\beta$ each Balmer line has been shifted upward by 0.5 flux units.

Name	g' [mag]	Period [min]	Temp. [K]	Gravity [dex]	Z [$Z_\odot$]
RAT J050751.28+343155.5	16.31	22.15	8528 ± 51	5.04 ± 0.29	−0.72 ± 0.32
RAT J065515.30+103859.0	15.92	33.87	6568 ± 53	3.69 ± 0.27	−0.66 ± 0.05
RAT J180250.62+004352.8	18.97	34.14	8525 ± 125	5.68 ± 0.54*	−4.06 ± 1.27
RAT J195306.30+184839.4	17.87	32.19	8066 ± 79	6.23 ± 0.27*	−0.80 ± 0.21
RAT J210503.14+462745.5	15.11	32.97	8138 ± 36	5.03 ± 0.17	−0.60 ± 0.07
RAT J210512.19+462038.3	14.98	31.82	8195 ± 27	4.97 ± 0.17	−0.41 ± 0.06
RAT J210514.75+461541.9	15.77	22.42	8586 ± 25	4.70 ± 0.16	−2.03 ± 0.35
RAT J234906.89+562440.4	18.06	22.73	8510 ± 65	5.05 ± 0.35	−0.63 ± 0.37

Table 5.2: Summary of the best fitting parameters when models are fit to the spectra of seven A and one F-type star. The period is taken from the a Lomb-Scargle periodogram of the light curve of the source. Metallicity, Z, is the abundance relative to solar metallicity. Uncertainties are calculated using a bootstrapping technique. Surface gravities marked with a * should not be relied upon as they are outside the model grid and therefore are extrapolated. They are also in the degenerate regime and therefore are probably not physical.

(Elkin et al., 2005). These sources can be identified owing to their optical variability and the chemical peculiarities in their spectra whose signature is an unusual metal abundance relative to solar metallicity. Specifically, they have over-abundances in rare earth metals (e.g. Kochukhov et al., 2009).

Alternatively, all the stars could be low amplitude δ Scuti stars with a pulsation period at the very short period end of the δ Scuti period distribution. δ Scuti stars typically have periods longer than 40 min but at least two examples (HD 13038 and V1366 Ori, Rodríguez et al., 2000; Amado et al., 2004) has a periods less than this. The F star is likely a short-period δ Scuti star as it has too low a temperature to be a roAp star but we note that the only δ Scuti stars with a pulsation period less than 40 min are rather unusual: one likely has strong metal lines (Martinez et al., 1999) while the other is a pre-main sequence star (Amado et al., 2004).

The derived metal abundances are all sub-solar though two of the sources are within 2.5σ of solar metallicity. Two sources, RAT J210514.75+461541.9 and RAT J180250.62+004352.8 (hereafter J1205+4615 and J1802, respectively), have a very low metal abundance of -2.03 ± 0.35 and -4.06 ± 1.27, respectively. As roAp stars have super-solar metallicities, it is unlikely that J1205+4615 and J1802 are roAp stars. However, δ Scuti stars typically have solar metallicities and it is also unlikely that this source is a δ Scuti variable.

One possibility is that this source is a very short period SX Phe star (as these sources have low metallicities) though I consider this unlikely as these sources have periods greater than 50 min.

The remaining sources have metallicities between -0.80 and -0.41. While it would seem unlikely these could be consistent with the high metallicities seen in roAp stars, we have not fit any super-solar metallicity models. In addition, our spectra are of low resolution and it is possible, even probable, that metal lines required for classification as a roAp star are missing as a result of the low resolution. However, a classification of these sources as very short period δ Scuti variables seem likely with the data available.

Medium–high resolution spectroscopic observation are planned in order to distinguish between there two scenarios: roAp stars show evidence of heavy metals in their spectra, whereas the δ Scuti stars show abundances similar to the Sun. With these observations it will be possible to more robustly determine the nature of these sources. I think that they are likely to be either roAp or δ Scuti stars, whatever the results found using high resolution spectra, they represent either the long or short period tail of their class.

5.3 SX Phoenicis and δ Scuti stars

This section describes stars similar to those described above but the stars discussed in this section are variable on periods that are longer than those in the previous section. The stars discussed here have periods more typical of δ Scuti stars and for this reason I differentiate between those discussed in the previous section and those discussed here. These longer period variables may either be δ Scuti stars or SX Phe stars which are similar classes of pulsating stars. Both classes pulsate with both radial and non radial modes with periods as short as 18 and 56 min for the δ Scuti and SX Phe stars, respectively. They differ in their metal abundances: δ Scutis have abundances typical of Population I stars while SX Phe stars have Population II abundances. In the first epoch of observations (INT1) a small number of sources which fit into these classes were detected (Ramsay et al., 2006). In this

section I describe a study of 31 such sources for which we derive distances and discuss their nature.

5.3.1 Identification

Both SX Phe and δ Scuti stars are blue pulsating sources. SX Phe stars have $(B-V)$ colours of 0.1–0.35 mag (Poretti et al., 2008) which equates to $(g'-r')$ ranging from -0.12–0.14. δ Scutis have very similar colours to the SX Phe stars(Rodríguez et al., 2000) and are therefore very difficult to distinguish from SX Phe stars. Many of the RATS fields lie at low Galactic latitudes where the extinction is high. We limit our search for these sources to regions of the sky where the extinction $E(B-V) < 0.18$ which equates to $E(g'-r') < 0.18$, for blue sources. This sets our colour search range to $-0.12 < (g'-r') < 0.4$ if we give some leeway to account for errors in measuring the colour.

The shortest period SX Phe has pulsations on a period of 56 min (BL Cam Rodriguez et al., 1990), to account for an estimated 10 per cent error in our period measure we set the minimum period search for at 51 min whilst the longer end is set by the sensitivity of the RATS data which becomes poor at periods longer than 90 min (see §3.2.2 and Fig. 3.8).

Since many sources fitted description of having periods from 51–90 min and $-0.12 < (g'-r') < 0.4$, we manually inspected these and removed sources which showed signs of obvious systematic effects (such as several sources having the same period and phase in the same field), had large gaps in the data or where the periodic signal was weak. This left 31 sources with periods ranging from 51 to 83 min, brightnesses from $15.9 < g' < 20.8$ and full-amplitudes from 0.05–0.65 mag. The properties of these sources is shown in Table 5.3, their light curves in Figures 5.2–5.4 and they are shown in a colour-magnitude diagram as crosses in Fig. 5.5.

Source name	l [J2000]	b [J2000]	g' [mag]	$(g'-r')$ [mag]	Period [min]	Amp. [mag]
RAT J000114.7+534305.4	115.46	-8.42	17.8	-0.12	64.3	0.50
RAT J000134.8+535142.2	115.54	-8.29	17.0	0.19	73.5	0.07
RAT J000147.5+532318.7	115.48	-8.76	16.8	0.35	69.6	0.45
RAT J030556.8-003616.2	179.16	-48.23	20.3	-0.08	82.9	0.28
RAT J050351.4+350802.1	169.90	-3.83	18.4	0.30	62.9	0.14
RAT J065521.2+104158.9	203.82	5.72	15.9	0.12	60.9	0.13
RAT J065541.8+104421.5	203.82	5.81	19.3	0.30	56.0	0.10
RAT J120232.2-242917.4	288.96	37.05	20.2	0.04	55.7	0.33
RAT J120709.2-225449.5	289.81	38.82	17.8	0.30	74.7	0.24
RAT J120902.4-231139.0	290.43	38.65	17.2	0.39	72.3	0.17
RAT J135646.3+225440.4	20.61	74.62	18.2	-0.09	53.8	0.13
RAT J135912.9+233655.3	23.76	74.30	17.9	0.03	63.9	0.07
RAT J155955.4-254320.2	347.69	20.35	17.3	0.37	60.8	0.08
RAT J160103.5-254244.6	347.89	20.17	17.6	0.36	58.7	0.08
RAT J175816.2+281752.8	53.97	23.35	19.1	0.04	54.4	0.12
RAT J175836.5+280913.0	53.85	23.23	18.1	0.05	66.1	0.07
RAT J175932.1+011940.4	28.14	12.14	18.2	0.36	74.7	0.50
RAT J180331.0+020840.2	29.34	11.63	17.8	-0.09	72.5	0.65
RAT J180416.2+020832.4	29.43	11.47	18.1	0.23	82.9	0.65
RAT J181727.9+063401.0	34.97	10.53	18.3	0.22	76.9	0.10
RAT J181736.2+062426.0	34.84	10.42	18.6	0.22	60.8	0.06
RAT J181753.2+063149.5	34.98	10.41	18.5	0.34	59.6	0.08
RAT J181816.0+073043.0	35.92	10.77	18.5	0.24	53.0	0.50
RAT J182250.6+075436.8	36.79	9.93	19.1	0.31	64.5	0.13
RAT J182347.7+075345.5	36.88	9.71	19.9	0.24	61.2	0.26
RAT J195235.3+184354.8	56.56	-4.34	18.0	0.38	63.2	0.05
RAT J200210.0+184307.3	57.72	-6.29	18.2	0.39	74.5	0.07
RAT J220915.4+553438.5	101.37	-0.35	15.8	0.03	51.6	0.07
RAT J230507.9+341723.4	99.14	-23.62	20.8	0.25	75.3	0.21
RAT J233907.3+570802.3	113.21	-4.36	18.4	0.18	67.6	0.15
RAT J234635.6+562323.7	114.00	-5.35	15.8	0.38	68.6	0.18

Table 5.3: A summary of the details of the blue pulsators obtained from the RATS observations. The period determined from a Lomb-Scargle periodogram and the amplitude is the full-amplitude of the best fitting sine curve when using least squares fitting on the period found from the Lomb-Scargle periodogram. The source name is in the format RAT JHHMMSS.s±DDMMSS.s where the coordinates use the J2000 epoch and equinox.

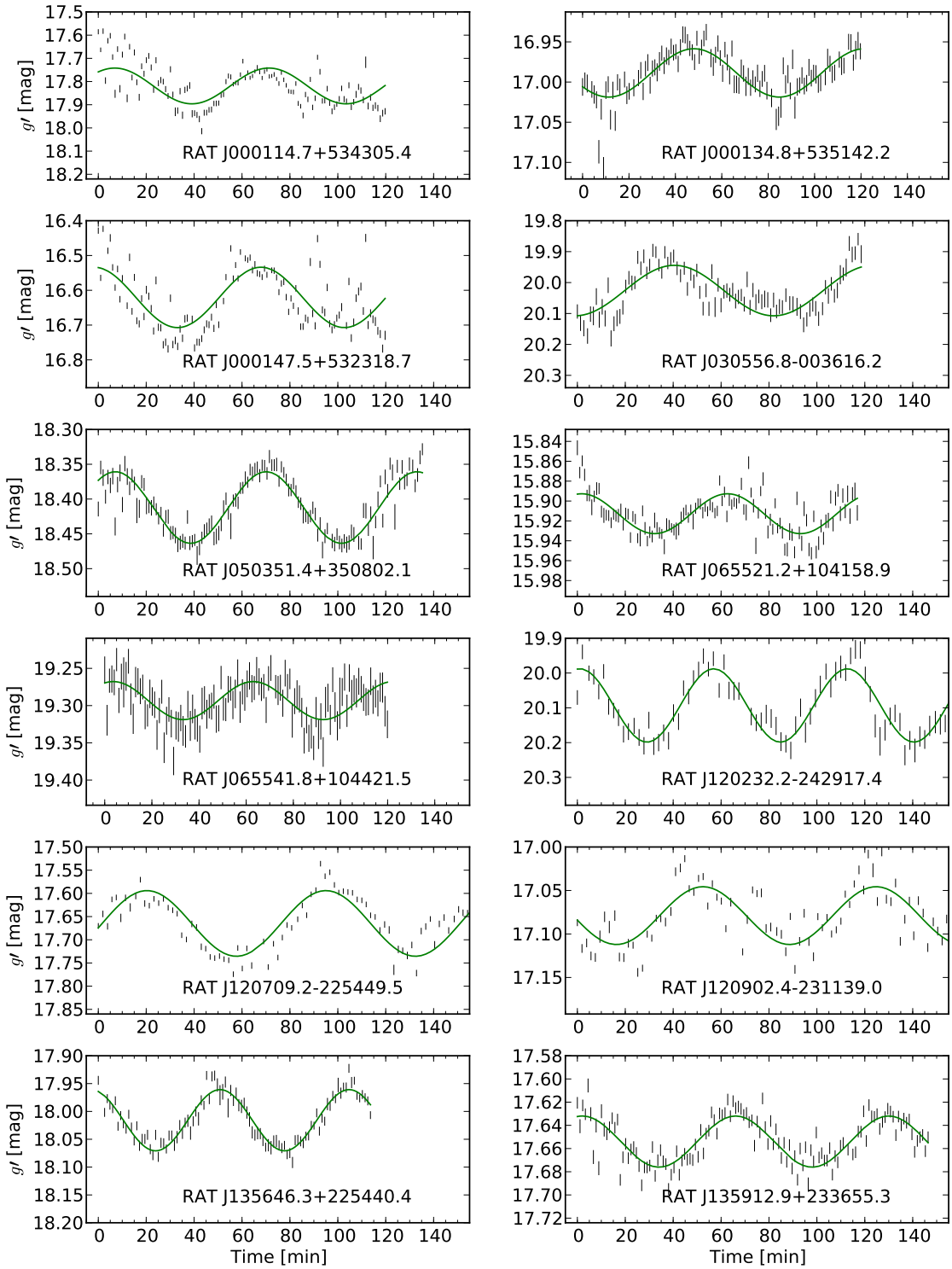

Figure 5.2: Light curves of blue pulsators. The green curve is the best fitting sinsoid.

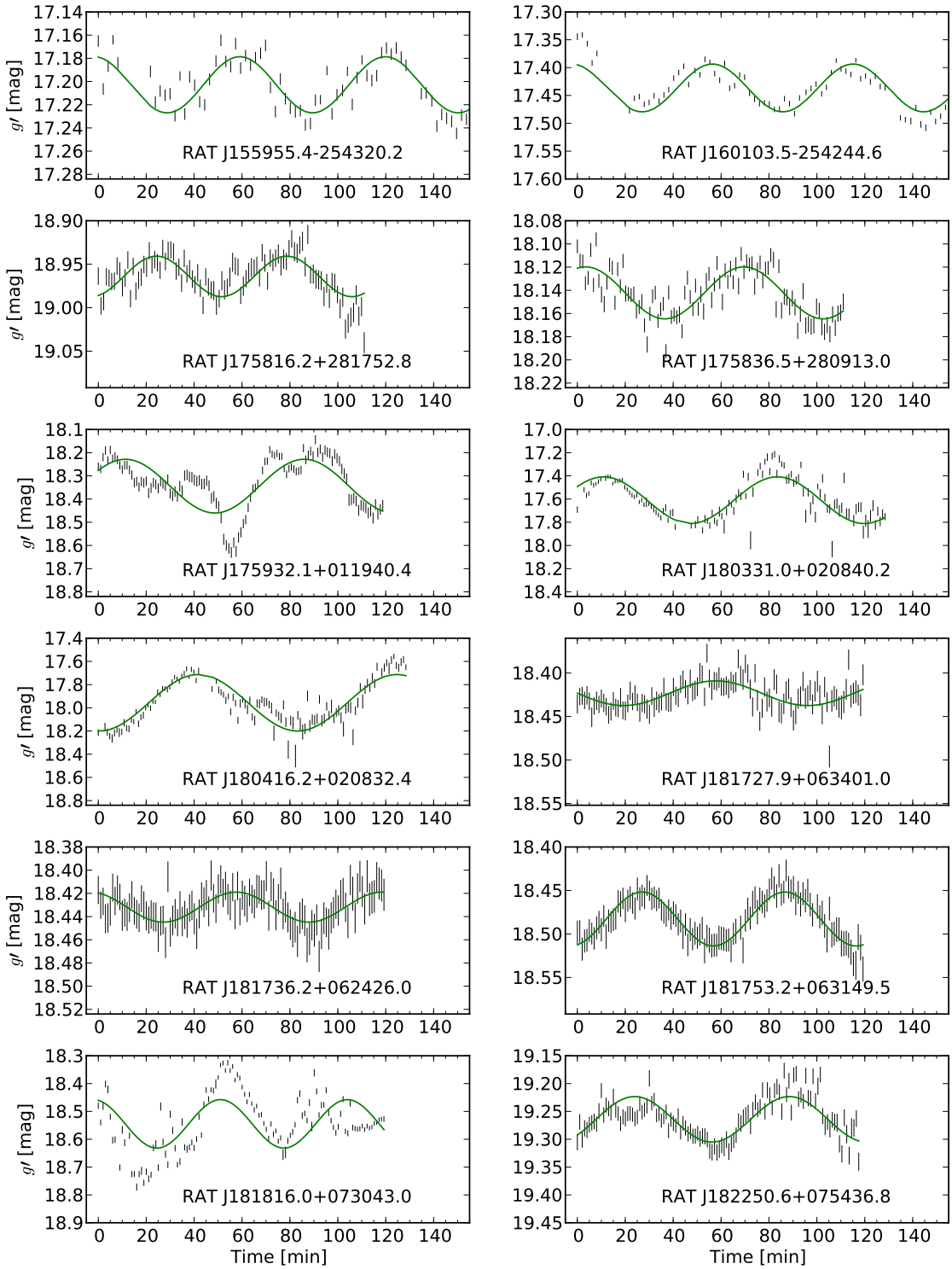

Figure 5.3: Light curves of blue pulsators.

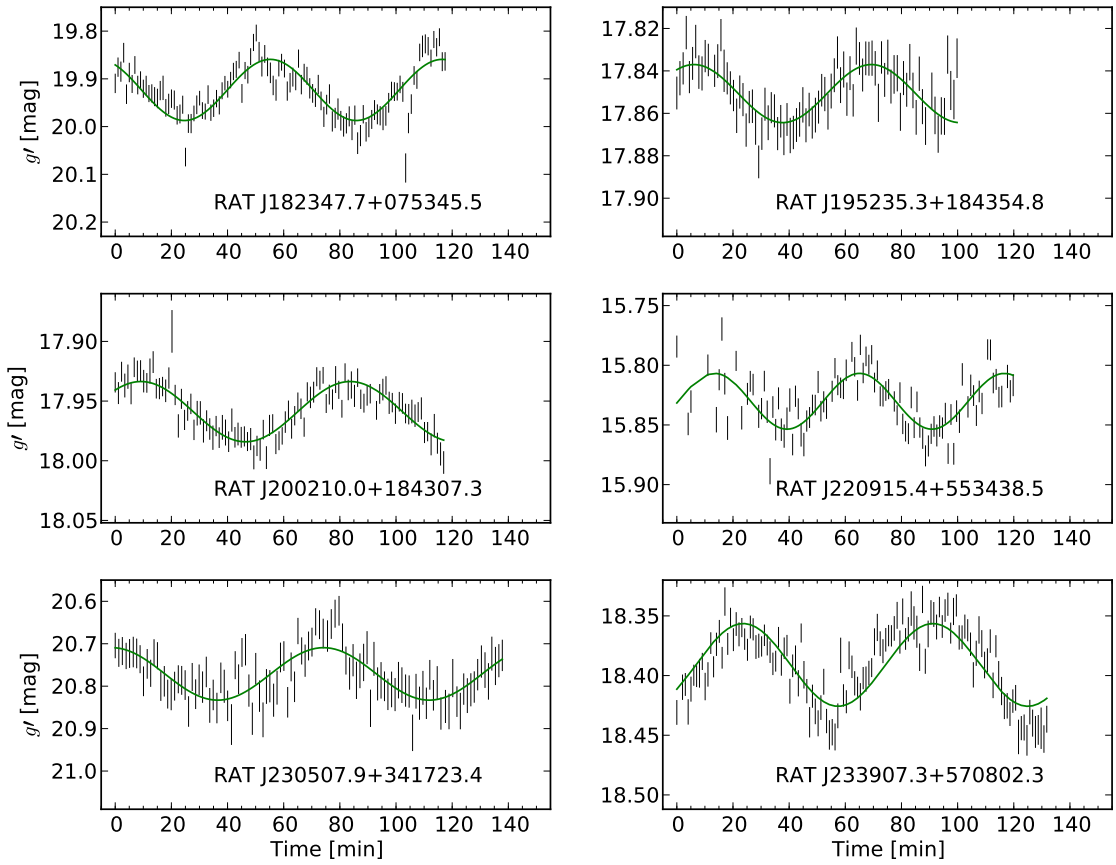

Figure 5.4: Light curves of blue pulsators.

5.3.2 Distances

The distance to SX Phe and δ Scuti stars can be computed using equ. 4 in McNamara (1997) where he derives a semi-empirical period-luminosity relation of

$$\langle M_V \rangle = -3.725 \log P - 1.933 \tag{5.1}$$

where P is the period in days and M_V the absolute magnitude in the V filter. To convert our g' magnitudes to V we use

$$V = g' - 0.59 \times (g' - r') - 0.01 \tag{5.2}$$

taken from Jester et al. (2005). Using the Schlegel et al. (1998) dust maps we determined the extinction to the edge of the Galaxy and calculate the optical extinction in the V band, A_V, using Equ.4.1.

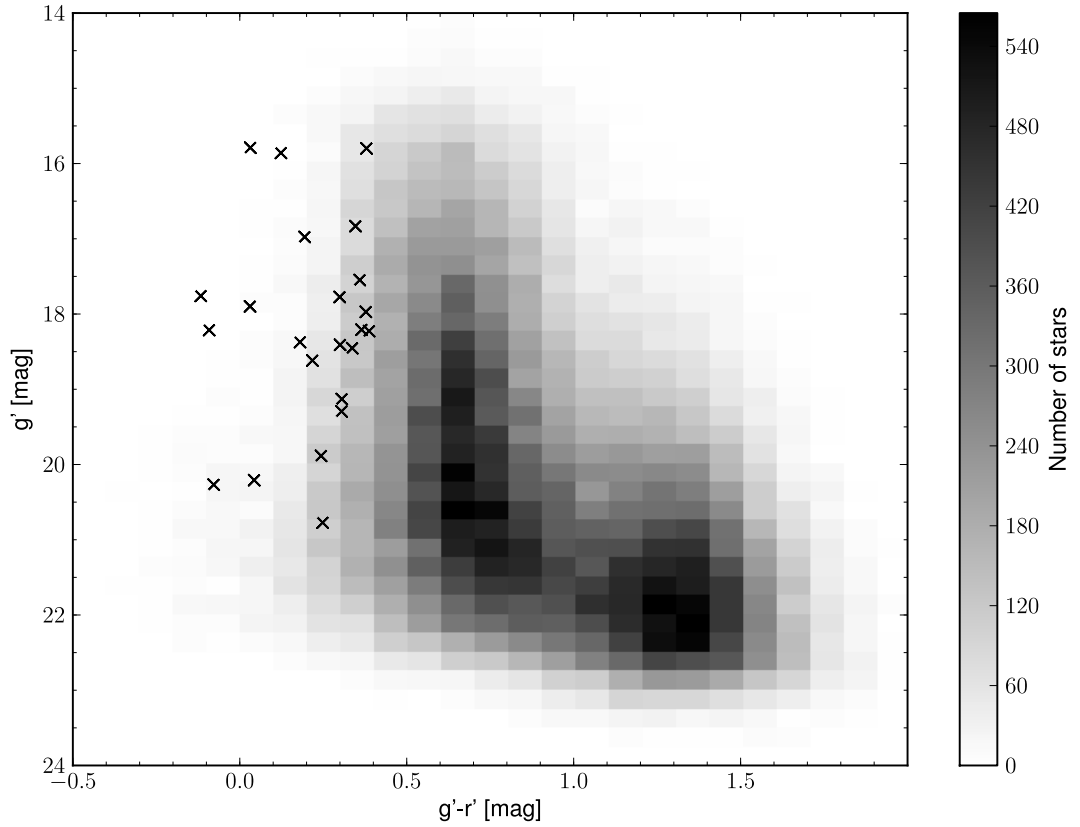

Figure 5.5: A colour-magnitude diagram showing all the stars in the RATS data which have absorption in the V band, $A_V < 0.6$. The blue pulsators discussed shown in Table 5.3 plotted as crosses.

The distance is calculated using the equation

$$V_{\rm corr} = M_V + 5(\log d - 1) \tag{5.3}$$

where $V_{\rm corr}$ is the V magnitude corrected for extinction, M_V is the absolute magnitude and d is the distance in parsec. The distance to the star and distance from the Galactic plane to the star are given in Table 5.4. The error on the period is roughly 10 per cent and the error on the g' band magnitude is roughly 0.1 mag for sources brighter than $g' = 20$ and 0.2 mag for sources fainter than this. We estimate that the error on the distance will be of order 10–20 per cent. It is possible that for a number of sources we measure half the true pulsation period, in this case the distance to the source would be underestimated by a factor of ~ 1.7. Similarly, if the extinction is less than the extinction to the edge of the Galaxy then we would be underestimating the distances.

The distances to these sources vary from 0.6–30 kpc while the median distance is 7.0 kpc. We also find that there is a large range in z, where z is the height above the Galactic equator. The values of z range from 200 pc to over 20 kpc with the median being 1.4 kpc. This is, neatly, twice the scale height of the thick disc of the Galaxy (de Jong et al., 2010). The three sources furthest away from us (RAT J030556.8-003616.2, hereafter J0305; RAT J120232.2-242917.4; and RAT J230507.9341723.4) are at distances well beyond the excepted limits of the spiral structure of the Milky Way (21.1, 30.0 and 32.1 kpc, for the three sources, respectively, while the scale hight of the thin disc is around 100 pc, Kong & Zhu 2008) and their high Galactic latitude (all 10 kpc above the galactic plane) place these sources deep into the Galactic halo.

J0305 is in a particularly surprising location, being at a Galactic longitude very close the Galactic anti-centre ($l = 179.16$). We wished to confirm the period measured during the initial RATS observations. To do this a colleague – Pasi Hakala – obtained optical photometry using the ALFOSC instrument on the Nordic Optical Telescope on 2010 December 31. We windowed the CCD and observed without a filter in order to maximize the signal-to-noise. The total observation lasted 3.8 h, the resulting light curve is shown in Fig. 5.6. The periodogram has a peak at a period of 90 min which is consistent with the period we mea-

Source name	Distance [kpc]	Height [kpc]
RAT J000114.7+534305.4	6.0	-0.9
RAT J000134.8+535142.2	4.2	-0.6
RAT J000147.5+532318.7	3.4	-0.5
RAT J030556.8-003616.2	30.0	-22.4
RAT J050351.4+350802.1	3.4	-0.2
RAT J065521.2+104158.9	2.7	0.3
RAT J065541.8+104421.5	11.6	1.2
RAT J120232.2-242917.4	21.1	12.8
RAT J120709.2-225449.5	8.2	5.2
RAT J120902.4-231139.0	5.8	3.6
RAT J135646.3+225440.4	9.0	8.7
RAT J135912.9+233655.3	8.7	8.3
RAT J155955.4-254320.2	5.2	1.8
RAT J160103.5-254244.6	5.7	2.0
RAT J175816.2+281752.8	12.7	5.0
RAT J175836.5+280913.0	9.2	3.6
RAT J175932.1+011940.4	6.5	1.4
RAT J180331.0+020840.2	7.0	1.4
RAT J180416.2+020832.4	8.2	1.6
RAT J181727.9+063401.0	8.6	1.6
RAT J181736.2+062426.0	8.2	1.5
RAT J181753.2+063149.5	7.4	1.3
RAT J181816.0+073043.0	7.1	1.3
RAT J182250.6+075436.8	10.8	1.9
RAT J182347.7+075345.5	15.7	2.6
RAT J195235.3+184354.8	4.9	-0.4
RAT J200210.0+184307.3	5.1	-0.6
RAT J220915.4+553438.5	0.6	0.0
RAT J230507.9+341723.4	32.1	-12.8
RAT J233907.3+570802.3	4.1	-0.3
RAT J234635.6+562323.7	1.8	-0.2

Table 5.4: The distance to each source, derived from the apparent magnitude and the pulsation period, are shown in this table. The height refers to the height above the Galactic plane (i.e. height, $z = b \sin d$, where b is Galactic latitude and d is the distance to the source).

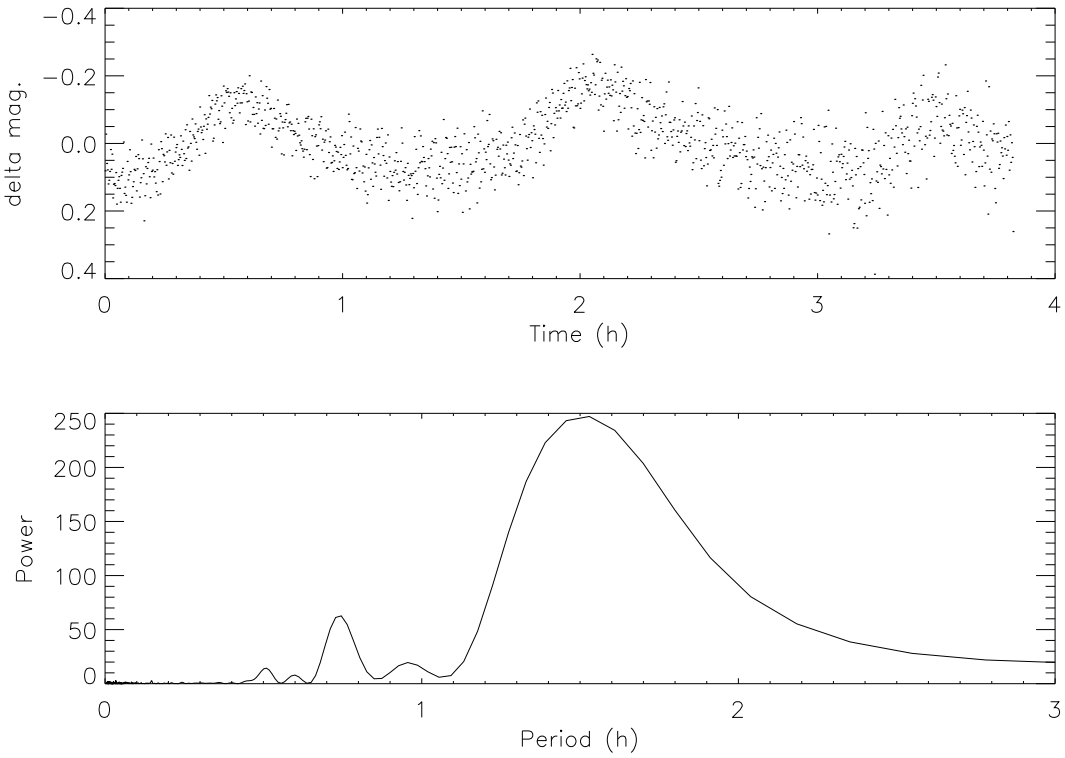

Figure 5.6: J0305 was observed in December 2010 using the ALFOSC instrument on the NOT. The top panel shows a light curve of those observations while the bottom is a Lomb-Scargle periodogram of the light curve. The periodogram has a peak at 90 min which represents the dominant pulsation period we detected from the source.

sured during wide field observations (where I found a period of 82.9) if we assume a ~10 per cent error on these periods. If we take this longer period it implies that the source is at a distance of 31.9 kpc rather than the 30.0 kpc figure we previously found.

5.3.3 Spectroscopic observations

We were able to observe six of the blue pulsators using the NOT, WHT and SAAO 1.9-m telescopes (see §4.2 for a description of the spectroscopic instruments mounted on these telescopes, which e used). In addition we obtained a spectrum of one source (J0305) from the Sloan Digital Sky Survey archive. In total we have spectra of seven sources which were extracted and reduced using the techniques described in §4.2.6. The spectra are shown in Fig. 5.7 and details of the observations are given in Table 5.5.

Using the methods described in §5.1, we fit these spectra using ATLAS9 models (Castelli

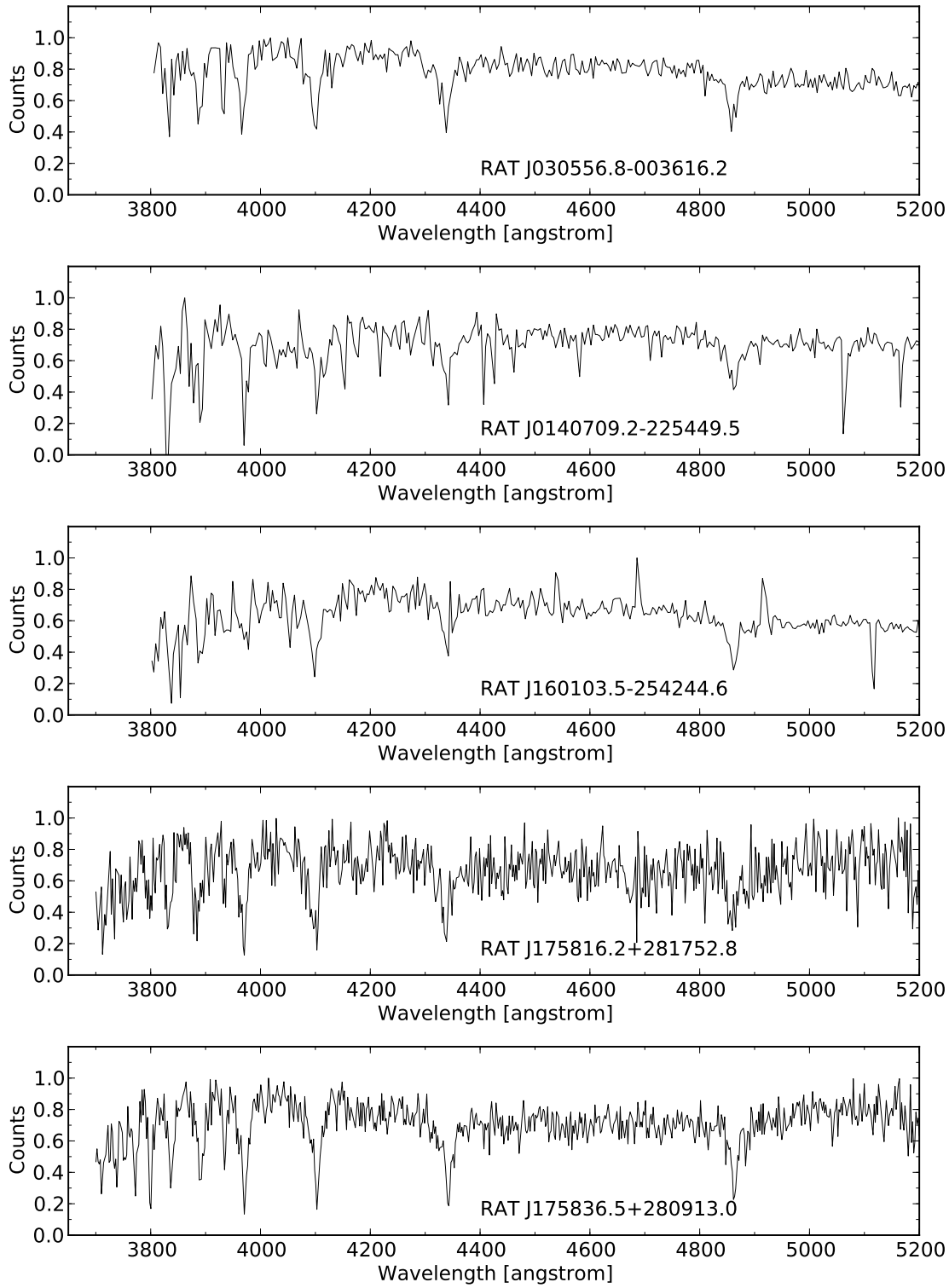

Figure 5.7: The spectra of seven candidate SX Phe stars (details given shown in Table 5.5). Two are these sources have low signal to noise and are therefore useful only in classifying the sources as A-type stars. Five source have spectra with sufficient signal-to-noise for fitting purposes.

Source name	Telescope	$T_{\rm eff}$ [K]	Metallicity [$Z_\odot$]
RAT J030556.8-003616.2	SDSS	7259 ± 91	−0.9 ± 0.7
RAT J120709.2-225449.5	SAAO	7415 ± 130	−4.4 ± 1.0
RAT J135646.3+225440.4	NOT	–	–
RAT J135912.9+233655.3	NOT	–	–
RAT J160103.5-254244.6	SAAO	7341 ± 102	−1.1 ± 0.96
RAT J175816.2+281752.8	WHT	7763 ± 184	−0.6 ± 1.3
RAT J175836.5+280913.0	WHT	7815 ± 79	−0.3 ± 0.2

Table 5.5: The best-fitting effective temperature,surface gravity and metallicity of seven candidate SX Phe stars are shown here. The telescope column key is: SDSS – taken from Sloan Digital Sky Survey archive data; SAAO – Cassegrain spectrograph on the SAAO 1.9-m telescope; NOT – ALFOSC on the Nordic Optical Telescope; WHT – ISIS instrument on the Willian Herschel Telescope. Sources which have spectra with a signal-to-noise high enough to allow fitting with model spectra are have effective temperatures and metallicities shown. The metallicity is relative to solar.

& Kurucz, 2004). The effective temperature of each source was determined by fitting model spectra to the Balmer lines of the source (see Fig. 5.8 for an example fit). Our model spectra which we fit ranged from 65500–8000 K. As there are no gravity sensitive features in the spectra (Napiwotzki priv. comm.) we set log g at 4.0 which is typical for SX Phe and δ Scuti stars (McNamara, 1997).

The resolution of the spectra is too low to see individual metal lines but it is possible to get an estimate of the overall abundance by fitting model spectra with different metallicities to regions of the spectra which contain a large number of metal lines. The low signal-to-noise in a number of our spectra causes us to be able to use this technique in only five of our spectra. The metallicities of our models ranged from −3.0 to 0.0 dex in steps of 0.5. We selected the regions 4160–4260 Å, 4435–4635 Å, 4960–5105Å and 5105–5455 Å. In these regions the dominant species is FeI, therefore our derived metallicities is a proxy for iron abundance. These metallicities are given in Table 5.5.

Our sources range in effective temperature from 7000-8000 K. The metallicities are less well constrained owing to the difficulty in fitting metal lines in low resolution spectra. Each fit is less than solar metallicity though perhaps we should not draw too many conclusions for this as we did not use any super-solar metallicity models in the fitting process. One

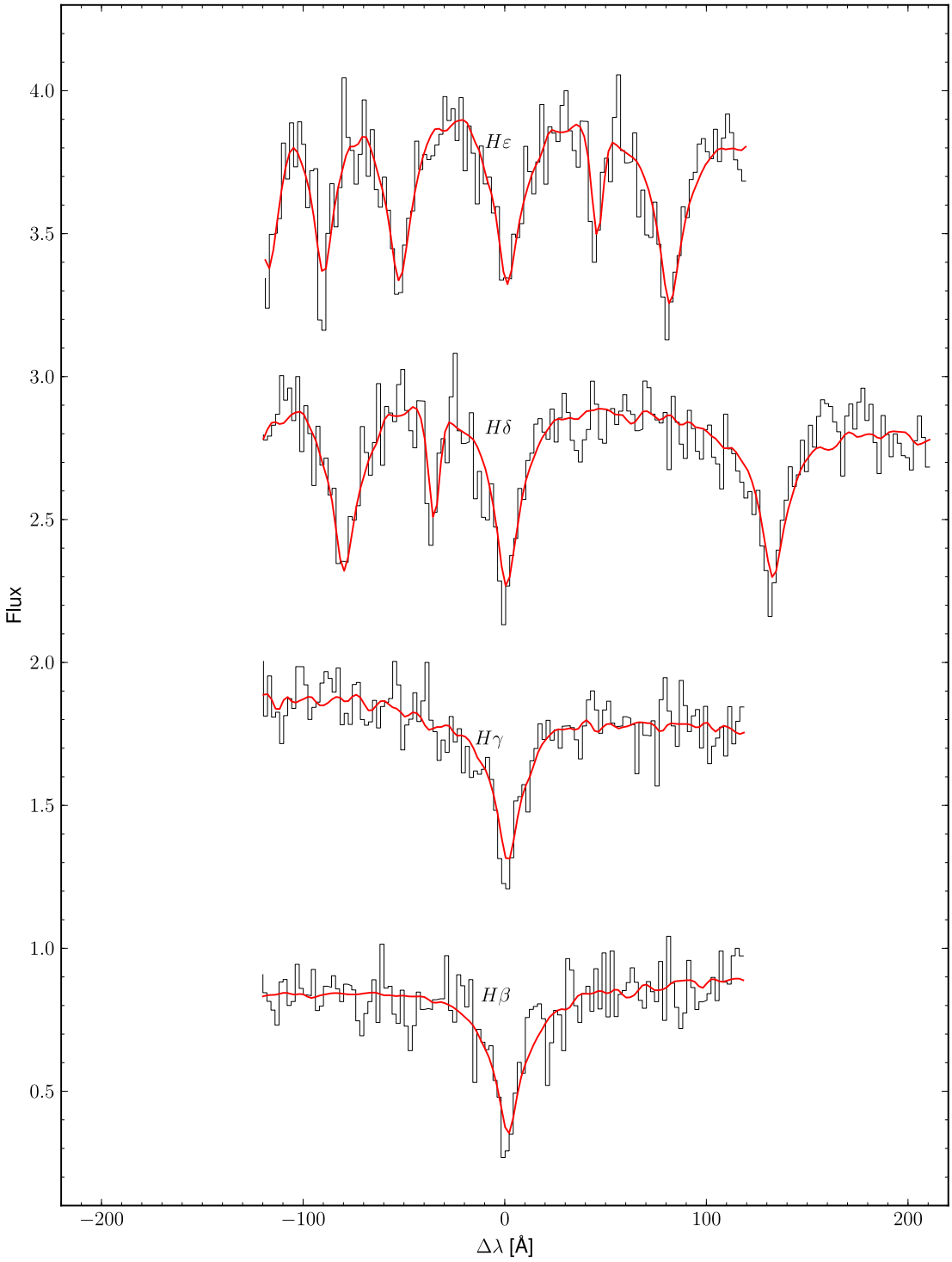

Figure 5.8: An example of a model atmosphere fitted to a spectrum of one of the blue pulsators. This spectrum is of RAT J175836.5+280913.0 and was observed using the WHT telescope. The spectrum has been normalised to the continuum and the best fitting model atmosphere has $T_{\rm eff}$ = 7815 ± 79 K, and $Z_{\odot}$ = −0.3 ± 0.2.

source has significantly lower metallicities than the Sun, RAT J120709.2-225449.5 (hereafter J1207), which has a metallicity of $Z = -4.4 \pm 1.0$ dex with respect to the solar metallicity.

5.3.4 The nature of our sources

We are convinced that the sources presented in this section are stellar pulsators. Three classes of blue pulsators have periods consistent with the periods we observe; SX Phe stars, δ Scutis and sub-dwarf B (sdB) stars. The fitted temperatures rule out the possibility that these sources are sdB stars as these have temperatures typically in the range 20000–35000 K (Pereira & Jeffery, 2008). The low metallicities in one of our sources, J1207, indicate that it is likely to be an SX Phe pulsator as these are known to have low metallicities, whereas δ Scutis have solar metalicities. The uncertainties on the metalicities derived for the other three sources do not allow us to distinguish whether they are SX Phe or δ Scuti stars.

There are 131 field δ Scuti and 20 SX Phe stars in the General Catalogue of Variable Stars (Samus et al., 2009). Our discovery of 31 new blue pulsators represents a significant increase on these numbers although we are not able to distinguish the class of the majority of them. The SX Phe star with the shortest period is BL Cam which has a period of 56.3 min. Six of our sources have periods lower than this. If they were to be identified through higher resolution spectra as SX Phe source they would represent the shortest known period systems in their class.

Most of our sources are many kpc distant and are also far from the Galactic plane which places them in the halo, indeed at distances of over 30 kpc several sources are at the very limit of the Galaxy. In principle, they can be used to trace Galactic structure such as streams and merger remnants (e.g. Vivas et al., 2001, have been able to trace a merger remnant using RR Lyr stars). J0305 which lies over 30 kpc away in the direction of the Galactic anti-centre may well be associated with a sub-structure in the halo and sources like this could be used to map this structure. On the other hand, it could have been ejected from the galactic plane and be in the process of leaving our Galaxy.

Wide-field, high cadence variability surveys are well suited to the discovery of short period pulsators. We have identified 31 blue pulsators periods from 51–83 min. Future surveys such as LSST can expect to discover many more. We have found sources both in the disc and in the Galactic halo meaning that they can be used to trace the sub-structure of both these regimes. This work has been performed using RR Lyr type variables (e.g. Kinemuchi et al., 2006), our shorter period pulsators provide another method with which to map these structures without the longer observation baseline needed to observe periodicities in RR Lyr stars.

Determining conclusively the nature of these 31 sources will require median-high resolution spectra in order to measure metal lines present in the spectra. This will also provide a method to test metallicity-period relations (e.g. McNamara, 1997).

5.4 Pulsating white dwarfs

DAV or ZZ Ceti stars are white dwarfs with hydrogen atmospheres that vary on periods from 100 s to 25 min (Fontaine & Brassard, 2008) and have effective temperatures of 11000–13000 K (for a more detailed description see §6.2). We have discovered two such sources which appear to fit this description, RAT J073919.05+235239.9 (hereafter J0739) and RAT J205902.93+453735.9. RAT J205902.93+453735.9 is subject to an in depth discussion in §6.2; we have obtained multi-wavelength observations of this source which hint that it may have an unusual nature. In this section I will discuss J0739 which we have identified much more recently.

J0739 is a $g' = 0.8$ mag source which varies on a period of 14.7 min with an amplitude of 0.07 mag (the light curve is shown in Fig. 4.2). As it is also significantly blue ($g' - r' = 0.06$), it was a prime candidate for follow-up spectroscopy. However, because of the star's faintness we required the use of an 8-m class telescope. We were successful in obtaining time on the Gemini-South telescope using the GMOS instrument (see §4.2.5 for a description of the instrument). J0739 was observed for 600 s on 2011 01 11 using the B600 grism which

gives a wavelength coverage of 2760 Å and used a 1.0″ slit. The spectrum was extracted in the manner described in §4.2.6 (see Fig. 4.11 in the previous Chapter for the reduced spectrum of the source).

I fit the spectrum of J0739 with a grid of DA white dwarf model atmospheres with effective temperatures from 6000-100000 K and and log g from 5.5–9.5 calculated by Koester et al. (2001) using modified Stark broadening profiles in the Balmer lines which were calculated by (Tremblay & Bergeron, 2009). I included four Balmer lines in the fit – $H\beta$, $H\gamma$, $H\delta$ and $H\varepsilon$. $H\alpha$ is not within the spectral range of the spectrum and the Balmer lines past $H\varepsilon$ are not of a high enough signal-to-noise to be included in the fit. The best fitting model is shown in Fig. 5.9 over-plotted on the Balmer lines of J0305. The model has a best fitting effective temperature of 9724 ± 94 a log g of 7.25 ± 0.3.

A temperature of 9724 ± 94 K is less than that of the coolest known DAV pulsator which has a temperature of around 11000 K – both BPM 24754 and G30–20 have temperature of 11070 K (Fontaine & Brassard, 2008). The besting fitting surface gravity of 7.25 ± 0.3 seen J0739 is also lower than any other DAV white dwarf (a log g of 8 is typical, the lowest is 7.82, Fontaine & Brassard 2008). The red edge of the DAV instability strip is poorly defined (Fontaine & Brassard, 2008). In fig. 9 of Fontaine & Brassard (2008) (which is reproduced as Fig. 1.11) is shown a $logg/T_{\rm eff}$ plot, the lowest surface gravity plotted is at $logg$ = 7.5. However, if we were to extend this strip down to $logg$ = 7.25, J0739 would appear close to the, albeit poorly defined, unstable parameter regime.

J0739 is a white dwarf which exhibit periodic modulations which are very likely caused by pulsations. The low surface gravity and effective temperature are unusual in DAV white dwarfs and if confirmed will help to increase our understanding of the DAV instability strip and to extend the parameter space in which we can model these sources

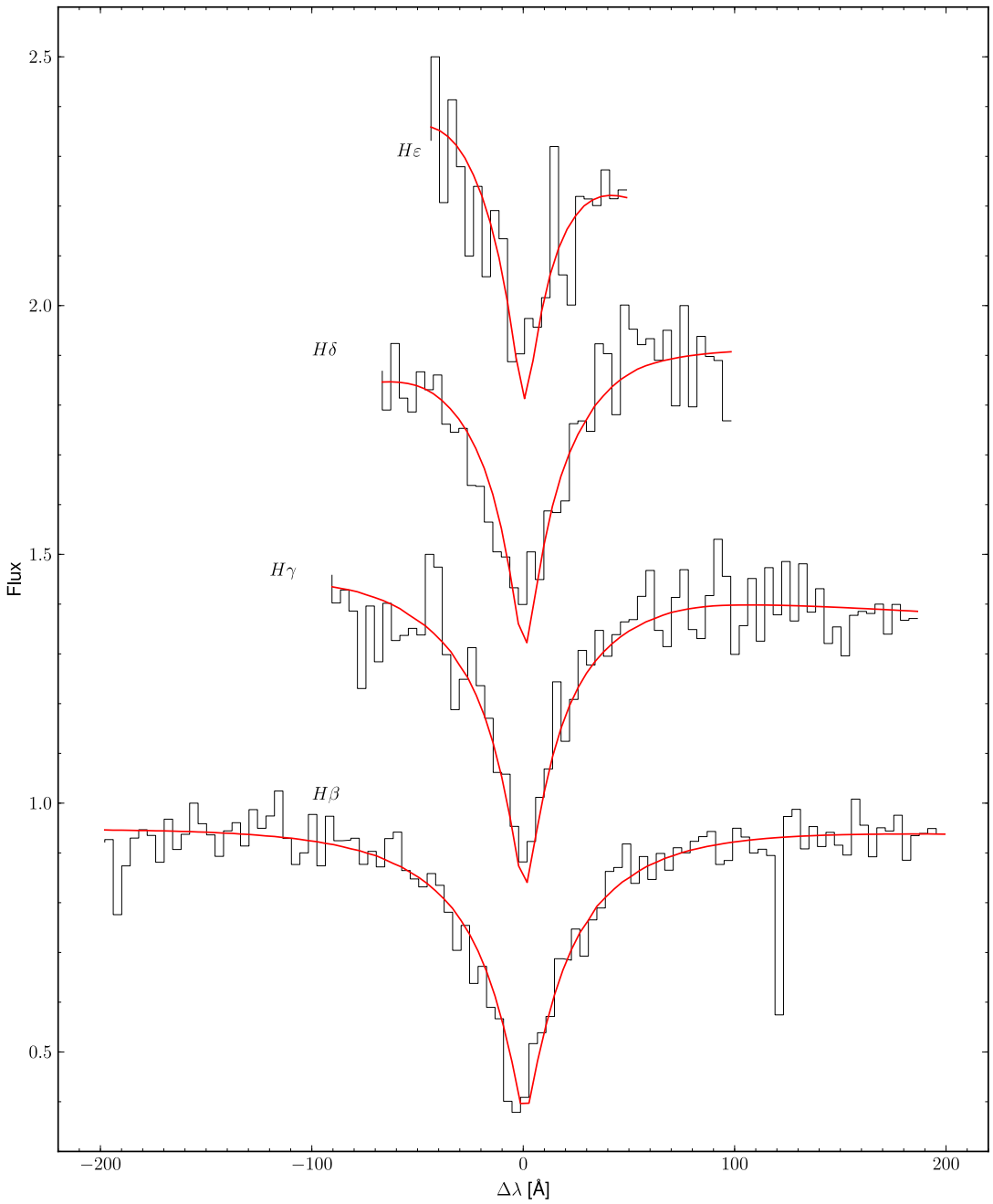

Figure 5.9: The Balmer lines of J0739 in red with the best fitting DA white dwarf model atmosphere. The best fitting model has a temperature of 9724 ± 94 K and a surface gravity of 7.25 ± 0.3.

5.5 Summary

In this Chapter I have looked at three different groups of pulsating stars: short period main sequence stars, longer period pulsators and degenerate pulsators. In all three groups I find interesting and unexpected results. The short period A-type stars are likely to be a sub-set of a larger class of pulsating variable: either they long period roAp stars or short period δ Scutis. They present an interesting question: why has this subset of pulsators never been noticed before. One possibility is that no one has been looking in the right place before. RATS samples a relatively unexplored parameter space which leads unexpected discoveries such as this. They are therefore likely to present an interesting proposition to pulsation modellers who will need to extend their models to this new regime.

A number of the members of the second class of pulsators discussed here – the SX Phe/δ Scuti stars – seem to be at very large distances from the region of the Galaxy usually associated with objects as young as A-type stars. The discovery of these sources can help us to understand the structure of the Galaxy better. If some of these sources were born in the halo then they will likely have left some evidence of this in the form of other stars in their stellar neighbourhood. Further study of these objects and sources around them will allow for the study of Galactic steam and even mergers of dwarf galaxies.

The final section discusses the DAV white dwarf J0739. At first glance this appeared to be a rather standard DAV. However, further investigation revealed it to be rather different to the other members of the DAV class – the effective temperature and surface gravity are both much lower than that seem in any other DAVs. Compared to other DAV stars, J0739 has very low temperature and surface gravity. This source allows us to test the theoretical red edge of the DAV instability strip and also to extend the range of surface gravities where pulsations have been seen.

I think the sources contained in this Chapter highlight how sources that would initially appear to be well understood, can provide significantly interesting results if one spends the time to look carefully at the data available. In the next Chapter I will discuss two stars. These sources were both found as short-period blue variables in RATS data and detailed

follow-up observations revealed them to be of a rather different nature to what I initially expected.

Chapter 6

A tale of two variable stars

> If you do not expect the unexpected, you will not find it; for it is hard to be sought out, and difficult.
>
> *Heraclitus of Ephesus, 535–475 BC*

In the previous Chapter, I discussed some of the different types of variable sources present in the RATS data. In this Chapter I describe in detail two of these sources: RAT J1953+1859, which is a dwarf nova discovered through high amplitude quasi-periodic oscillations in quiescence; and RAT J205902.93+453735.9, a pulsating hydrogen-rich white dwarf which appears to have a hot close companion.

6.1 RAT J1953+1859: a new dwarf nova

In this section I discuss RAT J1953+1859 which was found in the RATS data and for which we obtained follow-up spectroscopy and photometry on various telescopes.

6.1.1 INT photometry

RAT J1953+1859 was first observed on 2005 June 30 a part of the RATS INT2 campaign as a $g' = 20.0$ mag source. These observations consisted of 90 exposures of 30 s; the series of observations covered 140 min. The light curve and a power spectrum resultant from a Fast Fourier Transform are shown in Fig. 6.1, as can been seen from the plot, the source has a dominant period at 20.0 min with an amplitude of 0.24 mag. There are also prominent peaks at 15.5 and 9.2 min. The light curve was pre-whitened on a period of 20.0 min and the peaks at 15.5 and 9.2 min were still present and therefore are unlikely to be due to the window function. I folded the data on each of the 3 main periods in the power spectrum but found that the source is not strictly periodic on any of the periods. I deduce from this that the variability is likely due to quasi-periodic oscillations (QPOs). As this source was blue in colour ($g' - r' = -0.07$), it was selected as a candidate for follow-up observations (cf Chapter 3).

6.1.2 Follow-up photometry

I made photometric observations using the Andalucia Faint Object Spectrograph and Camera (ALFOSC) on the Nordic Optical Telescope (NOT) on 2008 September 28. As shown in Fig 6.2, it was immediately clear that RAT J1953+1859 was significantly brighter than in the discovery data. Observations were obtained in white light but from comparisons with the INT images I estimate RAT J1953+1859 was ~4 mag brighter than in the discovery data which is a flux increase typical of a dwarf nova outburst (e.g. VW Hyi; Woudt et al., 2010). A series of 15 s unfiltered exposures of RAT J1953+1859 were obtained using a windowed CCD which reduced the read-out time to just 5 s.

The light curve (shown in the top left panel for Fig 6.3) shows evidence for a 0.4 mag modulation which repeats on a ~90 min period though this cannot be claimed to be a periodic oscillation as the observation length was only 140 min. In the Fast Fourier Transform of the light curve (shown in the lower left panel of Fig 6.3) there is evidence for power at a period of ~46 min. The dominant 90 min period was removed from the data and the

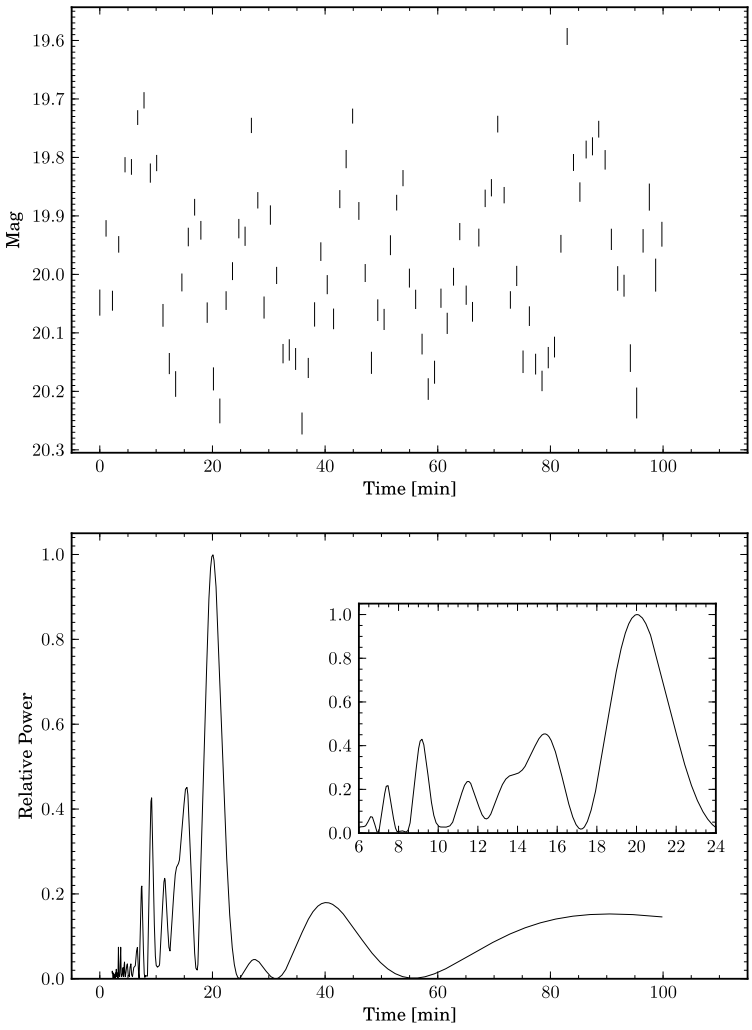

Figure 6.1: The light curve (upper plot) and power spectrum (lower plot) of RAT J1953+1859. The insert in the lower plot zooms in on the peak periods in the power spectrum.

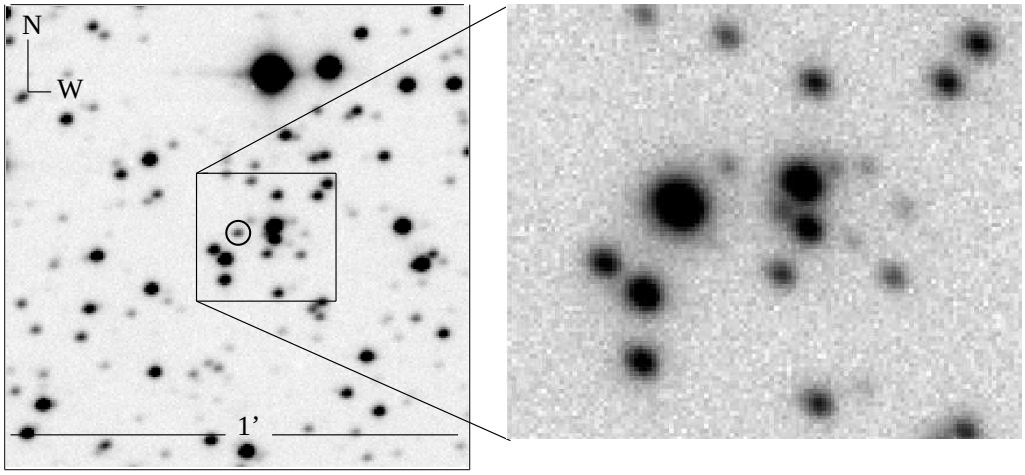

Figure 6.2: The left-hand panel is a white light image of a portion of the field containing RAT J1953+1859 made using the WFC on the INT. RAT J1953+1859 is circled in this image. The right panel is an image taken at the NOT using ALFOSC. RAT J1953+1859 is approximately 4 mag brighter in these observations compared with the INT data.

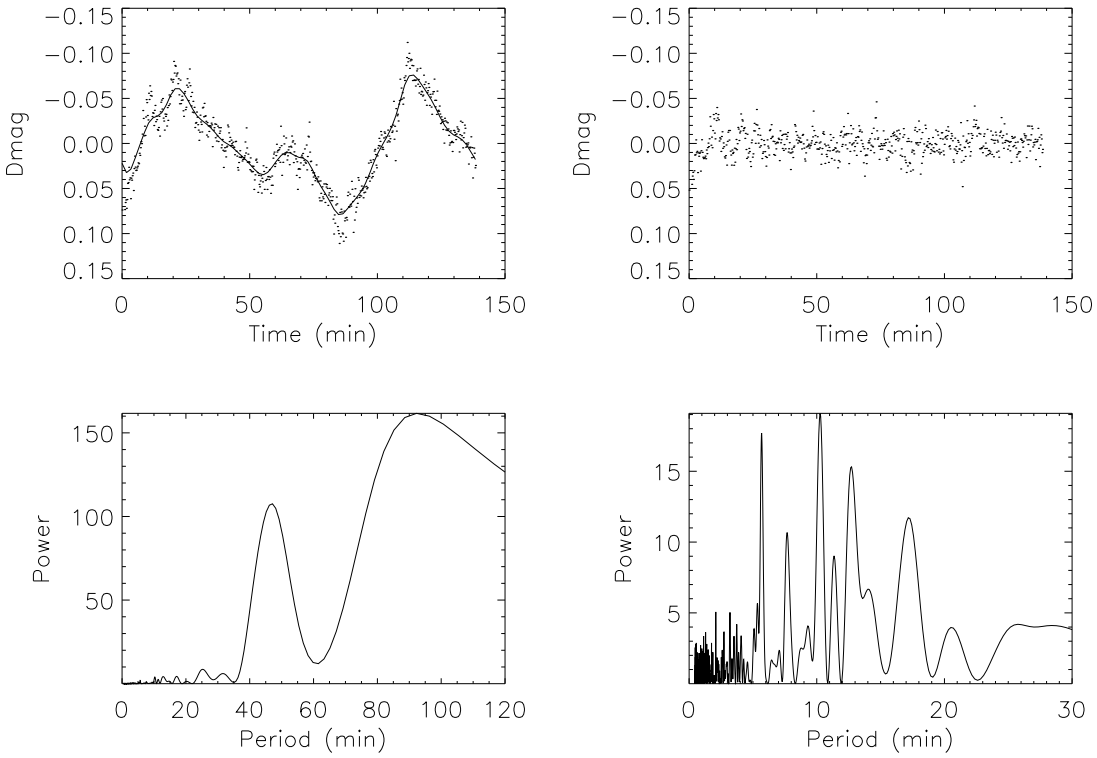

Figure 6.3: Photometric observations of RAT J1953+1859 made using the ALFOSC instrument on the NOT. The top left and bottom left panels show the light light curve and power spectrum, respectively. The right-hand plots are the same observations with the dominant ~90 min period removed. Clear modulations are still visible in the pre-whitened light cure and power spectrum at periods between 5 and 13 min. These modulations are typical of QPO-type behaviour. The plot is taken from Ramsay et al. (2009).

resulting (pre-whitened) light curve is shown in the top right panel of Fig 6.3. It is possible to see evidence for QPO-type behaviour, particularly at the beginning of this light curve. The power spectrum of this pre-whitened light curve (in the low right panel of Fig 6.3) has evidence of power at 5.7, 10.2 and 12.7 min. There is no evidence for variability on the periods seen in the INT data shown in Fig. 6.1.

6.1.3 Optical spectroscopic observations

RAT J1953+1859 was observed on three occasions using the dual-beam ISIS instrument on the 4.2-m WHT as part of RATS follow-up observations. These observations are summarised in Table 6.1. These data were reduced in the manner described in §4.2 using Starlink packages and Molly and Pamela. which were written by Tom Marsh (cf. §4.2.6). For

Date	Num. spectra	Gratings	Slit (arcsec)	Res. (Å)	Accretion State
2008 Auguest 03	6	R158R, R158B	0.6	5, 5	QU
2008 September 29	24	R316R, R300B	1.5	8, 5	OB
2008 October 06	53	R158R, R300B	0.8	8,3	QU

Table 6.1: A summary of the spectroscopic observation obtained with the dual-beam ISIS instrument on the WHT during 2008. I show the date on which the observations were taken; the number of spectra, which refers to the number observed in each arm; the gratings used for the red and blue arms, respectively; the width of the slit used; the spectral resolution of the spectra in the red and blue arms, respectively; and the accretion state: whether the source is in outburst (OB) or quiescence (QU).

each epoch, arc calibrations exposures were taken before and after each sequence of science images and the nearest arc wavelength calibration was applied to each science spectrum.

6.1.3.1 First epoch of spectra

Six spectra in each arm were observed on 2008 August 03, two spectra were had an exposure time of 420 s, two of 120 s and two of 240 s. These spectra were not taken sequentially and therefore could not be used to measure any periodic radial velocity shifts. The average spectrum is shown in the lower panel of Fig. 4.12. The Balmer lines are present and strong: $H\alpha$ is in emission and split whereas the $H\beta$–$H\varepsilon$ lines are all in absorption and show some evidence of being split. No other lines are visible although given the low signal to noise this is perhaps not surprising.

6.1.3.2 Second and third epoch of spectra

The second epoch of spectra were obtained using the WHT on 2008 September 29, the same night as I observed the source in outburst on the NOT. These spectra were taken sequentially with an exposure time of 90 s followed by 12 s for readout. The mean spectrum of these observations is shown as the top spectrum in Fig. 6.4. $H\alpha$, $H\beta$ and $H\gamma$ are seen in emission and there is some evidence that the emission is in the core of a broader absorption component, while $H\delta$ appears to have no emission and is weakly present in absorption. The

HeII 4686 Å line is weak and emission which is typical of a dwarf nova in outburst (e.g. SS Cyg; Martinez-Pais et al., 1994), and though there is a HeI lines at 6678 Å there is no evidence for a HeI 5876 Å line.

On 2008 October 06 we observed RAT J1953+1859 for a third time and the source had returned to its quiescent state. These observations consisted of 53 sequential exposures in each arm using an exposure time of 240 s. The exposures were separated by a readout time of 25 s. The mean spectrum of these observations in shown as the lower spectrum in Fig. 6.4. The Balmer $H\alpha$, $H\beta$ and $H\gamma$ lines are all in emission and are split. All the Balmer lines are seen in emission and decrease in strength from $H\alpha$ down to $H\varepsilon$. $H\alpha$ is most prominently split and the FWHM of this line is ~40 Å, which corresponds to a $v \sin i$ of 1800 km s^{-1}, indicative of an accretion disc. HeI lines are also seen at 5876 and 6678 Å in emission, HeI 5876 Å is split and is very strong, stronger then even $H\beta$. The strong Balmer and neutral helium emission lines are typical of dwarf novae in quiescence (e.g. VW Hyi; Smith et al., 2006). Unlike the spectrum of RAT J1953+1859 in outburst, HeII 4686 Å line is not seen in the quiescent spectrum. This line is sometimes seen in some quiescent dwarf nova (e.g. YZ Cnc; Shafter & Hessman, 1988) though not always (e.g. SS Cyg; Martinez-Pais et al., 1994).

6.1.3.3 A search for periods in the spectra

Fig. 6.5 shows the $H\alpha$ emission line of the spectra which were observed on 2008 October 06 when RAT J1953+1859 was is a quiescent state. The spectra have been stacked on top of one another with time increasing from the bottom of the plot. In order to increase signal-to-noise the spectra have been binned so that each line in the stacked plot is the average of two spectra. The spectra were normalised to the continuum before being averaged. The total time taken to observe each line in the plot is 530 s. It is clear that the line, which has a width of ~1800 km s^{-1}, changes over the course of the observations with the line changing from being double peaked to single peaked and back to being double peaked again. When there is only a single peak, the position of the peak is at the same wavelength as the redder peak when two peaks are seen. This suggests that what were are seeing is not an orbital motion

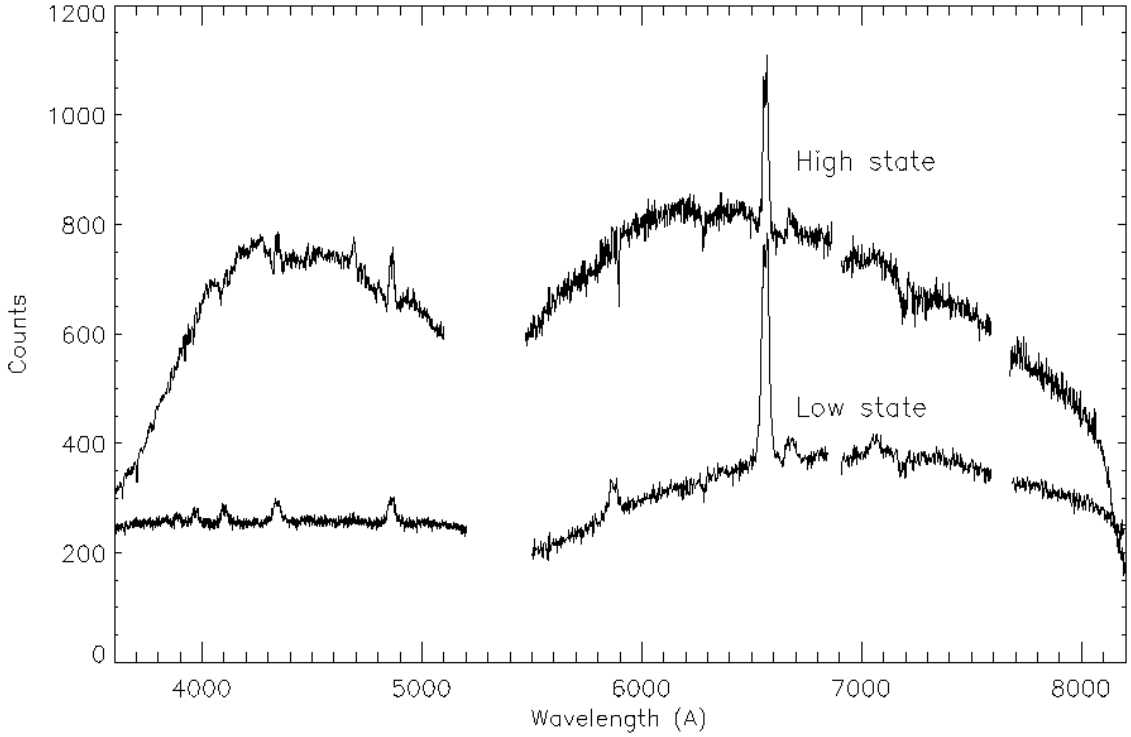

Figure 6.4: The average red and blue optical spectra taken with the WHT on 2008 September 29 and 2008 October 06. The source was in a high state – outburst – on the first of these dates and in the low state – quiescence – in the second. These spectra have not been flux calibrated and so the instrumental response is partly reflected in the shape of the spectra. This figure is taken from Ramsay et al. (2009).

but, perhaps, an obscuring of the blue-shifted component. There is also no evidence for any repetition of the single peaked feature during our observation length and therefore no evidence for any periodic radial velocity motion.

6.1.4 Discussion

RAT J1953+1859 has all the hallmarks of a classical dwarf nova. It has two clear states; a brighter outburst state which is approximately 4 mag brighter than a fainter quiescent state. The width of the Balmer lines are around 1800 km s^{-1} and there are neutral helium emission lines in both the quiescent and outburst spectrum which are commonly seen in cataclysmic variables.

What makes RAT J1953+1859 unusual is the method through which it was discovered. Over half of dwarf nova were discovered though optical outburst activity while the vast majority of the rest have been found through their X-ray emission, very blue colour or

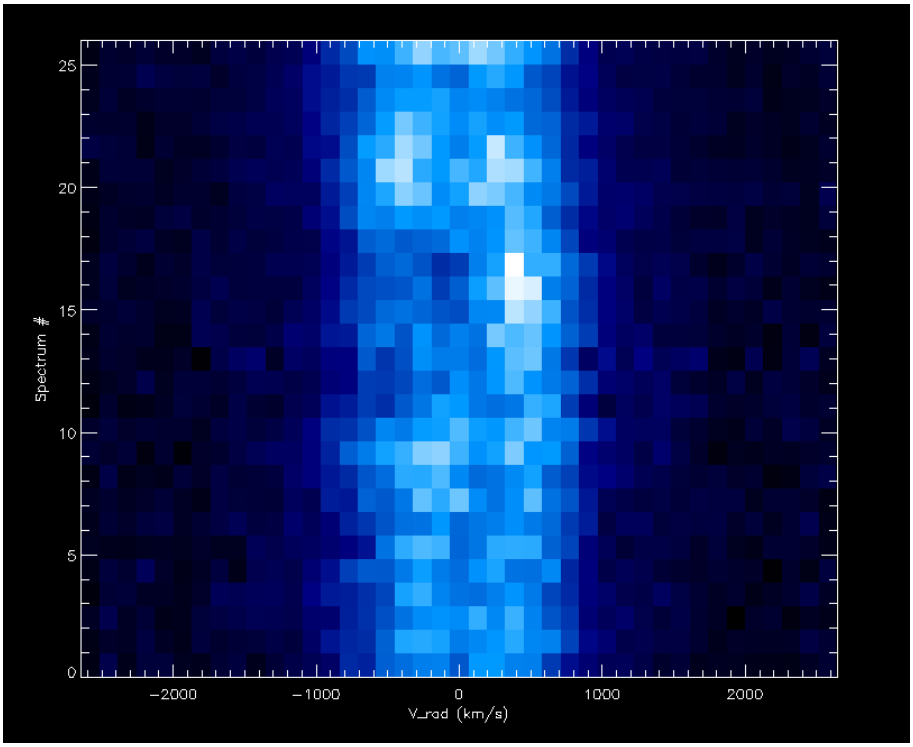

Figure 6.5: Spectra obtained on 2008 October 06 showing the *Hα* emission line have been stacked with time increasing upward on the y-axis and velocity on the x-axis. The spectra have been normalised and binned so that each line in the stacked spectra consists of the average of two observed spectra. Each average spectra in the plot took 530 s to observe which includes two 240 s exposure and 25 s to read out each exposure. This figure is taken from Ramsay et al. (2009).

spectroscopic properties (Gänsicke, 2005). Until this work none has been found through quiescent QPO behaviour. In addition, while QPOs are commonly seen during the rising and falling in brightness during a dwarf nova outburst cycle, quiescent QPOs have only been seen in two other dwarf novae; V893 Sco (Bruch et al., 2000) and WX Hyi (Pretorius et al., 2006). These two sources exhibited QPOs with much shorter periods than RAT J1953+1859 (5.7 and 3 min, respectively) making RAT J1953+1859 rather different as the period here seen was 20.0 min.

Pretorius et al. (2006) suggests that the apparent lack of sources observed to display quiescent QPO behaviour could well be attributed to selection effects – it should not be surprising that they have not been seen if no one has been looking for them. If these QPOs are common place, many more such systems will be discovered by future surveys such as that which will be undertaken by the Large Synoptic Survey Telescope.

QPO behaviour is usually modelled using the low inertia magnetic accretor (LIMA) model (Paczyński, 1978; Warner & Woudt, 2002, 2006; Warner & Pretorius, 2008). This model assumes magnetically controlled accretion on to a rapidly rotating equatorial belt of the white dwarf from the inner edge of the disc. This model is similar to the intermediate polar model, it differs because in high magnetic field systems, material accreted onto the surface of the white dwarf is coupled to the interior (Katz, 1975) but in sources with magnetic field below 10^5 G the accretion torque is not coupled to the interior of the star and the accretion forms a low mass surface layer at the equatorial region of the white dwarf (Warner & Woudt, 2008). The changing in the mass transfer rate during an outburst causes the disc radius to change on short time-scales and the low inertia material is coupled to the rotation of the disc. When the star starts fading the inner radius of the disc radius increases, leaving the accreted equatorial surface layer moving so rapidly that it lies beyond the inner edge of the disc and so gas is propelled outward into the outer disc which extracts angular momentum from the surface layer (Warner & Woudt, 2008). The quasi-periodic change is brightness is caused by the interaction between the surface layer and the inner disc being optically thick and rotating with the period of the QPOs. This leads to the observers line of sight alternating between the disc partly obscured and an intersection of a rotating beam

(Warner & Woudt, 2008).

However, this model assumes that QPOs are seen only when the accretion rate is changing. If quiescent QPOs are indeed commonplace this has implications for both the choice of parameters used when modelling these behaviours (e.g. Piro & Bildsten, 2004, assume that QPO behaviour occurs only during outbursts) and indeed the model itself. Further observations of quiescent dwarf novae are needed to determine the frequency of quiescent QPO behaviour which will lead to improvements in the model.

Observations of quiescent QPOs RAT J1953+1859 not only presents an interesting and as yet unexplained phenomena but also leads to a new method with which to discover dwarf novae. This study highlights the need for work to be performed on both the observation side – searching for more dwarf novae white QPOs in quiescence – and the theoretical side in order to give a more complete understanding of dwarf novae QPOs.

6.2 RAT J205902.93+453735.9

White dwarfs are classified based on the chemical composition of their photosphere using a classification system introduced by Sion et al. (1983). Three quarters of these have a hydrogen-rich photosphere with a temperature of 4.5–170 kK (Kurtz et al., 2008); these are known as DA white dwarfs. They cool from pre-white dwarfs with temperatures ranging from almost 200 to 80 kK (Kurtz et al., 2008) and follow a well defined cooling track on the HR diagram. During their evolution they will pass through an instability strip when at temperatures of 13–11 kK (Fontaine & Brassard, 2008). This instability is caused by recombination in the hydrogen envelope which leads to an increase in opacity which limits the flow of radiation and causes instabilities to g-mode pulsations. At this point they are known as DAV or ZZ Ceti stars. There are at least 148 DAVs known (Castanheira et al., 2010); these have periods ranging from 100–1400 s with amplitudes at the dominant frequency of a few per cent (Fontaine & Brassard, 2008).

At least 8 DAVs are found in cataclysmic variable systems (CVs); for example, Gän-

sicke et al. (2006) find that the accretor in SDSSJ133941.11+484727.5, which has an 83 min orbital period, is a DAV pulsator. Other than these, only one DAV is known to exist as a component of a binary system (Jordan et al., 1998) and this is a wide visual binary. It is remarkable that no other DAV had been found in a non-interacting binary system despite the majority of stars being in binary systems and being expected to pass though the DAV instability strip at some point in their evolution.

In this Section, I present the discovery of a new DAV source which appears to have a close, hot companion. If confirmed it would represent the first such binary.

6.2.1 INT Photometry

I observed the field containing RAT J205902.9+453735.9 – hereafter RAT2059 – on 2007 October 15 for a total duration of 141 min. The mean airmass of the observations was 1.085 and the seeing ranged from 1.0–1.3". 131 unfiltered 30 s exposures of the field were observed as well as single images in each of; the RGO U filter, SDSS g' and SDSS r' filters. I use these single images to calculate stellar colour.

I identified a blue star ($g' = 18.4$, $g' - r' = -0.06$, $U - g' = -0.39$) with a 920 s periodic signal in its light curve. The peak-to-peak amplitude in white light is 0.08 mag. A finding chart for RAT2059 is shown in Fig. 6.6 and the white light light curve and resulting power spectrum is shown in Fig. 6.7.

6.2.2 Followup Optical Photometry

Since the original INT photometric data were in white light – and has a time resolution of ~1 min – I obtained further broad-band data to get a better overall picture of its pulsation characteristics and also filtered data to determine the pulsation amplitude at different wavelengths.

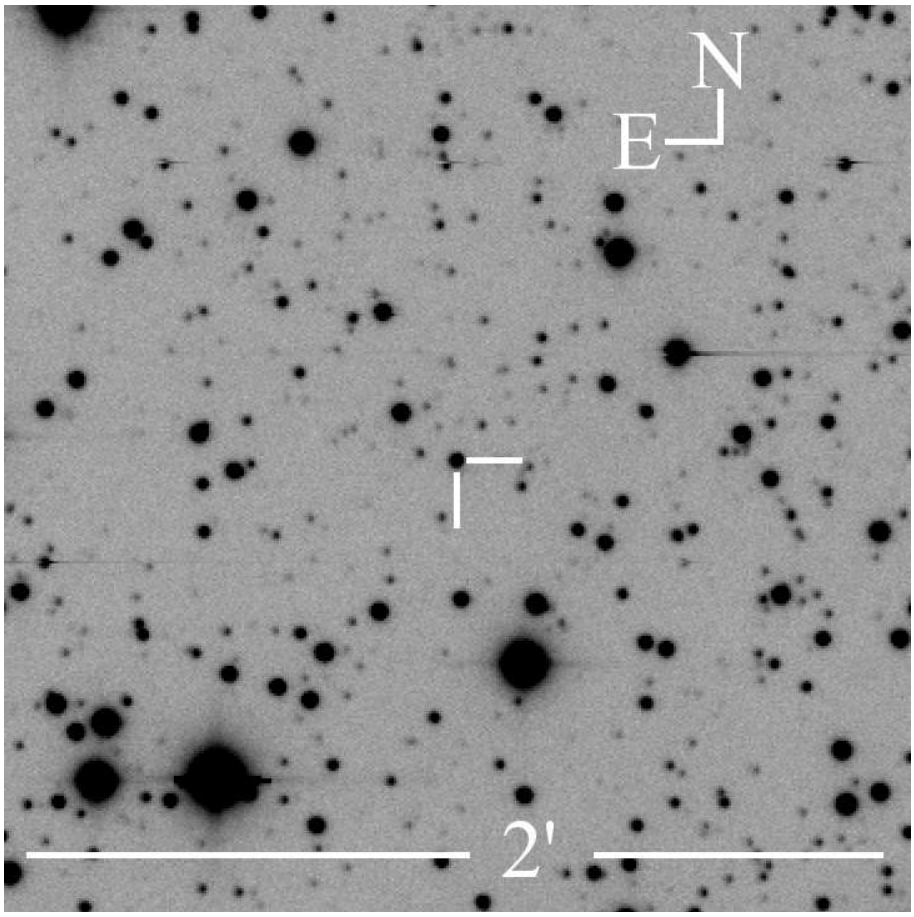

Figure 6.6: A white light finding chart of RAT2059 made using the WFC on the INT. The exposure time was 30 s and the image is 2 × 2 arcmin and the pixel scale is 0.33 arcsec.

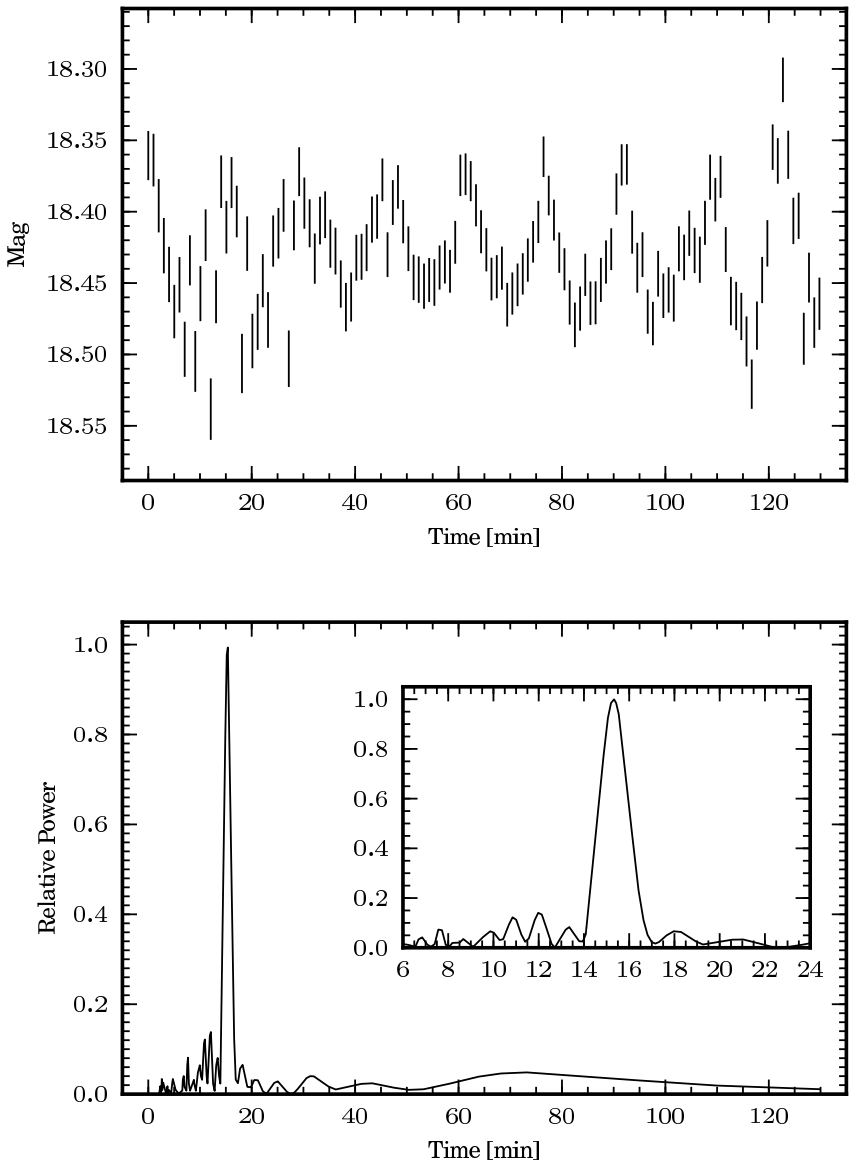

Figure 6.7: White light photometric observations of RAT2059 made using the INT. Each exposure was 30 sec which resulted in a cadence of ~1 min. The upper panel shows the light curve while the lower panel shows the normalised power spectrum with the insert showing a zoomed-in view of the peak in the power spectrum.

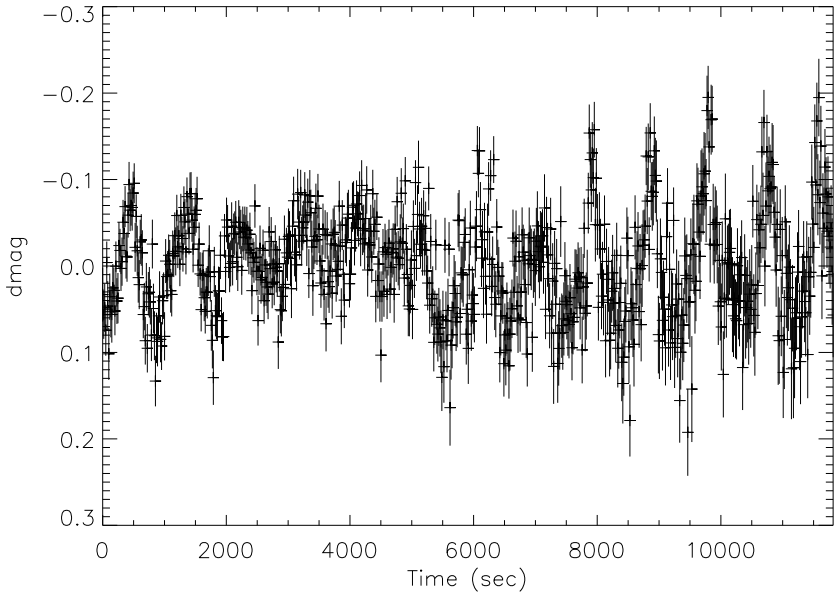

Figure 6.8: The light curve of RAT2059 obtained using the NOT. The time resolution is 16 s. A 'sky contrast' filter was used. The y-axis refers to the differential magnitude with respect to several reference stars and has had the mean of the light curve subtracted from each data-point.

6.2.2.1 Nordic Optical Telescope

I obtained a series of images using the 2.5-m Nordic Optical Telescope and the Andalucia Faint Object Spectrograph and Camera (ALFOSC) on La Palma on 2010 August 24 in 'Fast-Track' service mode, when the seeing ranged from 0.9–1.1 arcsec. Each exposures was for 10 s the CCD was windowed so the cadence was 16 s. The 'sky contrast' filter[1] was used in order to limit the effects of differential diffraction on the star images and second order colour effects on the differential photometry. I show in Fig. 6.8 the resulting photometric light curve. There is a strong pulsation on a period of 937 s with the amplitude varying over the course of the observation which lasted 3.3 h.

[1]The details of the 'sky contrast' filter are shown as filter #92 at http://www.not.iac.es/instruments/filters/filters.

6.2.2.2 IAC 80 cm Telescope[2]

A series of images were obtained in Bessell B and SDSS g' and r' filters using the Cámara Mejorada Ligera del Observatorio del Teide (CAMELOT) detector on the IAC 80-cm telescope (IAC80) at in Tenerife. The CCD was windowed and the exposures were between 60 and 70 sec with 10 sec dead-time. Photometric light curves were obtained in each band using standard reduction software and these were used to obtain power spectra. A clear peak in these power spectra was obtained, the period of which varied between 830 and 880 sec (given the uncertainty on the period these differences are not significant). I folded the data on the strongest period in the power spectra for the appropriate data-set and show these folded light curves in Fig. 6.9. The peak-to-peak amplitude in the r' band is 0.05 mag, and 0.10 in the B and g' filters. However, given that the NOT light curve shows significant variation in amplitude of the pulsations and the observations were not simultaneous, the pulsation modes present in RAT2059 cannot be strongly constrained (such as is done by Clemens et al., 2000).

6.2.3 *Swift* observations

In order to extend the spectral energy coverage to shorter wavelengths, I obtained target of opportunity observations of RAT2059 using the NASA *swift* satellite (Gehrels et al., 2004) between Aug 29 and Sept 01 2010. The observations used the UVOT instrument and the available UV filters plus the U filter (see Table 6.2). The UVOT exposures were obtained in fast mode allowing light curves to be made in different bin sizes. For the three UV filters the exposures were over 1700 s while for the U filter the duration was ~1000 s. Simultaneous exposures were taken using the X-ray Telescope but the source was not detected (the count rate measured was -0.0002 ± 0.0003 ct s^{-1}).

To determine the flux of RAT2059 the *swift* tool UVOTMAGHIST was used which is part of the HEASOFT[3] package of software. This tool takes into account effects such as

[2] These observations were performed by Anna Hourihane, Heather Patrick and Colin Wade from University College Cork.

[3] http://heasarc.gsfc.nasa.gov/docs/software/lheasoft/

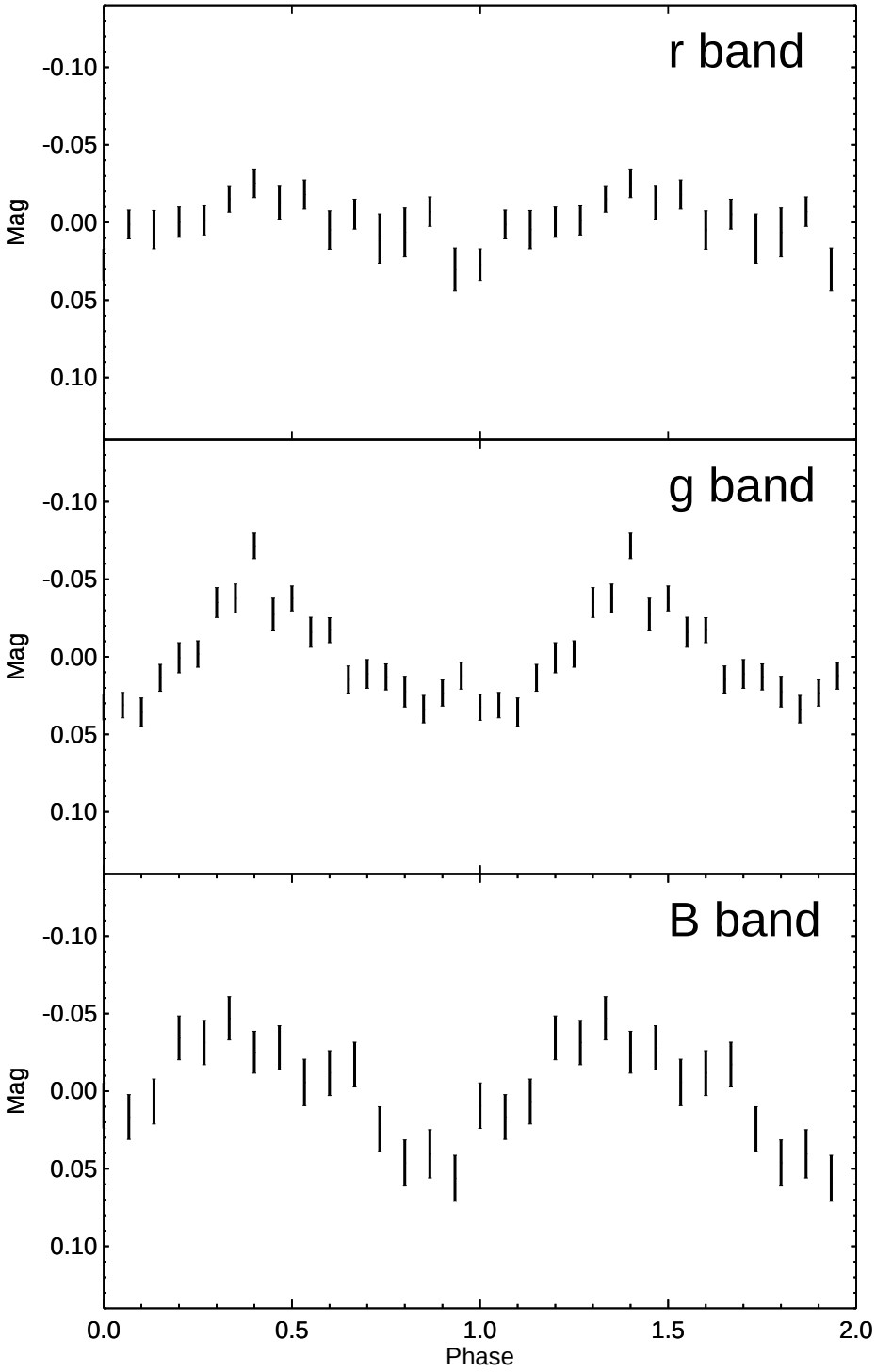

Figure 6.9: The folded light curves of RAT2059 obtained in $Bg'r'$ filters using the IAC80 telescope.

Filter	Wavelength (nm)	FWHM (nm)	Ct/s	Flux erg s^{-1} cm^{-2} Å^{-1}
UVW2	188	76	0.66±0.02	$4.07\pm0.14 \times 10^{-16}$
UVM2	225	50	0.46±0.02	$3.88\pm0.02 \times 10^{-16}$
UVW1	251	70	0.79±0.03	$3.17\pm0.10 \times 10^{-16}$
$U_{\rm Swift}$	347	79	1.43±0.06	$2.33\pm0.09 \times 10^{-16}$
$U_{\rm RGO}$	358.1	63.8		$2.24\pm0.04 \times 10^{-16}$
g'	484.6	128.5		$2.27\pm0.05 \times 10^{-16}$
r'	624.0	134.7		$1.24\pm0.02 \times 10^{-16}$

Table 6.2: The integrated count rate and fluxes of RAT2059 is four different filters made using the *Swift* UVOT and the three observations made using the INT – converted to flux using the zeropoints found by Holberg & Bergeron (2006) – for comparison. The wavelength shown is the central wavelength of the filter.

coincidence loss and converts the count rate to flux based on observations of white dwarfs made as part of the *swift* calibration process (Poole et al., 2008). As recommended in the UVOT software guide[4] a source radius of 3 arcsec was used. Shown in Table 6.2 is the count rate and flux of RAT2059 in the four filters: it is clear that the flux increases towards shorter wavelengths.

Despite the low count rate a search for periodic signal was made but none was detected I used a bootstrapping technique to inject periodic signals into the data and determined an upper limit of 0.2–0.3 mag on the amplitude of a periodic signal. This higher than amplitudes seen in either the filtered or white light observations so a non-detection was perhaps not surprising.

6.2.4 The UV-Optical photometric spectrum

The broad-band photometric observations ranged from the UV to the red. From these data I constructed a spectral energy distribution with which to constrain the temperature of the RAT2059. I corrected the fluxes for reddening using the relationships given by Cardelli et al. (1989), and have assumed a ratio of total selective extinction in the V band, $A_V/E(B-V)$, of 3.1 (Fitzpatrick, 1999). The reddening at UV wavelengths is very sensitive to the extinction, $E(B-V)$. I compared the $(g'-r')$ colour of RAT2059 to white dwarfs in the

[4] http://swift.gsfc.nasa.gov/docs/swift/analysis/UVOT_swguide_v2.pdf

Filter	Corrected Flux erg s^{-1} cm^{-2} Å^{-1}
UVW2	$2.48\pm0.09 \times 10^{-15}$
UVM2	$1.95\pm0.01 \times 10^{-15}$
UVW1	$9.22\pm0.29 \times 10^{-16}$
$U_{\rm Swift}$	$5.92\pm0.23 \times 10^{-16}$
$U_{\rm RGO}$	$5.08\pm0.10 \times 10^{-16}$
g'	$4.61\pm0.09 \times 10^{-16}$
r'	$2.04\pm0.04 \times 10^{-16}$

Table 6.3: Reddening corrected fluxes of RAT2059 assuming $E(B-V) = 0.23$.

SDSS survey and found typical de-reddened colour of $(g'-r') = -0.31$ and -0.36 mag for effective temperatures of 12.0 ± 0.2 and 20.0 ± 0.2 kK, respectively. RAT2059 has a $(g'-r')$ colour of -0.06 which implies a reddening of $E(g'-r') = 0.25$ and 0.30 for the cooler and hotter white dwarfs, respectively, which equates to $E(B-V) = 0.23$ and 0.27. I adopted the more conservative reddening of $E(B-V) = 0.23$ and give the corrected fluxes in Table 6.3. These data are plotted in Fig. 6.10 along with two black-body curves of temperatures of 10 and 40 kK. Neither single black-body temperatures fit all the data. The optical data is consistent with the source having a temperature in the region 10–15 kK and the UV observations with a temperature above 25 kK.

6.2.5 Optical Spectroscopy

To get a better understanding of RAT2059 I resolved to obtain optical spectra of the sourch which were of a sufficient resolution and signal-to-noise to classify the spectral type of the source. On 2008 August 3 and October 6, RAT2059 was observed using the dual-beam Intermediate dispersion Spectrograph and Imaging System (ISIS) instrument on the 4.2-m William Herschel Telescope (WHT) on La Palma. The observations are summarised in Table 6.4. The spectra obtained in these two nights do not show significant differences in the positions, and depths of the spectral lines and the same lines were visible on each night so I created an average spectrum of the 9 observed spectra which is shown in Fig. 6.11. The spectrum of RAT2059 shows strong Balmer absorption lines and is consistent with it being a DA white dwarf. The $H\beta - H\delta$ Balmer lines are all deeper than the $H\alpha$ line and the $H\alpha$

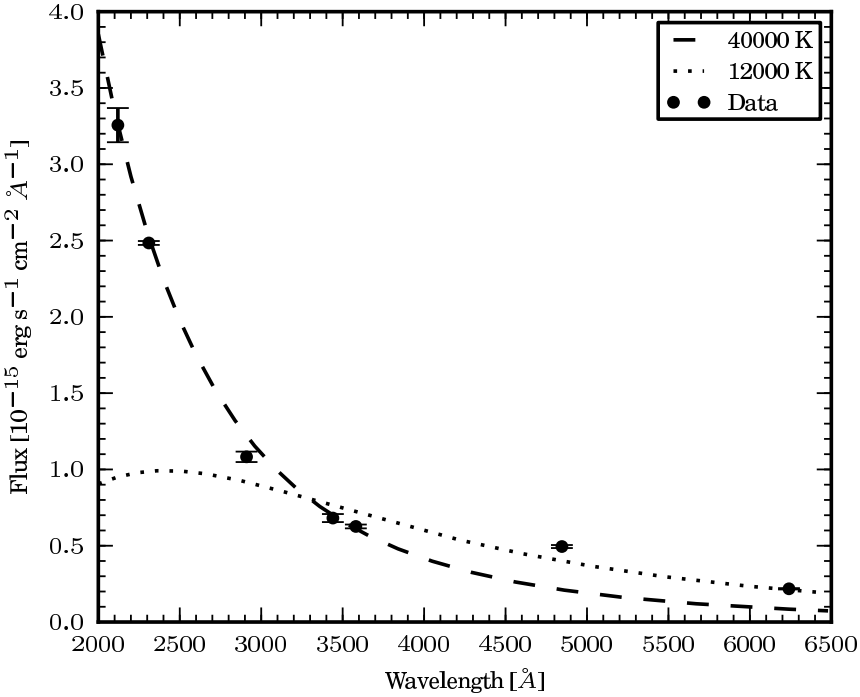

Figure 6.10: A spectral energy distribution of RAT2059. The *Swift* and INT de-reddened fluxes are plotted as filled circles. Black-body curves of temperatures 40 kK and 12 kK are plotted for comparison. The hotter and cooler black-bodies are normalised to the UVW2 and r' fluxes, respectively. It is clear that one temperature does not fit the data.

Date	# spectra	Exp. time (s)	Grism	Slit width (″)	FWHM (″)
20080803	2	240	a	0.6	4
20081006	7	240	b	0.8	4

[a]R158R + R300B, [b]R158R + R158B

Table 6.4: Summary of the spectroscopic observations of RAT2059 made using the WHT. The ISIS spectrograph is a dual beam instrument with a red and blue arm, the number of spectra refers to the number observed in each arm.

line – and to a lesser extent $H\beta$ and $H\gamma$ – shows structure in the core of the line, though given the relatively low signal-to-noise of the spectrum I do not draw firm conclusions from this.

6.2.5.1 Fits to optical spectra

Although the spectra obtained of RAT2059 were primarily for identification and classification purposes, it was also possible to fit the average spectrum of RAT2059 with model

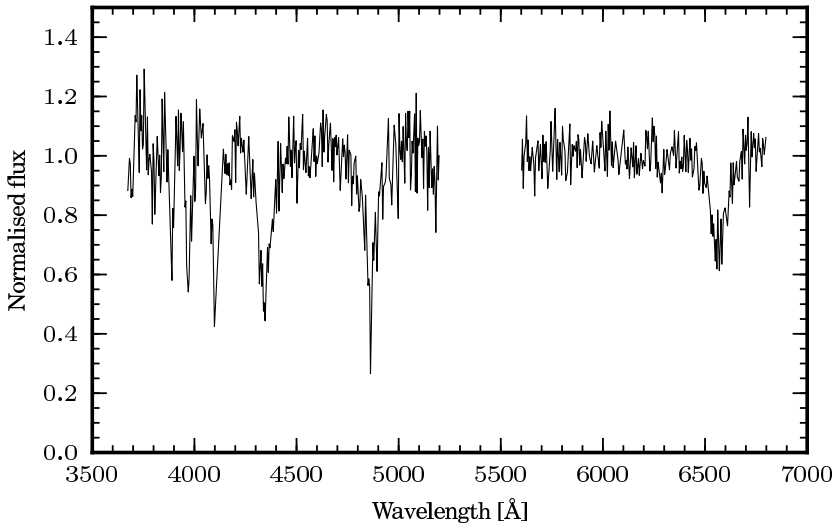

Figure 6.11: The average of 9 optical spectra of RAT2059 observed with the WHT and the ISIS instrument. The flux has been normalised individually for each arm and re-binned to the instrumental resolution, which was estimated from arc-lamp emission lines.

spectra of various effective temperatures and surface gravities. I used the FITSB2 fitting program (Napiwotzki et al., 2004) to fit a grid of white dwarf atmospheres[5] to the average spectrum of RAT2059. I found that the best-fitting single star model has an effective temperature and surface gravity of $T_{\rm eff}$ = 17.0 ± 0.7 kK and $\log g$ = 7.80 ± 0.20, respectively. FITSB2 is allows the fitting of a spectrum with a composite model containing two model atmospheres. I found a solution was obtained by using a two-component model with the scaling of the two models is left as a free parameter. Using this method I get best-fitting effective temperatures of $T_{\rm eff}$ = 17600 ± 5800 and 12400 ± 2500 K and surface gravities of $\log g$ = 7.7 ± 0.4 and 7.8 ± 0.5 for the hot and cool component, respectively. The scaling factor of the fluxes of the two stars found by the fitting routine is $F_{\rm cooler}/F_{\rm cooler}$ = 11.52 ± 1.37 implying the ratios of the two stars radii is at least 3:1. This is discussed further in the next subsection

[5] A grid of hot white dwarf models was kindly supplied by Detlev Koester. These models range from a $T_{\rm eff}$ of 6000–100000 K and log g of 5.5–9.5.

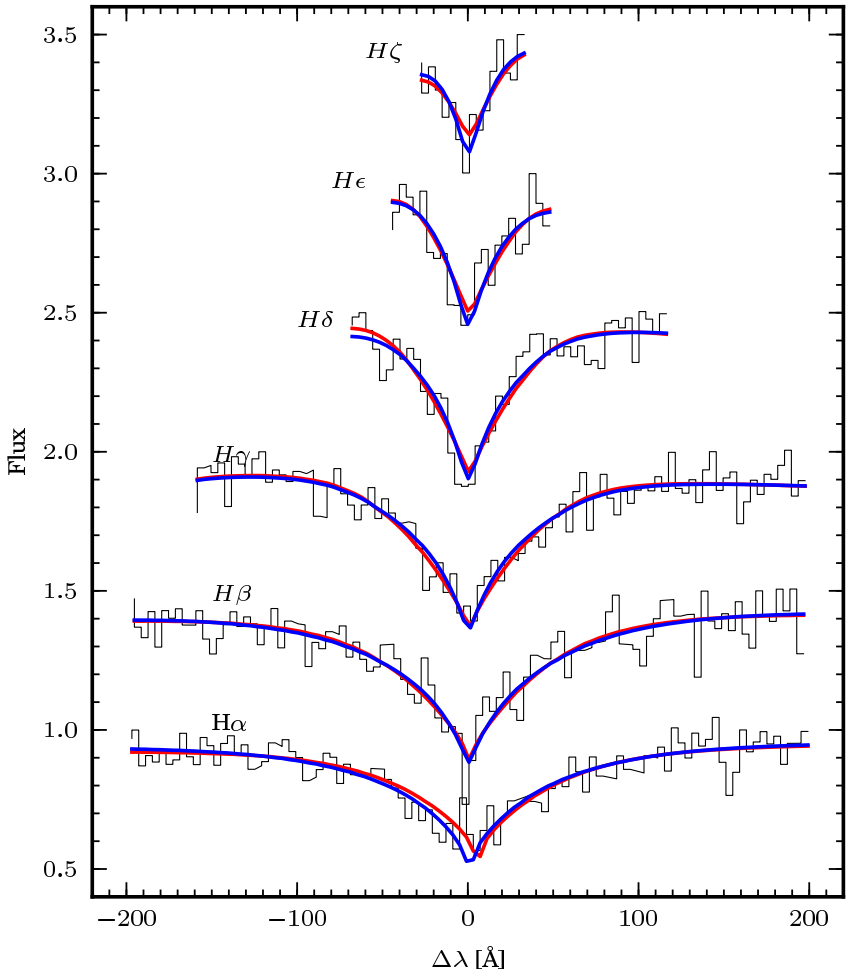

Figure 6.12: The Balmer lines of RAT2059 over-plotted, in red with our best-fitting single star, and in blue with the best-fitting two-component, DA white dwarf model. Each line has been normalised to 1.0 and every line after $H\alpha$ has been shifted up by 0.5 flux unit. The reduced χ^2 of the fit of the data to the model is 0.98.

6.2.6 Discussions

I have discovered a source which has a periodic modulation in its light curve at an amplitude and period of 0.08 mag and 937 s. These parameters are consistent with that seen in DAV white dwarfs. The pulse profile of the NOT and INT light curves varies over time, this is also quite normal for a DAV source and indicates the presence of more than just a single pulsation mode. The photometric data at optical and UV wavelengths suggests that a single temperature is not appropriate for this source. Model atmosphere fits to the optical spectra reveal that a single temperature would be well above that seen in any other DAV white dwarfs. The two-temperature model fits are consistent with the hotter source having > 15 kK and the cooler source having a temperature in the range expected for a regular DAV pulsator. A visual inspection of the spectrum indicates that the source is DA white dwarf. Given this, the two-component fits are curious as if the system contained a hot un-evolved source it would be expected to dominate the observed emission. The hot component in the spectrum could be due to a chance alignment, however, given the rarity of sources with temperatures over 15 kK this is unlikely.

The fitting of the two-component model is unlikely to accurately constrain the surface gravity of the hotter star adequately as the hotter star will act only to dilute the Balmer lines with continuum. For this reason I do not judge the low surface gravity found on the hot star to be significant and the surface gravities found are likely to be relatively unconstrained. The ratio of luminosities is of more interest. At first glance the value found – 11.52 – seems to be wholly unphysical but the relatively high amplitude of the pulsations implies that the light from the hotter star is not blanketing the variability significantly. If the flux ratio is within a factor of 2–3, it implies that the hotter star (assuming it is degenerate) must be more much massive (and have a higher surface gravity) than the DAV white dwarf. This is something that would not be expected from single star evolution suggesting the system must have gone through a phase of binary interaction. In this case there must have been a period of stable mass transfer from the progenitor of the star which is now a DAV to the hot star.

If confirmed to be a binary system, this source would represent the first close binary consisting of a DAV and a companion. However, further observations are needed in order to determine the nature of the hotter source and what effect the binary nature of the system has on the DAV white dwarf. High resolution optical and UV spectroscopy will likely be the best way in which to reveal the individual temperatures of the system and any radial velocity shift related to the binary nature of the system.

6.3 Summary

The method used to select the sub-set of sources which are follow-up with observations, is a simple one. The sources must be interesting in both its colour and its photometric properties. If it passes these criteria then it is (usually) observed spectroscopically and if necessary observed again (sometimes at wavelengths other than optical) in order to constrain the source's nature. This path has been taken for the work carried out to understand RAT J1953+1859 and RAT2059. It is important to note that, while both these sources were prime candidates for initial follow-up observations, these observations revealed them to be something other than the main science goal of the project. Had we limited our follow-up work to only AM CVn systems the interesting nature of these sources would never have been revealed. As the RATS project samples a parameter space that has been relatively untapped it is important not to restrict ourselves but be open to the discovery of more unexpectedly interesting sources. More generally, the strength and importance of survey astronomy lies in the ability to discover sources which provide tests of our understanding of the physical world.

Chapter 7

Conclusions and Future Work

> Yes, she thought, laying down her brush in extreme fatigue, I have had my vision.
>
> *V. Woolfe, To the Lighthouse, 1927*

I have been working on the RATS project for the previous three years. This began with me having to get to grips with the huge (and growing) dataset at my disposal but as time has gone on this has been an enormous bonus as I have never wanted for data. In this final chapter I will sum up the project and highlight some of the successes that I and the project have achieved as well has discussing some of the weaknesses and why some expectations have not been fulfilled while others have been surpassed. I go on to discuss the future of the project both in its current form with the data already collected and in a modified form with observations in the field observed by the *Kepler* satellite.

7.1 The variability detection code

The RATS survey has detected variability on the time-scale of minutes in sources as faint as $g' = 23$. This parameter space has been relatively poorly studied and so learning to understand and process the data has taken a good deal of time. The first step taken by

me was to switch to a new method of performing photometry using a difference imaging analysis (DIA) technique. This method was much faster than using aperture photometry but came with an infuriating number of headaches. Large amounts of time were taken up with tweaking parameters but eventually I was able to produce results which were consistent and reliable. The software I used – DANDIA – was rather unwieldy as it was not designed for public consumption. The results coming from DANDIA, while reliable were not always optimal. Often better light curves could be produced using aperture photometry techniques. Issues encountered were poor subtraction of the reference image in some fields and strange periodic trending that was difficult to remove using the detrending algorithms. For one field the trending was so bad that the entire field was abandoned and not included in any further data analysis. Though the reason for the trending is still not understood it seems likely that the cause was to do with the subtraction performed by DANDIA. One of the biggest weaknesses with DANDIA is the lack of good documentation. Often the tweaking for parameters was more of a 'dark art' than a science with dramatic changes caused by the smallest tweak of an apparently trivial parameter. For this reason I do not believe that, going forward, DANDIA is the appropriate tool to use. However, DIA has recently become the de facto standard for performing wide-field photometric observations. Any future work will likely still use a form of DIA and work will include having to assess recently developed alternatively to DANDIA such as DIAPL (written by Wojtek Pych, DIAPL it is a modified version of DIA which is described in Wozniak, 2000).

The light curves created for over three million sources are presented in this thesis and searched for variability. As short-period variability (on time-scales < 40 min) is the forte of this project, detection of this was prioritized when developing the software to find variables. I quickly found that the Lomb-Scargle (LS) and Analysis of Variance (AoV) algorithms produced poor results when taken alone. They would be fine if dealing with only a few hundred or even a few thousand sources but when you have millions of stars and 10's to 100's of thousands of variables it becomes important to have a reliable method with which to discriminate between between variables and non-variables that has a very low rate of false positives. I developed a method for combining the Lomb-Scargle and AoV algorithms which consists of binning the data in period, finding sources that are signifi-

cantly above the median in each bin and finally seeing if the period found by each algorithm matches. The creation and tuning of this technique took a large number of iterative improvements till the algorithm was able to reliably find periodic variables of low amplitude. One of the challenges was to determine where the significance threshold cutoff should be. My method for doing this was to visually inspect hundreds of light curves with various different significance values and to set the threshold below which I believed that sources were no longer significantly variable (i.e. the variability seen was entirely due to noise). This method, however, is inherently subjective and while I tried to be as consistent as possible it was inevitable that on some days I was more charitable than others. There is definitely a better, less subjective way of performing this task. One method would be to combine the false positive and sensitivity testing to iteratively set the cut-off. This was not done due to the processing time needed when calculating the sensitivity (each plot shown in Fig.3.8 took more than one day to calculate). The code to do this would be relatively easy to parallelise and this is probably the best way to proceed in future work in order to push down the amplitude of variability that the survey is sensitive to.

Future work will need to work on improving my algorithm such as mentioned above but to also look at other periodic variability detection algorithms. The increase in the number of wide-field variability surveys has also led to the development of new algorithms with which to detect variability. Two of these that seem to be of particular interest to the RATS project are the Plavchan et al. (2008) algorithm and The Fast Chi-squared Period Search (Palmer, 2009). Both of these techniques are capable of finding similar sources to the current techniques and also sources with light curve that are non-sinusoidal (e.g. a saw-tooth shape). If it is possible to detect non-sinusoidal variability and still keep the low false positive rate then these method would be a significant upgrade on our current method. A disadvantage to using either of these methods is they are significantly more computationally intensive than current routines. This, though, can be offset by performing the parameter generation in parallel on a cluster.

It will also be important to develop techniques to discover sources with non-periodic variability. Some work has been done on developing methods for the detection of sources

such as flare stars and contact binaries. This is discussed further in §7.3.

An effective method to discover optical transient events would also be an interesting endeavour that could provide some exciting scientific results. The types of events which may be detected are gamma-ray bursts (GRBs) and transient nuclear activity from normal galaxies. GRB events are not just seen at very short wavelengths but at a range of energies. The time at which the so-called afterglow is observed increases as the energy decreases. The optical afterglow is typically seen several minutes to hours after the GRB event and last for several weeks but they have been seen to appear within seconds of the GRB (e.g. Racusin et al., 2008). This prompt optical optical emission can last for a matter of seconds. It is also thought that GRBs are strongly beamed though the opening angle of the beam is not known and it is thought that it may vary depending on wavelength (Nakar et al., 2002). An observation by the RATS project of prompt orphan afterglows would present a major discovery and would help to constrain the opening angle of GRBs.

Another source of optical transients could be due to a star passing too close to a super-massive black hole in a distant Galaxy. The star would be tidally disrupted and accreted which would produce a bright flare (Rees, 1988). Such a flare would provide unambiguous evidence for the presence of a super-massive black hole. In addition to GRB afterglows and tidally disrupted stars, the Pi of the Sky experiment (Burd et al., 2005) has discovered a handful of optical transient whose cause was unknown. One event lasted for ~1 min and no star or host galaxy was found[1].

A search for optical transients would be relatively straight forward, one would only need to look for sources that appear in only a few frames. However, the current data reduction pipeline is not capable of looking for optical transients as the detection of sources relies on a catalogue made up of sources which appear in the image with the best seeing. Someone would therefore have to write a bespoke reduction routine to perform this work – a simple script using SExtractor may well do the job. There would probably be a high chance of finding nothing but the rewards would be great given the limited amount of effort involved.

[1] http://grb.fuw.edu.pl/pi/index.html

7.2 Detecting AM CVn systems

I was able to create a list of candidate AM CVn systems using the colours and periods of the sources detected as variable. There were 66 sources in this list after a visual inspection removed sources where the light curves were sub-prime (e.g. had large gaps in the data, was a faint star with too low an amplitude to be realistic, obvious trending in the data etc.). Of the 66 good light curves, I obtained optical spectra of 15 sources, though only 11 of these source have spectra of a high enough signal-to-noise for identification of their nature. While I have managed to find some very interesting sources, none of them have been found to be an AM CVn system. This begs the question, how appropriate are photometric variability surveys for finding AM CVn systems?

So far the RATS project has used 37 nights of telescope time for the wide-field observations (though only ~30 nights in total has been clear). In addition, we have used ~17 nights for follow-up spectroscopy. If the goal is to discover AM CVn systems, could those 54 nights be better spent using a different strategy? A direct comparison can be made between the RATS project and the search for AM CVn systems in SDSS photometric data (Roelofs et al., 2009; Rau et al., 2010). Their strategy has been to identify AM CVn candidates via their colours and confirm them from follow-up spectroscopic observations. They have observed using the INT, NOT and WHT on La Palma and the 1.5-m Tillinghast telescope at Mt. Hopkins, for a total number of nights comparable to RATS, obtaining ~750 spectra. Five of these sources has been found to be an AM CV systems which is rather more than the RATS project has found.

So, is the RATS strategy a the best way to discover AM CVn systems? Probably not. It is clear that the method used by Roelofs et al. (2009) and Rau et al. (2010) has had much more success on this front, if the sources found by the SDSS spectroscopic searches are included the number found increases to 13. That said, all the AM CVn systems discovered in SDSS data have had periods longer than 25 min and most are probably low state systems. This reduces their importance somewhat as they are therefore likely to be intrinsically faint and also much weaker gravitational wave sources than the high state systems (too weak to

be detected by a satellite such as *LISA*). The RATS project is only capable of discovering the shorter period systems and in this aspect there is no evidence that there are any better strategies than the one RATS employs.

Should RATS, therefore, be dismissed as a failure? Perhaps not. An important distinction between our work and that or Roelofs et al. (2009) and Rau et al. (2010) is strength of the 'other' science that can be performed with our data. The majority of sources found by the SDSS photometric search turned out to be helium-rich DB helium white dwarfs or quasars, sources which, while interesting, are relatively numerous and probably better identified in a more efficient manner (i.e. techniques requiring less telescope time). On the other hand, the data obtained during RATS observations has found many and various different classes of variable sources which are not related to the main science driver of the project. Indeed, it is likely that the most important science to come out of the RATS project will be wholly unrelated to AM CVn systems. A number of these are discussed in this thesis such as the DAV white dwarf with a hot companion, the SX Phe stars at large Galactocentric distances and the dwarf nova with high amplitude QPOs in quiescence. In many way, however, these sources are merely scratching the surface of information contained in the survey. In the next section I describe some classes of variable sources which could provide interesting scientific results in the future.

7.3 Detection of different classes of variability

Work is still very much ongoing with the RATS project, more wide-field data is currently being reduced while the reduced data is being picked though in order to discover individual sources of interest and also to study the Galactic population of whole classes of variable sources. Over the next few years many more publications are expected to come from this project, not least from a new Ph.D student who is working full time on the new data. Below I outline a few of the area of study which I think are of particular interest and which I very much hope the RATS team (myself included) will pursue.

7.3.1 Flare stars

One area where considerable effort has already been expended is on flare stars (indeed the first draft of this thesis contained some of our preliminary results but was later cut due the need to perform a proper statistical analysis of the flaring rate for the results to be comparable with other studies). Stellar flaring is due to magnetic reconnection events at the stellar photosphere such as those that occur on our Sun. These eruptions last for as short a time as only a few minutes and can increase the optical brightness of the star by a factor of over 100 (e.g. Kowalski et al., 2010). They are much more common on late type stars (typically M-dwarfs) than on earlier type stars. M-dwarfs are currently the subject of considerable interest from the exoplanet community because discovering a habitable planet via the transit method is considerably easier if the host star is intrinsically faint but apparently bright. For this reason it is of some importance to determine both what effect flaring has on the habitability of a planet and how often flaring events occur.

The method which we developed to identify flare stars combines the Alarm algorithm and the kurtosis of the light curve (see Chapter 4). We identified several hundred candidates but unfortunately flares bare a strong similarity to a minor planet passing though the PSF of a stellar source. The only method which we found to differentiate between these two scenarios is to manually examine a number of images of the star before and after the flare-like event and then remove those candidates where a body can be seen moving between frames. After this precess we were left with ~50 flares. Interestingly not all these appear to be late type dwarf stars. Future work will require an analysis of the completeness of this sample, taking this and the number of flares on M-dwarfs we can compare this to the total number of M-dwarfs in the survey on which we would be able to detect a flare. This will give us the flaring rate which can be directly compared with the results of Kowalski et al. (2009) who use the SDSS survey to estimate the rate of flaring in M-dwarfs. The advanced stage at which this work is at will ideally result in the submission of a paper before the year is out.

7.3.2 Contact binaries

Another area of science that is in a fairly advanced stage our analysis of the population of contact binaries in RATS data. These are main sequence binaries which are close enough to be in contact and have orbital periods from 0.23–0.7 d. Estimates on their number are as high as 1 per cent of main sequence stars (Rucinski, 1998). They are variable due to the heating of one side of each star by the other and the method which we use to identify them does not rely on sampling a whole orbit, indeed it is possible to determine very accurate system parameters (within a few per cent) with photometry of a section which makes up only 10–20 per cent of the orbital period.

This work has been performed in collaboration with Pasi Hakala in Finland who has been been working on identifying sources using POLY_FIT routine from the IDL astro library. We have so far discovered several thousand contact binaries a handful of which have fitted orbital period below the currently accepted period minimum of ~0.21 d (Rucinski & Pribulla, 2008). The future direction of this project will involve the identification of all contact binaries in the RATS data and the determining of both the sample completeness and false positive detection rate. One area where this work could have important implications is in distance measurements. There is a relatively well constrained period-luminosity-colour relation for contact binaries (Rucinski & Duerbeck, 1997) and with this we will be able to identify the special distribution of the Galaxy.

7.3.3 Variable M dwarfs

An area that we have recently started to look at is that of intrinsically periodically variable M stars. Though none have yet been discovered, it is thought that M dwarfs will show periodic variability if there is a strong enough magnetic field present (Amado Gonzalez, priv. comm.). The period of this variability is likely to be of an amplitude of only a few per cent and on a period of less than 2 h (Amado Gonzalez, priv. comm.). The are many tens of thousand stars in our data which vary on time-scales less than two hours and have colours consistent with M-dwarfs (though as reddening is high in some fields, the identification

of true M stars may prove to be a tricky proposition). A handful of apparently red stars have short-period variability (P < 40 min), if these can be confirmed to be M stars they have the potential to be very interesting candidates for further study, for example spectro-polarimetry of them will allow us to constrain the magnetic field strength of them.

7.4 RATS in Kepler

The *Kepler* satellite was launched in March 2009 and will operate for at least 3.5 years [the length of this mission is dependent on funding but given the high impact science which this mission has already produced (e.g. the discovery of a star with 6 transiting planets, Lissauer et al., 2011) a mission extension is likely]. The primary aim of this mission is the discovery of exoplanets, specifically Earth-mass planets in the habitable zone. *Kepler's* field of view is 105 deg^2 (an plot of the *Kepler* fields is shown in Fig. 7.1) and they are able to observe down to a depth of ~20 mag (Borucki et al., 2010). However, although there are millions of stars in the field of view, the spacecraft is only able to download the light curves data of ~150,000 stars at a cadence of 30 min. They also have a short-cadence mode which has a cadence of ~1 min and can observe 512 stars. Sources for which data is downloaded from the spacecraft must be predefined and the target lists are updated every month and every three months for the short- and long-cadence modes, respectively. Although the number of stars observed in the short-cadence mode is small, this is offset due to the fact that this list can be and is updated every month and this mode is currently somewhat under-utilised.

Considerable effort was made to identify stars which could host Earth-mass planets such as identifying – bright G and K-type stars with minimal stellar activity are prioritised. Aside for a few long cadence surveys of relatively bright sources (Hartman et al., 2004; Feldmeier et al., 2006) there was very little consideration of the stellar variability which *Kepler* is able to observe on short time-scales.

There have been several remarkable results from the observations of short period variables with *Kepler* but the majority of these were added to the *Kepler* input catalogue based

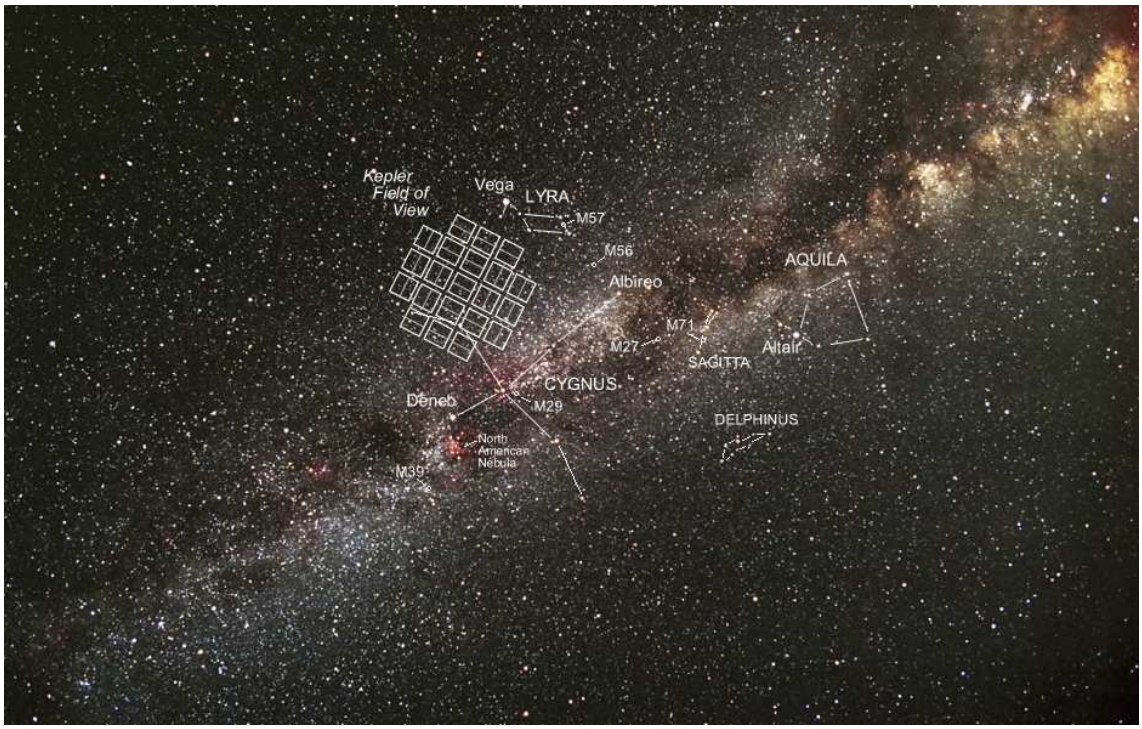

Figure 7.1: The field observed by the *Kepler* satellite. This field is observed almost continuously for the entire mission. The 42 CCDs are shown over the star field that is observed.

on their colour rather than any confirmed variability. Sources observed have included subdwarf B stars (Østensen et al., 2011) and accreting sources (Still et al., 2010). The impact of these is in allowing for the constraints to be placed on the internal stellar structure and to give insight into the evolution of an accretion disc before, during and after an outburst. Is is, however, disappointing that no pulsating white dwarf has yet been found as *Kepler* observation of these sources would allow for measurements of the depth of the hydrogen rich layer (Charpinet et al., 2006), the extent of radiative levitation and diffusion of heavy metal (Charpinet et al., 2008) and the degree of internal differential rotation (Kawaler & Hostler, 2005).

The RATS project will soon be taking a exciting new direction. To rectify the problem of a lack of short time-scale variability data we will be observing the *Kepler* field during the summer of 2011. The strategy is slightly modified from that of the original RATS design. While still using the INT, we will be performing all observations in the SDSS g' filter using a 20 s exposure, we are going to do this because the *Kepler* satellite is only capable of observing stars down to a brightness of $g' \sim 21$ which is the confusion limit so going deeper than this is surplus to our needs. We will also be reducing the length of our time-series

observations to one hour in order to observe as much of the field as possible (we aim to observe around a third of the field during 2011).

The plan is to use the same (or an updated) RATS pipeline as was used for the work in this thesis to identify the variable sources but to perform the photometry using the Cambridge Wide Field Unit's difference imaging pipelines which will allow us to produce a data produce much faster than if we use DANDIA (see § 2.2.1 for details of this method). We will then release a list of short period variables found in these data to the public as soon as possible. The reason for the need for expedience is to maximise the scientific output of the satellite while it is still flying (and the value of the data we produce will, hopefully, help to extend the mission funding). The lessons learnt during the work on this thesis will have a direct impact on the productivity of the *Kepler* mission.

In conclusion, the RATS project has produced some exciting discoveries so far and will increase in scientific productivity in the months and years to come as I have developed an efficient method to process the data. The two strands of the project – to study the data obtained using the RATS strategy discussed here and the RATS in *Kepler* project – mean that wide-field high cadence surveys from the INT have a bright (but potentially short due to funding) future. The techniques I have developed will also be used in other projects to increase the scientific impact of these works (for example the *Kepler* Guest Observer Office will be using the techniques I developed to identify stellar variables).

The End

Selected Acronyms & Abbreviations

ALFOSC	Andalucia Faint Object Spectrograph and Camera
AoV	Analysis of variance
AoV-FAP	Analysis of variance false-alarm probability
CCD	Charge-coupled device
CE	Common envelope
CV	Cataclysmic Variable
DAV	Variable hydrogen-rich white dwarf
DIA	Difference image analysis
DN	Dwarf Nova
FSVS	Faint Sky Variability Survey
FWHM	Full width at half maximum
EFOSC2	ESO Faint Object Spectrograph and Camera (v.2)
ESO	Eurpoean Southern Observatory
GMOS	Gemini Multi-Object Spectrograph
INT	Isaac Newton Telescope
ISIS	Intermediate dispersion Spectrograph and Imaging System
LISA	Laser Interferometer Space Antenna
LS	Lomb-Scargle periodogram
LS-FAP	Lomb-Scargle false-alarm probability
NOT	Nordic Optical Telescope
PSF	Point spread function
QPO	Quasi-peroidic oscillation
RATS	Rapid Temporal Survey
RGO	Royal Grennwich Observatory
rms	Root mean square
sdB	Sub-dwarf B star
SAAO	South African Astronomical Observatory
SDSS	Sloan Digital Sky Survey
SJS	Stetson J statistic
WFC	Wide Field Camera
WFI	Wide Field Imager
WHT	William Herschel Telescope

Bibliography

Abazajian K. N., Adelman-McCarthy J. K., Agüeros M. A., Allam S. S., Allende Prieto C., An D., Anderson K. S. J., Anderson S. F., Annis J., Bahcall N. A., et al., 2009, ApJS, 182, 543

Alard C., Lupton R. H., 1998, ApJ, 503, 325

Amado P. J., Moya A., Suárez J. C., Martín-Ruiz S., Garrido R., Rodríguez E., Catala C., Goupil M. J., 2004, MNRAS, 352, L11

Anderson S. F., Becker A. C., Haggard D., Prieto J. L., Knapp G. R., Sako M., Halford K. E., Jha S., Martin B., Holtzman J., Frieman J. A., Garnavich P. M., Hayward S., 2008, AJ, 135, 2108

Anderson S. F., Haggard D., Homer L., Joshi N. R., Margon B., Silvestri N. M., Szkody P., Wolfe M. A., Agol E., Becker A. C., Henden A., Hall P. B., Knapp G. R., Richmond M. W., Schneider D. P., Stinson G., 2005, AJ, 130, 2230

Andrews A. D., 1967, PASP, 79, 368

Argelander F. W. A., 1869, Beobachtungen und Rechnungen Ãijber verÃd̈nderliche Sterne. Bonn, M.

Astier P., Guy J., Regnault N., Pain R., Aubourg E., Balam D., Basa S., Carlberg R. G., Fabbro S., Fouchez D., Hook I. M., Howell D. A., Lafoux H., Neill J. D., Palanque-Delabrouille N., Perrett K., Pritchet C. J., Rich J., Sullivan M., Taillet R., Aldering G., Antilogus P., Arsenijevic V., Balland C., Baumont S., Bronder J., Courtois H., Ellis R. S., Filiol M., Gonçalves A. C., Goobar A., Guide D., Hardin D., Lusset V., Lidman C., McMahon R.,

Mouchet M., Mourao A., Perlmutter S., Ripoche P., Tao C., Walton N., 2006, A&A, 447, 31

Augusteijn T., van der Hooft F., de Jong J. A., van Paradijs J., 1996, A&A, 311, 889

Balmforth N. J., Cunha M. S., Dolez N., Gough D. O., Vauclair S., 2001, MNRAS, 323, 362

Baran A. S., Gilker J. T., Fox-Machado L., Reed M. D., Kawaler S. D., 2010, MNRAS, 1689

Barclay T., Ramsay G., Steeghs D., Wheatley P., Rosen S., 2009, The Astronomer's Telegram, 2334, 1

Barron J. T., Stumm C., Hogg D. W., Lang D., Roweis S., 2008, AJ, 135, 414

Barros S. C. C., Marsh T. R., Dhillon V. S., Groot P. J., Littlefair S., Nelemans G., Roelofs G., Steeghs D., Wheatley P. J., 2007, MNRAS, 374, 1334

Bertin E., Arnouts S., 1996, A&AS, 117, 393

Bond I. A., Abe F., Dodd R. J., Hearnshaw J. B., Honda M., Jugaku J., Kilmartin P. M., Marles A., Masuda K., Matsubara Y., Muraki Y., Nakamura T., Nankivell G., Noda S., Noguchi C., Ohnishi K., Rattenbury N. J., Reid M., Saito T., Sato H., Sekiguchi M., Skuljan J., Sullivan D. J., Sumi T., Takeuti M., Watase Y., Wilkinson S., Yamada R., Yanagisawa T., Yock P. C. M., 2001, MNRAS, 327, 868

Borucki W. J., Koch D., Basri G., Batalha N., Brown T., Caldwell D., Caldwell J., Christensen-Dalsgaard J., Cochran W. D., DeVore E., Dunham E. W., Dupree A. K., Gautier T. N., Geary J. C., Gilliland R., Gould A., Howell S. B., Jenkins J. M., Kondo Y., Latham D. W., Marcy G. W., Meibom S., Kjeldsen H., Lissauer J. J., Monet D. G., Morrison D., Sasselov D., Tarter J., Boss A., Brownlee D., Owen T., Buzasi D., Charbonneau D., Doyle L., Fortney J., Ford E. B., Holman M. J., Seager S., Steffen J. H., Welsh W. F., Rowe J., Anderson H., Buchhave L., Ciardi D., Walkowicz L., Sherry W., Horch E., Isaacson H., Everett M. E., Fischer D., Torres G., Johnson J. A., Endl M., MacQueen P., Bryson S. T., Dotson J., Haas M., Kolodziejczak J., Van Cleve J., Chandrasekaran H., Twicken J. D., Quintana E. V., Clarke B. D., Allen C., Li J., Wu H., Tenenbaum P., Verner E., Bruhweiler F., Barnes J., Prsa A., 2010, Science, 327, 977

Bramich D. M., 2008, MNRAS, 386, L77

Breger M., 1972, ApJ, 176, 367

—, 1995, in Astronomical Society of the Pacific Conference Series, Vol. 76, GONG 1994. Helio- and Astro-Seismology from the Earth and Space, R. K. Ulrich, E. J. Rhodes Jr., & W. Dappen, ed., pp. 596–+

Bruch A., Steiner J. E., Gneiding C. D., 2000, PASP, 112, 237

Budding E., Erdem A., Çiçek C., Bulut I., Soydugan F., Soydugan E., Bakiş V., Demircan O., 2004, A&A, 417, 263

Burd A., Cwiok M., Czyrkowski H., Dabrowski R., Dominik W., Grajda M., Husejko M., Jegier M., Kalicki A., Kasprowicz G., Kierzkowski K., Krupska K., Kwiecinska K., Mankiewicz L., Nawrocki K., Pilecki B., Piotrowski L. W., Pozniak K., Romaniuk R., Salanski R., Sokolowski M., Szczygiel D., Wrochna G., Zabolotny W., 2005, New A, 10, 409

Burwitz V., Reinsch K., 2001, X-ray Astronomy: Stellar Endpoints, AGN, and the Diffuse X-ray Background, 599, 522

Cardelli J. A., Clayton G. C., Mathis J. S., 1989, ApJ, 345, 245

Carrington R. C., 1859, MNRAS, 19, 81

Castanheira B. G., Kepler S. O., Kleinman S. J., Nitta A., Fraga L., 2010, MNRAS, 405, 2561

Castelli F., Kurucz R. L., 2004, preprint (astro-ph/0405087)

Charpinet S., Fontaine G., Brassard P., Chayer P., 2008, Communications in Asteroseismology, 157, 168

Charpinet S., Silvotti R., Bonanno A., Fontaine G., Brassard P., Chayer P., Green E. M., Bergeron P., Bernabei S., Leccia S., Kjeldsen H., Janulis R., Frasca A., Østensen R., Kim S., Park B., Jiang X., Reed M. D., Patterson R. S., Gietzen K. M., Clark P. J., Wolf G. W., Lipkin Y., Formiggini L., Leibowitz E., Oswalt T. D., Rudkin M., Johnston K., 2006, A&A, 459, 565

Chen B., Stoughton C., Smith J. A., Uomoto A., Pier J. R., Yanny B., Ivezić Ž., York D. G., Anderson J. E., Annis J., Brinkmann J., Csabai I., Fukugita M., Hindsley R., Lupton R., Munn J. A., the SDSS Collaboration, 2001, ApJ, 553, 184

Chevalier C., 1971, A&A, 14, 24

Chornock R., Filippenko A. V., 2003, IAU Circ., 8084, 3

Clemens J. C., van Kerkwijk M. H., Wu Y., 2000, MNRAS, 314, 220

Collier Cameron A., Pollacco D., Street R. A., Lister T. A., West R. G., Wilson D. M., Pont F., Christian D. J., Clarkson W. I., Enoch B., Evans A., Fitzsimmons A., Haswell C. A., Hellier C., Hodgkin S. T., Horne K., Irwin J., Kane S. R., Keenan F. P., Norton A. J., Parley N. R., Osborne J., Ryans R., Skillen I., Wheatley P. J., 2006, MNRAS, 373, 799

Copperwheat C. M., Marsh T. R., Littlefair S. P., Dhillon V. S., Ramsay G., Drake A. J., Gänsicke B. T., Groot P. J., Hakala P., Koester D., Nelemans G., Roelofs G., Southworth J., Steeghs D., Tulloch S., 2011, MNRAS, 410, 1113

Cox A. N., King D. S., Tabor J. E., 1973, ApJ, 184, 201

Cox J. P., 1980, Theory of stellar pulsation, Cox, J. P., ed.

Cropper M., Harrop-Allin M. K., Mason K. O., Mittaz J. P. D., Potter S. B., Ramsay G., 1998, MNRAS, 293, L57

de Jong J. T. A., Yanny B., Rix H., Dolphin A. E., Martin N. F., Beers T. C., 2010, ApJ, 714, 663

Devor J., 2005, ApJ, 628, 411

Djorgovski S. G., Baltay C., Mahabal A. A., Drake A. J., Williams R., Rabinowitz D., Graham M. J., Donalek C., Glikman E., Bauer A., Scalzo R., Ellman N., 2008, Astronomische Nachrichten, 329, 263

Drake A. J., Djorgovski S. G., Mahabal A., Beshore E., Larson S., Graham M. J., Williams R., Christensen E., Catelan M., Boattini A., Gibbs A., Hill R., Kowalski R., 2009, ApJ, 696, 870

Dupret M., Théado S., Noels A., 2008, Journal of Physics Conference Series, 118, 012052

Duquennoy A., Mayor M., 1991, A&A, 248, 485

Eaton N., Draper P. W., Allan A., 2003, Starlink User Note 45

Eggen O. J., 1970, PASP, 82, 274

Elkin V. G., Riley J. D., Cunha M. S., Kurtz D. W., Mathys G., 2005, MNRAS, 358, 665

Elvius A., 1975, A&A, 44, 117

Feldmeier J. J., Howell S., Harding P., Mihos C., Rudick C., Sherry W., Lee T., Knox C., Ciardi D., von Braun K., Everett M., Proctor M., van Belle G., 2006, in Bulletin of the American Astronomical Society, Vol. 38, American Astronomical Society Meeting Abstracts, p. 162.15

Fitzpatrick E. L., 1999, PASP, 111, 63

Fontaine G., Brassard P., 2008, PASP, 120, 1043

Fontaine G., Brassard P., Green E. M., Charpinet S., Dufour P., Hubeny I., Steeghs D., Aerts C., Randall S. K., Bergeron P., Guvenen B., O'Malley C. J., Van Grootel V., Østensen R. H., Bloemen S., Silvotti R., Howell S. B., Baran A., Kepler S. O., Marsh T. R., Montgomery M. H., Oreiro R., Provencal J., Telting J., Winget D. E., Zima W., Christensen-Dalsgaard J., Kjeldsen H., 2011, ApJ, 726, 92

Fontaine G., Lacombe P., McGraw J. T., Dearborn D. S. P., Gustafson J., 1982, ApJ, 258, 651

Frieman J. A., Bassett B., Becker A., Choi C., Cinabro D., DeJongh F., Depoy D. L., Dilday B., Doi M., Garnavich P. M., Hogan C. J., Holtzman J., Im M., Jha S., Kessler R., Konishi K., Lampeitl H., Marriner J., Marshall J. L., McGinnis D., Miknaitis G., Nichol R. C., Prieto J. L., Riess A. G., Richmond M. W., Romani R., Sako M., Schneider D. P., Smith M., Takanashi N., Tokita K., van der Heyden K., Yasuda N., Zheng C., Adelman-McCarthy J., Annis J., Assef R. J., Barentine J., Bender R., Blandford R. D., Boroski W. N., Bremer M., Brewington H., Collins C. A., Crotts A., Dembicky J., Eastman J., Edge A., Edmondson E., Elson E., Eyler M. E., Filippenko A. V., Foley R. J., Frank S., Goobar A., Gueth T.,

Gunn J. E., Harvanek M., Hopp U., Ihara Y., Ivezić Ž., Kahn S., Kaplan J., Kent S., Ketzeback W., Kleinman S. J., Kollatschny W., Kron R. G., Krzesiński J., Lamenti D., Leloudas G., Lin H., Long D. C., Lucey J., Lupton R. H., Malanushenko E., Malanushenko V., McMillan R. J., Mendez J., Morgan C. W., Morokuma T., Nitta A., Ostman L., Pan K., Rockosi C. M., Romer A. K., Ruiz-Lapuente P., Saurage G., Schlesinger K., Snedden S. A., Sollerman J., Stoughton C., Stritzinger M., Subba Rao M., Tucker D., Vaisanen P., Watson L. C., Watters S., Wheeler J. C., Yanny B., York D., 2008, AJ, 135, 338

Gabriel K. R., Zamir S., 1979, Technometrics, 21, 489

Galilei G., Welser M., de Filiis A., 1613, Istoria E dimostrazioni intorno alle macchie solari E loro accidenti comprese in tre lettere scritte all'illvstrissimo signor Marco Velseri ..., Galilei, G., Welser, M., & de Filiis, A., ed.

Gänsicke B. T., 2005, in Astronomical Society of the Pacific Conference Series, Vol. 330, The Astrophysics of Cataclysmic Variables and Related Objects, J.-M. Hameury & J.-P. Lasota, ed., pp. 3–+

Gänsicke B. T., Rodríguez-Gil P., Marsh T. R., de Martino D., Nestoras J., Szkody P., Aungwerojwit A., Barros S. C. C., Dillon M., Araujo-Betancor S., Arévalo M. J., Casares J., Groot P. J., Kolb U., Lázaro C., Hakala P., Martínez-Pais I. G., Nelemans G., Roelofs G., Schreiber M. R., van den Besselaar E., Zurita C., 2006, MNRAS, 365, 969

Gehrels N., Chincarini G., Giommi P., Mason K. O., Nousek J. A., Wells A. A., White N. E., Barthelmy S. D., Burrows D. N., Cominsky L. R., Hurley K. C., Marshall F. E., Mészáros P., Roming P. W. A., Angelini L., Barbier L. M., Belloni T., Campana S., Caraveo P. A., Chester M. M., Citterio O., Cline T. L., Cropper M. S., Cummings J. R., Dean A. J., Feigelson E. D., Fenimore E. E., Frail D. A., Fruchter A. S., Garmire G. P., Gendreau K., Ghisellini G., Greiner J., Hill J. E., Hunsberger S. D., Krimm H. A., Kulkarni S. R., Kumar P., Lebrun F., Lloyd-Ronning N. M., Markwardt C. B., Mattson B. J., Mushotzky R. F., Norris J. P., Osborne J., Paczynski B., Palmer D. M., Park H., Parsons A. M., Paul J., Rees M. J., Reynolds C. S., Rhoads J. E., Sasseen T. P., Schaefer B. E., Short A. T., Smale A. P., Smith I. A., Stella L., Tagliaferri G., Takahashi T., Tashiro M., Townsley L. K.,

Tueller J., Turner M. J. L., Vietri M., Voges W., Ward M. J., Willingale R., Zerbi F. M., Zhang W. W., 2004, ApJ, 611, 1005

Greenstein J. L., Matthews M. S., 1957, ApJ, 126, 14

Groot P. J., Vreeswijk P. M., Huber M. E., Everett M. E., Howell S. B., Nelemans G., van Paradijs J., van den Heuvel E. P. J., Augusteijn T., Kuulkers E., Rutten R. G. M., Storm J., 2003, MNRAS, 339, 427

Güver T., Özel F., 2009, MNRAS, 400, 2050

Hampel F. R., 1974, Journal of the American Statistical Association, 69, 383

Hartman J. D., Bakos G., Stanek K. Z., Noyes R. W., 2004, AJ, 128, 1761

Hartman J. D., Gaudi B. S., Holman M. J., McLeod B. A., Stanek K. Z., Barranco J. A., Pinsonneault M. H., Kalirai J. S., 2008, ApJ, 675, 1254

Holberg J. B., Bergeron P., 2006, AJ, 132, 1221

Horne J. H., Baliunas S. L., 1986, ApJ, 302, 757

Howell S. B., 2000, Handbook of CCD Astronomy, Howell, S. B., ed.

Howell S. B., Dobrzycka D., Szkody P., Kreidl T. J., 1991, PASP, 103, 300

Humason M. L., Zwicky F., 1947, ApJ, 105, 85

Iben Jr. I., Tutukov A. V., 1987, ApJ, 313, 727

Israel G. L., Panzera M. R., Campana S., Lazzati D., Covino S., Tagliaferri G., Stella L., 1999, A&A, 349, L1

Ivezic Z., Tyson J. A., Allsman R., Andrew J., Angel R., for the LSST Collaboration, 2008, ArXiv e-prints

Jacoby G. H., Hunter D. A., Christian C. A., 1984, ApJS, 56, 257

Jarrett T. H., Chester T., Cutri R., Schneider S., Skrutskie M., Huchra J. P., 2000, AJ, 119, 2498

Jester S., Schneider D. P., Richards G. T., Green R. F., Schmidt M., Hall P. B., Strauss M. A., Vanden Berk D. E., Stoughton C., Gunn J. E., Brinkmann J., Kent S. M., Smith J. A., Tucker D. L., Yanny B., 2005, AJ, 130, 873

Jordan S., Koester D., Vauclair G., Dolez N., Heber U., Hagen H., Reimers D., Chevreton M., Dreizler S., 1998, A&A, 330, 277

Joshi Y. C., 2005, MNRAS, 362, 1259

Kalberla P. M. W., Burton W. B., Hartmann D., Arnal E. M., Bajaja E., Morras R., Pöppel W. G. L., 2005, A&A, 440, 775

Katz J. I., 1975, ApJ, 200, 298

Kawaler S. D., Hostler S. R., 2005, ApJ, 621, 432

Kepler S. O., 1987, IAU Circ., 4332, 2

Kinemuchi K., Smith H. A., Woźniak P. R., McKay T. A., 2006, AJ, 132, 1202

Kochukhov O., Bagnulo S., Lo Curto G., Ryabchikova T., 2009, A&A, 493, L45

Koester D., Napiwotzki R., Christlieb N., Drechsel H., Hagen H., Heber U., Homeier D., Karl C., Leibundgut B., Moehler S., Nelemans G., Pauli E., Reimers D., Renzini A., Yungelson L., 2001, A&A, 378, 556

Kong D., Zhu Z., 2008, Chinese Astron. Astrophys., 32, 360

Kovács G., Zucker S., Mazeh T., 2002, A&A, 391, 369

Kowalski A. F., Hawley S. L., Hilton E. J., Becker A. C., West A. A., Bochanski J. J., Sesar B., 2009, AJ, 138, 633

Kowalski A. F., Hawley S. L., Holtzman J. A., Wisniewski J. P., Hilton E. J., 2010, ApJ, 714, L98

Kraft R. P., Mathews J., Greenstein J. L., 1962, ApJ, 136, 312

Kramer M., Stairs I. H., Manchester R. N., McLaughlin M. A., Lyne A. G., Ferdman R. D., Burgay M., Lorimer D. R., Possenti A., D'Amico N., Sarkissian J. M., Hobbs G. B., Reynolds J. E., Freire P. C. C., Camilo F., 2006, Science, 314, 97

Kurtz D. W., Shibahashi H., Dhillon V. S., Marsh T. R., Littlefair S. P., 2008, MNRAS, 389, 1771

Landolt A. U., 1992, AJ, 104, 340

Lang D., Hogg D. W., Mierle K., Blanton M., Roweis S., 2010, AJ, 139, 1782

Law N. M., Kulkarni S. R., Dekany R. G., Ofek E. O., Quimby R. M., Nugent P. E., Surace J., Grillmair C. C., Bloom J. S., Kasliwal M. M., Bildsten L., Brown T., Cenko S. B., Ciardi D., Croner E., Djorgovski S. G., van Eyken J., Filippenko A. V., Fox D. B., Gal-Yam A., Hale D., Hamam N., Helou G., Henning J., Howell D. A., Jacobsen J., Laher R., Mattingly S., McKenna D., Pickles A., Poznanski D., Rahmer G., Rau A., Rosing W., Shara M., Smith R., Starr D., Sullivan M., Velur V., Walters R., Zolkower J., 2009, PASP, 121, 1395

Lissauer J. J., Fabrycky D. C., Ford E. B., Borucki W. J., Fressin F., Marcy G. W., Orosz J. A., Rowe J. F., Torres G., Welsh W. F., Batalha N. M., Bryson S. T., Buchhave L. A., Caldwell D. A., Carter J. A., Charbonneau D., Christiansen J. L., Cochran W. D., Desert J., Dunham E. W., Fanelli M. N., Fortney J. J., Gautier III T. N., Geary J. C., Gilliland R. L., Haas M. R., Hall J. R., Holman M. J., Koch D. G., Latham D. W., Lopez E., McCauliff S., Miller N., Morehead R. C., Quintana E. V., Ragozzine D., Sasselov D., Short D. R., Steffen J. H., 2011, Nature, 470, 53

Lomb N. R., 1976, Ap&SS, 39, 447

Maciel S. C., Osorio Y. F. M., de Medeiros J. R., 2011, New A, 16, 68

Malmquist K. G., 1936, Stockholms Observatoriums Annaler, 12, 7

Mandel K., Agol E., 2002, ApJ, 580, L171

Marsh T. R., 1989, PASP, 101, 1032

Martinez P., Ashoka B. N., Kurtz D. W., Gupta S. K., Chaubey U. S., 1999, Information Bulletin on Variable Stars, 4677, 1

Martinez-Pais I. G., Giovannelli F., Rossi C., Gaudenzi S., 1994, A&A, 291, 455

McNamara D., 1997, PASP, 109, 1221

McNamara D. H., Redcorn M. E., 1977, PASP, 89, 61

Morales-Rueda L., Groot P. J., Augusteijn T., Nelemans G., Vreeswijk P. M., van den Besselaar E. J. M., 2006, MNRAS, 371, 1681

Motch C., Haberl F., Guillout P., Pakull M., Reinsch K., Krautter J., 1996, A&A, 307, 459

Murphy S., Keller S., Schmidt B., Tisserand P., Bessell M., Francis P., Costa G. D., 2009, in Astronomical Society of the Pacific Conference Series, Vol. 404, Astronomical Society of the Pacific Conference Series, S. J. Murphy & M. S. Bessell, ed., pp. 356–+

Nakar E., Piran T., Granot J., 2002, ApJ, 579, 699

Napiwotzki R., Yungelson L., Nelemans G., Marsh T. R., Leibundgut B., Renzini R., Homeier D., Koester D., Moehler S., Christlieb N., Reimers D., Drechsel H., Heber U., Karl C., Pauli E., 2004, in Astronomical Society of the Pacific Conference Series, Vol. 318, Spectroscopically and Spatially Resolving the Components of the Close Binary Stars, R. W. Hilditch, H. Hensberge, & K. Pavlovski, ed., p. 402

Nather R. E., Robinson E. L., Stover R. J., 1981, ApJ, 244, 269

Nather R. E., Wood M. A., Winget D. E., Liebert J., 1984, IAU Circ., 4021, 2

Nelder J. A., Mead R., 1965, Computer Journal, 7, 308

Nelemans G., 2005, in Astronomical Society of the Pacific Conference Series, Vol. 330, The Astrophysics of Cataclysmic Variables and Related Objects, Hameury J.-M., Lasota J.-P., eds., p. 27

Nelemans G., Portegies Zwart S. F., Verbunt F., Yungelson L. R., 2001a, A&A, 368, 939

Nelemans G., Steeghs D., Groot P. J., 2001b, MNRAS, 326, 621

Nelemans G., Yungelson L. R., Portegies Zwart S. F., 2004, MNRAS, 349, 181

Nemec J., Mateo M., 1990, in Astronomical Society of the Pacific Conference Series, Vol. 11, Confrontation Between Stellar Pulsation and Evolution, C. Cacciari & G. Clementini, ed., pp. 64–84

Nitta A., Kleinman S. J., Krzesinski J., Kepler S. O., Metcalfe T. S., Mukadam A. S., Mullally F., Nather R. E., Sullivan D. J., Thompson S. E., Winget D. E., 2009, ApJ, 690, 560

O'Donoghue D., Kilkenny D., Chen A., Stobie R. S., Koen C., Warner B., Lawson W. A., 1994, MNRAS, 271, 910

O'Donoghue D., Menzies J. W., Hill P. W., 1987, MNRAS, 227, 347

Østensen R. H., Silvotti R., Charpinet S., Oreiro R., Bloemen S., Baran A. S., Reed M. D., Kawaler S. D., Telting J. H., Green E. M., O'Toole S. J., Aerts C., Gänsicke B. T., Marsh T. R., Breedt E., Heber U., Koester D., Quint A. C., Kurtz D. W., Rodríguez-López C., Vučković M., Ottosen T. A., Frimann S., Somero A., Wilson P. A., Thygesen A. O., Lindberg J. E., Kjeldsen H., Christensen-Dalsgaard J., Allen C., McCauliff S., Middour C. K., 2011, ArXiv e-prints

Paczyński B., 1967, Acta Astron., 17, 287

—, 1978, in Nonstationary Evolution of Close Binaries, A. N. Zytkow, ed., pp. 89–+

Palmer D. M., 2009, ApJ, 695, 496

Pecker J., ed., 1970, Astrophysics and Space Science Library, Vol. 21, Space observatories

Pereira C., Jeffery C. S., 2008, in Astronomical Society of the Pacific Conference Series, Vol. 392, Hot Subdwarf Stars and Related Objects, U. Heber, C. S. Jeffery, & R. Napiwotzki, ed., p. 123

Piro A. L., Bildsten L., 2004, ApJ, 616, L155

Plavchan P., Jura M., Kirkpatrick J. D., Cutri R. M., Gallagher S. C., 2008, ApJS, 175, 191

Podsiadlowski P., Han Z., Rappaport S., 2003, MNRAS, 340, 1214

Poggendorff J. C., 1863, 1: Biograpisch-Literarisches Handworterbuch zur Geschischte der Extacten Wissenschaften enhaltend nachwe isungen uber lebensverhaltinisse und Leistungen von Mathematikern

Pollacco D. L., Skillen I., Cameron A. C., Christian D. J., Hellier C., Irwin J., Lister T. A., Street R. A., West R. G., Anderson D., Clarkson W. I., Deeg H., Enoch B., Evans A., Fitzsimmons A., Haswell C. A., Hodgkin S., Horne K., Kane S. R., Keenan F. P., Maxted P. F. L., Norton A. J., Osborne J., Parley N. R., Ryans R. S. I., Smalley B., Wheatley P. J., Wilson D. M., 2006, PASP, 118, 1407

Poole T. S., Breeveld A. A., Page M. J., Landsman W., Holland S. T., Roming P., Kuin N. P. M., Brown P. J., Gronwall C., Hunsberger S., Koch S., Mason K. O., Schady P., vanden Berk D., Blustin A. J., Boyd P., Broos P., Carter M., Chester M. M., Cucchiara A., Hancock B., Huckle H., Immler S., Ivanushkina M., Kennedy T., Marshall F., Morgan A., Pandey S. B., de Pasquale M., Smith P. J., Still M., 2008, MNRAS, 383, 627

Poretti E., 1989, A&A, 220, 144

Poretti E., Clementini G., Held E. V., Greco C., Mateo M., Dell'Arciprete L., Rizzi L., Gullieuszik M., Maio M., 2008, ApJ, 685, 947

Press W. H., Rybicki G. B., 1989, ApJ, 338, 277

Press W. H., Teukolsky S. A., Vetterling W. T., Flannery B. P., 1992, Numerical recipes in C. The art of scientific computing

Pretorius M. L., Warner B., Woudt P. A., 2006, MNRAS, 368, 361

Pribulla T., Kreiner J. M., Tremko J., 2003, Contributions of the Astronomical Observatory Skalnate Pleso, 33, 38

Prieto J., Anderson S., Becker A., Marriner J., Sako M., Jha S., 2006, Central Bureau Electronic Telegrams, 692, 1

Quimby R. M., 2006, PhD thesis, The University of Texas at Austin

Racusin J. L., Karpov S. V., Sokolowski M., Granot J., Wu X. F., Pal'Shin V., Covino S., van der Horst A. J., Oates S. R., Schady P., Smith R. J., Cummings J., Starling R. L. C., Piotrowski L. W., Zhang B., Evans P. A., Holland S. T., Malek K., Page M. T., Vetere L., Margutti R., Guidorzi C., Kamble A. P., Curran P. A., Beardmore A., Kouveliotou C., Mankiewicz L., Melandri A., O'Brien P. T., Page K. L., Piran T., Tanvir N. R., Wrochna G., Aptekar R. L., Barthelmy S., Bartolini C., Beskin G. M., Bondar S., Bremer M., Campana S., Castro-Tirado A., Cucchiara A., Cwiok M., D'Avanzo P., D'Elia V., Della Valle M., de Ugarte Postigo A., Dominik W., Falcone A., Fiore F., Fox D. B., Frederiks D. D., Fruchter A. S., Fugazza D., Garrett M. A., Gehrels N., Golenetskii S., Gomboc A., Gorosabel J., Greco G., Guarnieri A., Immler S., Jelinek M., Kasprowicz G., La Parola V., Levan A. J., Mangano V., Mazets E. P., Molinari E., Moretti A., Nawrocki K., Oleynik P. P., Osborne J. P., Pagani C., Pandey S. B., Paragi Z., Perri M., Piccioni A., Ramirez-Ruiz E., Roming P. W. A., Steele I. A., Strom R. G., Testa V., Tosti G., Ulanov M. V., Wiersema K., Wijers R. A. M. J., Winters J. M., Zarnecki A. F., Zerbi F., Mészáros P., Chincarini G., Burrows D. N., 2008, Nature, 455, 183

Ramsay G., Cropper M., Wu K., Mason K. O., Hakala P., 2000, MNRAS, 311, 75

Ramsay G., Hakala P., 2005, MNRAS, 360, 314

Ramsay G., Hakala P., Barclay T., Wheatley P., Marshall G., Lehto H., Napiwotzki R., Nelemans G., Potter S., Todd I., 2009, MNRAS, 398, 1333

Ramsay G., Hakala P., Cropper M., 2002a, MNRAS, 332, L7

Ramsay G., Kotko I., Barclay T., Copperwheat C., Rosen S., Jeffery C. S., Marsh T., Steeghs D., Wheatley P., 2010, MNRAS, accepted, ArXiv eprint: http://arxiv.org/abs/1005.3398

Ramsay G., Napiwotzki R., Hakala P., Lehto H., 2006, MNRAS, 371, 957

Ramsay G., Wu K., Cropper M., Schmidt G., Sekiguchi K., Iwamuro F., Maihara T., 2002b, MNRAS, 333, 575

Rau A., Kulkarni S. R., Law N. M., Bloom J. S., Ciardi D., Djorgovski G. S., Fox D. B., Gal-Yam A., Grillmair C. C., Kasliwal M. M., Nugent P. E., Ofek E. O., Quimby R. M., Reach

W. T., Shara M., Bildsten L., Cenko S. B., Drake A. J., Filippenko A. V., Helfand D. J., Helou G., Howell D. A., Poznanski D., Sullivan M., 2009, PASP, 121, 1334

Rau A., Roelofs G. H. A., Groot P. J., Marsh T. R., Nelemans G., Steeghs D., Salvato M., Kasliwal M. M., 2010, ApJ, 708, 456

Rees M. J., 1988, Nature, 333, 523

Richer H. B., Auman J. R., Isherwood B. C., Steele J. P., Ulrych T. J., 1973, ApJ, 180, 107

Ritter H., 2008, ArXiv e-prints

Robin A. C., Reylé C., Derrière S., Picaud S., 2003, A&A, 409, 523

Rodríguez E., López-González M. J., López de Coca P., 2000, A&AS, 144, 469

Rodriguez E., Rolland A., Lopez de Coca P., 1990, Ap&SS, 169, 113

Roelofs G. H. A., 2007, PhD thesis, Radboud Universiteit Nijmegen

Roelofs G. H. A., Groot P. J., Benedict G. F., McArthur B. E., Steeghs D., Morales-Rueda L., Marsh T. R., Nelemans G., 2007a, ApJ, 666, 1174

Roelofs G. H. A., Groot P. J., Marsh T. R., Steeghs D., Barros S. C. C., Nelemans G., 2005, MNRAS, 361, 487

Roelofs G. H. A., Groot P. J., Marsh T. R., Steeghs D., Nelemans G., 2006, MNRAS, 365, 1109

Roelofs G. H. A., Groot P. J., Nelemans G., Marsh T. R., Steeghs D., 2007b, MNRAS, 379, 176

Roelofs G. H. A., Groot P. J., Steeghs D., Nelemans G., 2004, in Revista Mexicana de Astronomia y Astrofisica, vol. 27, Vol. 20, Revista Mexicana de Astronomia y Astrofisica Conference Series, G. Tovmassian & E. Sion, ed., pp. 254–254

Roelofs G. H. A., Groot P. J., Steeghs D., Rau A., de Groot E., Marsh T. R., Nelemans G., Liebert J., Woudt P., 2009, MNRAS, 394, 367

Roelofs G. H. A., Nelemans G., Groot P. J., 2007c, MNRAS, 382, 685

Roelofs G. H. A., Rau A., Marsh T. R., Steeghs D., Groot P. J., Nelemans G., 2010, ApJ, 711, L138

Rousseeuw P. J., Croux C., 1993, Journal of the American Statistical Association, 88, 1273

Rucinski S. M., 1998, AJ, 116, 2998

Rucinski S. M., Duerbeck H. W., 1997, PASP, 109, 1340

Rucinski S. M., Pribulla T., 2008, ArXiv e-prints, 805

Ryabchikova T., Piskunov N., Kochukhov O., Tsymbal V., Mittermayer P., Weiss W. W., 2002, A&A, 384, 545

Samus N. N., Durlevich O. V., et al., 2009, VizieR Online Data Catalog, 1, 2025

Savonije G. J., de Kool M., van den Heuvel E. P. J., 1986, A&A, 155, 51

Scalo J., Kaltenegger L., Segura A. G., Fridlund M., Ribas I., Kulikov Y. N., Grenfell J. L., Rauer H., Odert P., Leitzinger M., Selsis F., Khodachenko M. L., Eiroa C., Kasting J., Lammer H., 2007, Astrobiology, 7, 85

Scargle J. D., 1982, ApJ, 263, 835

Schlegel D. J., Finkbeiner D. P., Davis M., 1998, ApJ, 500, 525

Schultheis M., Robin A. C., Reylé C., McCracken H. J., Bertin E., Mellier Y., Le Fèvre O., 2006, A&A, 447, 185

Schwabe M., 1844, Astronomische Nachrichten, 21, 233

Schwartz M., 1998, IAU Circ., 6982, 1

Schwarzenberg-Czerny A., 1989, MNRAS, 241, 153

—, 1991, MNRAS, 253, 198

Segura A., Walkowicz L. M., Meadows V., Kasting J., Hawley S., 2010, Astrobiology, 10, 751

Shafter A. W., Hessman F. V., 1988, AJ, 95, 178

Sion E. M., Greenstein J. L., Landstreet J. D., Liebert J., Shipman H. L., Wegner G. A., 1983, ApJ, 269, 253

Smak J., 1967, Information Bulletin on Variable Stars, 182, 1

Smartt S. J., 2009, ARA&A, 47, 63

Smith A. J., Haswell C. A., Hynes R. I., 2006, MNRAS, 369, 1537

Solheim J., 2010, PASP, 122, 1133

Solheim J. E., Robinson E. L., Nather R. E., Kepler S. O., 1984, A&A, 135, 1

Stetson P. B., 1987, PASP, 99, 191

—, 1996, PASP, 108, 851

Still M., Howell S. B., Wood M. A., Cannizzo J. K., Smale A. P., 2010, ApJ, 717, L113

Tamuz O., Mazeh T., North P., 2006, MNRAS, 367, 1521

Tamuz O., Mazeh T., Zucker S., 2005, MNRAS, 356, 1466

Todd I., Pollacco D., Skillen I., Bramich D. M., Bell S., Augusteijn T., 2005, MNRAS, 362, 1006

Tremblay P., Bergeron P., 2009, ApJ, 696, 1755

Tutukov A., Yungelson L., 1996, MNRAS, 280, 1035

Vivas A. K., Zinn R., Andrews P., Bailyn C., Baltay C., Coppi P., Ellman N., Girard T., Rabinowitz D., Schaefer B., Shin J., Snyder J., Sofia S., van Altena W., Abad C., Bongiovanni A., Briceño C., Bruzual G., Della Prugna F., Herrera D., Magris G., Mateu J., Pacheco R., Sánchez G., Sánchez G., Schenner H., Stock J., Vicente B., Vieira K., Ferrín I., Hernandez J., Gebhard M., Honeycutt R., Mufson S., Musser J., Rengstorf A., 2001, ApJ, 554, L33

Voges W., 1992, The ROSAT all-sky X ray survey. Tech. rep.

Warner B., 1972, MNRAS, 159, 315

—, 1995, Cambridge Astrophysics Series, 28

Warner B., Pretorius M. L., 2008, MNRAS, 383, 1469

Warner B., Woudt P. A., 2002, PASP, 114, 129

—, 2006, MNRAS, 367, 1562

—, 2008, in American Institute of Physics Conference Series, Vol. 1054, American Institute of Physics Conference Series, M. Axelsson, ed., pp. 101–110

Westin B. A. M., 1980, A&A, 81, 74

Wilson E. R., 1917, Popular Astronomy, 25, 88

Wood M. A., Casey M. J., Garnavich P. M., Haag B., 2002, MNRAS, 334, 87

Wood M. A., Winget D. E., Nather R. E., Hessman F. V., Liebert J., Kurtz D. W., Wesemael F., Wegner G., 1987, ApJ, 313, 757

Wood M. A., Winget D. E., Nather R. E., Liebert J., Hessman F. V., 1985, in Bulletin of the American Astronomical Society, Vol. 17, Bulletin of the American Astronomical Society, pp. 886–+

Wood-Vasey W. M., Aldering G., Nugent P., Li K., 2003, IAU Circ., 8077, 1

Woudt P. A., Warner B., 2001, MNRAS, 328, 159

—, 2003, MNRAS, 345, 1266

Woudt P. A., Warner B., O'Donoghue D., Buckley D. A. H., Still M., Romero-Colemero E., Väisänen P., 2010, MNRAS, 401, 500

Woudt P. A., Warner B., Pretorius M. L., 2004, MNRAS, 351, 1015

Woudt P. A., Warner B., Rykoff E., 2005, IAU Circ., 8531, 3

Wozniak P. R., 2000, Acta Astron., 50, 421

Yanny B., Rockosi C., Newberg H. J., Knapp G. R., Adelman-McCarthy J. K., Alcorn B., Allam S., Allende Prieto C., An D., Anderson K. S. J., Anderson S., Bailer-Jones C. A. L., Bastian S., Beers T. C., Bell E., Belokurov V., Bizyaev D., Blythe N., Bochanski J. J.,

Boroski W. N., Brinchmann J., Brinkmann J., Brewington H., Carey L., Cudworth K. M., Evans M., Evans N. W., Gates E., Gänsicke B. T., Gillespie B., Gilmore G., Gomez-Moran A. N., Grebel E. K., Greenwell J., Gunn J. E., Jordan C., Jordan W., Harding P., Harris H., Hendry J. S., Holder D., Ivans I. I., Ivezič Ž., Jester S., Johnson J. A., Kent S. M., Kleinman S., Kniazev A., Krzesinski J., Kron R., Kuropatkin N., Lebedeva S., Lee Y. S., Leger R. F., Lépine S., Levine S., Lin H., Long D. C., Loomis C., Lupton R., Malanushenko O., Malanushenko V., Margon B., Martinez-Delgado D., McGehee P., Monet D., Morrison H. L., Munn J. A., Neilsen E. H., Nitta A., Norris J. E., Oravetz D., Owen R., Padmanabhan N., Pan K., Peterson R. S., Pier J. R., Platson J., Fiorentin P. R., Richards G. T., Rix H., Schlegel D. J., Schneider D. P., Schreiber M. R., Schwope A., Sibley V., Simmons A., Snedden S. A., Smith J. A., Stark L., Stauffer F., Steinmetz M., Stoughton C., Subba Rao M., Szalay A., Szkody P., Thakar A. R., Thirupathi S., Tucker D., Uomoto A., Vanden Berk D., Vidrih S., Wadadekar Y., Watters S., Wilhelm R., Wyse R. F. G., Yarger J., Zucker D., 2009, AJ, 137, 4377

Yau K. K. C., Stephenson F. R., 1988, QJRAS, 29, 175

York D. G., Adelman J., Anderson Jr. J. E., Anderson S. F., Annis J., Bahcall N. A., Bakken J. A., Barkhouser R., Bastian S., Berman E., Boroski W. N., Bracker S., Briegel C., Briggs J. W., Brinkmann J., Brunner R., Burles S., Carey L., Carr M. A., Castander F. J., Chen B., Colestock P. L., Connolly A. J., Crocker J. H., Csabai I., Czarapata P. C., Davis J. E., Doi M., Dombeck T., Eisenstein D., Ellman N., Elms B. R., Evans M. L., Fan X., Federwitz G. R., Fiscelli L., Friedman S., Frieman J. A., Fukugita M., Gillespie B., Gunn J. E., Gurbani V. K., de Haas E., Haldeman M., Harris F. H., Hayes J., Heckman T. M., Hennessy G. S., Hindsley R. B., Holm S., Holmgren D. J., Huang C., Hull C., Husby D., Ichikawa S., Ichikawa T., Ivezić Ž., Kent S., Kim R. S. J., Kinney E., Klaene M., Kleinman A. N., Kleinman S., Knapp G. R., Korienek J., Kron R. G., Kunszt P. Z., Lamb D. Q., Lee B., Leger R. F., Limmongkol S., Lindenmeyer C., Long D. C., Loomis C., Loveday J., Lucinio R., Lupton R. H., MacKinnon B., Mannery E. J., Mantsch P. M., Margon B., McGehee P., McKay T. A., Meiksin A., Merelli A., Monet D. G., Munn J. A., Narayanan V. K., Nash T., Neilsen E., Neswold R., Newberg H. J., Nichol R. C., Nicinski T., Nonino M., Okada N., Okamura S., Ostriker J. P., Owen R., Pauls A. G., Peoples J., Peterson R. L., Petravick

D., Pier J. R., Pope A., Pordes R., Prosapio A., Rechenmacher R., Quinn T. R., Richards G. T., Richmond M. W., Rivetta C. H., Rockosi C. M., Ruthmansdorfer K., Sandford D., Schlegel D. J., Schneider D. P., Sekiguchi M., Sergey G., Shimasaku K., Siegmund W. A., Smee S., Smith J. A., Snedden S., Stone R., Stoughton C., Strauss M. A., Stubbs C., SubbaRao M., Szalay A. S., Szapudi I., Szokoly G. P., Thakar A. R., Tremonti C., Tucker D. L., Uomoto A., Vanden Berk D., Vogeley M. S., Waddell P., Wang S., Watanabe M., Weinberg D. H., Yanny B., Yasuda N., 2000, AJ, 120, 1579

Young D. R., Smartt S. J., Mattila S., Tanvir N. R., Bersier D., Chambers K. C., Kaiser N., Tonry J. L., 2008, A&A, 489, 359